UNIVERSITY OF BIRMINGHAM

CELLULOSE-BASED BIOINK FORMULATIONS FOR 3D BIOPRINTING

by

NA LI

A thesis submitted to the University of Birmingham for the degree of

DOCTOR OF PHILOSOPHY

Nano-Formulation Engineering Research Group

School of Chemical Engineering

College of Engineering and Physical Sciences

University of Birmingham

January 2024

UNIVERSITY OF
BIRMINGHAM

University of Birmingham Research Archive

e-theses repository

This unpublished thesis/dissertation is copyright of the author and/or third parties. The intellectual property rights of the author or third parties in respect of this work are as defined by The Copyright Designs and Patents Act 1988 or as modified by any successor legislation.

Any use made of information contained in this thesis/dissertation must be in accordance with that legislation and must be properly acknowledged. Further distribution or reproduction in any format is prohibited without the permission of the copyright holder.

© Copyright by NA LI, 2024

All Rights Reserved

Abstract

In tissue engineering, although three-dimensional (3D) bioprinting has emerged as a revolutionary technology for precise manufacture of living biomimetic scaffolds, challenges persist in fulfilling the technical requirements concerning the processability of bioink formulations (scaffold precursors), the desired mechanical properties in scaffolds, and the cell-guided functionality of the biomaterials. To surmount the technical constraints of 3D bioprinting, cellulose-composited, including microfibrillated cellulose (MFC) (width of 0.3-2 μm) and nanofibrillated cellulose (NFC) (width of 30-100 nm), gelatin methacryloyl (G)/sodium alginate (A) bioink formulations were developed and constructed to cellulose-composited ionic-covalent entanglement (ICE) G/A hydrogel scaffolds. Cellulose is proven to enhance the printability of G/A bioink formulation. Hydrogen bonds between cellulose and G/A impart a yield stress of the formulation, improving the stability of formulations before printing. The shear-induced orientation behaviours of MFC and NFC by hydrogen bond breaking can enhance the shear-thinning of G/A formulation, enabling it to smoothly pass through nozzles during printing. Also, due to the reformation of hydrogen bonds within cellulose network and between cellulose and G/A, cellulose introduces excellent thixotropy to G/A bioink and thus high recoverability after shear deformation, allowing it to maintain filament shape post-printing. MFC-composited G/A formulations with varying contents of MFC produce scaffolds with distinct printability indices under identical printing conditions, which can be explained by disparities in the yield stress and thixotropy among these formulations. The linear relationship between the layer numbers and the height of the 3D structure prepared by cellulose-composited G/A formulations can

guide the building of complex structures with great shape fidelity.

Cellulose not only improves the macroscopic Young's modulus of ICE hydrogel but also diversifies its microscopic Young's modulus distributions, attributed to three different reinforcement types in hydrogel: cellulose network distributes energy evenly across the hydrogel; ICE network dissipates energy by ionic bonds breaking; synergy of fibril network and ICE G/A dissipates energy by hydrogen bonds. The increases in MFC concentration and fibril size from NFC to MFC are all beneficial to the strength of cellulose network and synergy of cellulose and ICE. From the perspective of micromorphology, the mechanical enhancement of ICE hydrogel by cellulose is because cellulose fibril networks fill large pores in ICE hydrogel and concentrate pores in a small range of 25 to 50 micros, thus avoiding stress concentration.

While the mechanical properties of cellulose-composited ICE hydrogels are enhanced, the high water-holding capabilities (87.83 to 89.71%) are also maintained, which is vital for hydrogels to balance between mechanical and biological functions. Also, cellulose extends the half-life of ICE hydrogels in enzymatic biodegradation from less than 7 to 12 days, which contributes to the biostability of hydrogels for performing mechanical support functions in the initial stage. Moreover, cells elongate in bioprinted cellulose-composited ICE scaffolds after 14 days and proliferate significantly after 21 days. Meanwhile, porosities of scaffolds rise after 21 days due to hydrogel degradation. Thus, degradation process of cellulose-composited ICE hydrogel scaffolds aligns exceptionally well with tissue remodelling process. Furthermore, cellulose prolongs the half-life of ampicillin release process from hydrogels and changes drug release kinetics from diffusion-controlled to anomalous transport, which facilitates the controlled, gradual release of drugs within hydrogel systems.

Overall, cellulose, particularly MFC, demonstrates great potential in simultaneously improving the printability of bioink formulations, the mechanical properties, and the biological functionality of hydrogel scaffolds. This thesis provides meaningful guidance for designing bioprinted biomimetic scaffolds that more closely align with the extracellular matrix of human tissues.

Dedicated to my paternal grandmother and maternal grandmother.

Acknowledgements

Foremost, I extend my sincerest gratitude to my supervisor, Prof. Zhenyu Jason Zhang for providing me the valuable opportunity to do the research that I am enthusiastic about. In academics, his scholarly insights and supervision were invaluable in shaping the substance of my research. In daily life, particularly during the challenging times of the COVID-19 pandemic, his encouragement and support are a vital source of strength for me.

I would like to extend my heartfelt thanks to the University of Birmingham and the China Scholarship Council (201906950042) for their generous PhD studentship and comprehensive financial support. Their assistance makes my international PhD studies possible.

Many thanks are due to all colleagues in the Nano-Formulation Engineering Research Group for their advice on the experiment and concerns in life.

Special thanks go to Professor Alicia El Haj, Dr David Bassett, Dr Richard Moakes, Dr Pranav Vasanthi, Dr Lucy Arkinstall, Ms Emma Lardner, Ms Sakaorna Jeyanathan, Ms Miruna Chipara, and Ms Melissa Vieira in the Healthcare Technologies Institute for their guidance and help in the experiment of cell culture and bioprinting.

I would like to express my gratitude to my boyfriend, Fengshen, whose companionship during these four years has been invaluable to me.

Finally, I show my deepest gratitude towards my parents for their unconditional love, support, and faith in me throughout my life.

Contents

List of Figures

List of Tables

Acronyms

$\dot{\varepsilon}$ creep strain rate. 71

αMEM Alpha Minimum Essential Medium. 169, 170

$CaCl_2$ calcium chloride. xvii, 43, 44, 81, 84, 99, 102, 103, 116, 138, 174

D_2O deuterium oxide. 81, 85

Δh depth variation. 70, 142, 150, 155

µCT micro-computed tomography. xxi, xxvi, 5, 62, 64, 137, 156, 159, 161, 162, 164, 172

E_i the Young's modulus of indenter diamond tip. 71

E_r reduced modulus. xx, 70, 71, 144, 145, 150

E_s Young's modulus of the sample. 70, 71, 150

F_{max} maximum load. xix, xx, xxv, 69, 70, 142–145, 149, 150, 155

H_I indentation hardness. 70, 150, 151

R_i radius of the spherical indenter. 70, 133

SR_n swelling ratio at a different time. 170, 171

W_0 initial dry weights. 171

W_1 remaining dry mass after 1 day. 171

W_3 remaining dry mass after 3 days. 171

W_7 remaining dry mass after 7 days. 171

W_n remaining dry masses. 171

W_{10} remaining dry mass after 10 days. 171

W_{dry} initial mass. 170

$W_{wet,n}$ wet mass at a different time n. 170

h_0 initial depth. xix, 69, 142, 143, 149, 150, 155

h_c contact depth. 70, 150

h_e depth of elastic recovery. 70, 150

h_r depth of residual impression. 70, 150

h_s depth of the contact circle. 70

h_{cr} creep depth. 71

h_{max} maximum depth. xix, 70, 142, 143, 147, 150

n_f flow index. 65, 66, 110, 112, 113

n_r release index. 77, 78, 204, 206

v_i the Poisson's ratio for indenter. 71

v_s the Poisson's ratio for sample. 71

^{1}H-NMR proton nuclear magnetic resonance. 55, 85, 88

E. Coli *Escherichia coli.* xxiv, 170, 177, 178, 206, 207, 209, 210

S. Aureus *Staphylococcus aureus.* xxiv, 170, 177, 178, 206, 208–210

A/h_0 *creep strain rate sensitivity.* 155

BDR *biodegradation rate.* 171, 183

CR *cumulative release.* 176

C *creep rate.* 71, 142

DoM *degree of modification.* 4, 85, 88, 89, 95

EE *encapsulation efficiency.* 176, 202, 203

EHD *equilibrium hydration degree.* 171, 181, 183

G" *loss modulus.* 98, 99, 106, 114

G' *storage modulus.* 98, 99, 106, 114, 116, 117

LC *drug loading capacity.* 176, 202–204

POI *parameter optimisation index.* xvi, 73, 74, 101, 118, 129

Pr *printability index.* xvi, 74, 101, 124–126, 129

Ro *roundness.* 74

S *contact stiffness.* 70, 150

f *load.* 69

h *depth of penetration.* 69

t *dwelling time.* 71

1D *one-dimensional.* xvi, 6, 73, 98, 100, 101, 118, 123

2D *two-dimensional.* xvi, xviii, 6, 44, 73, 74, 98, 101, 123, 124

3D *three-dimensional.* i, xii, xvi, 1–4, 6, 8–12, 14, 31–34, 38, 48, 51, 62, 72, 73, 98, 100–102, 126

4D *four-dimensional.* 12, 51

A *sodium alginate.* i, xvi, xvii, 3–7, 53, 60, 62, 64, 66, 68, 71, 78, 80–85, 91, 94, 95, 98, 104–109, 112–116, 125–127, 129, 131, 132, 138, 165, 173, 213, 214

AFM *atomic force microscopy.* 4, 55–57, 68, 69, 86

ATR *attenuated total reflection.* 52, 53, 85

ATR-FTIR *attenuated total reflection Fourier-transform infrared.* 52, 53, 85

CNC *cellulose nanocrystals.* 25, 27

dPBS *Dulbecco's phosphate-buffered saline.* 170

ECM *extracellular matrix.* xi, 8, 13, 14, 51

EDX *energy-dispersive X-ray.* 61, 62

FBS *fetal bovine serum.* 169, 170

FTIR *Fourier-transform infrared.* 4, 52, 85, 88, 92, 94

G *gelatin methacryloyl.* i, xv–xvii, 3–7, 37, 53, 55, 60, 62, 64, 66, 68, 71, 78, 80–85, 87–89, 91, 94, 95, 98, 104–109, 112–116, 125–127, 129, 131, 132, 138, 139, 165, 173, 187, 198, 213, 214

ICE *ionic-covalent entanglement.* i, 4–7, 53, 60, 62, 64, 68, 71, 78, 84, 85, 91, 94, 95, 126, 131, 132, 138, 139, 147, 151, 156, 162, 165, 169, 179–181, 183, 185, 187, 198, 199, 210, 211, 213

ICEs *ion-covalent entanglement networks.* 42, 43

IPNs *interpenetrating networks.* xii, 36, 42

LB *Luria-Bertani.* 170, 177, 178

MA *methacrylic anhydride.* 81

MFC *microfibrillated cellulose.* i, xv–xvii, 3, 4, 6, 24, 27, 53, 57, 58, 60, 62, 64, 66, 68, 72, 81, 82, 84–86, 91–98, 104–107, 109–111, 113–116, 125, 127, 129, 131, 132, 138, 139, 147, 156, 162, 165, 173, 179–181, 185, 198, 199, 203, 211, 213, 214

NaOH *sodium hydroxide.* 81

NFC *nanofibrillated cellulose.* i, xv, xvi, 3, 4, 6, 24, 25, 27, 29, 53, 57, 58, 60, 62, 64, 66, 68, 72, 81, 82, 85, 86, 91–98, 104, 105, 109, 126, 127, 131, 132, 156, 165, 173, 183, 198, 199, 211, 213

NMR *nuclear magnetic resonance.* 4, 54, 88

NPs *nanoparticles.* 44

PBS *phosphate buffered saline.* 81, 82, 84

PCL *polycaprolactone.* 21, 22, 49, 50

PEG *poly(ethylene glycol).* xii, 21

PLA *polylactic acid.* 21, 22, 49

PLCL *poly(lactide-co-caprolactone).* 21, 22

ppm *parts per million.* 54

RGD *arginine-glycine-aspartate.* 15, 18

SEM *scanning electron microscope.* 5, 60–62, 64, 136, 156, 172, 175

TSB *Tryptic Soy Broth.* 170, 177, 178

UV/Vis *ultraviolet and visible.* 6, 75

Chapter 1

INTRODUCTION

1.1 Background

Tissue engineering integrates principles from biology, chemistry, material, and engineering to develop living functional substitutes for damaged tissues/organs [1, 2]. Tissue-engineered substitutes offer significant advantages over non-living artificial substitutes (joint prostheses) and transplantation (autografts and allografts), including enhanced biocompatibility, reducing the risk of rejection [3–5]. Tissue engineering allows for personalized, anatomically tailored implants, promoting better integration and natural tissue regeneration [6]. This approach lessens the reliance on donor tissues, addressing shortages in transplantation [7]. However, tissue-engineered substitutes still face challenges, including replicating the complex structure and function of native tissues [8, 9], vascularization [10, 11], and achieving suitable cell-material interactions [12, 13].

Among advanced material fabrication techniques employed in the field of tissue engineering, three-dimensional (3D) bioprinting has emerged as a transformative approach compared to electrospinning, self-assembly, photolithography et al [14]. Three-dimensional bioprinting enables the precise fabrication of complex tissue constructs by layer-by-layer deposition of biomaterials, cells, and bioactive molecules, collectively termed as "bioink" [15, 16]. Three-dimensional bioprinting

offers unparalleled control over the spatial distribution of cells and matrix components, essential for recreating the native tissue architecture [17].

In the realm of 3D bioprinting for tissue engineering, the convergence of several intricate challenges forms the key to ongoing research and development. The central challenge to 3D bioprinting is the formulation of bioinks that not only emulate the complexity of natural extracellular matrices but also maintain a delicate balance between processability, biocompatibility, and mechanical strength, ensuring structural integrity and promoting cell growth and differentiation [5, 18, 19]. Equally pivotal is the preservation of cell viability throughout the bioprinting process, especially given the mechanical stresses and environmental changes involved in bioprinting [18, 20]. Simultaneously, developing vascular networks within bioprinted tissues is essential for nutrient and oxygen supply, cell survival and function, requiring advanced techniques to mimic native capillary systems [11]. This is closely tied to the need for high-resolution printing that can replicate complex tissue microarchitecture, including gradients and structural features [21, 22]. Moreover, scaling up from small-scale laboratory prototypes to larger, clinically relevant tissue constructs without compromising on the quality and functionality of the printed tissues is a complex endeavour [23], which includes ensuring reproducibility in the bioprinting process [24], a key aspect in the transition from experimental models to practical, real-world applications.

In summary, the intersection of these challenges - formulation innovation, cell viability, vascularization, resolution and fidelity, along with reproducibility - delineates the current landscape of 3D bioprinting in tissue engineering. Addressing these issues is pivotal for advancing tissue-engineered constructs from the realm of experimental research to viable clinical solutions in regenerative medicine [25, 26].

1.2 Motivation

Derived from the most abundant biopolymer on Earth, cellulose offers several advantages in tissue engineering and 3D bioprinting applications due to its sustainability, biocompatibility, low toxicity, tunable mechanical, optical, thermal, and fluidic properties, along with its potential for large-scale production [27–30]. The hierarchical structure of cellulose, such as microfibrillar and nanofibrillar can provide mechanical strength and flexibility, essential for building stable and resilient tissue-engineered scaffolds [31]. Cellulose's natural abundance and biodegradability ensure the sustainability and environmental friendliness of bioprinted constructs [32]. The biocompatibility of cellulose is critical for supporting cell adhesion and proliferation [33]. Cellulose-based materials have shown promise in providing scaffolds that support cell growth and tissue formation, thanks to their structural similarity to the extracellular matrix of many tissues [34]. Additionally, the versatility of cellulose allows for chemical modifications [35, 36], enhancing its functionality as a bioink and making it suitable for various tissue engineering applications.

Therefore, the present project is driven by the significant potential of cellulose, especially fibrillated cellulose, in overcoming the current challenges in 3D bioprinting for tissue engineering. Taking bioink formulation innovation as a breakthrough point, the project concentrates on studying the ability of fibrillated cellulose with varying sizes in adjusting the balance between printability of formulations, mechanical strength, and biological function of corresponding hydrogel scaffolds. The integration of cellulose-based bioink formulations with extrusion bioprinting techniques is emphasised to fabricate tissue alternatives with excellent shape fidelity, mechanical strength, and cytocompatibility.

1.3 Aim and objectives

The project aims to develop novel cellulose-composited, including microfibrillated cellulose (MFC) and nanofibrillated cellulose (NFC), gelatin methacryloyl (G)/sodium alginate (A) bioink formu-

lations with high processability during extrusion printing, and to fabricate corresponding tissue-engineered cellulose-composited ionic-covalent entanglement (ICE) G/A hydrogel scaffolds with strong mechanical properties and superior biological characteristics beneficial to cell growth and proliferation.

The objectives of this work are the following:

1) **Preparation and general characterisation of MFC-composited and NFC-composited ICE G/A bioink formulations/hydrogels with different cellulose contents.**

   Before doping cellulose with G/A formulation, it is necessary to assess the dimensions and dispersion levels of MFC and NFC within aqueous solutions, the chemical structure and the degree of modification (*DoM*) of ingredient G. This involves using atomic force microscopy (AFM), fluorescence microscopy, Fourier-transform infrared (FTIR) spectroscopy and nuclear magnetic resonance (NMR) spectroscopy to characterise the physical morphology and chemical functional groups of each component in bioink formulations. Additionally, it is of particular importance to examine the molecular structure of the cellulose-composited ICE G/A hydrogels and interactions between cellulose and the G/A system, which helps to understand the role cellulose plays in ICE G/A hydrogels.

2) **Elucidate the role of cellulose in augmenting the printability of G/A bioink formulation, guided by the study of the rheological properties of bioink formulations.**

   To investigate the impact of cellulose on the printability of G/A bioink formulation, the processing environments at three distinct stages - pre-extrusion, during extrusion, and post-extrusion - are simulated through the establishment of corresponding rheological testing protocols. This approach enables a detailed examination of the yield behaviour, shear-thinning properties, recoverability, and gelation kinetics of the cellulose-composited bioink formulations. The rheological findings are then directly employed to guide the processability of cellulose-composited G/A bioink formulations. Subsequently, hydrogel scaffolds and 3D constructs are fabricated via an

extrusion printer. These printed structures are analysed through different evaluation systems to ascertain the contribution of cellulose to the shape fidelity of the printed bodies.

3) **Evaluate the mechanical reinforcement of ICE G/A hydrogels by cellulose and reveal the reinforcement mechanism of the hydrogel system.**

The effect of cellulose on mechanical properties, specifically Young's modulus, yield strength, and compressive strength of ICE G/A hydrogels is analysed through macroscopic compression testing. Additionally, leveraging the advantages of micro-indentation techniques, elastic properties, such as the distribution of Young's modulus and hardness of cellulose-composited ICE G/A hydrogels in micro-scale can be examined to uncover potential reinforcement effects within the system. Furthermore, an investigation into the creep behaviour of cellulose-composited ICE G/A hydrogels provides deeper insight into how cellulose affects plastic deformation characteristics of G/A hydrogels. Moreover, a comprehensive analysis of micromorphology and pore structure of hydrogel samples is conducted to demonstrate the underlying reinforcement mechanisms, which involves employing scanning electron microscope (SEM) and micro-computed tomography (μCT) to gather information on the pore size distribution and porosity of the samples.

4) **Identify biological characteristics of cellulose-composited ICE G/A hydrogels.**

Biological characteristics of cellulose-composited ICE G/A hydrogels involve water retention capacity, enzymatic biodegradation, cytocompatibility, controlled drug release, and *in vitro* antimicrobial properties, all of which are closely related to the pore structure of the hydrogel system and interactions of cellulose and G/A. Thus, to analyse the effects of cellulose on the biological properties of ICE G/A hydrogels, it is necessary to combine enhancement mechanisms of hydrogel system built in the third objective. Comprehending the biological characteristics of specimens is crucial in determining whether the incorporation of cellulose contributes to the hydrogel system towards an extracellular matrix environment to support cell proliferation and differentiation.

1.4 Thesis overview

Chapter 2 comprehensively reviews existing literature on the evolution of polymer materials in bioink formulations, of which applications of cellulose materials in tissue engineering are emphasised. The historical and current state of 3D bioprinting technologies and network enhancement strategies of bioink/hydrogels are also reviewed.

Chapter 3 details the principles of material characterisation techniques employed in this research. These material characterisation techniques can be divided into the following categories: chemical analysis, physical characterisation, and mechanical characterisation. Additionally, the theory of 3D printing, ultraviolet and visible (UV/Vis) spectrometer, and controlled drug release is also encompassed.

Chapter 4 describes experimental procedures, including synthesis of component G, preparation of cellulose slurries (MFC, NFC, and hybrid cellulose of MFC and NFC), preparation and crosslinking of bioink formulations. General characterisation is employed to confirm the successful synthesis of different samples.

Chapter 5 investigates the effects of cellulose on the printabilities of G/A bioink formulations. The macroscope fluidities and rheological properties, such as yield, shear-thinning, recoverability, and gelation kinetics of cellulose-composited G/A bioink formulations are discussed. For printabilities of bioink formulations, the effects of printing parameters on the accuracy of one-dimensional (1D) filament are emphasized, followed by the discussion of the printability index of 2D sheet scaffolds and shape fidelity of 3D constructs.

Chapter 6 focuses on the key benefits of cellulose for increasing the mechanical properties of ICE G/A hydrogels. Macroscopic compression tests demonstrate that cellulose improves Young's modulus and compressive strength of ICE G/A hydrogels. Micro-indentation testing further illustrates the multiple mechanical strengthening effects present in cellulose-composited ICE G/A hydrogel system by mapping the micro-distribution of Young's modulus and hardness. Pore struc-

ture analysis demonstrated that cellulose strengthens hydrogels by reducing the pore size distribution of the hydrogels.

Chapter 7 delves into the role of cellulose in improving the biological properties of ICE G/A hydrogels. Incorporating cellulose into G/A hydrogel effectively maintains the equilibrium hydration degree (about 87%) of the hydrogel at a level highly similar to that of human tissues. Cellulose improves the physiological stability of G/A hydrogels by slowing down their natural and enzymatic biodegradation processes. The successful growth and proliferation of cells within bioprinted cellulose-composited ICE G/A hydrogel scaffolds further demonstrate the cytocompatibility of the hydrogel sample. Additionally, cellulose significantly alters the ampicillin release kinetics of G/A hydrogels, aiding in controlled and sustained ampicillin delivery. Meanwhile, cellulose does not adversely affect the expression of antimicrobial properties in ampicillin-loaded hydrogels.

Chapter 8 presents a comprehensive summary of key findings in this project and provides some recommendations for future scientific investigations in the field of tissue engineering.

Chapter 2

LITERATURE REVIEW[1]

2.1 Introduction

There are a number of challenges associated with the current restoration methods for tissue defects, such as autografts and allografts [37, 38], which include limited supply of donor tissues, risk of complications, transplant rejection, and biocontamination [39]. Tissue engineering, an emerging route, first presented by Robert Langer and Joseph P. Vacanti in 1993 [40], has demonstrated great potential: replacing damaged tissue with three-dimensional (3D) living scaffold implants containing cells; using tissue extracellular matrix (ECM) mimics and the bioactive factors to activate growth of cells [41]. Here, the ECM mimics are commonly cytocompatible polymeric matrices, such as hydrogels, polyesters, and polymer-ceramic composites [42–44], which requires extensive research input from the material, in particular polymer, research community. It has been demonstrated extensively that hydrogels with excellent biocompatibility and biodegradability, outstanding hydrophilicity, controllable permeability and simple manufacturing methods are highly

[1]This chapter partially refers to the review article (doi: 10.3389/fbioe.2021.630488) published by Na Li (author herself), Rui Guo, and Zhenyu Jason Zhang. Statement of author contributions is below: NL drafted the original manuscript with contributions by RG and ZZ. NL and ZZ contributed to the revision of the draft. ZZ and RG contributed to the supervision, validation, and funding acquisition. All authors contributed to the article and approved the submitted version.

desirable for biomedical applications [45].

Over the past two decades, a plethora of fabrication routes of bionic 3D scaffolds have been developed [46–48], which include phase separation [49], electrospinning [50], freeze-drying [51], salt leaching [52]. These strategies demonstrated an excellent capability of producing interconnected pores of requisite surface morphology, with adjusted processing variables [53]. However, these methods offered limited control over material diversity and structural gradient within the same scaffold, thus hindering the development of scaffolds for tissues with poor regeneration capabilities [54]. The need for precise distribution of cells, bioactive signals, and polymeric matrices leads to the growing use of 3D bioprinting in tissue engineering.

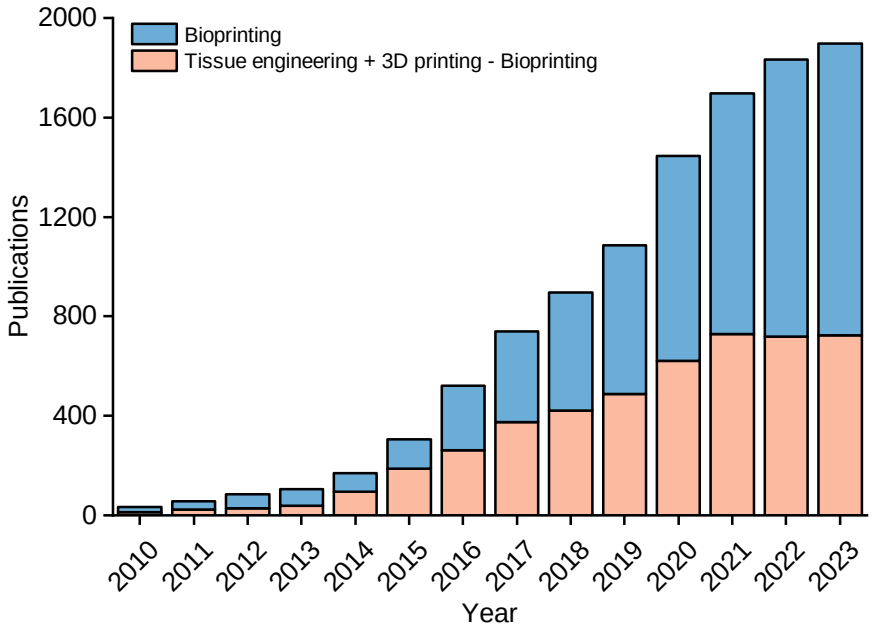

Figure 2.1: The number of publications by searching either 'bioprinting' or 'tissue engineering AND 3D printing NOT bioprinting' from 2010 to 2023 in PubMed.

First demonstrated by Charles Hull in 1986 with stereolithography [55, 56], 3D printing/additive manufacturing entered the tissue engineering field in 1998 when researchers used it to build porous scaffolds from poly(lactide-co-glycolide) for hepatocyte culture [54, 57]. After that, 3D printing has become increasingly popular for constructing tissue-engineered scaffolds. The emergence of

the term 'bioprinting' in 2003 reflects an expansion of this technique in the realm of bioengineering research [58–60]. Remarkably, since 2018, the field of 3D bioprinting for tissue engineering has seen over 800 publications annually (Figure 2.1).

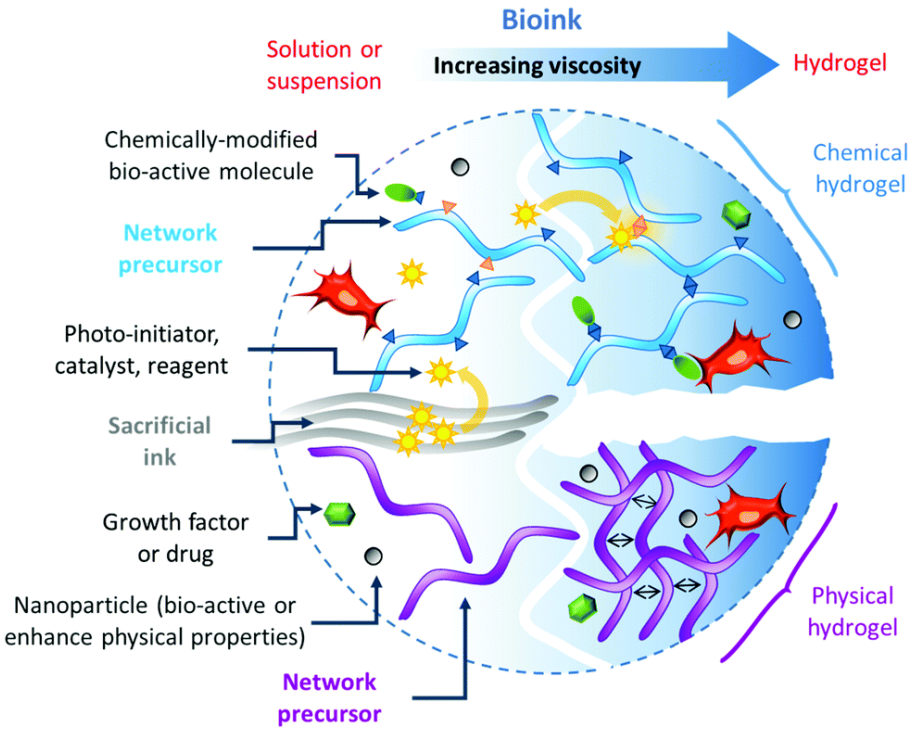

Figure 2.2: Compositions of the proposed bioink and changes in bioink structure before and after gelation [61].

When manufacturing tissue-engineered scaffolds via 3D bioprinting technology, the materials loaded into the bioprinter, including cells, polymer matrices, and bioactive factors, are collectively referred to as bioink formulation. Figure 2.2 illustrates the transition of bioink to hydrogel, a key process in 3D bioprinting for tissue engineering [61]. Bioink starts as a low-viscosity solution or suspension. Upon exposure to specific stimuli like light, heat, or magnetic fields [62], network precursors in bioink form crosslinks, leading to increased viscosity. This process results in a hydrogel with a 3D network, essential for sustaining cell growth and preserving structural integrity. Hydrogels are categorized as chemical, formed by covalent bonds, or physical, derived from non-covalent interactions such as entanglement, hydrogen bond, and van der Waals interactions [61],

providing a complex heterogeneous graded scaffold for tissue engineering applications [21].

2.2 Property requirements of bioinks/scaffolds [63]

To produce a hard or elastic 3D scaffold, with orderly distributed components and a fixed geometric shape, bioink formulation of defined rheological properties would undergo a complex manufacturing process. The following characteristics are therefore desirable for the bioinks:

1) Printability: The concept of "printability" in bioink refers to the material's suitability for 3D bioprinting, which encompasses a range of factors including the ability of bioinks to be extruded in a laminar flow through a nozzle, maintain the intended shape (shape fidelity), and support cellular functions [42]. Printability is influenced by the rheological properties of bioinks, which include viscosity, shear-thinning behaviour, and yield stress [64]. These rheological properties must balance the need for easy extrusion with the requirement to form stable structures post-extrusion. Additionally, printability encompasses the material's ability to maintain cell viability during the printing process. High printability is crucial for establishing structurally stable, and functionally effective tissue constructs [65, 66].

2) Biocompatibility: Following construction the scaffold will cooperate with the host, without triggering adverse reactions, to actively promote the adhesion and proliferation of cells, for instance, osteocytes in a scaffold. This would facilitate the formation of extracellular matrix on the surface and pores of scaffolds, and gradually induce the development of new bone [67]. Furthermore, the microenvironment within the scaffold would encourage the formation of blood vessels in or around the implant within a few weeks after implantation, thereby providing a favourable condition for the transportation of nutrients, oxygen and waste [68].

3) Mechanical properties: An appropriate network enhancement mechanism could be formed between the components of the scaffold to prevent material failure and fracture of the scaffold

under large deformation [69]. The specific mechanical properties of a hydrogel scaffold can vary significantly depending on the type of hydrogel, its composition, the crosslinking density, and the fabrication method [70]. It is preferable that the mechanical properties of the fabricated scaffold should match those of the host tissue, enabling suitable load transfer.

4) Biodegradability: The printed scaffold is expected to degrade *in vivo* with time. Ideally, the degradation rate of scaffolds could match the production rate of ECM [71], whilst the products following degradation have no side effects on the host [72, 73].

5) Surface characteristics: The interface between the scaffold and the damaged tissue is critical to the success of scaffold transplantation, with numerous reactions and interactions taking place. Therefore, surface characteristics of scaffolds, such as porosity, wettability, and morphology require significant attention when designing the scaffold. For instance, the diameter of the initially interconnected pores should maintain at least 100 μm, allowing nutrients and oxygen that are necessary for cell survival to diffuse and the waste produced by cells to transfer [74]. A pore size range of 200-350 μm was recommended for the growth of bone tissue [75]. Surface of the scaffold should be engineered to control cell adherence and proliferation. The morphology of the scaffold is also of great significance for anchoring cells and proteins on the surface [48].

6) Stimulus responsiveness: When the hydrogel is subjected to external stimuli or internal stimuli from the contained cells, it can respond to the stimuli in a timely manner by changing its physiochemical properties [76]. These stimuli can include changes in pH, temperature, light, magnetic or electric fields, and the presence of specific molecules, such as enzymes and glucose [62]. In the context of tissue restoration, this responsiveness, particularly reversible responsiveness, enables the hydrogel scaffolds to adapt dynamically to the physiological environment or to specific needs of the tissue regeneration process [77, 78]. Correspondingly, 3D bioprinting technique for constructing stimuli-responsive scaffolds can be evolved into four-dimensional (4D) bioprinting as an updated strategy for tissue engineering, whereby time is integrated as a

processing parameter [79].

The properties aforementioned do not exist independently at a certain stage. From the initial bioink to the scaffold constructed, and finally to the functional implant, these characteristics are interrelated and could influence each other throughout the entire process that involves structure and function transformations of materials, as shown in Figure 2.3.

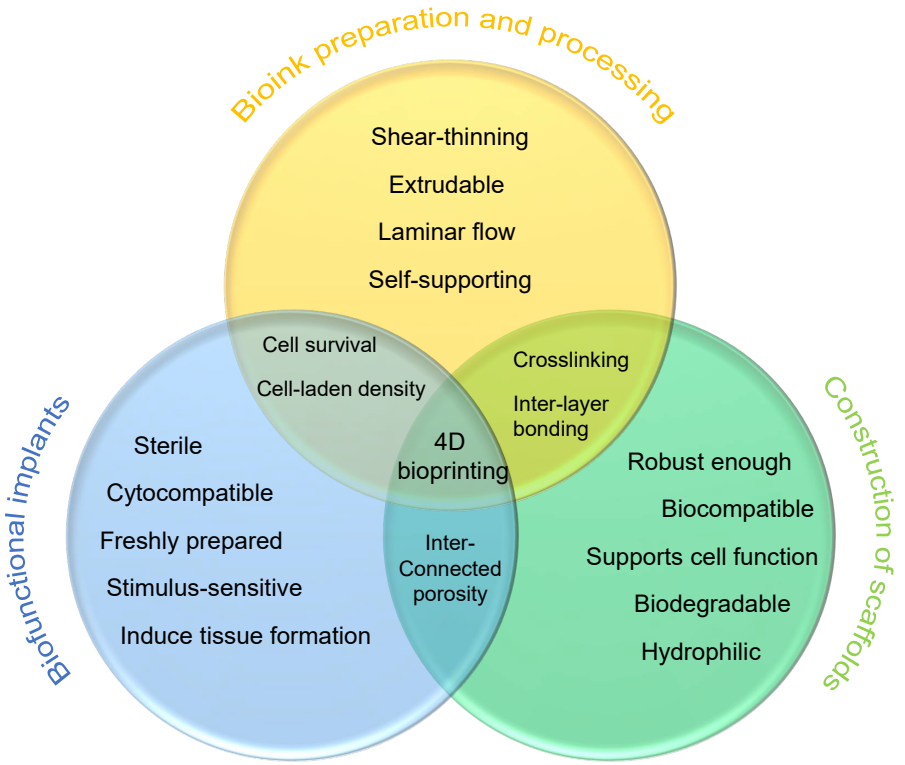

Figure 2.3: Requirements for bioink formulation design: the shear-thinning bioink is extruded in the form of laminar flow and forms the desired scaffold shape through its self-supporting (yellow zone); bioink formulations can be crosslinked to enhance the mechanical strength of the hydrogel scaffold; biocompatibility and biodegradability of scaffold promote encapsulated cell diffusion and proliferation (green zone); to achieve damaged tissue regeneration, the formula should be able to induce new tissue ECM formation and respond to external stimuli as the new tissue matures (blue zone) [63].

2.3 Polymer materials in bioink formulations

Initial applications of 3D printing in tissue engineering utilise single-material, acellular formulations to build scaffolds that encourage cell growth and tissue repair [80, 81]. The development of 3D modelling and printing technologies makes it feasible to explore complex, multi-material constructs in biological systems. These advanced bioprinted structures, irrespective of their complexity, primarily use bioinks composed of either natural or synthetic polymers [54]. These polymers, already well-established in hydrogel forms, are pivotal in bioprinting due to their material characteristics [54]. This section focuses on the fundamental properties of these polymeric components within bioink formulations in the context of bioprinting. Emphasis will be placed on understanding how the chemical structure of each polymer influences its effectiveness as a bioink and on discussing their biocompatibility and biodegradability.

2.3.1 Natural polymers

Inspired by the composition (structural proteins, proteoglycans, and glycosaminoglycans et al.) of natural ECM [82], the preferred choice for preparation of bioink formulations is often naturally derived polymers that can help maintain the biochemical cues and inherent properties characteristic of native biomaterials [83]. Thus, this approach not only ensures biocompatibility but also preserves the bioactivity essential for effective tissue engineering.

Naturally derived polymers commonly used in bioink formulations can be divided into the following categories based on the composition of natural ECM and their chemical structures [84] are displayed in Figure 2.4:

- Proteins: Collagen [85–87], gelatin [88–90], fibrin [91, 92], silk fibroin [93–95].
- Polysaccharides: Alginate [89, 96, 97], agarose [98–100], chitosan [101–103].
- Glycosaminoglycans: Hyaluronic acid [104–106].

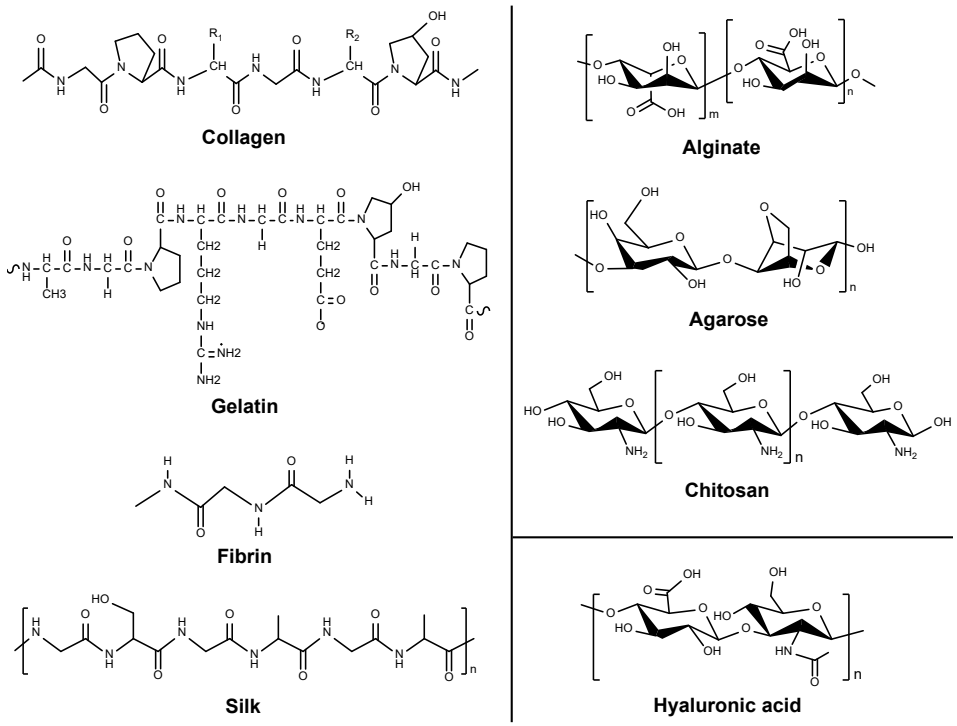

Figure 2.4: Representative chemical structures of common naturally derived polymers in bioink formulations.

Collagen plays a vital role as a structural component in diverse animal tissues, including bone, cartilage, tendons, and skin. The unique triple α-helix supramolecular structure of collagen [107], composed of repeating glycine-X-Y sequences (where X and Y are typically proline and hydroxyproline), is fundamental to its overall mechanical strength, elasticity, and functionality [108]. Gelatin, obtained from the denaturation of collagen [109], shares similar biocompatibility and cell-adhesion properties when deployed as a bioink formulation for bioprinting. This is due to their arginine-glycine-aspartate (RGD) amino acid sequence which facilitates cell attachment and signaling [109, 110]. Additionally, degradation of collagen and gelatin *in vivo* can occur through enzymes like matrix metalloproteinases and collagenase type II [111]. Therefore, it is necessary to combine either collagen or gelatin with other materials like synthetic polymers to enhance the mechanical strength and versatility of corresponding scaffolds. The effectiveness of these combinations [85–87, 89] has been proven.

Unlike collagen, gelatin transitions from a solution to a gel with decreasing temperature (about 26°C) [112]. The controlled deposition of gelatin, facilitated by its physical gelation properties, is crucial in bioprinting. Gelatin can be fine-tuned for specific applications using heated or cooled printing platforms. Sol-gel transitions of gelatin also enable its use as sacrificial inks in more complex bioprinting processes [113].

Fibrin emerges from its monomeric form, fibrinogen, which itself is a dimer comprising three polypeptide chains [114]. The transformation from fibrinogen to fibrin, a process catalyzed rapidly by thrombin [114], takes place in less than 10 seconds, signifying an efficient gelation mechanism that is central to its use in bioink formulations [54]. Particularly, the potential of fibrin in *in situ* bioprinting applications is noteworthy [115]. In such scenarios, printed fibrinogen can rapidly crosslink with naturally occurring thrombin, facilitating immediate and localized gelation [115]. Despite this efficiency, the stability of the fibrin network is not permanent. Over time, encapsulated cells within the fibrin matrix can secrete plasminogen and matrix metalloproteinases, leading to the gradual degradation of the fibrin network [116]. This process may pose challenges, particularly in terms of the longevity and structural integrity of tissue-engineered implants. However, the structural properties of fibrin networks can be governed by a range of crosslinking factors, such as the ionic strength of the medium, pH levels, and the ratios of fibrinogen to thrombin and thrombin to Ca^{2+} [91]. By optimizing these variables, it is possible to regulate the density, porosity, and permeability of the fibrin network. Such control over the network's physical characteristics directly impacts cell behaviour, including adhesion, proliferation, and differentiation, and thus the overall efficacy of the tissue engineering process [91].

Alginate, a polysaccharide extracted from brown algae, stands out as the most utilized biopolymer in bioprinting [61]. Its molecular structure, featuring β-D-mannuronate (M block) linked to α-L-guluronate (G block) (Figure 2.5), allows for a variable molecular weight ranging from 10 to 200 kDa [61]. This structural composition is integral to gelation properties of alginate, which are triggered by adding non-toxic divalent cations like calcium or magnesium ions. The process

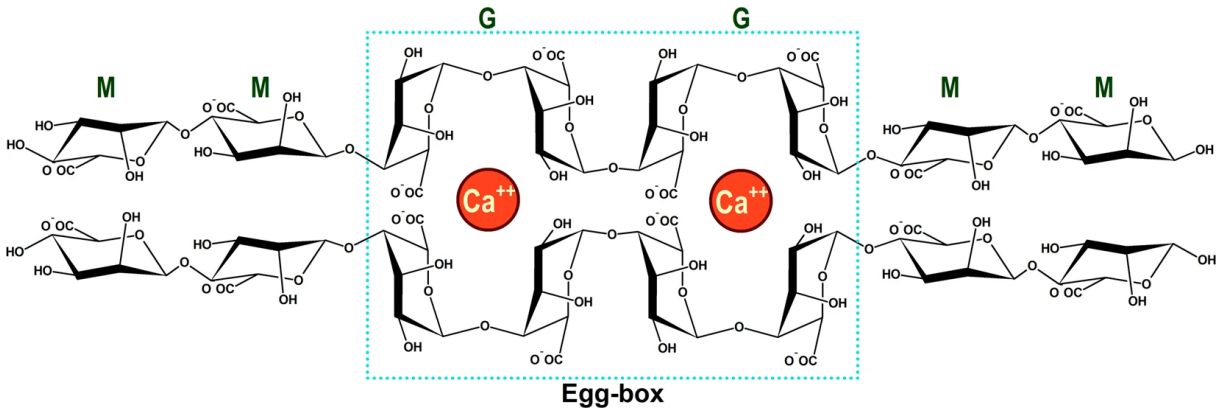

Figure 2.5: Schematic of 'Egg-box' structure in crosslinked alginate hydrogel. Only G blocks (α-L-guluronate) in alginate combine with calcium ions [117].

involves negatively charged G blocks of alginate binding to positively charged ions, leading to nearly instantaneous gelation [117]. This reaction forms an "egg-box" 3D shape (Figure 2.5), where at least two polysaccharide chains are crosslinked [117]. The viscosity of alginate can be modulated based on the concentration of divalent cations, enabling its use with various bioprinters [61]. In bioprinting, gelation of alginate is typically manipulated in two ways: by incorporating a small amount of low-concentration divalent cations into the bioink formulation, slightly increasing its viscosity and thus improving the processability of the formulation; by employing high concentrations of divalent cations during or post-printing to enhance the mechanical properties of the resulting hydrogel scaffolds [54]. Furthermore, despite the widespread use of alginate in bioprinting, alginate has limitations in mammalian systems, primarily its non-biodegradability [118]. Nevertheless, crosslinked alginate hydrogels can gradually lose their structural integrity and gelation over time within *in vivo* implant sites due to physical ion-exchange processes. Additionally, alginate lacks cell-binding sites on its polymer chain and the presence of calcium ions can potentially cause inflammation *in vivo* [54].

Hyaluronic acid (HA) is a naturally occurring glycosaminoglycan in the human body, consisting of repeated units of D-glucuronic acid and N-acetyl-D-glucosamine (Figure 2.4) [61]. The molecular weight of hyaluronic acid varies, typically falling between 10^5 and 10^7 Da, which depends on its

source tissue [61]. Playing a crucial role in the extracellular matrix of humans, hyaluronic acid contributes significantly to tissue elasticity and hydrophilicity. Widespread presence in the human body and excellent cytocompatibility make hyaluronic acid a valuable asset in biomedical research. Despite its benefits, hyaluronic acid in gel form poses challenges for tissue-engineered implant applications. For instance, cells struggle to adhere to pure hyaluronic acid gels, and these gels often degrade too quickly in the body, preventing cells from migrating into the gel and converting the matrix into natural tissue [54]. To address these issues, HA is often chemically modified by the addition of functional groups like methacrylate or thiol [119, 120], which are crucial for crosslinking and stability in bioinks.

Agarose, derived from red marine algae, is primarily made up of alternating structures of galactopyranosyl and 3,6-anhydrogalactopyranosyl [121]. This biopolymer forms a key part of agar, obtained through the removal of agaropectin [122]. The popularity of agarose as a bioink component stems from its two straightforward physical gelation properties: it forms an ionic crosslinked network when combined with multivalent cations, similar to alginate [54]; it exhibits reversible temperature sensitivity, allowing it to gel below 30 and 40°C. The gelation temperature of agarose varies based on factors like molecular weight, concentration, and the presence of side groups [123]. These gelation properties enable fine-tuning of the viscosity of agarose-based bioinks and the mechanical strength of the resultant hydrogels to meet specific requirements. While marine microorganisms can degrade agarose through enzymatic action, it is not biodegradable in the human body [54]. A notable limitation of agarose is lower cell attachment capabilities due to the lack of RGD sequence.

Chitosan is derived from chitin, a biopolymer of N-acetyl glucosamine found in crustacean exoskeletons, particularly in crabs and shrimps [124]. The synthesis of chitosan is through N-deacetylation of chitin, which involves removing over half of the acetyl groups from chitin and replacing them with amine groups [125]. On the chemical structure of chitosan, functional groups include C2-NH_2, C3-OH, and C6-OH along with acetyl amino and glycoside bonds, of which the

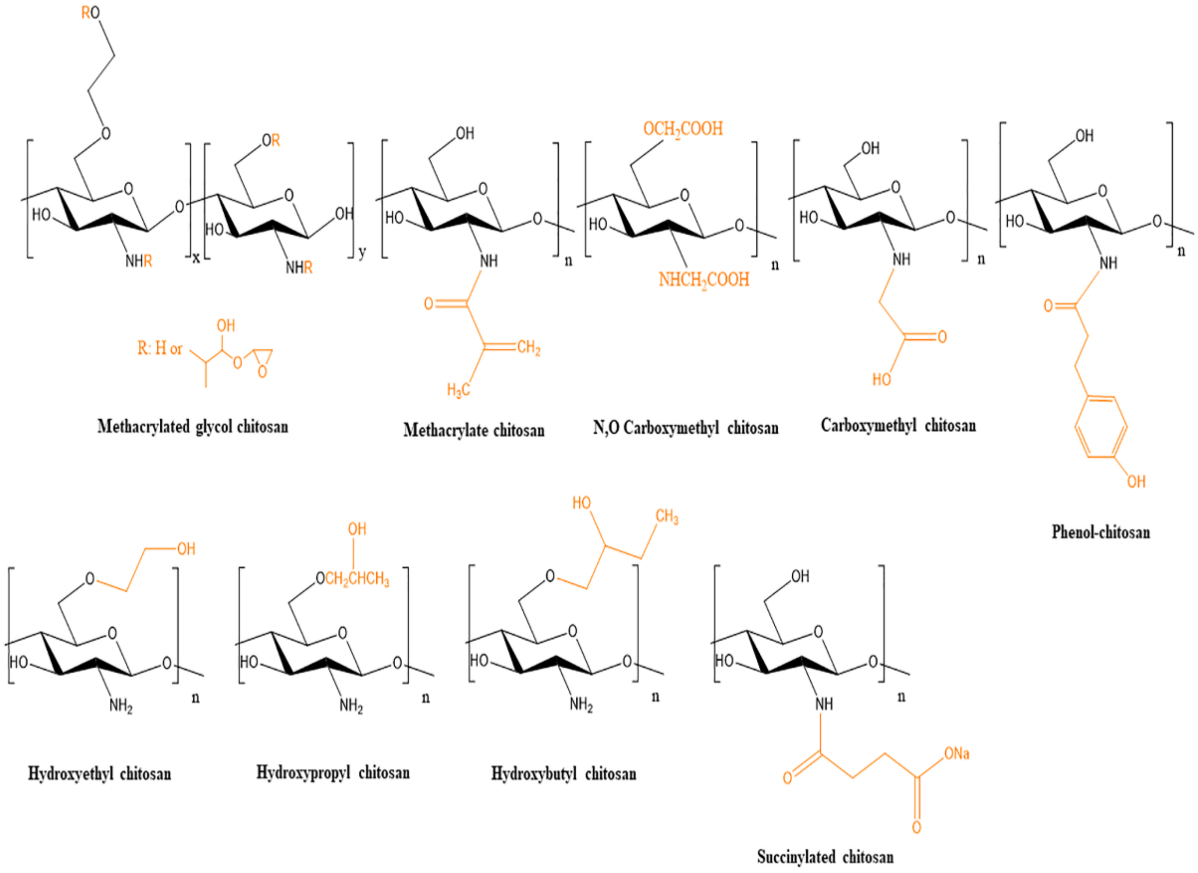

Figure 2.6: Modified chitosans used in bioink formulations [124].

acetyl amino and glycosidic bonds are relatively stable and less reactive, whereas the reactivity of C3-OH group is significantly reduced due to steric hindrance [126]. Consequently, the C6-OH and C2-NH_2 groups are more reactive and suitable for introducing modifications to chitosan, enhancing its physical and chemical properties as bioink formulation, as shown in Figure 2.6 [124, 125, 127]. C2-NH_2, particularly reactive and protonated in acidic conditions, largely define the distinct properties of chitosan [124]. For instance, the mucoadhesive properties of chitosan are due to the interactions between its protonated amino groups and the negatively charged components of mucin, a key protein in mucus. This interaction facilitates the adhesion of chitosan to mucosal surfaces. Additionally, the positive charges in chitosan can reorganize cell membrane proteins, enhancing permeability [124]. The antimicrobial properties of chitosan can be attributed to electrostatic interactions between its

polycationic nature and microbial cell surfaces [128]. However, the biodegradability of chitosan is because its glycosidic bonds are susceptible to enzymatic cleavage by proteases like lysozyme, leading to non-toxic byproducts that are easily excreted [124].

2.3.2 Synthetic polymers

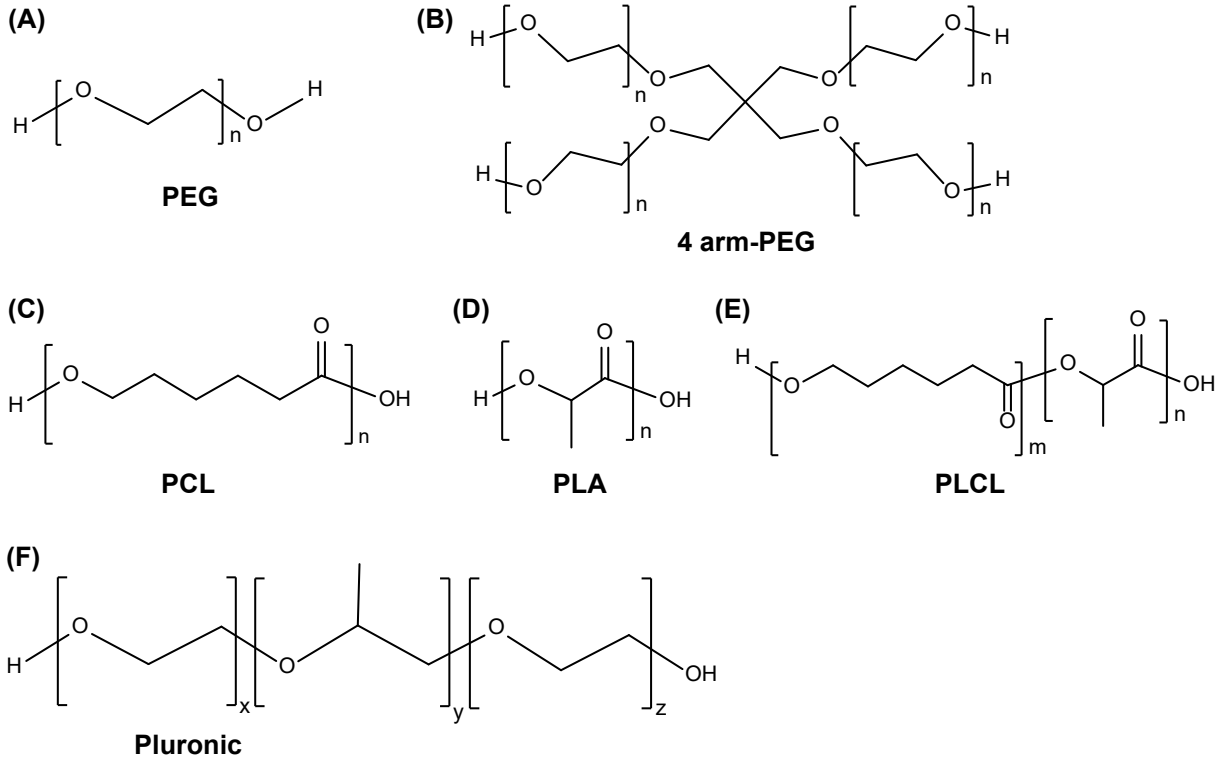

Figure 2.7: Chemical structures of synthetic polymers used in bioink formulations.

Within bioink formulations, the integration of natural polymers is crucial as they emulate the vital components of the extracellular matrix (ECM), fostering a conducive environment for cells. On the other hand, synthetic polymers, typically bioinert, offer the advantage of being chemically modifiable, which enhances the structural integrity, mechanical strength, and degradation of the scaffolds [129]. Merging these two types of materials opens up a promising avenue for the development of advanced bioinks. This section summarises the common synthetic polymers used

in bioink formulations, including poly(ethylene glycol) (PEG), polycaprolactone (PCL), polylactic acid, poly(lactide-co-caprolactone) (PLCL), and Pluronic. The chemical structures of these synthetic polymers are listed in Figure 2.7.

Poly(ethylene glycol), known for its excellent biocompatibility, is a material sanctioned by the FDA for use in various applications, such as pharmaceutical drugs and medical devices [61]. Available in diverse forms, PEG can be found in linear or branched structures (3, 4, or 8 arms), and in molecular weights varying from 0.5 to 20 kDa [61]. One of the notable characteristics of PEG is its water solubility, which makes it an ideal candidate for encapsulating cells [129]. However, the base form of PEG cannot establish physical or chemical networks essential for forming hydrogels. This limitation can be overcome by modifying the terminal ends of linear or branched PEG [129], as shown in Figure 2.8. Such functionalization allows the achievement of stable and robust hydrogel networks through 'click chemistry' or UV crosslinking, aligning well with the requisites of bioprinting technologies. Additionally, unlike common polyesters that degrade through hydrolysis, or natural materials that rely on enzymatic pathways for biodegradation, the breakdown of PEG necessitates oxidation [54].

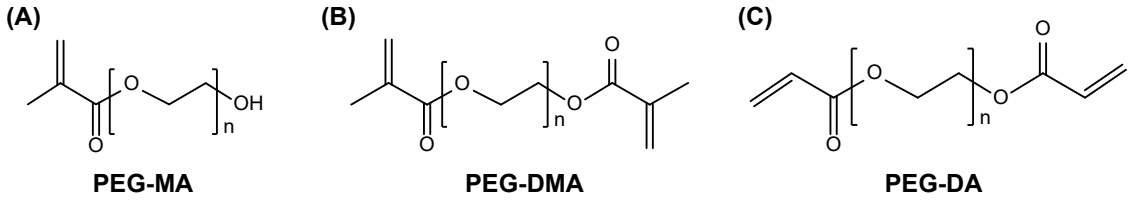

Figure 2.8: End-functionalized PEG: (A) poly(ethylene glycol) monomethacrylate (PEG-MA), (B) poly(ethylene glycol) dimethacrylate (PEG-DMA), and (C) poly(ethylene glycol) diacrylate (PEG-DA). They can be crosslinked to form a rigid hydrogel network.

Although water-insoluble thermoplastic polyesters, such as PCL and PLA, along with their copolymers poly(lactide-co-caprolactone) (PLCL), are not suitable for cell encapsulation, their biocompatibilities make them excellent choices for cell-free supporting inks in tissue engineering [61]. Both PCL and PLA are FDA-approved for manufacturing medical devices, offering a combination of

rigidity, biocompatibility, and cost-effectiveness [130]. In bioink applications, PCL and PLA can be processed using Fused Deposition Modeling at their respective glass transition temperatures (60°C for PCL and 65°C for PLA) [129, 130]. These polyesters then can be layered to provide long-term structural integrity to scaffolds, a useful property especially when the cell-encapsulating materials degrade rapidly. Although the breakdown of ester linkages results in hydrolytic degradation of PLA [54], the degradation duration for PLA, influenced by size and porosity, ranges from 10 months to about 4 years [131]. In particular, for PLCL, copolymerization not only improves the mechanical strength of the scaffold but also further prolongs the degradation process of the scaffold [61].

Pluronic polymers are triblock copolymers, each featuring a polyoxypropylene core that is hydrophobic, bordered by two hydrophilic polyoxyethylene chains [132]. There exists a variety of 11 distinct Pluronic types, differentiated by factors such as their molar mass, composite percentages, functionalities, and the specific crosslinking temperatures [133]. A popular characteristic of pluronic polymer is reversible temperature response behaviour: it transitions from a gel to a sol state when the temperature drops below its lower critical gelation temperature, typically around 4°C [134]. This thermally induced sol-gel transition in concentrated Pluronic solutions, occurring via a micellar mechanism, renders it a frequently chosen material as a sacrificial bioink in bioprinting. This property is pivotal in constructing intricate structures that incorporate diffusible channels and sustain high cell densities [135]. Wu and colleagues utilized F127, a type of Pluronic, for omnidirectional printing within a photopolymerizable hydrogel matrix to create 3D biomimetic microvascular networks [136]. These fabricated channels can then be seeded with endothelial cells, promoting vascularization upon implantation [135].

2.3.3 Cellulose

2.3.3.1 Sources and extraction of cellulose

Cellulose stands as the most plentiful natural polymer on Earth, with its annual production and decomposition rates reaching approximately 1.5×10^{12} tons [137]. This staggering quantity is on par with the world's reserves of major fossil fuels and minerals [137], highlighting its significant presence in the biosphere. Cellulose is found across various life forms including plants, animals, algae, fungi, and even in some minerals [137]. Predominantly, it is sourced from plant fibers, contributing to about 40% of their carbon content [137]. As shown in Figure 2.9, as a key structural component in the intricate design of plant cell walls, cellulose commonly exists alongside hemicelluloses and lignins [138].

The industrial process of extracting cellulose from wood involves several key steps: preparation of raw material, the pulping process and bleaching [139, 140]. The pulping process aims to break down lignin and hemicellulose bound to the cellulose [141]. The chemical method, such as sulfite pulping, the Kraft process and soda process involves cooking the wood chips in a chemical solution [142]. Bleaching further removes lignin and impurities, resulting in a purer form of cellulose. This step often involves a series of chemical treatments using chlorine dioxide, oxygen, or hydrogen peroxide[138].

2.3.3.2 Structure and physical modification of cellulose

As shown in Figure 2.9, the molecular structure of cellulose is characterised by a long chain of β-d-glucopyranose units, connected through β-1,4 glycosidic linkages. The length of this polymer, typically exhibiting a degree of polymerization ranging from 10,000 to 15,000 units, varies depending on the type of plant [138]. Each anhydroglucose unit within cellulose features three hydroxyl groups: C2-OH, C3-OH, and C6-OH (Figure 2.9). These groups play a pivotal role in establishing robust hydrogen bonds. Intramolecular hydrogen bonds are formed between the

hydroxyl groups and the adjacent glucose unit within the same cellulose chain, while intermolecular hydrogen bonds occur between the hydroxyl groups of one anhydroglucose unit and the glucose units of a neighboring chain [137]. This dual bonding mechanism is particularly strong in the crystalline areas of cellulose, leading to its notable properties like high strength, rigidity, and resistance to dissolution in water and most organic solvents [138, 143].

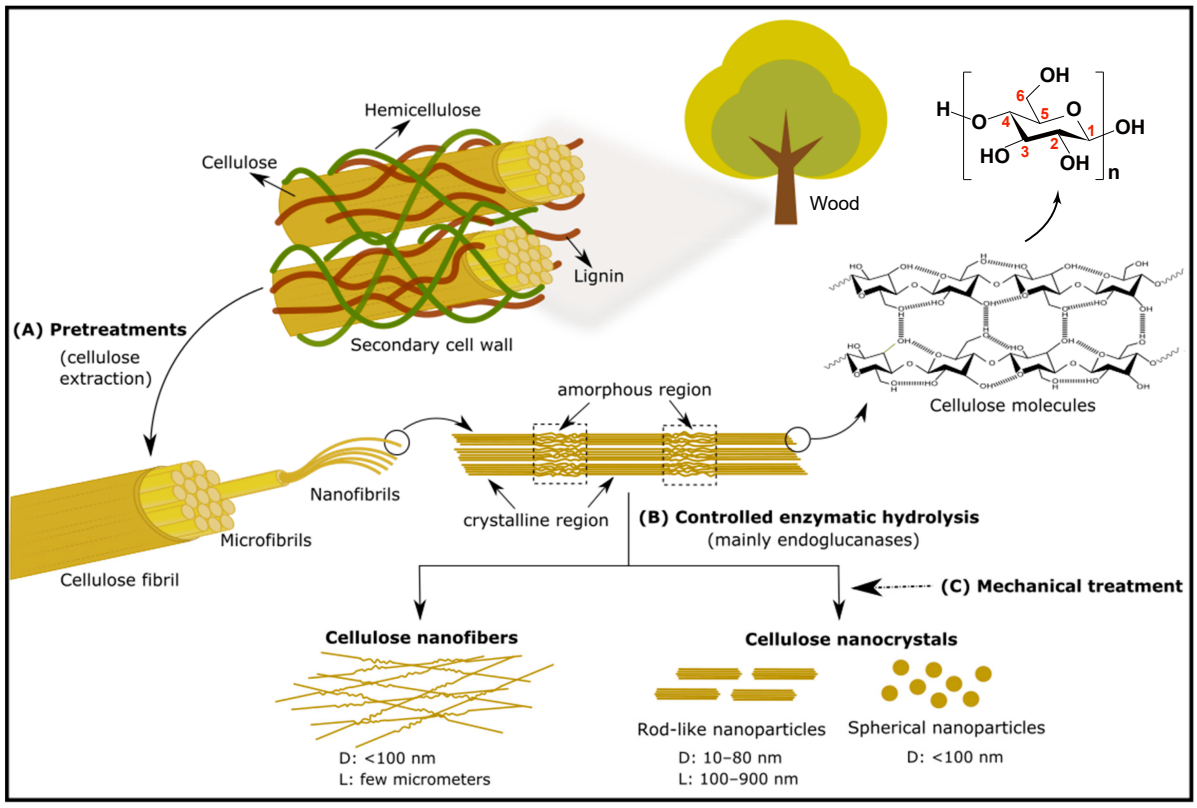

Figure 2.9: (A) Cellulose extraction and hierarchical structure of cellulose. (B) Production of cellulose nanofibers and cellulose nanocrystals (rod-like and spherical) by controlled enzymatic hydrolysis. (C) The mechanical treatment employed to obtain more uniform particles [138].

In its natural state, approximately 36 cellulose molecules group together to form the smallest units known as protofibrils [144]. These protofibrils contain regions that are either crystalline, showing a highly organized structure, or amorphous, which are less ordered [145]. The protofibrils are then bundled into larger units called nanofibrils (also called nanofibrillated cellulose (NFC)), which subsequently aggregate into microfibrils (also called microfibrillated cellulose (MFC)). The

culmination of this hierarchical assembly results in the formation of cellulose fibrils [138].

By performing controlled hydrolysis of NFC, such as sulfuric acid hydrolysis and enzymatic hydrolysis [146], the crystalline and amorphous regions in protofibrils can be separated, thereby obtaining cellulose nanocrystals (CNC) and cellulose nanofibers with a diameter of less than 100 nm. Mechanical treatment, such as high-pressure homogenizers, microfluidizers, supermass colliders, and ball milling [147], usually following chemical hydrolysis, is used to produce more homogeneous and stable CNC, such as rod-shaped nanoparticles and spherical nanoparticles [138]. In summary, the physical modification process of cellulose increases the specific surface area of cellulose, thereby boosting its reactivity and enabling more effective interactions with other substances [148]. This is particularly important in composite material reinforcement applications. Through these physical transformations, the versatility and functionality of cellulose in various industrial and scientific domains are greatly expanded.

2.3.3.3 Chemical modifications of cellulose

Chemical modifications of cellulose are often necessary for several reasons, particularly to enhance or introduce new properties that are not present in its natural form. For instance, cellulose is not soluble in water and most organic solvents due to strong intra- and intermolecular hydrogen bonds, limiting its applications. Chemical modifications can improve its solubility in various solvents, making it compatible with different matrices and systems [149]. Furthermore, the functionality of cellulose can be enhanced by introducing specific functional groups. Superhydrophobic groups can be added for water-repellent surfaces [150], or biologically active molecules can be attached for biomedical applications [151].

Following the molecular structure of cellulose (Figure 2.9), the chemical modification potential of cellulose is closely linked to the behaviour of its three hydroxyl functional groups [152]. When considering factors like steric hindrance and their contributions to the formation of hydrogen bonds, these hydroxyl groups exhibit varying levels of chemical reactivity, typically obeying the

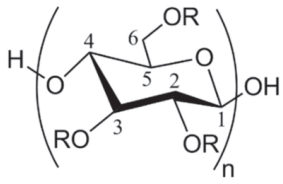

Cellulose derivatives

Cellulose ethers	R	Cellulose esters	R
Methyl cellulose	H or CH_3	Cellulose acetate	H or $(C{=}O)CH_3$
Carboxymethyl cellulose	H or CH_2COOH	Cellulose nitrate	H or NO_2
Ethyl cellulose	H or CH_2CH_3	Cellulose sulfate	H or SO_3H
Hydroxyethyl cellulose	H or CH_2CH_2OH		
Hydroxypropyl cellulose	H or $CH_2CH(OH)CH_3$		

Figure 2.10: Types and chemical structures of cellulose derivatives [27].

following order: C6-OH » C2-OH > C3-OH [153]. Therefore, as shown in Figure 2.10, cellulose can be modified to either cellulose ethers (methyl cellulose, carboxymethyl cellulose, hydroxyethyl cellulose, et al.) or cellulose esters (cellulose acetate, cellulose nitrate, and cellulose sulfate) through etherification and esterification, respectively [27]. For example, carboxymethyl cellulose enhances water solubility and provides negatively charged sites for protein binding [154, 155]. Hydroxyethyl cellulose increases hydrophilicity and can be used to further improve the scaffold's mechanical properties [156, 157]. To summarise, the increasing use of cellulose and its derivatives in tissue-engineered hydrogel scaffolds is driven by their favourable properties and the need for advanced functionalities in biomedical applications. While native cellulose offers excellent biocompatibility, biodegradability, and mechanical properties, functionalised cellulose provides added value through enhanced mechanical strength, tailored degradation rates, improved bioactivity, and additional functionalities such as antimicrobial properties and electrical conductivity [158–160]. The choice between using native or functionalised cellulose depends on the specific requirements of the tissue engineering application, with functionalised cellulose offering a customisable platform for more sophisticated and effective scaffold designs.

Faced with the great potential advantages of functionalised cellulose in advanced bioink formulations, the motivation for the current project to still choose natural cellulose as a modifier for traditional formulations is based on the unique hierarchical structure of cellulose. Although nanoscale cellulose products have been extensively studied in the field of tissue-engineered hydrogel scaffolds and even NFC has been marketed, studies on the improvement of conventional formulations by MFC and the effect of changes in the cellulose hierarchical structure on the formulations have not been sufficiently advanced. A comprehensive study of MFC and NFC will provide new ideas to overcome the bottlenecks in the current bioink formulation and bioprinting technology.

2.3.3.4 Cellulose applications in bioprinting and tissue engineering

Lately, there has been a growing interest in using cellulose and its derivatives as bioinks in the 3D bioprinting of tissue/organ scaffolds [35, 161–165], primarily due to their inherent sustainability, biocompatibility, slow degradation rate, rheological properties, and mechanical strength. Additionally, the flexible functionalization of cellulose and its derivatives facilitate the introduction of adaptable surface characteristics for protein adsorption and cellular aggregation, making it an increasingly popular choice in tissue engineering. In particular, NFC provided by CELLINK (Sweden) has been commercialised and widely used in the research of tissue engineering scaffolds [166]. This subsection will review the applications of cellulose and its derivatives in improving the printability of bioink formulations, mechanical strength and bioactivity of scaffolds.

The rheological behaviours of cellulose nanomaterials, such as yield stress, shear-thinning behaviour, and thixotropy, closely align with the requirements for printability in ideal bioink formulations, thus garnering sustained interest in the field of biomaterials and tissue engineering [167]. When present in suitable concentrations, cellulose nanomaterials, such as NFC and CNC are capable of forming highly viscous suspensions in aqueous solutions because of the formation of percolation networks and various interactions including van der Waals forces, hydrogen bonds, electrostatic forces, and hydrophobic interactions, along with molecular entanglement [167]. In

conditions of sustained shear, cellulose nanomaterials align themselves in the direction of flow by breaking the above interactions, leading to a marked decrease in viscosity, a phenomenon known as shear-thinning. When the shearing action ceases, cellulose nanomaterials quickly revert to their initial viscosity and viscoelastic properties, displaying excellent thixotropic characteristics [167]. Taking advantage of the shear-induced orientation of cellulose nanomaterials [168–170], some bioink formulations [171–176] have been developed.

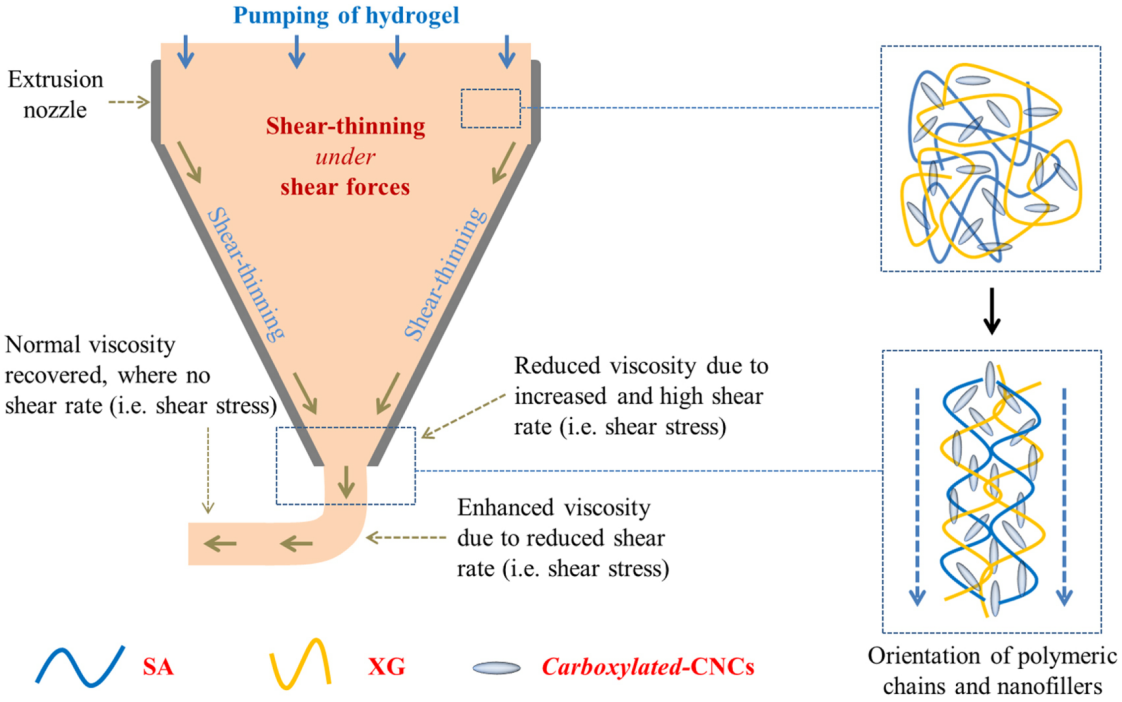

Figure 2.11: Schematic representation of the behaviour of bioink formulation sodium alginate (SA)/xanthan gum (XG)/carboxylated cellulose nanocrystals (cCNCs) under shear stress via conical extrusion nozzle [177].

As shown in Figure 2.11, Kumar and co-workers [177] designed a 3D printable carboxylated cellulose nanocrystal (cCNC)-reinforced hydrogel bioinks for tissue engineering. This formulation with 2.52 w/v% alginate, 0.15 w/v% xanthan gum, and 1.4 w/v % cCNC displays shear-thinning behaviour, with the viscosity dropping from 2×10^5 cP to 1.5×10^4 cP with increasing shear rate from 3.5 to 100 1/s [177]. The incorporation of cCNC facilitates a stable printed construct, showing clear printed filament lines. The observed printability behaviour of this formulation is attributed

by authors to the shear-thinning property of xanthan gum and, more importantly, the high aspect ratio of cCNCs. Carboxylated cellulose nanocrystals tend to align in parallel during the extrusion process. This alignment is likely reversible, leading back to the normal viscosity [177]. The fidelity on mesh area (82.6%) of the printed constructs using this formulation is closer to the theoretical mesh area (100%) compared to that (39.6%) with a formulation of 2.52 w/v% alginate and 0.6 w/v% xanthan gum [177].

One of the commercially available cellulose-gelatin composites is gelatin methacrylamide/NFC developed by CELLINK [178]. The incorporation of NFC significantly enhances the shear-thinning properties of the hydrogel composite. Research indicates that a concentration of 2% w/v NFC is optimal for building stable 3D constructs suitable for tissue engineering applications [179]. These 3D structures are noted for their high porosity and biocompatibility. The study demonstrated the successful development of nose and ear 3D structures using this bioink. Consequently, this bioink has found extensive use in various 3D printer-based tissue culture studies [179].

The mechanical reinforcement and toughening effects of cellulose materials as fillers in printed hydrogel scaffolds have also been extensively studied [180–183]. Its enhancement mechanism is considered to be the introduction of a new energy dissipation mechanism [45]. In a previous study, cellulose nanofibers/chitosan bioink were extruded as hydrogel filaments using a conic needle with an inner diameter of 410 µm [184]. After the physical coagulation of hydrogel filaments, the mechanical properties of hydrogel filaments were investigated by microtensile test. It was found that varying cellulose nanofibers concentrations from 0 to 0.4 w/v% results in a significant reinforcement from about 1.85 MPa to 2.7 MPa in tensile young's moduli of hydrogel filaments with 3 w/v% chitosan [184]. The enhanced mechanical properties of hydrogel filaments are because the aspect ratio typical of cellulose nanofibers promotes an efficient matrix/reinforcement interaction, contributing to the stress transfer from the chitosan matrix to the nanofibers and thereby yielding higher stiffness and strength [184].Furthermore, a study by Jiang et al. focused on the development of a composite bioink of unmodified gelatin and cellulose nanofibers [185]. The research indicated

that CNF:gelatin at 10:5% w/v ratios offered optimal rheological properties suitable for 3D printing. This formulation demonstrated a mechanical strength that was six times greater than that of plain gelatin hydrogel and exhibited a well-spread interconnected porous structure. The biocompatibility was also confirmed using CCK-8 and Hoechst 33342/PI double staining assays on 3T3 cells [185]. Consequently, gelatin/modified gelatin-cellulose composite hydrogels show significant potential as bioinks for 3D printing in tissue engineering applications.

As a hydrophilic material, cellulose has low non-specific protein adsorption [186], hindering the cell-adhesion behaviour of cellulose-based hydrogel scaffolds [187–189]. Several efforts have been made to improve the bioactivity and cell attachment capabilities of cellulose-based scaffolds. In a study from Courtenay's group [188], bacterial cellulose was chemically modified with glycidyltrimethylammonium chloride or by oxidation with sodium hypochlorite in the presence of sodium bromide and 2,2,6,6-tetramethylpipiridine 1-oxyl radical to introduce positive, or negative charges, respectively [188]. The mechanical integrity of the material remained intact following its modification. However, when a positively charged group was added to the cellulose's surface, the resulting cationic cellulose showed an increase by 70% in mammalian MG-63 cell adhesion compared to unmodified cellulose. In contrast, anionic cellulose carrying negative charges exhibited even lower cell attachment levels than that of the unmodified cellulose [188]. Therefore, applying surface-functionalized cellulose with cationic properties in tissue engineering opens up a spectrum of possibilities for creating novel scaffold materials. On the other hand, acetylation of bacterial cellulose was also evidenced as a positive method for improving the biological properties of cellulose-based scaffolds [190]. NIH 3T3 cells cultured on the acetylated bacterial cellulose scaffolds predominantly adopted a spindle-like shape, with extensive filopodia formation after 72 h, of which the average spread area of cells on the acetylated bacterial cellulose scaffold was 1438 ± 163 μm^2 [190]. In contrast, NIH 3T3 cells retained a rounded shape on unmodified bacterial cellulose scaffolds, leading to a significantly smaller average spread area of 821 ± 158 μm^2 after the same period [190]. Furthermore, the acetylated bacterial cellulose scaffolds demonstrated an enhanced

ability to bind proteins such as human serum albumin, γ-globulin, and human fibrinogen [190]. These results suggest that acetylation of bacterial cellulose not only augments protein adsorption properties of scaffolds but also facilitates the formation of a 3D microenvironment conducive to NIH 3T3 cell growth [190].

In addition to the improvement of cellulose scaffold formulations, advanced techniques have also been developed to capture the interaction of cells with cellulose scaffolds in three dimensions. In a study conducted by Brackmann et al. from Chalmers University of Technology, multimodal nonlinear microscopy was introduced for label-free imaging of bacterial cellulose scaffolds [191]. The formation of bacterial cellulose nanofiber networks was visualised and supra-structures (layered structures, cavities) in bacterial cellulose scaffolds was revealed. More importantly, cell integration in bacterial cellulose scaffolds with different structures was emphasised. The compact scaffolds showed distinct boundaries to adipocytes in the native tissue, while gradual cell integration was observed for the porous scaffolds [191].

2.4 Bioprinting process [63]

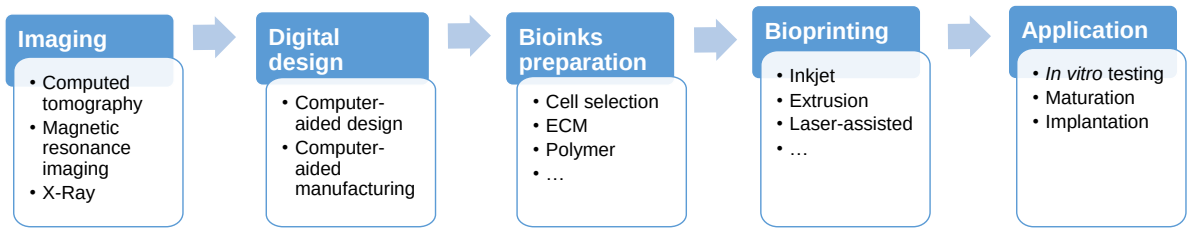

Figure 2.12: A typical process of bioprinting 3D scaffolds: imaging of damaged tissue zone; digital design of models; preparation of bioink formulations; bioprinting a scaffold with defined geometry and structure; in vitro testing and transplantation [63].

As an advanced approach to tissue engineering, 3D bioprinting was developed upon the significant advances achieved in 3D printing technology, cell biology, and materials science/engineering in recent years. Figure 2.12 illustrates the overall bioprinting process, whereby bioactive scaffolds

can be fabricated via a layer-by-layer positioning of bioinks by different bioprinters, such as inkjet, microextrusion, and laser-assisted bioprinter.

As the very first step, it is essential to establish the geometry and structure of the biomimic scaffold, upon examination of the impaired tissue. Computed tomography and magnetic resonance imaging are the imaging technologies commonly used [192]. Computer-aided design and manufacturing tools would then be deployed to construct the corresponding 3D structures. The composition of the bioinks will then be formulated, taking the desired characteristics specified in Section 2.2 into account. Commonly used materials include biocompatible synthetic or natural polymers such as polycaprolactone and hyaluronic acid [193], ceramics like bioactive glass [194], calcium phosphate [195], and natural decellularized ECM [196]. It is worth noting that cells encapsulated in the bioink can be derived from autologous or allogeneic sources [2].

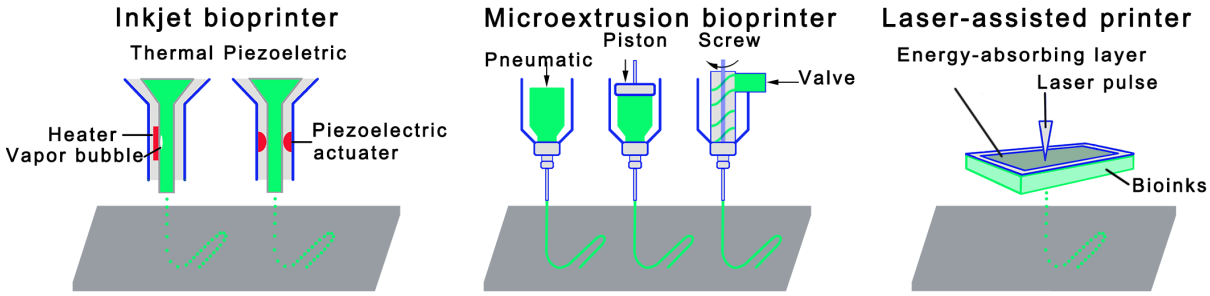

Figure 2.13: Schematic diagrams of three primary bioprinting technologies: inkjet bioprinting, extrusion bioprinting, and laser-assisted bioprinting [63].

As shown in Figure 2.13, a variety of bioprinting technologies have been developed to deposit bioink with high spatial resolution on a supporting substrate. Until 2023, numerous bioprinter brands have been established, such as Organovo, RegenHU, CELLINK, 3D Bioprinting Solutions, BioBots, Fluicell, Aspect Biosystems, and Allevi.

An inkjet bioprinter can convey small droplets of formulation over predefined locations by either thermal [197, 198] or acoustic mechanisms [199, 200]. The heat acts as a driving force to evaporate the deposited bioink into bubbles that burst and cause the bioink to be ejected [201]. Piezo actuators

eject bioink from nozzles by offering transient pressure [202]. Although thermal inkjet printing has several technical advantages such as high printing speed/efficiency and low operating cost, there are serious limitations, for example, the droplets cannot be completely uniformly transferred, resulting in an irregular droplet size or shape. In addition, cells and formulations that are not heat-resistant or mechanically resistant may be compromised. Piezoelectric inkjet printers have shown the capability to address the above limitations associated with the thermal one [203, 204], but there have been concerns with regard to the potential damage to the cell membrane and lysis induced by acoustic waves at 15–25 kHz frequencies [198].

Amongst all 3D bioprinting technologies developed, extrusion bioprinter is arguably the most widely used one due to its exceptional capability of accommodating a broad spectrum of fluids whose viscosities range from 30 mPa.s to just under 6×10^7 mPa.s [205, 206]. In this process, bioink formulation is dispensed as hydrogel filaments with microscale diameter on the substrate either pneumatically [207] or mechanically (piston- or screw-driven) [208, 209]. Since the bioink is subjected to strong shear stress when flowing through the nozzle, its rheological characteristics, particularly the shear thinning characteristic, are critical to the processing condition and cell viability [210]. Compared with inkjet bioprinter, the obvious advantages offered by extrusion bioprinter are high cell deposition density (> 10^8 /mL), as summarized in Table 2.1 [2, 54, 211, 212]. However, the survival rate of cells is not as satisfying as that with inkjet bioprinter because cells may be subjected to increased shear stress and mechanical pressure during the dispensing process, especially when using a relatively thinner nozzle (about 150 μm inner diameter). Some countermeasures, such as reducing the extruding pressure, increasing the nozzle size, are necessary to improve cell survival rate, which would compromise the printing speed and resolution.

The third fabrication strategy is laser-assisted bioprinting that is consists of three primary components: a pulsed laser source; a ribbon coated with a metallic absorbing layer (e.g., gold or titanium) and a layer of bioink; and a receiving substrate such as quartz disk [213]. During the construction of a scaffold, a pulsed laser beam scans over a ribbon, which triggers vaporization of

Table 2.1: Comparison of the advantages and disadvantages of inkjet bioprinter, extrusion bioprinter, and laser-assisted bioprinter [2, 54, 211, 212].

Bioprinter	**Advantages**	**Disadvantages**
Inkjet bioprinter	Low operating cost. High efficiency (1 ~ 10000 droplet/s). High resolution (10 ~ 50 μm).	Non-uniformity of droplet size. Inaccurate deposition location. Heat damage to cell behaviours (cell viability >85%). Requirement for low viscous bioinks (3 ~12 mPa.s). Low density of loaded cell (10^6 /mL).
Extrusion bioprinter	Low operating cost. Wide viscosity range (30 ~ 6×10^7 mPa.s). High cell deposition densities (> 10^8 /mL). High shape fidelity.	Low cell viability (about 70 %) using a nozzle of 150 μm diameter. Low resolution (100 ~ 500 μm). Low printing speed.
Laser-assisted bioprinter	High density of cell encapsulation (> 10^8/mL). High cell viability (>90%) due to no shear stress. Accurate and fast printing. High resolution (20 ~100 μm).	High operating cost. Complicated preparation process. The trace metallic residues.

the sacrificial absorbing layer. The resulting vapor bubbles would initially collapse on the surface of the absorbent layer, with no ejection. However, as the energy accumulates in the bubble, the pressure in the bubble increases before it bursts, expelling the bioink onto the receiving substrate [214]. The technology could accommodate bioinks of various viscosities (1 ~ 300 mPa.s) and can achieve a high density of encapsulated cells and cell survival rate because bioink does not have to endure shear forces. There are also limitations such as the complex preparation of the ribbon, a trace amount of metallic residues in the scaffolds, and the high production cost [2].

Following the 3D printing process, bioink formulations will experience a sol-gel transformation to form stable networked hydrogel scaffolds. To ensure the survival rate of the cells, the prepared scaffold must be matured in a bioreactor for a period of time, and undergo a series of necessary *in vitro* tests before transplantation.

2.5 Network reinforcement strategies of bioink/hydrogels [63]

Once extruded from the nozzle, bioink is expected to crosslink rapidly and solidify to maintain its geometrical integrity with an enhanced mechanical property. Given the significant mechanical property differences in tissues such as skin, liver, cartilage, and bone, it is essential to employ varied hydrogel network reinforcement strategies to develop hydrogel scaffolds that match the mechanical properties of target tissues [16]. Designing hydrogel network reinforcement strategies is closely linked to understanding hydrogel fracture processes. The fracture energy of hydrogels comprises two parts: the intrinsic fracture energy of the network and the viscoelastic mechanical energy propagated into the surrounding network [45, 215, 216]. The intrinsic fracture energy is related to the polymer chain length, number of chains, and interchain bond energy [45, 217, 218], while the latter is associated with the capacity of rearrangement for polymer chains under load [45, 219].

In traditional single-component hydrogels, enhancing mechanical strength typically involves augmenting the crosslinking density or polymer concentration, which is primarily aimed at bolstering the intrinsic fracture energy of the hydrogels [220]. However, in long-term continuous load-bearing scenarios, such as in tissue engineering, the overall robustness of these conventional hydrogels remains insufficiently strong (stiffness of around 10 kPa and toughness of less than 10 $J\,m^{-2}$ [221]. The inherent weakness of such hydrogel is primarily due to a lack of effective energy dissipation and propagation mechanisms [45]. Variations in reactivity levels between monomers and crosslinkers lead to uneven distribution of crosslinking points and inconsistent lengths of polymer chains between crosslinking points [218]. The heterogeneity in the single polymer network structure causes stress concentration, exacerbating fracture and failure of hydrogels. Therefore, the development of hydrogel systems with advanced reinforcement strategies is crucial for expanding the application of hydrogels in the field of tissue engineering.

Excluding traditional hydrogel reinforcement strategies, advanced reinforcement strategies aimed at increasing viscoelastic mechanical energy include homogeneous networks, dynamic

supramolecular, interpenetrating networks (IPNs), and multifunctional crosslinkers (Figure 2.14), which will be reviewed in this section. In addition, two different enhancement schemes, including polymer functionalization and thermoplastic reinforcement are also covered.

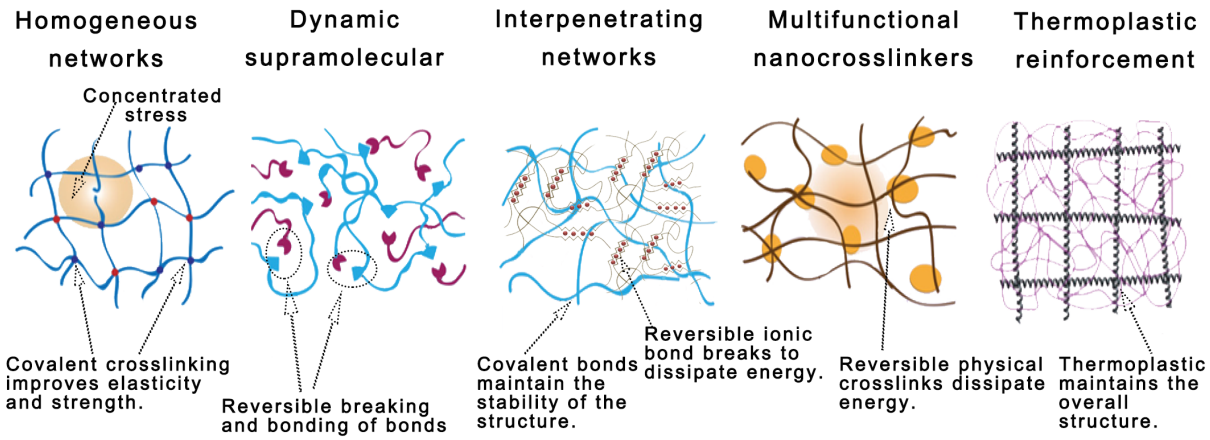

Figure 2.14: Schematic diagrams of established mechanical reinforcement strategies for hydrogel-based bioinks: homogeneous networks, dynamic supramolecular, interpenetrating networks (IPNs), multifunctional crosslinkers and thermoplastic reinforcement.

2.5.1 Polymer functionalisation

Of the many natural polymers used in bioink formulations, some can form a physically crosslinked network through reversible conformational transitions [63]. However, the formed network has a low bonding energy: changes in the surrounding environment can easily disrupt the conformation of the polymer chains, resulting in unsatisfactory mechanical properties [222]. To enhance the crosslinking ability of natural polymers, a common strategy is to incorporate some new functional moieties or modify the end/side groups of the natural polymers [223], which lays the foundation for designing natural hydrogels into advanced reinforcement strategies.

One of the common functionalization approaches is to modify the side groups of polymers with methacrylate moieties, which has been applied to many natural polymers, including gelatin [224–227], alginate [228, 229], hyaluronic acid [230–232], collagen [233–235], and kappa carrageenan

[236–238]. Modified polymers are equipped with carbon-carbon double bonds in the side chain, which can be easily crosslinked by a light source of different wavelengths in the presence of photo-initiators. Because methacrylated polymer networks suffer from the same shortcomings as traditional hydrogels, they are generally composited with other functional networks to synergistically improve the mechanical properties of the hydrogel system [215]. For example, methylcellulose (MC)/gelatin methacryloyl (G) bioink demonstrated outstanding shape integrity [239]: MC offered the bioink formulation excellent processability whilst ingredient G was used not only to form a covalently crosslinked network through light radiation but also to establish the physical interaction with the MC, improving the mechanical strength of the formed hydrogel. The addition of ingredient G to pure MC can significantly improve the critical shear stress required to initiate the viscous flow of the hydrogel, with a progressive rise in yield stress from 1356 ± 43 Pa (for pure MC) to 2354 ± 53 Pa (MC/GelMA hydrogel) [239]. Furthermore, Gao and coworkers designed a composited bioink formulation 8 w/v% methacrylated alginate (AlgMA)/ 16 w/v% methacrylated ϵ-polylysine (ϵ-PLMA) [240]. Electrostatic interaction of AlgMA and ϵ-PLMA and covalently crosslinked networks of the two increase the compression modulus to 0.926 MPa [240]. Also, human bone marrow mesenchymal stem cells and rat stem cells encapsulated in this hydrogel maintain viabilities of 72% and 75% after 4 days of post-printing [240].

2.5.2 Homogeneous hydrogel networks

Building a homogeneous network is considered an effective strategy for hydrogel network reinforcement because homogeneous networks can evenly distribute loads and reduce microcrack (defect) formation sites [45]. A homogeneous network can be deployed by combining two types of symmetrical multi-arm polyethylene glycols (PEG) whose end groups can react with each other. There are a number of flexibilities offered by PEG: easily changed molecular configuration, number of branches, type of end groups, and length of the arms, which offer a great platform for hydrogel reinforcement [241] and for constructing a uniform network. Sakai and colleagues [223] reported

a tetra-PEG hydrogel with remarkable mechanical properties, of which maximum breaking stress is 9.6 MPa at a network concentration of 120 mg/mL. This strength surpasses that of conventional hydrogels, which typically range from tens to hundreds of kilopascals, and is comparable to native articular cartilage (approximately 6-10 MPa) [223]. These mechanical characteristics are attributed to the homogeneous network structure of the hydrogel, achieved through controlled synthesis using tetrahedron-like macromonomers. To summarize, strategies have been developed and demonstrated to significantly improve the mechanical properties of bioprinted scaffold, in terms of ductility and fracture toughness, by fabricating a hydrogel network that can distribute the applied stress evenly.

Another strategy to prepare strong hydrogels with homogeneous networks is to deploy click reactions. Click reactions, particularly thiol-ene click reactions [242], demonstrated exceptional advantages, such as ease of use, high efficiency, reliability, and high selectivity [243], in synthesizing functional polymers or preparing polymers with topological structure for surface modification and biopharmaceutical applications [244]. For example, norbornene-modified hyaluronic acid underwent a photo-crosslinking reaction with the tetrathiol [245]. Subsequently, the rheological measurements showed that the covalent networks improved the hydrogel mechanics whereby its storage modulus increased from 500 Pa to 5 kPa. Moreover, the Young's modulus of the hydrogel was enhanced from 1 to 3 kPa after photocuring. Additionally, thiolated hyaluronic acid and gelatin was co-crosslinked by alkene functional group modified four-arm PEG for fabricating vessel-like constructs by 3D bioprinting [246]. This hydrogel showed significantly higher shear storage moduli (above 800 Pa) when compared to hydrogel crosslinked by PEG diacrylate (under 150 Pa) [246]. It is worth noting that this bioink formulation was crosslinked before bioprinting. Although the printed scaffold has high shape fidelity and encapsulated cells can keep viability in culture for up to 4 weeks, its mechanical strength determines that the formulation is only suitable for the repair of vascular tissue.

2.5.3 Dynamic supramolecular

Enabled dynamic chemical bonds and/or physical interactions [15], polymer chains can self-assemble and form a dynamic supramolecular hydrogel. These dynamic interactions are readily disrupted, allowing for the dissipation of stress. Concurrently, their reversibility enables the rapid recombination of the polymer chains, hence the hydrogel network exhibits remarkable anti-fracture performance even after multiple deformation cycles [247, 248].

The prominent dynamic covalent chemical reactions currently used include reversible diels-alder reactions, disulfide exchange, boronate ester formation, and aldimine formation [15]. The nature of such dynamic bonds is attributed to the combination of thermodynamically stable but kinetically unstable interactions [249]. Reversible physical interactions include hydrogen bonding, ionic bonding, π-π stacking, hydrophobic interactions [250–252], coordination bonds [253–255], and non-covalent guest–host interactions [256–260].

It is worth noting that during the self-assembly process of the monomers that involve the dynamic interactions aforementioned, the inherent dynamicity does not facilitate the formation of a mechanically strong polymer structure [261]. However, if dynamic bonds are uniformly bound to a macromolecular backbone, macromolecular monomers enable entangle with each other and form dynamic supramolecular hydrogel. Such molecular configuration could reduce the free volume of chains, confine the migration ability of polymer chains, and improve the stability of the supramolecular network [15]. When being deformed, these dynamic interactions are constantly broken but reformed to mitigate a permanent disruption to the molecular network, which provides valuable guidance on the self-healing of bioinks/hydrogels.

Figure 2.15 presents a number of intermolecular interactions, e.g., hydrogen bonding of petrin rings in the molecular structure, π-π stacking, and zinc ions coordination, that were used to develop an injectable fibril network based on folic acid, a natural small molecule [262]. The bioink formulation exhibited a shear-thinning characteristic during the printing process, and was able to self-heal immediately after printing due to the dynamic nature of the interactions [262]. When

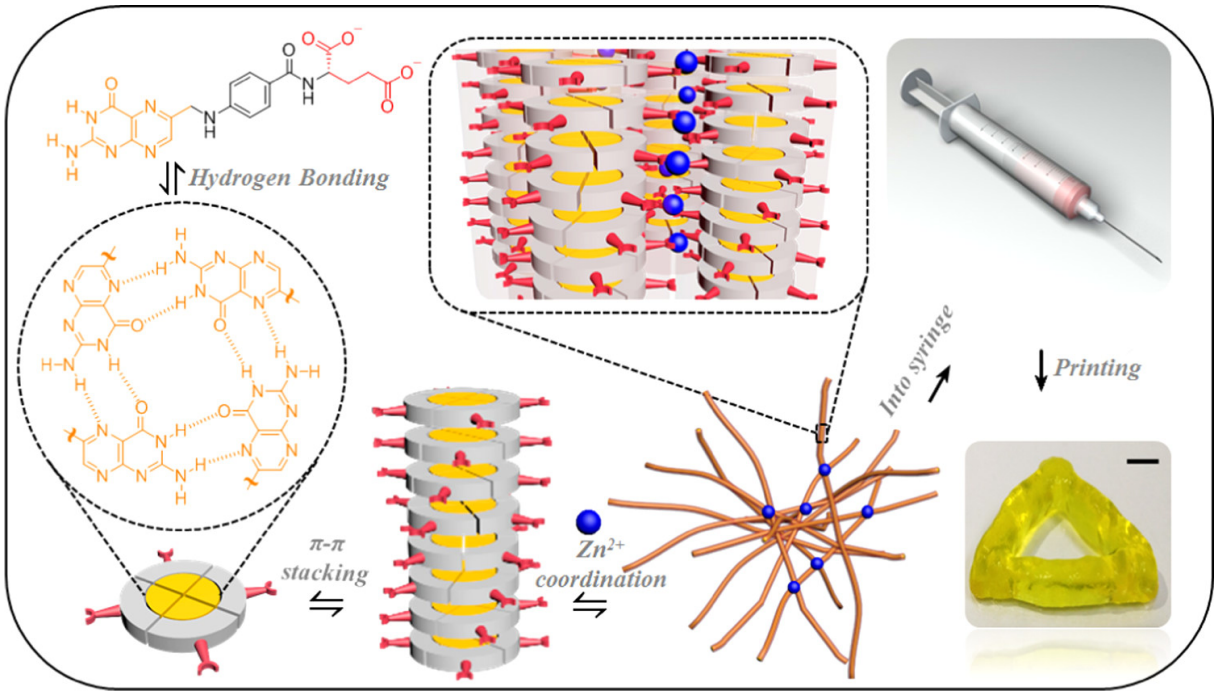

Figure 2.15: A folic acid fibril network formed through a series of physical interactions [262].

adjusting total concentration of the coordination system (folic acid and zinc ions), it was found that the mechanical properties of the hydrogel were improved significantly whilst maintaining the excellent printability [262]. For example, the elastic modulus of such fibril network was improved by around 5 orders (from 10 to 10^6 Pa) when changing the molar ratio of folic acid to zinc ions from 1.7 to 2.0 [262]. The adjustable mechanical properties could be invaluable to suit the requirements for repairing various biological tissues from cartilage to cancellous bone. Moreover, the simple preparation, excellent printability, biocompatibility, and mechanical properties of supramolecular hydrogels provide an excellent platform in applications such as drug delivery.

Wang and colleagues [245] developed a bioink formulation that was enriched by dynamic covalent hydrazone bonds: hyaluronic acid was modified by hydrazide and aldehyde groups through amidation reaction and oxidation reaction, respectively (Figure 2.16). Once being exposed to an aqueous environment, the hydrazine groups can react reversibly with aldehydes to form dynamic covalent bonds [245]. Rheological tests showed that the hydrogel exhibited the preferred shear

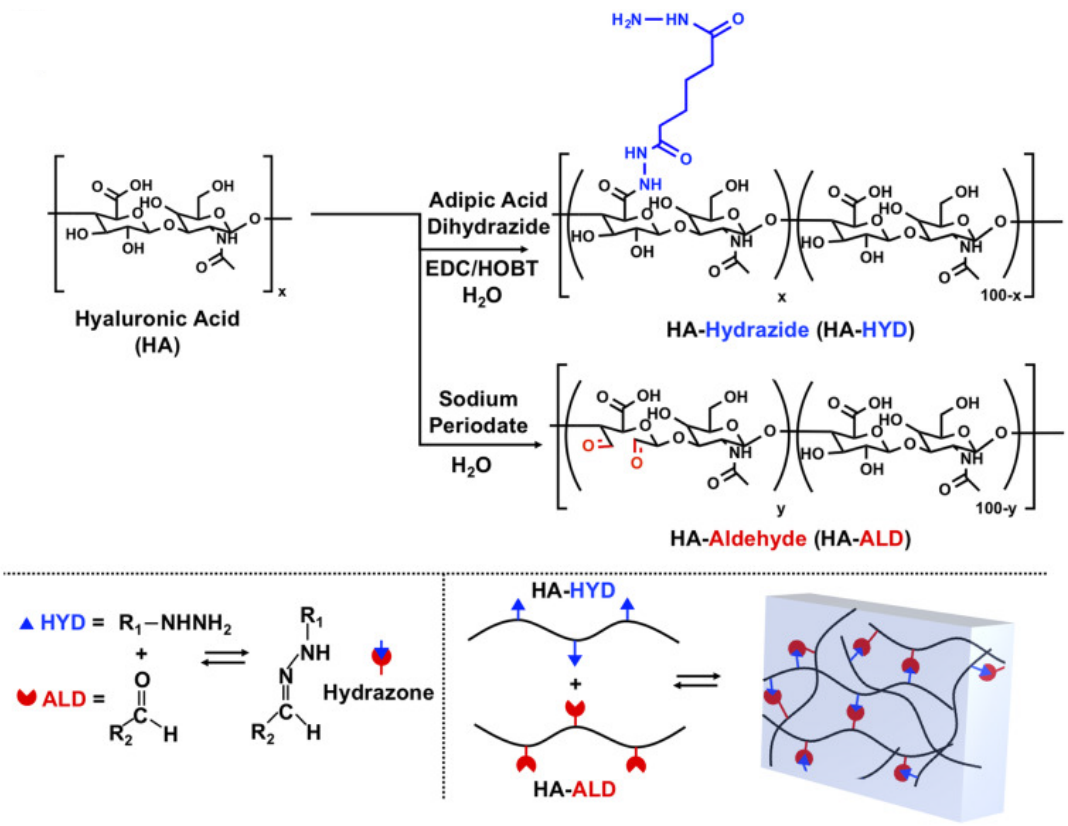

Figure 2.16: Schematic diagram of the hydrazide and aldehyde groups modified hyaluronic acid macromonomer and dynamic covalent network [245].

thinning, self-healing, and injectable properties [245]. Whilst maintaining an equal ratio between the two types of hyaluronic acid, an increased total mass fraction of the polymer (from 1.5 to 5 wt%) improved the shear modulus from c.a. 500 to 6,000 Pa, and Young's modulus to 15 kPa [245]. However, the increased concentration of hyaluronic acid limited the self-healing efficiency of the hydrogel. It is worth noting that the viability of fibroblasts encapsulated in the hydrogel remained at a high level for each mass fraction. To further improve the mechanical properties of the hydrogel, click chemistry of norbornene-modified hyaluronic acid was used to generate a second network, as mentioned in section 2.5.2. The resulting hybrid hydrogel network was shown with an increased elastic modulus, a significantly reduced degradation rate, and a prolonged lifespan. This study demonstrates that different enhancement strategies could be deployed together to address the

limitations associated with one particular crosslinking reaction, which expands the available options in developing a bioink formulation.

2.5.4 Interpenetrating networks

Interpenetrating networks (IPNs) consist of two polymer networks that can entangle through covalent bonds or random physical interactions [263]. Based on the nature of the interactions, IPNs can be divided into double networks (DNs), where each network is connected by covalent bonds, and ion-covalent entanglement networks (ICEs), where two networks rely on ionic bonds and covalent bonds, respectively [215, 264], as shown in Figure 2.14.

The extensive presence of covalent bonds ensures that there is substantial bond energy within the DNs. However, a long bonding time is required for the DNs, which might compromise their self-support ability following a bioprinting process. The interpenetrating networks of long-chain and short-chain molecules equip the DNs an excellent elasticity under deformation of up to 50% [265]. The short-chain network in the DNs would collapse first to dissipate energy, followed by the disintegration of the long-chain network when the DNs undergo a large deformation [266]. Since the rupture of the DNs network is irreversible, their overall mechanical properties are primarily determined by the long-chain network which has a better elasticity than the short-chain network. For example, Yang et al. used Laponite RDS (a layered silicate) to impart shear-thinning properties of a first network precursor solution sodium 2-acrylamido-2-methylpropanesulfonate [267]. Following extrusion and initial UV-curing, the structures were immersed in a second network precursor solution, then UV-cured again to form interpenetrating networks of poly(2-acrylamido-2-methylpropanesulfonate) and polyacrylamide. By adjusting the polyacrylamide to cross-linker ratio, it's possible to finely tune the balance between the stiffness and maximum elongation of the scaffold [267]. This method achieved a compression strength and elastic modulus of 61.9 MPa and 0.44 MPa, respectively, surpassing those of bovine cartilage. The gel also demonstrated maximum compressive and tensile strengths of 93.5 MPa and 1.4 MPa, which are double the strength of

previously reported 3D printed gels [267]. Obviously, the interpenetrating networks scaffold has excellent mechanical properties. However, the effect of the second network formation process on the final scaffold geometry and pore structure remains to be discussed.

In comparison with the dual networks aforementioned, ICEs systems have a greater potential in improving the mechanical properties of 3D printed hydrogel scaffolds because they are composed of two network structures with dissimilar properties [238, 268, 269]. ICEs aims to restrict the continuous propagation of macrocracks at the crack tips by using the differences between the two networks to dissipate energy. Here,

- The ionic cross-linked network is tightly arranged, with bonds formed via physical attraction of positive and negative charges, which has a fast bonding kinetics. However, the weak bonds formed are sensitive to changes in the external environment, such as temperature and ion concentration, which underpins the unstable and reversible nature of such network.

- The covalent cross-linked network is a flexible network with loose mesh and excellent ductility. It shows excellent stability due to its high bonding energy, but cannot be recovered once broken [270]. The advantage of ICEs over DNs is that the breakup of the sacrificial bonds is temporary [271]. Upon external deformation, the tightly cross-linked ionic bonds break due to their brittleness, resulting in a series of microscopic segments, but the soft covalent network could use the viscous dissipation mechanism to prevent such microcracks from developing into macrocracks [45]. If the external stress disappears at this point, ionic bonds could reform to repair the cracks. However, the cracks would likely cascade across the material if the stress gradually increases to the point where the covalent crosslinked network fails.

Recently, a biofunctional bioink formulation containing sodium alginate, poly (ethylene glycol) diacrylate (PEGDA), and sodium polyphosphate, was developed for bone tissue regeneration [272]. Bioprinted formulation undergoes stages of light radiation and immersion in 5 wt% $CaCl_2$ solution, which elevates the compression modulus of the pure ICEs network (alginate/PEGDA) to 0.7 MPa

[272]. Furthermore, by gradually increasing the content of sodium polyphosphate the compression modulus of such hybrid hydrogel can be further augmented to 4.6 MPa [272]. Additionally, to enhance the printability of the bioink formulation, $CaCl_2$ solution with low concenytration (0.89 wt%) is pre-added to establish a mildly crosslinked bioink formulation. This not only underscores the significance of the ionic cross-linking network but also inspires us to suitably adjust the concentration and addition order of calcium ions, thus optimising both the printability and mechanical strength of the bioink/hydrogel simultaneously.

2.5.5 Multifunctional crosslinker

Appropriate incorporation of multifunctional crosslinkers into bioink formulations enables efficient energy propagation and dissipation of hydrogels because multifunctional crosslinkers can not only control inter-crosslinking distances for forming homogeneous networks, but also dissipating energy through the disruption of physical interactions between the crosslinkers and polymer chains [45].

The versatility of multifunctional crosslinkers is primarily determined by the characteristics of the materials, such as shape, chemical nature, size, structure, and surface charge. According to the difference in their shapes, multifunctional crosslinkers with excellent biocompatibility can be divided into the following categories:

- Dot-shaped nanoparticles (NPs), such as hydroxyapatite NPs [273, 274], Fe_3O_4 magnetic NPs [275, 276], gold [277, 278], and silver NPs [279, 280].
- Nano/micro fibers [281] and nanotubes, such as cellulose nanofiber [176, 184, 282, 283], carbon nanotubes [284, 285].
- Layered 2D nanosheets, such as nanoclay [286–288], graphene [289, 290], and graphene oxide [291, 292].

With a large specific surface area, a single multifunctional crosslinker is able to interact with multiple polymer chains simultaneously [293]. The amplified adhesion between multifunctional

crosslinkers and polymers is primarily governed by physical interactions, such as hydrogen bonds, ionic bonds, and electrostatic interactions, but can be actuated by dynamic covalent crosslinking where appropriate or needed [215].

Once an external load is applied to a hydrogel containing multifunctional crosslinkers, a small fraction of polymer chains adsorbed on the multifunctional crosslinkers is forced to desorb and dissipate energy. However, such separation at molecular scale does not seem to have a notable impact on the overall structure of the hydrogel network. In addition, the detached polymer chains will re-adsorb onto the nanocrosslinker via physical interaction according to the principle of proximity [294]. The dynamic nature of the molecular interactions between multifunctional crosslinkers and polymers not only enhances the overall mechanical strength, but also improves the fatigue resistance of the network. Multifunctional crosslinkers can also help to improve the rheological properties and processibility of the hydrogel, introduce responsiveness to stimulus such as electric or magnetic field, and promote tissue regeneration processes, such as bone formation and mineralization [280, 295–297].

An example used here to demonstrate the capability of multifunctional crosslinkers for hydrogel reinforcement is nanoclay, known as nanosilicate or Laponite [264, 298, 299], that is a disc-like 2D nanoplatelet with good solubility in water and satisfactory biocompatibility. Possessing negative charge on its surface but positive charge around the edge, nanosilicate could interact easily with polyelectrolyte. Figure 2.17a presents nanosilicate (nSi) based ICEs bioink formulation (NICE) that contains gelatin methacryloyl (GelMA) and kappa-carrageenan (kCA) [264]. The addition of nanosilicates increases the viscosities and self-supporting of formulations based on GelMA and kCA alone so that NICE bioink formulation can be used to prepare scaffolds up to 3 cm tall (150 layers), which is 10 times greater than the maximum height constructed using the other single or binary bioink formulations (GelMA, GelMA/nSi, kCA, kCA/nSi, GelMA/kCA) [264], as shown in Figure 2.17b. This NICE scaffold shows high tough but elastic with a compressive modulus of 71.1 kPa and tensile modulus of 495 kPa [264]. The substantially improved mechanical properties

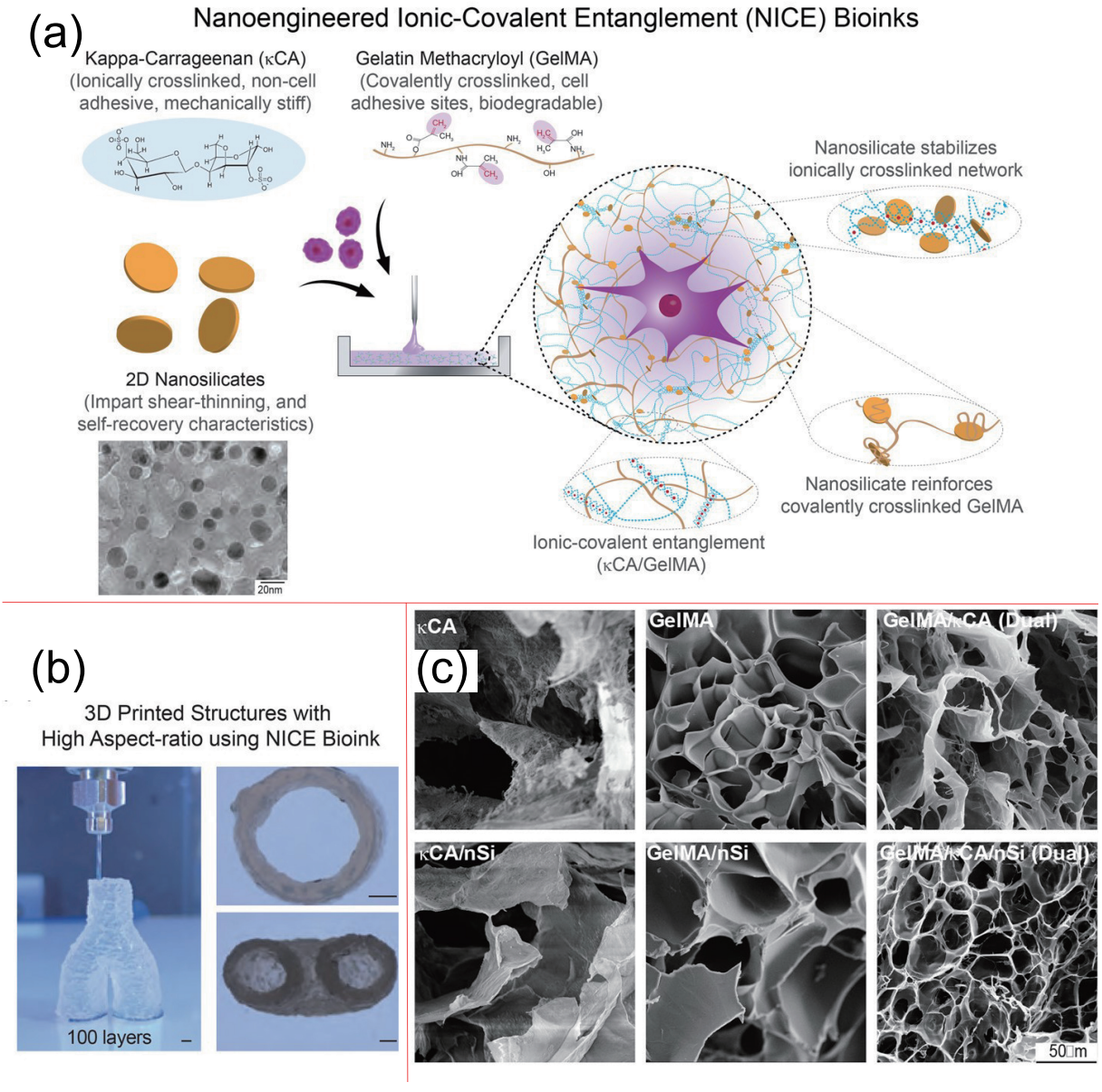

Figure 2.17: (a) Schematic diagram shows the function of nanosilicate, gelatin methacryloyl, and kappa-carrageenan in nanoengineered ionic-covalent entanglement (NICE) bioink formulation. (b) NICE bioink is capable to print a scaffold with high aspect-ratio, and the height of the construct reaches 3 cm. (c) Comparison of pore structure for various bioink formulations [264].

are attributed to a synergistic effect between nanosilicates and ICEs, which is much greater than the effect of the individual factor. While the synergistic effect enhances the mechanical properties of the NICE hydrogel, it also maintains the high hydration degree of the hydrogel (89.5%) in a range suitable for cell survival, thanks to the effect of nanosilicate incorporation on the pore size of the hydrogel Figure 2.17c. An additional benefit reported is that nanosilicates are able to stimulate the intrachondral differentiation of human mesenchymal stem cells and the accumulation of extracellular matrix [264].

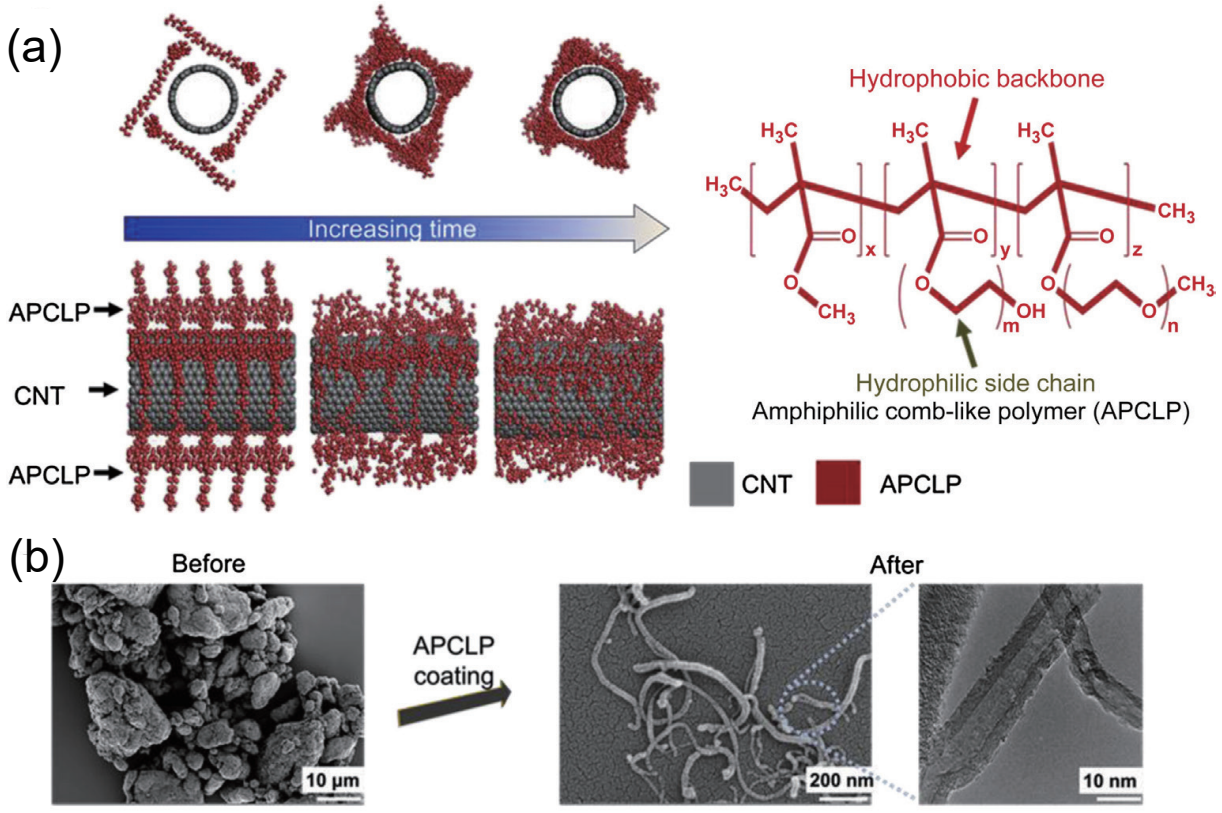

Figure 2.18: (a) Amphiphilic comb-like polymers (APCLP) are deployed to improve the dispersion of carbon nanotubes in aqueous solutions. The surface of carbon nanotubes is encapsulated by the hydrophobic methyl methacrylate backbone of APCLP through hydrophobic interactions. The hydrophilic side chains (hydroxyl polyoxyethylene methacrylate and polyethylene glycol methacrylate) of APCLP are exposed to the aqueous solution to enhance the *in situ* hybridisation of carbon nanotubes with bacterial cellulose for the preparation of 3D scaffolds. (b) Dispersion of carbon nanotubes before and after APCLP covering [300].

The dispersibility of multifunctional crosslinkers within hydrogel scaffolds is essential for them to perform their intended multifunctions. Homogeneously distributed nanoparticles could help to minimize the formation of localized microcracks upon externally applied stress [301]. However, hydrophobic nanocrosslinkers tend to form aggregates, instead of interacting with the macromolecules involved, which might compromise the overall stability and mechanical properties of the hydrogel. One of the possible solutions to address such issue is using amphiphilic compounds. In a previous report, a comb-like polymer with a hydrophobic backbone (methyl methacrylate) and hydrophilic side chains (hydroxyl polyoxyethylene methacrylate and polyethylene glycol methacrylate) (Figure 2.18) was included in a bioink formulation containing both hydrophobic carbon nanotubes and hydrophilic bacterial cellulose networks to increase the binding energy and improve the overall mechanical properties of the hydrogel system [300]. This approach not only improved the dispersibility of carbon nanotubes in the hydrogel, enhanced the structural integrity and mechanical properties of the hydrogel, but also exhibited excellent osteoinductivity and osteoconductivity [300]. This work inspires researchers that multifunctional crosslinkers can be further modified to give more functionality to the corresponding bioink formulations.

2.5.6 Thermoplastic reinforcement

Different from the above hydrogel network reinforcement strategies that establish energy dissipation and propagation mechanisms, thermoplastic strengthens the material by inserting hierarchical structures into 3D scaffold. Thermoplastics possess several inherent advantages as a candidate for tissue scaffolding, such as superior mechanical strength and excellent processibility for complex-shaped objects. However, thermoplastics are not suitable for cell-containing bioink formulations due to their hardness and high melting temperature [302]. To address these technical challenges, novel strategies were developed. Thermoplastics can be processed in a separate chamber and printed with hydrogel bioinks in either layers or pre-defined patterns, which results in a two-phase structure where the thermoplastic component acts as the backbone. To minimize any potential damage to

the cells by the thermoplastics, only the ones with low melting temperatures were considered. Of a broad range of biocompatible and biodegradable synthetic polymers, polyglycolic acid [303–305], polylactic acid-glycolic acid copolymer [306–308], PLA [309–312], PCL [313–316] with a melting temperature of about 65°C [317, 318] have been explored in the previous studies.

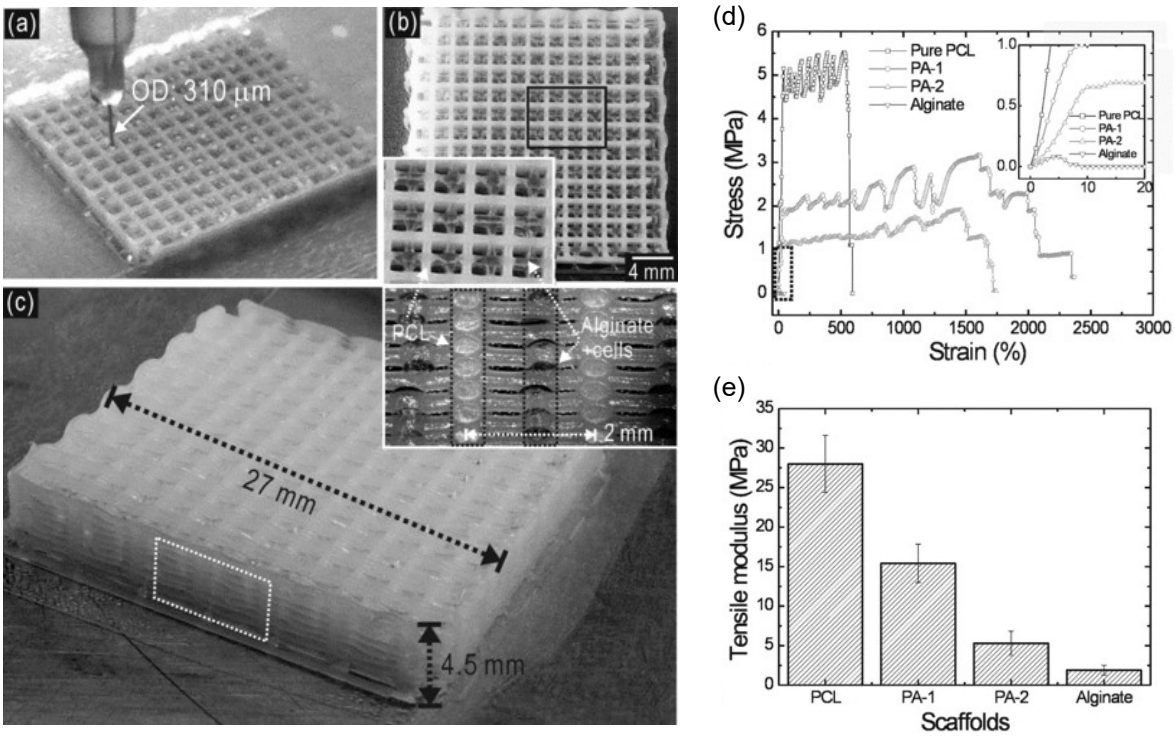

Figure 2.19: (a) Cell-encapsulated alginate bioink is printed between PCL layers using a nozzle with 310 μm outer diameter. (b) Surface image and (c) geometry shape of hybrid scaffold (PA) consisting of cell-laden alginate and PCL struts in layers. (d) Stress-strain curves for pure PCL, two hybrid scaffolds with varying heights PA-1 and PA-2, and alginate alone. The curves for PCL and two hybrid scaffolds experienced a similar trend, demonstrating the function of mechanical reinforcement for PCL. (e) Comparison of tensile moduli for PCL, PA-1, PA-2, and alginate scaffolds [319].

Figure 2.19a, b, and c present a hybrid scaffold with a two-phase structure, consisting of both cell-laden alginate struts and PCL struts [319]. As demonstrated by the stress-strain results of different formulations examined (Figure 2.19d), the PCL component could improve significantly the mechanical properties of the hybrid scaffolds, showing a similar characteristic to that of the pure PCL, which is significantly greater than that of the scaffold made of pure alginate. The substantial

improvement in tensile moduli from 2.5 MPa of alginate scaffolds alone to 15.4 MPa of PA-1 hybrid scaffolds (Figure 2.19e), is attributed to the adhesion between PCL struts. Moreover, the large mesh space of the PCL layers is beneficial for transporting nutrients and signal factors between biologically active layers. In summary, the hybrid scaffold with thermoplastic-reinforced structure meets the requirements for hard tissue regeneration, with additional benefits contributed by the thermoplastic components.

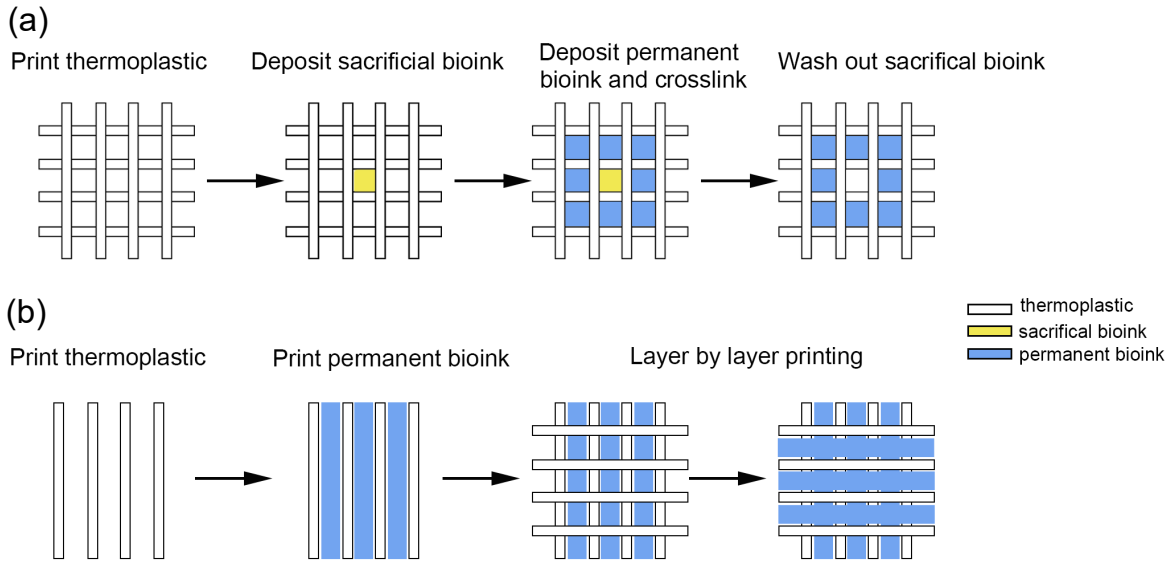

Figure 2.20: (a) Cell-containing bioink formulations are deposited into the square area formed by two layers of thermoplastic. (b) Cell-containing bioink formulations are deposited in the middle area of two thermoplastic filaments or customized shape to develop constructs with tailorable mechanical properties [320].

The other approach to integrating thermoplastic polymer with hydrogel is to construct a defined structure in a sequence, with individual components embedded, instead of layered bioprinting. Embedding methods offer an increased degree of flexibility: build a thermoplastic scaffold (Figure 2.20a), deposit hydrogel subsequently with the planned shape and structure (Figure 2.20b), and form a hybrid scaffold with tailorable mechanical properties [320]. It should be noted that some porous features can be planned to facilitate the diffusion of small molecules required for various behaviors of the cells when a cell-containing hydrogel fills the thermoplastic structure [321]. Moreover, signal

factors, DNA, and hydrogels with different functions can be placed in different regions of the same scaffold to mimic the complex microenvironment of a natural tissue.

To conclude, the aforementioned enhancement methods for bioink formulations have all been demonstrated with effectiveness but also limitations. Different natural tissues would have specific requirements for the matching 3D scaffolding, which is challenging to achieve with one single reinforcement strategy. It is therefore critical to design a bionic entity that couples effective bioink formulations, suitable bioprinting techniques, and further post-enhancement strategies to meet the requirements for tissue restoration.

2.6 Conclusion and outlook

To regenerate damaged tissue, constructing a complex 3D hydrogel structure with enriched compositions of ECM and matched mechanical strength to natural tissue is one of the most indispensable steps [322]. In addition, it is equally vital to establish the responsiveness of printed scaffolds to various stimuli [323]. After being implanted, hydrogel scaffolds are constantly in a dynamic environment due to changes in the surrounding damaged tissue and the cells encapsulated within the scaffold. Various stimuli, such as temperature, pH, ion concentration, pressure, and enzymes, may affect the output of the implant's intended functions. Therefore, to meet such technical requirements for tissue regeneration, 3D bioprinting technology will evolve into 4D bioprinting, whereby time is integrated as a processing parameter [324]. As time changes, the geometric shape and behaviour of 4D printed scaffolds are expected to transform, depending on the components' response to the surrounding and internal environmental factors [325]. This stimulus-responsive behaviour of the scaffold reflects the scaffold's intelligent control of its own geometric, mechanical, and surface/interface properties [326], thus making it more suitable for the complex dynamics of natural tissues. In conclusion, the development of 4D bioprintable, stimulus-responsive hydrogel scaffolds should be highlighted in the next step of tissue regeneration.

Chapter 3

METHODOLOGY

3.1 Chemical analysis

3.1.1 Attenuated total reflection Fourier-transform infrared spectroscopy

Infrared spectroscopy, based on the principle of absorption of specific wavelengths of infrared light by compound molecules during molecular vibrations, is widely used in various fields such as food, chemical, pharmaceutical, and environmental industries for determining the structural characteristics of compounds [327]. The attenuated total reflection (ATR) mode has become increasingly prevalent as an analytical technique in Fourier-transform infrared (FTIR) spectroscopy, primarily owing to its inherent advantage of obviating the need for sample preparation, in contrast to the conventional transmission mode [328]. A typical attenuated total reflection Fourier-transform infrared (ATR-FTIR) spectroscopy consists of an infrared source, a scanning interferometer (including a beam splitter, a fixed mirror, and a movable measurement mirror), a ATR crystal sampling cell, a detector and a fast Fourier transition computer system, as shown in Figure 3.1. The infrared source emits high-intensity broadband infrared radiation with a continuous wavelength. Within the interferometer, the beam splitter splits the incident infrared light into two beams: reflected and transmitted light. After travelling to the fixed mirror and the movable measurement mirror respec-

tively, the reflected and transmitted light are recombined by the beam splitter into interferometric light. Upon entering the ATR crystal, the beam experiences total internal reflection at the interface between the crystal and the sample, facilitated by the disparity in refractive index. This reflection results in an 'evanescent wave', which permeates the sample to a depth typically ranging from 0.5 to 3 µm [329]. Within this region, a minute fraction of the infrared light is absorbed, leading to a subtle attenuation of the total reflection. As a consequence, the intensity difference of the infrared light, as a function of the position of the movable mirror, also known as an interferogram, is collected by the detector. Such time-domain interferogram is eventually converted to a frequency-domain infrared spectrum by a fast Fourier transform computer, thus providing a representation of the molecular vibrations and absorbance bands characteristic of the sample [330].

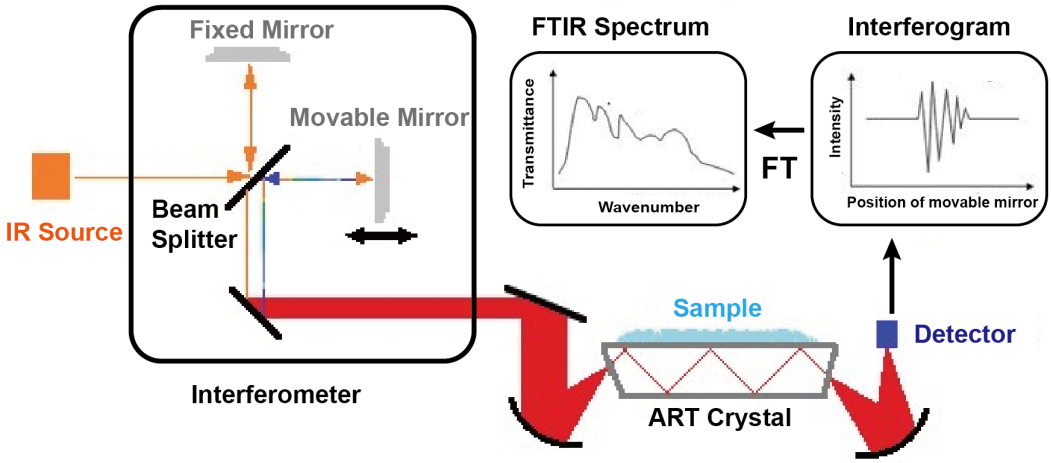

Figure 3.1: Principle of ATR-FTIR spectrometer.

In the present work, ATR-FTIR was firstly used to evaluate whether gelatin was modified with methyl acrylate by monitoring the characteristic absorption peaks of the alkene functional groups. Secondly, the successful crosslinking of microfibrillated cellulose (MFC)-composited or nanofibrillated cellulose (NFC)-composited ionic-covalent entanglement (ICE) gelatin methacryloyl (G)/sodium alginate (A) bioink formulations was interpreted by comparing ATR-FTIR spectra of different compositions.

3.1.2 Proton nuclear magnetic resonance spectroscopy

Nuclear magnetic resonance (NMR) spectroscopy is a highly potent technique utilised for elucidating chemical structure, conformation, and compound purity analysis [331]. The fundamental principle of NMR spectroscopy involves the interaction between atomic nuclei possessing a magnetic moment and an external magnetic field [332].

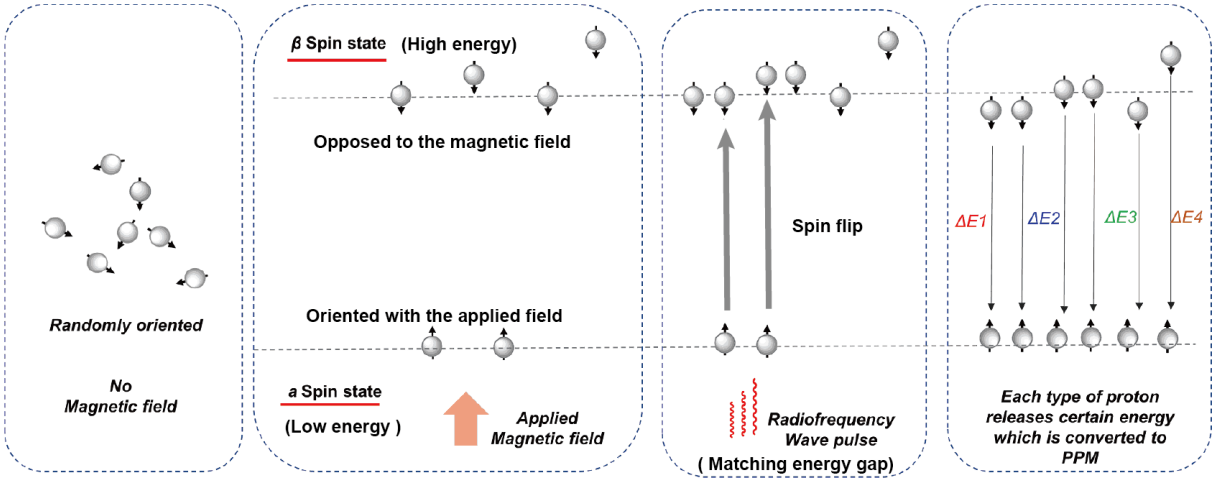

Figure 3.2: Principle of NMR spectrometer.

As shown in Figure 3.2[1], the nucleus exhibits two distinct spin states in the presence of the external magnetic field. The nucleus in the lower energy state, labeled as α spin state, aligns with the direction of the applied magnetic field, while the nucleus in the higher energy state, denoted as β spin, are opposed to the magnetic field. The α and β spin states possess an energy difference. When the sample is irradiated with a radiofrequency pulse precisely corresponding to this energy gap, the nucleus in the α spin state absorbs the radiofrequency energy and transitions to the higher energy state. Subsequently, the excited nucleus returns to its lower energy state by emitting energy at a resonant frequency. This energy signal is collected by a detector and transformed into an NMR spectrum [333]. The chemical shifts in the spectrum, expressed in parts per million (ppm), reveal the chemical environment surrounding the nucleus, while the signal intensity offers information

[1] https://www.chemistrysteps.com/nmr-chemical-shift/

regarding the relative quantities of different nuclear components within the sample. Therefore, proton nuclear magnetic resonance (^{1}H-NMR) in the present project was mainly used to determine the structure of sample G and to assess the degree of modification or purity of the substance.

3.2 Physical characterisation

3.2.1 Atomic force microscopy

Atomic force microscopy (AFM), as a form of scanning probe microscopy, is a crucial analytical instrument in scientific research, owing to its ability to elucidate the properties of materials and characterise the three-dimensional morphology of sample surfaces through the manipulation of atomic forces between the probe and the sample in nanoscale [334]. Its extensive applications span various fields, including surface science, materials science, and life science [335]. With the continual advancement of AFM technology, numerous analytical capabilities have been developed, cementing its position as an indispensable tool in academic research.

The most critical component in the AFM system is a micro-cantilever, with one end fixed and the other end suspending a sharp tip used to scan the sample surface. As the AFM tip raster-scans along the sample surface, both its vertical and lateral movements are continuously monitored by a position-sensitive optical sensor, which tracks the reflected laser beam from the backside of the tip, as shown in Figure 3.3a [336, 337]. AFM probe exhibits a lateral resolution in the range of a few nanometers, enabling the precise measurement and imaging of surface features at the nanoscale. More importantly, the exceptional vertical resolution of 0.1 nm allows for highly accurate profiling height variations on the sample surface [338].

Another key aspect of the AFM system is the feedback loop. AFM operates with different feedback parameters in various operating modes. In the contact mode, the tip remains in close contact with the sample surface, and the interaction between the sample and the probe tip is repulsive, with the feedback parameter being the cantilever deflection. In tapping mode, the

cantilever oscillates at its resonant frequency at a distance of 5-10 nm above the sample surface (Figure 3.3b) [336] and the interaction between the sample and the tip is van der Waals (attractive). The oscillation amplitude of the cantilever serves as the feedback parameter. Taking the contact mode as an example, when the repulsive force between the probe and the sample surface changes, the optical sensor detects the deflection of the probe. The Z-axis feedback controller compares the real-time deflection value with the setpoint and adjusts the Z-piezoelectric scanner to move the cantilever up or down, in order to maintain the cantilever deflection near the setpoint and thus maintain a constant interaction force between the sample and the probe [339]. The resulting movement of the Z-piezoelectric scanner provides height data for creating the surface topography of the sample.

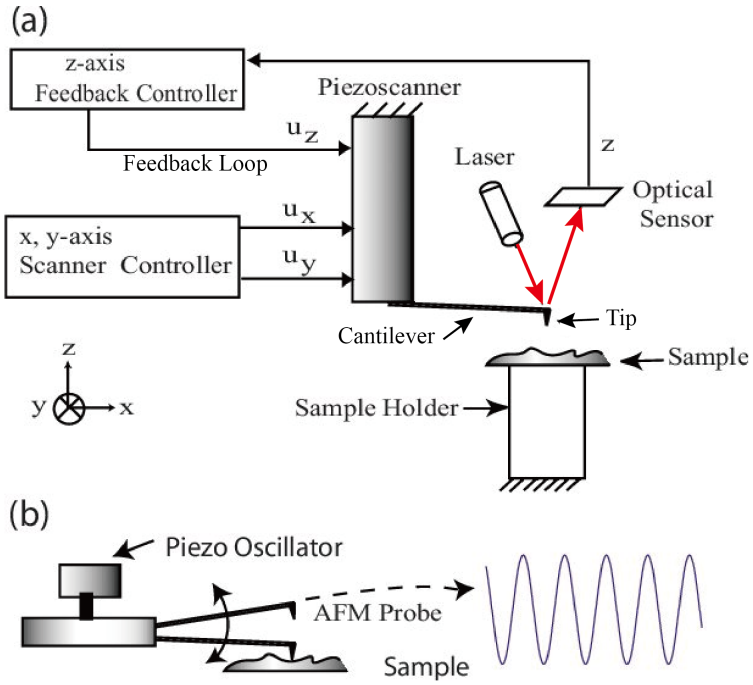

Figure 3.3: (a) The schematic of AFM and (b) AFM probe oscillation during tapping mode.

AFM demonstrates broad applicability in different operating modes and measuring environments such as ambient phase, liquid phase, and vacuum, primarily due to the high flexibility of the cantilever. The cantilever is available in various specifications, including shape (triangular,

rectangular), length (7 - 500 µm), spring constant (0.01 - 2000 N/m), resonance frequency (6 - 5000 kHz), material (silicon, silicon nitride, silicon oxide, quartz-like), tip shape (pyramidal, plateau, spherical), tip coating (uncoated, gold, platinum, diamond, cobalt alloy), tip height (2 - 50 µm), and tip curvature radius (1 - 20000 nm), among others [340]. This high degree of flexibility enables AFM to adapt to different types of samples and experimental requirements.

In this study, dimensions of MFC and NFC in aqueous solution are significant for various properties of bioink formulations and hydrogels, such as rheological properties and mechanical properties. Therefore, the morphology of MFC and NFC was investigated by AFM in tapping mode.

3.2.2 Fluorescence microscopy

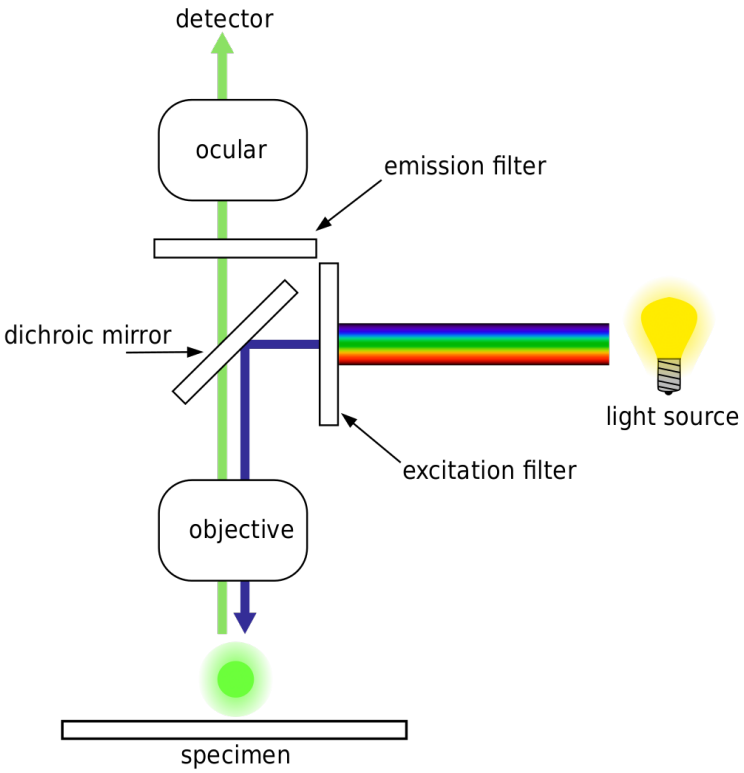

Figure 3.4: The principle of fluorescence microscopy.

The phenomenon of fluorescence refers to the process in which fluorescent molecules absorb

energy when exposed to light of a certain wavelength, transition to an excited state, and then rapidly return to the ground state, which emits fluorescent photons simultaneously. Fluorescence microscopy utilizes this principle to image samples. As shown in Figure 3.4[2], the complex colour light emitted from a strong light source is filtered into a specific band of excitation light after passing through an excitation filter. The excitation light passes through the dichroic mirror and the objective lens to illuminate the sample. The sample absorbs some of the energy and generates longer-wavelength emission light. The emission light in turn passes through the objective mirror, the emission filter and then enters the detector to obtain the sample image [341].

The homogeneity level and dispersion state of MFC and NFC directly affect the various characteristics of bioink formulations and hydrogels. Before mixing MFC and NFC with other components of the bioink formulation, fluorescence microscopy was used to evaluate the dispersity of cellulose in aqueous solution.

3.2.3 Confocal laser scanning microscopy

Confocal laser scanning microscopy is considered to be an advanced version of fluorescence microscopy as it overcomes some limitations of standard fluorescence microscopy. In conventional fluorescence microscopy, the sample is uniformly illuminated and the detector captures not only the desired in-focus light from the focal plane but also out-of-focus light from regions above and below the focal plane [342]. As a result, the collected out-of-focus light contributes to blurriness and low spatial resolution (about 200 nm lateral and 600 nm axial) of the image, particularly when imaging samples with a certain thickness [343].

In confocal laser scanning microscopy, "confocal" means that the light beam is focused twice along the optical path. As shown in Figure 3.5[3], instead of illuminating the entire sample at once, the laser is focused onto a specific point within the three-dimensional sample. This point lies precisely

[2] https://en.wikipedia.org/wiki/Fluorescence_microscope
[3] https://www.calm.ed.ac.uk/CALM%20UoE-CLSM%20tutorial%2001.html

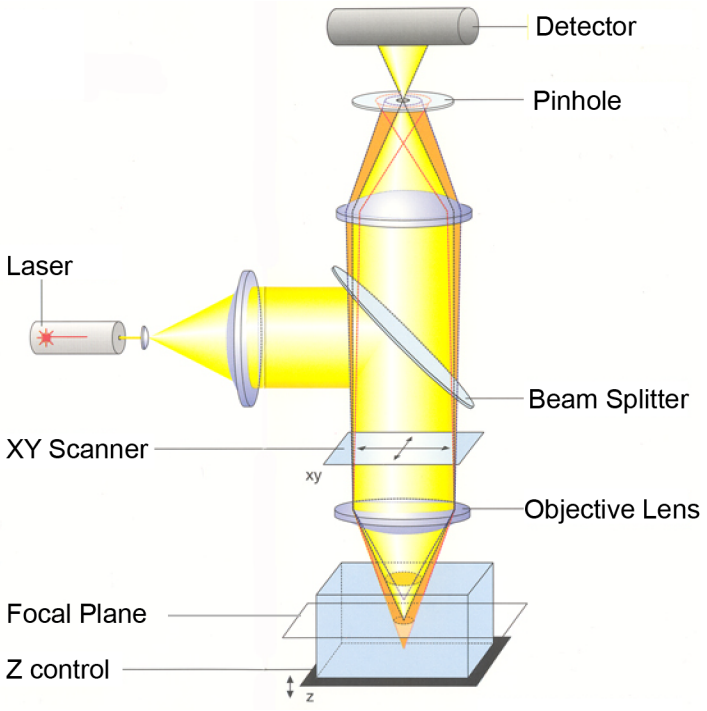

Figure 3.5: The basic imaging principle of confocal laser scanning microscopy.

at the focal plane of the objective lens. Secondly, the emitted light from this point is refocused when it passes through a pinhole and the resulting signal is collected by a detector. It is due to the obstruction of the pinhole that prevents out-of-focus light emitted above and below the focal plane from being imaged through the pinhole [344]. As a result, the resolution (< 400 nm axial) and signal-to-noise ratio of the image are significantly improved [345].

Furthermore, due to the limited imaging capability of the pinhole that can only capture a small region of the sample (approximately 100 nm), it is essential to perform a scanning of the sample across the entire focal plane using a XY scanner for comprehensive coverage. Subsequently, by gradually changing the position of the sample along the Z-axis, the morphology of different depth layers of the sample is sequentially collected. Finally, the 3D spatial morphology of the sample can be visualised by stacking multiple depth layers. Four-dimensional imaging by confocal laser scanning microscopy is also possible through the continuous dynamic tracking of live cell samples at the separation time [346].

To study the biocompatibility of MFC-composited and NFC-composited ICE G/A hydrogel scaffolds, the viability of cells encapsulated in printed 3D scaffold within three weeks was recorded by confocal laser scanning microscopy in this work. Before each imaging, cells in hydrogels were stained using a Live/dead viability kit (calcein AM/ethidium homodimer-1). Therefore, live cells appear green when imaged, while dead cells are red.

3.2.4 Scanning electron microscopy

Scanning electron microscope (SEM) is a powerful and flexible tool for investigating a wide range of organic and inorganic materials at a micro- to nanoscale level. The working principle of a SEM is based on the interaction between a high-energy electron beam (< 30 KeV) and the atoms of the sample [347].

Specifically, the electron beam emitted from a field emission gun or a thermionic emission gun is accelerated at an accelerated voltage of 5 - 30 KV by an anode and then focused by electromagnetic lenses to form a small electron spot (< 10 nm in diameter) that bombards the surface of the sample [348]. Excited regions of the sample can produce various signals depending on the penetration depth of the electron beam, including Auger electrons, secondary electrons, backscattered electrons, characteristic X-rays, continuous X-rays, cathodoluminescence, and transmitted electrons, just as shown in Figure 3.6 [349]. These signals contain information about various physical and chemical properties of the sample, such as morphology, composition, crystal structure, electronic structure, and internal magnetic field. To detect and analyse these signals, different types of signal detectors can be selectively installed in SEM [350]. As a versatile platform, SEM allows users to customise the functionality and configuration of SEM according to their specific needs.

The secondary electron imaging mode is the most fundamental operating mode of SEM. Secondary electrons are the electrons that are emitted from the atoms of the sample's surface when the incident electron beam bombards them and leave the sample. Secondary electrons are referred to as inelastic scattered electrons because the incident electron beam loses energy upon bombardment.

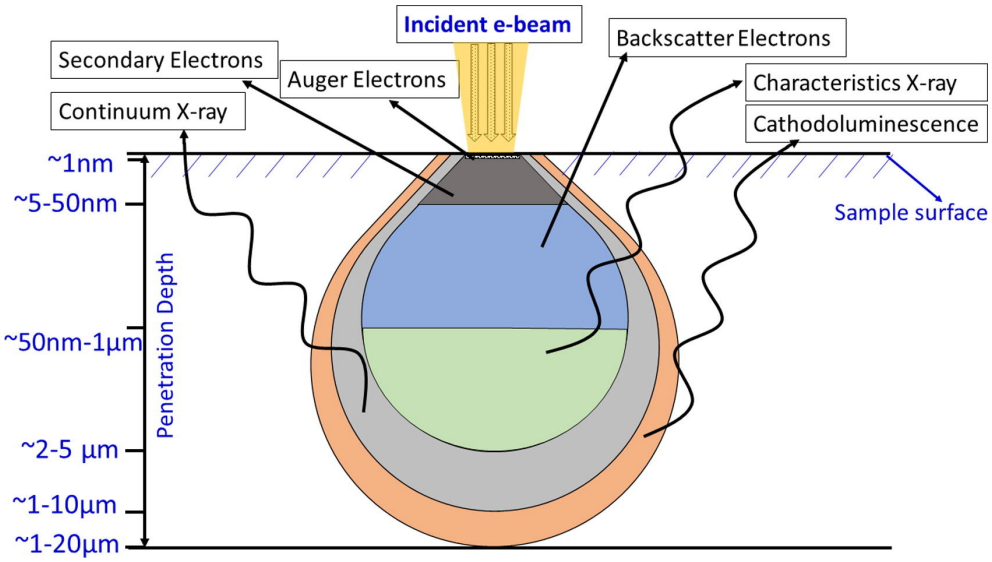

Figure 3.6: Different signals emitted from sample excited by an electron beam in different penetrated depth ranges in sample [349].

Generally, secondary electrons are emitted from a depth range of 5 to 50 nm from the surface of the sample (grey zone in Figure 3.6). They are highly sensitive to the surface morphology of the sample, which allows for high-resolution imaging of the sample's surface morphology [351].

The backscattered electron imaging mode is also a commonly used operating mode in SEM. When the incidenting electron beam interacts with the atomic nuclei of the sample, elastic scattering occurs within a depth range of 50 nm to 1 µm (blue zone in Figure 3.6), resulting in backscattered electrons. The characteristics and yield of backscattered electrons are strongly dependent on the atomic number of the material. The higher the atomic number of the sample atoms, the more backscattered electrons are collected, resulting in brighter regions in the image [349]. Therefore, backscattered electron imaging not only provides information about the morphology of the sample but, more importantly, reveals the distribution of chemical elements, which is commonly used to distinguish different phases or components within a sample [352].

Additionally, characteristic X-ray or energy-dispersive X-ray (EDX) detectors are commonly used in conjunction with SEM. The principle behind this is that when the incident electron beam bombards the atoms of the sample, it displaces inner-shell electrons, creating inner-shell vacancies.

The outer-shell electrons in higher energy levels will then fill these lower energy-level vacancies, emitting characteristic X-rays in the process [353]. Therefore, through characteristic X-rays, the types of elements present in the sample, and their respective quantities, can be reflected [354]. It is precisely due to this significant advantage that EDX-SEM is widely used for qualitative and quantitative analysis of samples.

In this project, freeze-dried hydrogel discs treated with gold coating were subjected to secondary electron imaging. By comparing the morphological information of different samples, the effect of MFC and NFC on the mechanical properties of G/A hydrogels and the enhancement mechanism of MFC-composited and NFC-composited ICE G/A hydrogel can be revealed. Additionally, the morphological changes that occur in the printed cell-encapsulated scaffold during cell growth and scaffold degradation were also recorded through secondary electron imaging mode of SEM.

3.2.5 Micro-computed tomography

X-ray micro-computed tomography (μCT) is a 3D imaging technique of matter's morphology and internal microstructure [355]. Samples can be directly tested by placing them on a rotating stage, without the need for cutting, spraying, staining, or vacuum treatment [356]. This non-destructive testing approach of μCT finds its extensive applications in various fields such as biological sciences[357–359], materials sciences[360, 361], food sciences[355, 362], and earth sciences [363]. It is worth mentioning that, in contrast to the widely used clinical CT (spatial resolution of 1 - 2.5 mm corresponding to 1 - 10 mm^3 voxel size), μCT reduces the imaging scale while significantly improving the resolution to the micro or sub-micron level (about 5 μm corresponding to 1×10^{-7} mm^3 voxel size) [364]. Furthermore, in terms of image acquisition, the X-ray source and detector remain fixed while the sample is rotated, whereas in clinical CT, the X-ray source and detector move around a fixed sample.

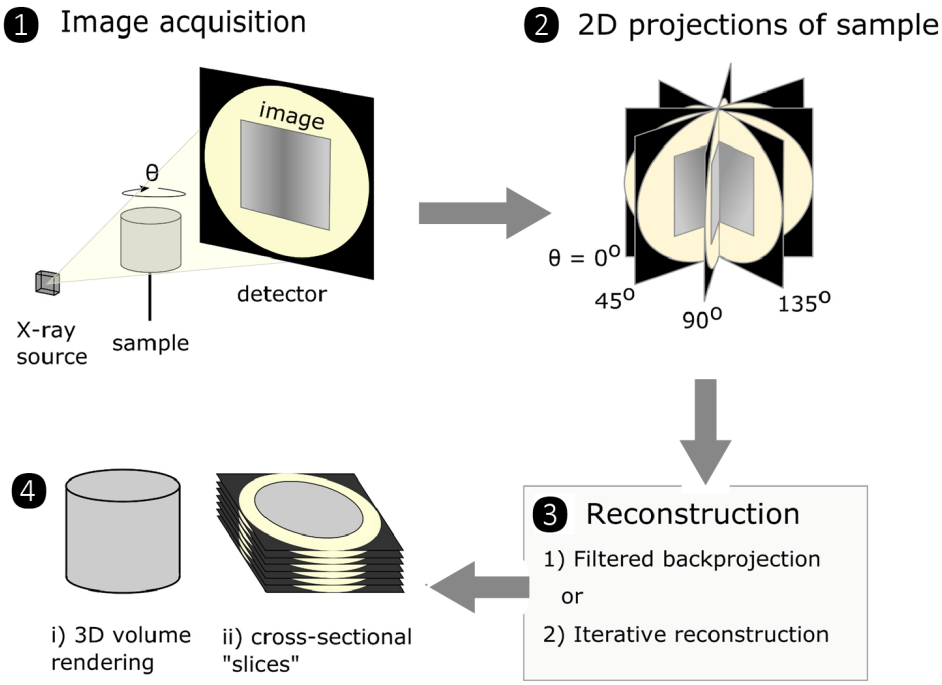

Figure 3.7: Basic flowchart of micro-computed tomography for 3D reconstruction of samples [358].

Figure 3.7 illustrates the sequential progression from the initial sample scanning to the ultimate visualization of a 3D model encompassing inherent internal characteristics [358]. First, the sample is subjected to direct exposure to electromagnetic radiation emitted by a conical X-ray beam. Owing to variations in properties such as thickness, density, elemental composition, and other factors within the sample, the incident X-ray radiation experiences differential absorption within the sample, leading to heterogeneous attenuation of the X-ray transmission intensity [365]. For instance, if a material is dense or contains heavy elements, it will attenuate X-rays more significantly, resulting in a reduction in X-ray transmission rate [366]. The detector converts the attenuated radiation passing through the sample along a straight path into a 2D digital projection image of the sample. Subsequently, the sample is rotated by a certain angle, and another X-ray 2D projection image is captured. This process is repeated multiple times, with the number of 2D projection images determined by the rotation step and the total rotation angle [365]. The process of converting the 2D

projection images of the sample into cross-sectional images of the sample is called reconstruction. This is achieved through complex computerized algorithms such as filtered back-projection and iterative reconstruction [367]. A series of cross-sectional images can be analyzed by relevant software to obtain information about the internal structure of the sample, such as porosity, pore size distribution, and other characteristics. These slices can also be further processed to create a 3D digital model or used to generate animations [358].

The application of µCT in this project was to uncover the principle of mechanical enhancement of MFC-composited and NFC-composited ICE G/A hydrogels by assessing the internal pore structure of lyophilised hydrogels, such as porosity, mean pore size, and pore size distribution. Consequently, µCT and SEM complemented each other, showcasing the internal characteristics and surface morphology of 3D crosslinked hydrogels in a comprehensive manner.

3.3 Mechanical properties

3.3.1 Rheology

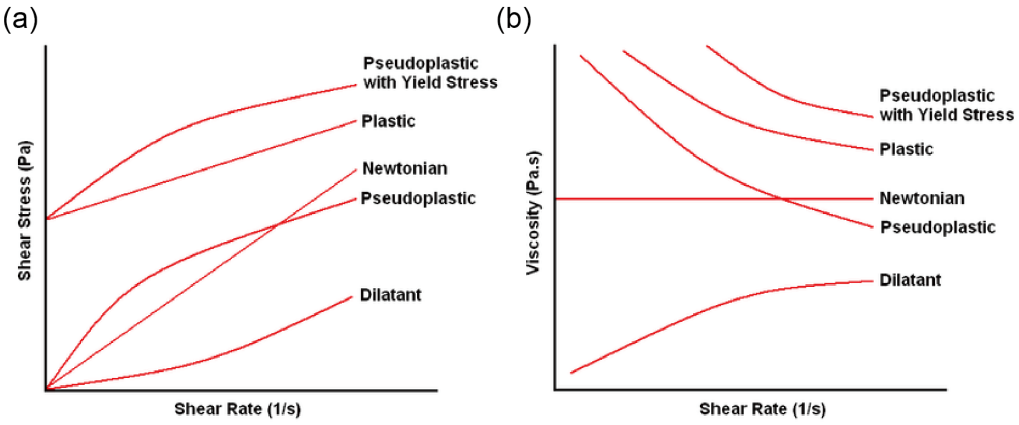

Figure 3.8: Classical flow curves of the most common fluids: (a) Shear stress against shear rate and (b) viscosity versus shear rate [368].

Table 3.1: Types of fluids and corresponding models and equations of flow behaviour.

Type of fluid	Flow model	Equation
Newtonian	Newtonian	$\sigma = \eta_0 \dot{\gamma}$
Pseudoplastic	Power law	$\sigma = k_{PL} \dot{\gamma}^{n_f}, n_f < 1$
Dilatant	Power law	$\sigma = k_{PL} \dot{\gamma}^{n_f}, n_f > 1$
Plastic	Bingham	$\sigma = \sigma_y + \eta_B \dot{\gamma}$
Pseudoplastic with yield stress	Herschel-Bulkley	$\sigma = \sigma_y + k_{HB} \dot{\gamma}^{n_f}, n_f < 1$

The rheological behaviour of bioink formulations depends on several factors such as formulation concentration, cellulose fibre size, environmental temperature, pressure, and the type of deformation in the application. To study the rheological performance of bioink formulations, it is necessary to introduce several recognized rheological types of fluids. Figure 3.8 illustrates the flow curves of the most common fluids currently. To analyse the differences in flow behaviour between fluids, different mathematical models are used to describe each type of flow behaviour. Table 3.1 lists the models and expressions corresponding to the common types of flow.

A fluid whose viscosity remains constant at different shear rates for a given temperature and pressure is a Newtonian fluid, and the flow curve obtained by plotting shear stress (σ) against shear rate ($\dot{\gamma}$) is a straight line through the origin. This is the ideal fluid behaviour, with η_0 in the corresponding equation called apparent viscosity [369]. For example, water, ethanol and most pure solvents are approximated as Newtonian fluids.

Most fluids encountered in practical applications do not have a constant ratio of shear stress to shear rate (viscosity). Instead, viscosity depends on the applied force or rate of deformation. Such fluids are collectively referred to as non-Newtonian fluids. Among them, pseudoplastic fluids exhibit a decrease in viscosity with increasing shear rate. This behaviour is known as shear thinning [370]. Examples of pseudoplastic fluids include ketchup, lotions, and blood. Conversely, dilatant fluids demonstrate shear thickening behaviour, where viscosity increases with increasing shear rate. An example of a dilatant fluid is a mixture of cornstarch and water. Both of these fluid behaviours can be described using the power-law flow model, where the power-law flow index (n_f), also known

as the viscosity index, is used to differentiate between shear thinning ($n_f < 1$) and shear thickening ($n_f > 1$) behaviour [371].

Some non-Newtonian fluids require a certain level of stress, known as yield stress (σ_y), to start flowing. Once the flow begins, if the relationship between shear stress and shear rate is linear and the viscosity remains constant, it is referred to as a Bingham plastic fluid, like toothpaste. On the other hand, if the viscosity decreases with an increasing shear rate, Herschel-Bulkley model is used to describe such pseudoplastic fluid with yield stress [372].

Rotational rheometer is the most widely used rheological measurement instrument in the material field. It allows the study of flow and deformation characteristics of samples ranging from low-viscosity fluids to high-strength solids. The instrument consists of two measurement plates or similar geometries (such as parallel plates, cone plates, or cup and bob systems) between which the sample is loaded. In rotation or oscillation mode, when a torque is applied to the upper plate, a rotational shear stress is applied on the material, which allows the measurement of the resulting strain or strain rate, as shown in Figure 3.9 [373]. This enables the determination of rheological parameters such as viscosity, storage modulus, loss modulus, and other rheological properties of the sample.

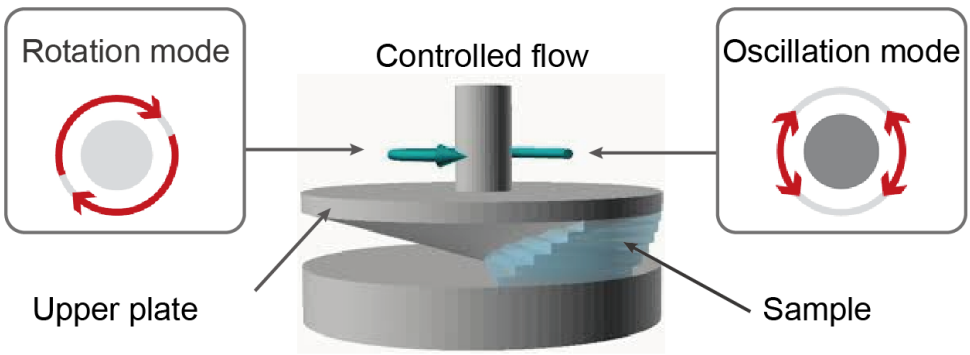

Figure 3.9: The principle of the rotational rheometer [373].

Therefore, this study used a rotational rheometer to measure the rheological properties of MFC-composited and NFC-composited G/A bioink formulations so as to justify the processibility of

bioink formulations in early stage and guide the setup of printing parameters in extrusion printing. The rotation mode was used to evaluate the viscosity trend of the specimen with shear rate, while the oscillation mode was applied to test the storage modulus and loss modulus of bioink under a series of procedures that simulate the printing process.

3.3.2 Macro-compression

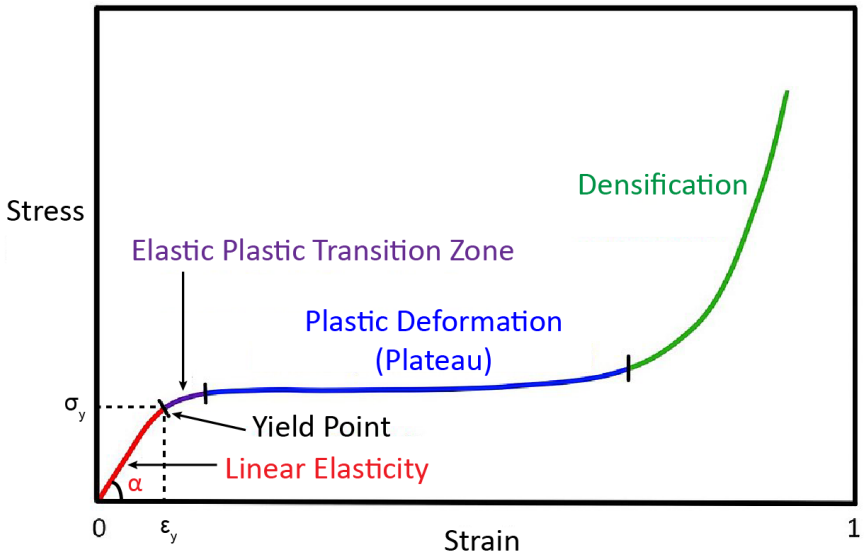

Figure 3.10: The typical compressive stress-strain curve of polymer networks.

Hydrogels, as highly hydrated crosslinked polymers, can be investigated for their mechanical properties by tracking the stress applied to the sample and the corresponding strain generated by the material in macroscale tensile or compression experiments. Stress is defined as the force applied to the sample surface divided by the initial cross-sectional area of the sample, also known as engineering stress or nominal stress. Strain is the ratio of the amount of change in the dimensions of the sample to the initial dimensions and is also referred to as engineering strain or nominal strain.

Figure 3.10 depicts a typical stress-strain curve of a crosslinked polymer in a macro-compression experiment. The first stage is the linear elastic region (red line). The sample follows Hooke's law,

with stress increasing proportionally to strain. After the stress is removed, the sample can fully recover to its initial state. The slope of the straight line is defined as Young's modulus or elastic modulus (tan α). The linear elastic deformation generally occurs within a strain range of 0 to 15%. As compression increases, the sample starts to yield, transitioning from elastic deformation to plastic deformation gradually. The stress and strain corresponding to the start of the elastic plastic transition zone are respectively referred to as yield stress (σ_y) and yield strain (ε_y). The stress-strain curve begins to bend (purple section). Subsequently, the sample enters a complete plastic deformation region. The stress-strain curve exhibits a plateau with minimal increase in stress but a significant increase in strain (blue line segment). When the plastic deformation of the sample reaches its limit, the sample is compressed very tightly. Therefore, even small deformations of the sample require higher stress to support, leading to densification of the sample (green line segment) [374]. It is worth noting that the composition of the polymer network, crosslinking density, network properties etc. determine the trend of the stress-strain curve, thereby affecting the mechanical properties such as Young's modulus, yield, and toughness of the material.

In the present project, macroscale coaxial compression testing of MFC-composited and NFC-composited ICE G/A hydrogels discs was employed to investigate Young's moduli, yield points and deformation trends of samples based on the corresponding engineering stress-strain curves. Moreover, synergistic enhancement effects of ICE G/A double networks and MFC or NFC were also revealed.

3.3.3 Micro-indentation

The precise extraction of mechanical properties of hydrogels depends on selecting length scale-matched testing techniques. Conventional mechanical property measurement techniques of soft materials include macroscopic compression and tensile[375–377], and AFM indentation at the nano or submicron scale [378, 379]. However, the modulus and hardness values of the hydrogel at different test length scales may vary by 3 orders of magnitude [380]. Because of indenters' force

working range of 1 μN to 500 mN and displacement range of 1 nm and 20 μm, it effectively fills the gap between AFM and macroscopic mechanical testing like a universal testing machine, becoming a powerful tool to characterise the local mechanical properties of small or heterogeneous samples from micro-scale with high resolution and speed while often being non-destructive. However, careful consideration of micro-indentation's limitations, like meticulous surface preparation and environmental sensitivity, is necessary for accurate and meaningful interpretations of its results. The indentation instrument investigates the microscale mechanical properties of materials by pressing into and withdrawing the material surface with a tiny indenter while recording both the force applied to the indenter and the displacement of the indenter. Similar to the macro-compression experiments, micro-indentation can track the corresponding displacement of the indenter by controlling the load applied to the indenter. Or a maximum depth of indenter can be set and the corresponding force can be recorded.

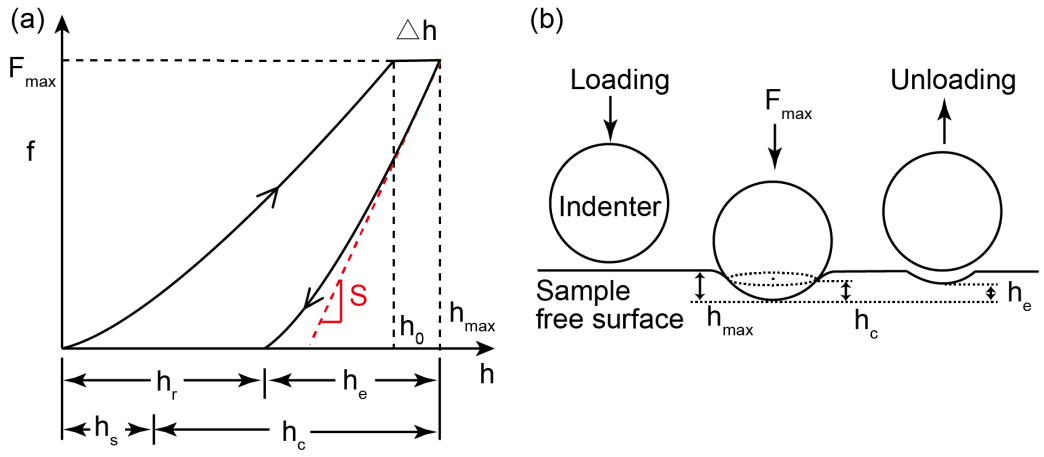

Figure 3.11: (a) A typical load-depth curve obtained by indenter and (b) schematic of indentation process.

In a typical micro-indentation test (Figure 3.11), after the indenter approaches the sample surface, load (f) is applied to the indenter and increased from 0 to the maximum load (F_{max}) at a loading rate. The depth of penetration (h) of indenter beneath the original sample free surface is recorded from 0 to initial depth (h_0) simultaneously. The indenter is then held at F_{max} on the sample

for a period of time, and the depth variation (Δh) with time and the final maximum depth ($h_{\max}$) are recorded to study the creep behaviour of the sample. Here, the distance from the circle of contact to the maximum depth is contact depth (h_c). The vertical distance from the original sample free surface to the circle of contact is the depth of the contact circle (h_s). Finally, the load is withdrawn from the surface at a certain unloading rate. Due to the reversible elasticity and irreversible plasticity of the sample, after complete unloading, a residual impression is left on the sample surface. The depth of residual impression and depth of elastic recovery are denoted as h_r and h_e, respectively.

The two most commonly used parameters to characterise the mechanical properties of materials, hardness and modulus, can be calculated based on the load–depth curve by the following equations:

$$H_I = \frac{F_{max}}{A_c} \tag{3.1}$$

$$E_r = \frac{S\sqrt{\pi}}{2\sqrt{A_c}}, \tag{3.2}$$

where H_I is indentation hardness, A_c is the projected contact area between the indenter and the sample at $F_{\max}$, E_r is reduced modulus (the composite modulus of the indenter and the specimen), and S is contact stiffness, represented in Figure 3.11a as the slope of the unloading curve dF/dh. Among them, A_c is related to the indenter geometry and h_c at $F_{\max}$. For a spherical indenter with radius R_i, A_c is determined by the equation:

$$A_c = 2\pi R_i(h_{max} - \frac{3}{4} \cdot \frac{F_{max}}{S}) \tag{3.3}$$

Moreover, as E_r is determined by both sample and indenter, the Young's modulus of the sample (E_s) can be calculated by the following equation:

$$\frac{1}{E_r} = \frac{1 - v_i^2}{E_i} + \frac{1 - v_s^2}{E_s}, \tag{3.4}$$

where v_i is the Poisson's ratio for indenter (0.07), E_i is the Young's modulus of indenter diamond tip (1141 Gpa), v_s is the Poisson's ratio for sample (0.5) [381]. Since E_i is much larger than that of soft material, the part about the indenter in Equation 3.4 can be ignored. Therefore, E_s can be determined from E_r if v_s is known.

In addition, as a typical viscoelastic polymer, hydrogels have a number of time-dependent deformation behaviours such as creep, stress relaxation, hysteresis and internal dissipation. In micro-indentation tests, creep behaviour is characterised by analysing creep depth (h_{cr}) – dwelling time (t) curve in the holding period at maximum load. The following relationships are applied to fit $h_{cr} - t$ curve:

$$h_{cr} = h_{max} - h_0 = A \cdot \ln(Bt + 1) \tag{3.5}$$

where A and B are the fitting parameters. A/h_0 is employed to describe creep strain rate sensitivity. A/h_0 pertains to the extent to which time-dependent deformation occurs in comparison to the deformation experienced when swiftly subjecting the specimen to a creep load [382, 383]. The creep strain rate ($\dot{\varepsilon}$) can explain materials' time-dependent deformation and is expressed as:

$$\dot{\varepsilon} = \frac{dh}{dt}\frac{1}{h_{ic}} \tag{3.6}$$

where dh/dt is the displacement rate of the indenter, and h_{ic} is the instantaneous indenter depth during creep.

Meanwhile, the creep rate (C) was used to compare the creep resistance of different materials and expressed as:

$$C(\%) = \frac{h_{max} - h_0}{h_0} \cdot 100 \tag{3.7}$$

In summary, based on the principles mentioned above, the micro-mechanical properties of cellulose-composited ICE G/A hydrogels were analysed in depth through micro-indentation testing.

Since specific testing procedures and environments were introduced for soft materials, the validity of the testing was verified by changing the loading rate, creep time, and unloading rate sequentially. Subsequently, the effect of MFC and NFC on the modulus, modulus distribution, and creep resistance of the hydrogel samples were elucidated.

3.4 Three-dimensional printing

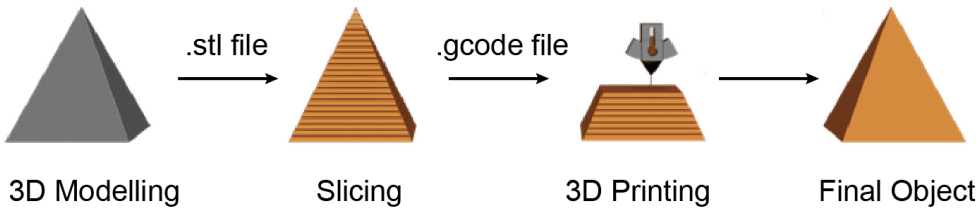

Figure 3.12: The process of 3D printing from a digital model to a solid object.

Three-dimensional printing can roughly be divided into three steps, as shown in Figure 3.12: 3D modelling, slicing, and 3D printing. First, 3D modelling is the process of producing a virtual model and defining the geometric parameters such as the size and shape of the model by a dedicated software[384], such as Blender, Onshape, and Solidworks. As a mechanical device, 3D printer does not have the ability to recognize geometric information. Therefore, the slicing process acts as a bridge between modelling and printing by converting the geometric information of the digital model (.stl file format) into a programming language that 3D printer can read and understand, namely G-code [385]. Slicing software, like Cura and Slic3r, slices the 3D digital model into multiple 2D planes. Each 2D plane is assigned specific values within the same X-Y coordinate system. Therefore, after slicing, the digital model becomes a stack of multiple different 2D planes in the Z direction. G-code is expressed as the form of the letter G followed by a number. Meanwhile, it also includes letters such as F, M, S, etc., followed by numbers [384]. This means that G-code not only provides information to 3D printers about the direction, distance, and speed of movement but

also controls printing temperature (bed heating or fan), feeding rate, fill density, and so on during the printing process. Finally, 3D printer follows the instructions in the G-code to print layer-by-layer to build the final physical object.

In this work, a nozzle-based pneumatic extrusion printer was used to achieve layer-by-layer printing of bioink formulations so as to create a variety of customised physical objects. Different bioink formulations were processed into 1D filament, 2D scaffolds, and 3D constructs and the printability in each dimension was figured out based on different evaluation metrics.

Bioink formulations were firstly printed to construct 1D filament pattern. One-dimensional printing performance evaluation aims to determine the optimal printing conditions for bioink formulations. Considering the printing resolution and the viability of cells encapsulated in the bioink, the evaluation criteria for the optimal printing conditions are the highest printing accuracy and precision, while minimising the theoretical shear stress [386]. During the extrusion printing process at room temperature, key parameters that affect printing accuracy and shear stress include dispensing pressure, nozzle diameter, and printing speed [387]. Maximising printing accuracy can be achieved by reducing the dispensing pressure and nozzle diameter, as well as increasing the printing speed [388]. In experiments, the width of the filament can be directly measured to characterise the printing accuracy under specific printing conditions [12]. Minimising shear stress can be achieved by reducing the dispensing pressure and increasing the nozzle diameter [12]. Therefore, parameter optimisation index (*POI*) was introduced to describe the effect of these adjustment parameters on printing performance and can be described as

$$POI_i = \frac{\text{Printing Accuracy}}{\text{Shear Stress}} = \frac{1}{W_L} \cdot \frac{1}{P \cdot G_N} \tag{3.8}$$

$$POI = \frac{POI_i}{POI_{MAX,n}} \tag{3.9}$$

where POI_i stands for the *POI* for an individual set of parameters, W_L represents the width of

the printed line without crosslinking, P means the dispensing pressure, G_N is the nozzle gauge and is inversely proportional to the inner diameter of the nozzle, and $POI_{MAX,n}$ denotes the maximum POI_i over the total range of parameter combinations n [12, 389]. Therefore, the value of *POI* is between 0 (the worst) to 1 (the best) [389].

Evaluation of 2D printability focuses on comparing the differences in printability of different bioink formulations. The evaluation criterion is the geometry of the grid or hole. After extrusion, sol-like bioink shows interlayer fusion and the formation of circular voids within the printed structure. However, gel-like bioink displays a coherent filament structure with consistent dimensions, yielding regular lattice patterns and square voids in the resulting constructs [390]. As roundness (*Ro*) measures how close a closed 2D figure is to a perfect circle, printability index (*Pr*) was introduced based on *Ro* [390, 391]. The expressions for *Ro* and *Pr* are as follows:

$$Ro = \frac{4\pi A}{L^2} \tag{3.10}$$

$$Pr = \frac{\pi}{4} \cdot \frac{1}{Ro} = \frac{L^2}{16A} \tag{3.11}$$

where A and L mean area and perimeter, respectively. Circles have the highest *Ro* of 1, while *Ro* of a square is $\pi/4$ [390]. Consequently, bioinks that produce square grids in the printed scaffolds have the optimum *Pr* of 1 while samples with circular holes due to interlayer fusion have the worst *Pr* of $\pi/4$ [65, 390].

Three-dimensional printability emphasises the shape fidelity of the printed constructs by measuring the thickness of the constructs with different numbers of layers and analysing the linear relationship between thickness and number of layers. Finally, mouse preosteoblast MC3T3-E1 was encapsulated in bioink formulations with excellent printability and printed as multilayer scaffolds. Cell viability is recorded over multiple days of *in vitro* culture.

3.5 Ultraviolet and visible spectrometer

In the realm of molecular biology, medicine, and the life sciences, the spectrometer holds great significance as a vital tool for research endeavours as well as routine quality assessment [392]. Ultraviolet and visible (UV/Vis) absorption spectrometry is a scientific technique that relies on quantifying the attenuation in intensity of UV/Vis electromagnetic radiation as it passes through a sample containing absorbing molecules [393]. Ultraviolet radiation has a wavelength range of about 200 - 400 nm, while the spectral range of visible light radiation is around 400-800 nm [394].

The principle underlying the quantification of radiation attenuation in UV/Vis spectrometry is based on Beer's Law, expressed as

$$A(\lambda) = a(\lambda) \cdot b \cdot c \tag{3.12}$$

where A(λ) means the measured absorbance at wavelength λ and is used to accurately describe attenuation of UV/Vis radiation, a(λ) is a wavelength-dependent molar absorption coefficient, b is optical path length of radiation through sample, and c represents the absorber concentration [395]. In this law, a(λ) of an absorber at a special wavelength is a constant and b is the width of a cuvette in spectroscopy. Therefore, A(λ) is directly proportional to c at wavelength λ. In other words, the higher the concentration of the sample solution, the greater the absorption of monochromatic light [395]. However, it is worth noting that the applicability of Beer's Law is limited to relatively dilute and homogeneous solutions [396]. Once the concentration of the solution exceeds a critical value, the absorbance of all concentrated solutions exhibits a meaningless plateau value.

In the present work, to study the effect of cellulose on controlled drug release for hydrogels, UV/Vis spectrometer was employed to measure the amount of drug loading for hydrogels and drug release at different times. The detailed methodology for controlled drug release in hydrogels is explained next part.

3.6 Controlled drug release

Hydrogel matrices are extensively employed in drug delivery systems owing to their exceptional biocompatibility, the ability for physicochemical tuning, controlled release properties, adaptability, and multifaceted delivery options encompassing oral administration, topical application, injections, and more [397–399]. Drugs can be embedded into hydrogels either post-loading or through *in-situ* encapsulation, enabling precise control over their release via diverse mechanisms [399].

Depending on variables such as the hydrogel type, crosslinking density, pore structure, surface characteristics, drug characteristics, release conditions, etc., drug release mechanisms within hydrogel matrices can involve single mechanisms or a composite interplay of multiple processes [399, 400]. There are four common release mechanisms:

1. Diffusion-controlled release: It is one of the most common release mechanisms. Drug molecules are gradually released from a non-degradable hydrogel into the surrounding environment by molecular diffusion driven by a concentration gradient [401]. Diffusion-controlled release follows Fickian's law of diffusion [402].

2. Swelling-controlled release: The change in pore structure of certain hydrogels upon swelling by water absorption results in the formation of channels for drug release [400, 403].

3. Erosion- or degradation-controlled release: In this mechanism, hydrogel matrices gradually erode (surface dissolution) or degrade (cleavage of internal chemical bond) under specific conditions, leading to the drug being released [404, 405]. The release rate depends on the rate of degradation or dissolution of the hydrogel.

4. Stimuli-responsive release: Designed hydrogels may release drugs in response to specific chemical physical stimuli, such as light, thermal, and pH changes or enzymatic activity [406].

Drug release kinetics models have been extensively developed for hydrogel matrices with the aim of comprehending and forecasting drug release patterns within hydrogels, ultimately optimising

Table 3.2: Drug release indices and release mechanisms for thin film, cylinder, and sphere polymer release systems [411, 412].

Release index, n_r			Drug release mechanism
Thin film	**Cylinder**	**Sphere**	
≤ 0.5	≤ 0.45	≤ 0.43	Fickian diffusion (Case I transport)
$0.5 < n_r < 1.0$	$0.45 < n_r < 0.89$	$0.43 < n_r < 0.85$	Anomalous transport
1	0.89	0.85	Case II transport
>1	>0.89	>0.85	Super case II

the design of drug delivery systems [407, 408]. The semi-empirical power-law model introduced by Peppas and co-workers [409] stands out among many drug release kinetics models, primarily because it accommodates a wide range of release behaviours, making it the preferred choice for numerous researchers in the field [410]. Power-law model is expressed as follows:

$$\frac{M_t}{M_\infty} = kt^{n_r} \tag{3.13}$$

where M_t and M_∞ are the cumulative release amount of the drug at time t and the total amount of drug that can be released, respectively; k is the release rate constant and related to structural and geometric features of the hydrogel matrix; n_r is the release index characterising the drug release mechanism. Equation 3.13 is valid for the first 60% of cumulative drug release [411].

Table 3.2 lists the drug release indices and release mechanisms for polymer controlled release systems with different geometries. Taking the thin film polymer controlled release system as an example, $n_r \leq 0.5$ indicates that drug release is controlled by Fickian diffusion, also called case I transport. In this situation, the half-life of drug release is short and release is usually completed within one day [400]. When n_r is 1, the drug is released at a constant rate, independent of drug concentration and time, which is called zero-order kinetics release [413]. The release mechanism is case II transport. Release can be controlled by polymer swelling, surface erosion, etc. In most cases, n_r lies between 0.5 and 1, indicating that drug release is caused by a combination of diffusion and other complex factors (swelling, degradation, nanocompositing, etc.) where the drug release

mechanism is anomalous transport. Only in rare cases, such as when the polymer matrix is severely modified, the release index is greater than 1 and super case II occurs [414].

To study the effect of cellulose on the drug release behaviour of ICE G/A hydrogels, ampicillin (drug model in our work) was incorporated into the hydrogel disc via post-loading. Then, the cumulative release concentration of ampicillin was recorded using a spectrometer at predetermined time intervals. Equation 3.13 was used to fit the cumulative release curve of ampicillin. The drug release mechanism of hydrogel discs can be further analysed based on the release index (n_r).

Chapter 4

PREPARATION AND CHARACTERISATION OF BIOINK FORMULATIONS AND HYDROGELS

4.1 Introduction

A definition of bioinks proposed by Groll et al. is 'a formulation of cells suitable for processing by an automated biofabrication technology that may also contain bioactive components and biomaterials' [415]. Bioinks may include cells in different forms, such as single cells, spherical cell aggregates, cellular rods, cells encapsulated in tailored colloidal microenvironments, etc [415]. In addition, bioinks can, but do not have to, contain bioactive molecules such as growth factors, DNA, miRNA, cytokines, exosomes, or biomaterials [415]. The use of bioinks is not restricted to any specific biofabrication technology, including but not limited to laser-assisted bioprinting, microfluidics, assembly, inkjet, and extrusion [415]. Furthermore, the application of bioinks extends across multiple domains within biofabrication. These applications range from cell printing to tissue/organ printing, the construction of organ- and body-on-a-chip systems, the development of *in vitro* models,

etc [415].

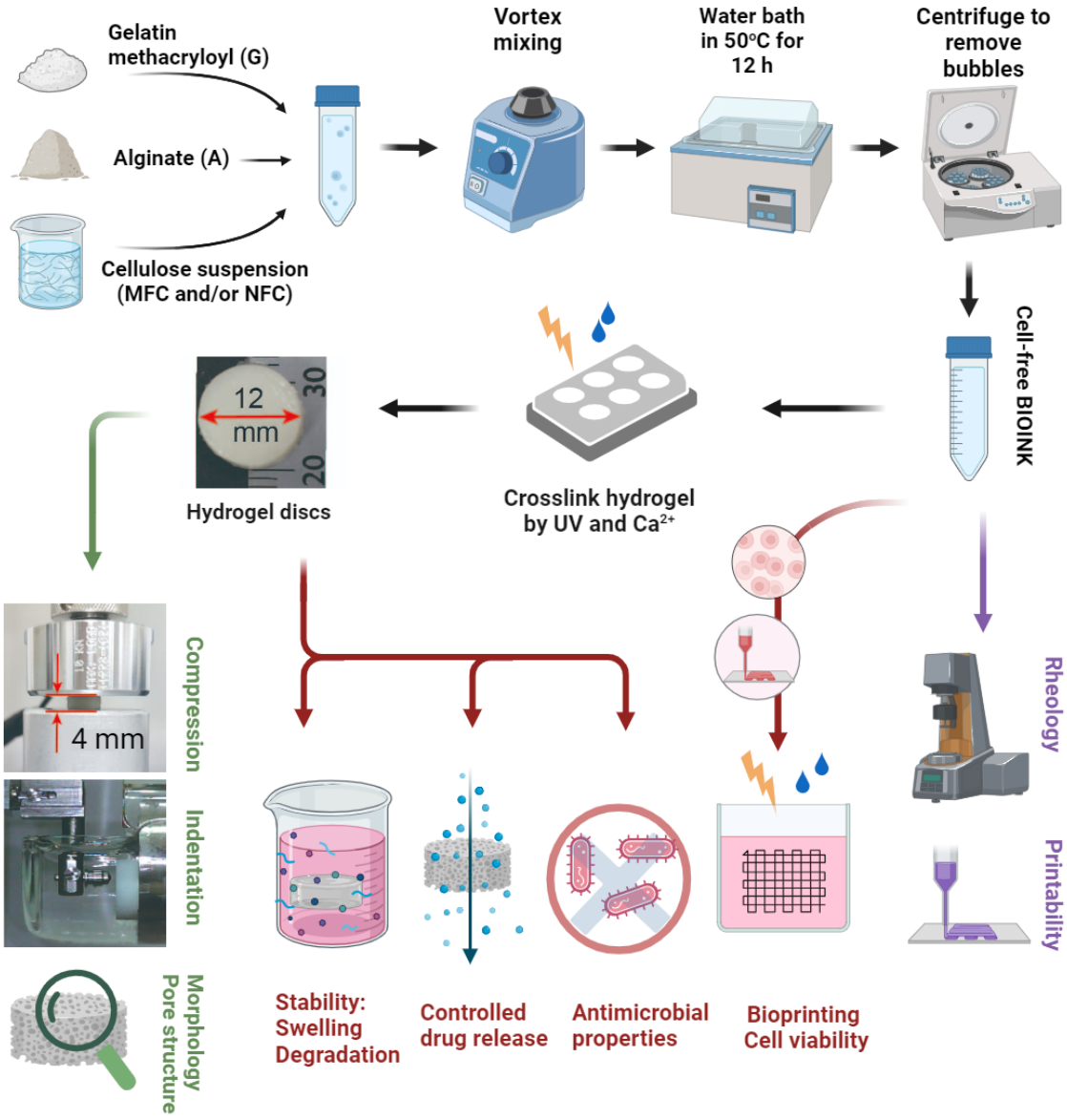

Figure 4.1: Illustrative blueprint for the preparation of cell-free bioink formulations and hydrogels (black part). Printability characterisations of the bioink formulations (purple part), mechanical properties characterisations (green part) and biological properties characterisations (red part) of the hydrogels are also illustrated and will be explained in Chapters 5, 6, and 7, respectively. (The illustration was created by BioRender.)

This chapter will demonstrate the preparation (Figure 4.1) and general characterisations of cell-free bioink formulations and hydrogels containing polymers gelatin methacryloyl, sodium alginate,

and cellulose.

4.2 Materials and Methods

4.2.1 Materials

Gelatin from porcine skin (gel strength 300, type A, powder), methacrylic anhydride (MA) (94%, liquid), sodium alginate (A) (powder), 2-Hydroxy-4′-(2-hydroxyethyl)-2- methylpropiophenone (or Irgacure 2959) (powder), and deuterium oxide (D_2O) (99.9 atom% D) were purchased from Sigma-Aldrich (UK). Microfibrillated cellulose (MFC) slurry (0.7 wt%, purify of 99.9% cellulose) was obtained from FiberLean Technologies Ltd (UK). Nanofibrillated cellulose (NFC) slurry (3 wt%, purify of 85% cellulose, 12% hemicellulose, and 3% lignin) prepared by high-pressure homogeniser was procured from Cellulose Lab (Canada). Calcium chloride ($CaCl_2$), sodium hydroxide (NaOH), phosphate buffered saline (PBS) tablets and dialysis tubing with molecular weight cutoff of 14 kDa were purchased from Fisher Scientific (UK). Calcium chloride was prepared as a 2% solution for use. Sodium hydroxide was prepared as a 1 M solution.

4.2.2 Synthesis of methacrylated gelatin

Gelatin methacryloyl (G) was first synthesised according to a previously reported method [241]. To synthesize sample G, gelatin from porcine skin was dissolved in PBS at 10 w/v% and heated to 60°C. The solution pH was adjusted to 9.5 using 1 M NaOH. Subsequently, MA was added dropwise into the solution while stirring continuously. The reaction lasts 6 hours at 60°C before adding excessive amount of PBS to terminate. The resulting solution was dialyzed against distilled water for a week at 45°C using a 14 kDa molecular weight cutoff. During this period, the distilled water was refreshed 2 to 3 times daily to remove unreacted MA and other by-products. The final product was subsequently frozen at -80°C overnight and lyophilized using a freeze dryer (Mini

Lablyo, Frozen in Time Ltd., UK) to obtain white foam-like G that was subsequently placed in -80°C freezer for long-term storage.

4.2.3 Preparation of MFC and NFC slurries

Either 0.7 wt% MFC in PBS or 3 wt% NFC in PBS was homogenized respectively at a speed of 8000 rpm by Silverson L5 Series Mixer for 30 min. Microfibrillated cellulose suspension was diluted to 0.4 and 0.55 wt%, separately. Nanofibrillated cellulose with 3 wt% was diluted to 1 wt% for use. Blended slurries with various MFC and NFC contents were also prepared by mixing 0.7 wt% MFC and 1 wt% NFC in different volume ratios, namely 25:75, 50:50, and 75:25. These three blended slurries were homogenized at a speed of 8000 rpm for 15 min before use.

4.2.4 Preparation of cell-free bioink formulations

To prepare cell-free MFC-composited G/A bioink formulation, 7.5 w/v% G, 2 w/v% A, 0.35 w/v% Irgacure 2959, and 0.7 wt% MFC slurry in PBS were added to a 50 mL centrifuge tube. The resulting product was repeatedly homogenised with a vortex mixer at room temperature (19°C) and heated in a 50°C water bath for 12 to 24 hours until G and A were completely dissolved in slurry. Next, the product was centrifuged (Eppendorf Centrifuge 5810) at 500 rpm for 1 min to remove any air bubbles in the mixture. The resulting product was named G/A/MFC-0.7. In order to investigate the effects of MFC incorporation and MFC content variation on the MFC-composited G/A bioink formulation, a set of formulations was prepared, of which the detailed composition is summarised in Table 4.1.

The preparation of NFC-composited G/A bioink formulation follows the same procedure described above. All the formulation details and labels for this group are listed in Table 4.1.

A series of hybrid cellulose-composited G/A bioink formulations were also prepared to study the difference in the effect of mixed cellulose slurries versus single slurries (0.7% MFC or 1% NFC)

on the properties of bioink formulations. Both the benchmark and hybrid cellulose-composited G/A bioinks are presented in Table 4.1 as well.

Table 4.1: Composition of all cell-free bioink formulations.

MFC-composited G/A bioink formulations				
Lable	**G (w/v%)**	**A (w/v%)**	**Igacure 2959 (w/v%)**	**MFC (wt%) in PBS**
G	7.5		0.35	
A		2		
G/MFC	7.5		0.35	0.7
A/MFC		2		0.7
G/A	7.5	2	0.35	
G/A/MFC-0.4	7.5	2	0.35	0.4
G/A/MFC-0.55	7.5	2	0.35	0.55
G/A/MFC-0.7	7.5	2	0.35	0.7
NFC-composited G/A bioink formulations				
Lable	**G (w/v%)**	**A (w/v%)**	**Igacure 2959 (w/v%)**	**NFC (wt%) in PBS**
G	7.5		0.35	
A		2		
G/NFC	7.5		0.35	1
A/NFC		2		1
G/A	7.5	2	0.35	
G/A/NFC-1	7.5	2	0.35	1
Hybrid cellulose-composited G/A bioink formulations				
Lable	**G (w/v%)**	**A (w/v%)**	**Igacure 2959 (w/v%)**	**Blended slurry with varying volume ratios of MFC and NFC**
G/A	7.5	2	0.35	
G/A/NFC100[1]	7.5	2	0.35	1% NFC only
G/A/MFC25/NFC75	7.5	2	0.35	25:75
G/A/MFC50/NFC50	7.5	2	0.35	50:50
G/A/MFC75/NFC25	7.5	2	0.35	75:25
G/A/MFC100[2]	7.5	2	0.35	0.7% MFC only

[1] G/A/NFC100 same as G/A/NFC-1, but with different labels within different groups.
[2] G/A/MFC100 same as G/A/MFC-0.7, but with different labels within different groups.

4.2.5 Crosslinking of bioink formulations

To prepare the MFC-composited ionic-covalent entanglement (ICE) G/A hydrogel, a four-step crosslinking process was carried out. The MFC-composited G/A bioink was transferred into a homemade silicone elastomer mold and sealed with a coverslip. The mixture was subsequently exposed to UV light (OmniCure S2000 Spot UV Curing System, wavelength of 365 nm, iris setting of 70%, working distance of 2 cm) for 3 mins, during which ingredient G formed the first covalently crosslinked network in the presence of the photoinitiator Irgacure 2959 [416]. Next, the sample was removed from the mold and immediately immersed in a 2% $CaCl_2$ solution for 6 hours, during which ingredient A interacted with calcium ions to form the second ionically crosslinked network. It is important to note that the first covalently crosslinked network provided the hydrogel with a certain level of strength, thus the formation time for the second ionically crosslinked network was extended to allow for a complete reaction between the calcium ions and A. Finally, the MFC-composited ICE G/A hydrogel was immersed in distilled water or PBS for 12 hours to remove any unreacted photoinitiator and achieve swelling equilibrium. Figure 4.2 shows the resulting hydrogel discs that were 4 mm thick and approximately 12 mm in diameter.

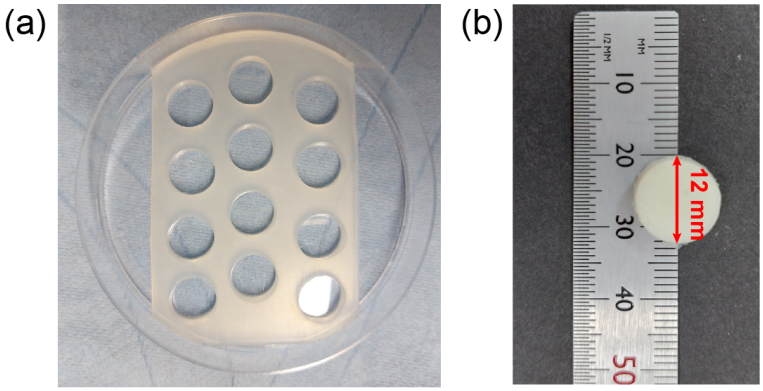

Figure 4.2: (a) Experimental elastomer mold and (b) the resulting hydrated hydrogel disc.

The MFC-composited G/A bioink formulations were used for extrusion printing to fabricate a variety of custom-shaped scaffolds, during which the UV irradiation time and calcium ion crosslinking time were adjusted appropriately depending on the size of the printed scaffolds. Lastly, the synthesis

of NFC-composited ICE G/A hydrogels and hybrid cellulose-composited ICE G/A hydrogels was always consistent with the method described above.

4.2.6 ATR-FTIR

ATR-FTIR spectroscopy (Thermo Nicolet 380 FTIR with Smart Accessory Sampling Modules) was deployed to monitor the methacrylation reaction of gelatin. Either gelatin or sample G was individually positioned onto the ATR crystal and then subjected to a controlled level of pressure using the slip-clutch mechanism of the clamp, which ensures optimal contact between the sample and the crystal. The spectral resolution is set to 4 cm^{-1}, whilst the wavenumber ranged from 4000 cm^{-1} to 400 cm^{-1}.

Additionally, to verify the light-initiated covalent crosslinking reaction in MFC-composited and NFC-composited G/A hydrogel, FTIR spectra of G/A hydrogel, G/A/MFC-0.7 hydrogel, and G/A/NFC-1 hydrogel were collected. To eliminate the effect of the absorption peak for water molecules, all hydrogel samples were freeze-dried before testing. As a comparison, bioink formulations of G/A, G/A/MFC-0.7, and G/A/NFC-1 were also lyophilised and subjected to ATR-FTIR testing. Furthermore, FTIR spectra of MFC and NFC were also collected and compared to G/A, G/A/MFC-0.7, and G/A/NFC-1 bioink or hydrogels to verify the successful incorporation of MFC or NFC into bioink formulations or hydrogels.

4.2.7 NMR

Proton nuclear magnetic resonance (^{1}H-NMR) spectra of gelatin and gelatin methacryloyl (G) were acquired by a Bruker 400 MHz NMR spectrometer equipped with a 5 mm BBFO "smart" probe and a 9.39 T Ultrashield magnet to analyse the degree of modification (*DoM*) of G. Dried gelatin and G were loaded into Norell Standard Series 5 mm precision NMR sampling tubes and fully dissolved in D_2O. Spectra were analyzed in Bruker TopSpin 4.1.1 software.

4.2.8 AFM

AFM (Dimension 3100, Veeco, Cambridge, UK) was deployed to capture the morphologies of dried MFC and NFC in tapping mode under the ambient condition. Gold-coated rectangular cantilevers of 110 µm, with a nominal resonant frequency of 90 kHz and a spring constant of 1 N/m (HQ: NSC36/Cr-Au, MikroMasch, APEX Probes Ltd) were used. The scan rate was set at 0.75 Hz. Image post-processing was carried out in Gwyddion software.

Dried MFC or NFC samples were prepared by placing a droplet (80 µL) of homogenised MFC or NFC dilution on mica and then drying naturally. Mica was chosen here as the supporting substrate for the specimen due to its minimal roughness.

To determine width distributions of MFC and NFC, diameters of MFC and NFC were measured using ImageJ. Two hundreds measurements were performed in each AFM image.

4.2.9 Fluorescence microscopy

The dispersion of the homogenised MFC and NFC slurries were analysed by Leica Z16 APO A fluorescence microscopy with Leica DFC3000 G CCD camera. MFC of 0.7 wt% and NFC of 1 wt% were diluted with deionised water (v/v = 1:10), followed by sonication for 15 min and homogenisation for 10 min before use. Round glass coverslips (Fisher Scientific, UK) with a 10 mm diameter were cleaned by an oxygen plasma chamber (HPT-100, Henniker Plasma) at an oxygen flow rate of 10 sccm[3] and a power of 100% for 5 min before use. MFC and NFC slurries of 80 µL were deposited onto a clean pre-treated glass coverslip by spin coating (SPIN150i, APT GmbH) at 6000 rpm for 60 s. Finally, samples were imaged by fluorescent microscope and Leica Application Suite X software was used for image analysis.

[3]Standard cubic centimeters per minute (sccm)

4.3 Results and discussion

4.3.1 Synthesis of methacrylated gelatin

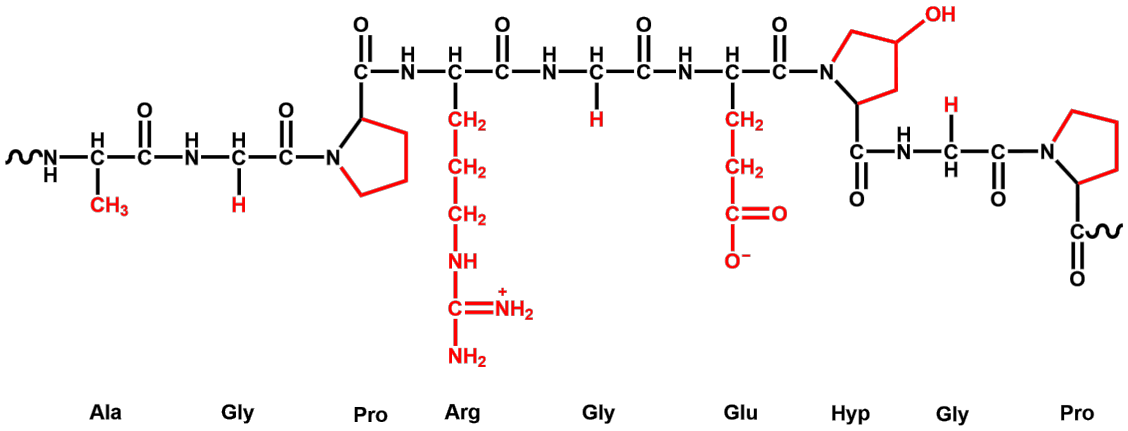

Figure 4.3: Representative chemical structure of gelatin.

Gelatin is a heterogeneous mixture of polypeptides obtained by cleaving specific peptide bonds of collagen, resulting in partial hydrolysis. The chemical structure of gelatin contains a large number of amino acid residues, such as glycine, proline, and hydroxyproline residues (Figure 4.3) [417], with arginine residues accounting for 8% [418]. In this study, the functionalization of gelatin was achieved through the reaction of arginine residues with methacrylic anhydride, with proposed mechanism shown in Figure 4.4.

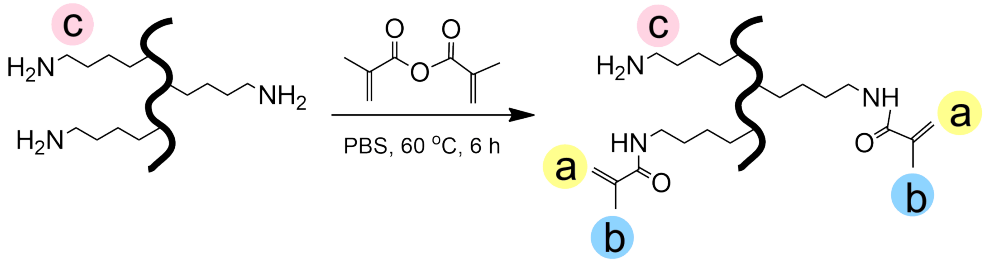

Figure 4.4: Methacrylation reaction of gelatin with methacrylic anhydride.

The presence of olefin functional groups in sample G is of significant importance for synthesising

covalently crosslinked hydrogels. To ascertain the successful occurrence of the methacrylation reaction of gelatin, FTIR were employed for the characterization of the resultant chemical structure, followed by NMR to determine the *DoM* of G. By comparing the FTIR spectra of gelatin and G in Figure 4.5, the peak at 3285 cm^{-1} that represents the stretching vibration of the nitrogen-hydrogen bond (N-H) in the amino group is significantly less intense in the spectrum of G. In addition, the new peak at 3073 cm^{-1} in the spectrum of G that corresponds to the stretching vibration of the unsaturated hydrocarbon bond (=C-H) in the alkene, evidences a successful methacrylation reaction.

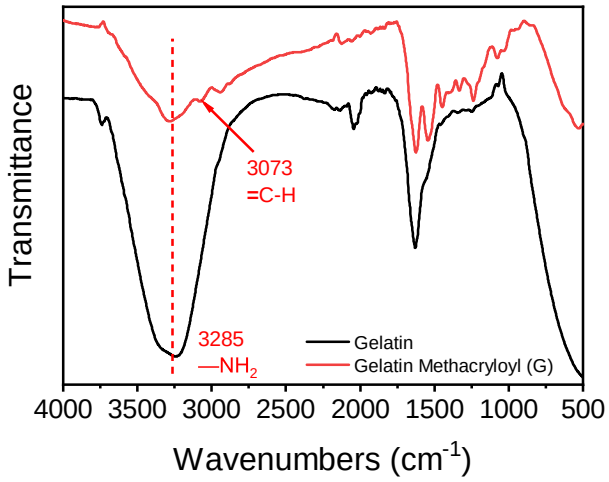

Figure 4.5: Representative FTIR spectra of sample gelatin and gelatin methacryloyl (G). The peak at 3285 cm^{-1} that represents the stretching vibration of N-H bond in the amino group is significantly less intense in the spectrum of sample gelatin methacryloyl (G). A new peak at 3073 cm^{-1} in sample G spectrum corresponds to the stretching vibration of =C-H bond in the alkene appears.

The representative ^{1}H-NMR spectrum of sample G in Figure 4.6 exhibits new peaks at 5.6 and 5.4 ppm, which corresponds to the presence of two protons from the methacrylate double bonds (located at yellow position *a* in the chemical structure in Figure 4.4 and 4.6). Additionally, a noticeable increase in the signal intensity of methyl protons at approximately 1.8 ppm (blue position *b* in Figure 4.4 and 4.6) is observed. Conversely, the signal of the methylene proton at 2.9 ppm (pink position *c* in Figure 4.4 and 4.6) displays a significant reduction in intensity. The above results also confirm the successful synthesis of sample G. As the aromatic amino acid moieties (phenylalanine) in gelatin do not participate in the reaction, their signal intensity at 7.4 to 7.1 ppm was used to

normalise the intensity of other protons in sample gelatin and methacrylated gelatin (G) [419, 420]. Therefore, by evaluating the peak area at position *c*, the degree of modification (*DoM*) of gelatin in this study is determined as 54.8% using the following equation:

$$DoM(\%) = \frac{\text{Area (Methylene of gelatin) - Area (Methylene of methacrylated gelatin)}}{\text{Area (Methylene of gelatin)}} \cdot 100 \quad (4.1)$$

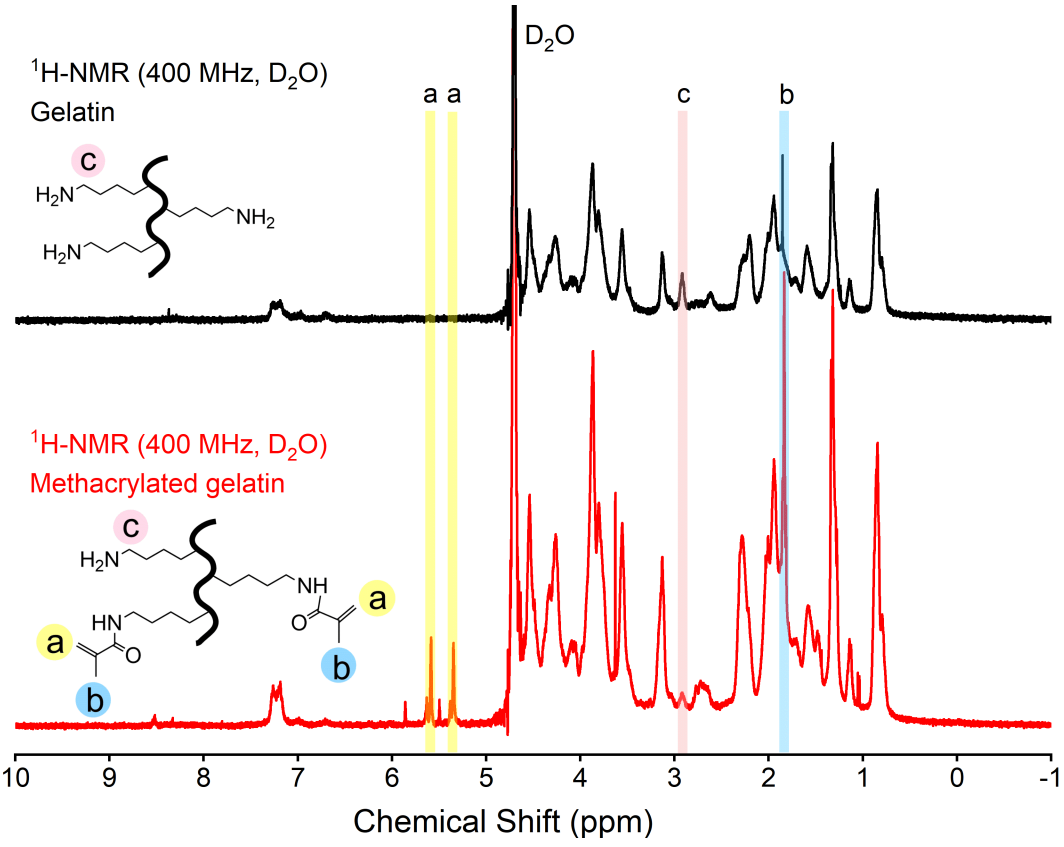

Figure 4.6: Representative ^1H-NMR spectra of sample gelatin (black line) and methacrylated gelatin (G, red line). Two new signals in yellow position *a* correspond to two protons from the methacrylate double bonds. Signal intensity of methyl protons (blue position *b*) increases. Signal intensity of the methylene proton (pink position *c*) drops.

4.3.2 Morphology of MFC and NFC

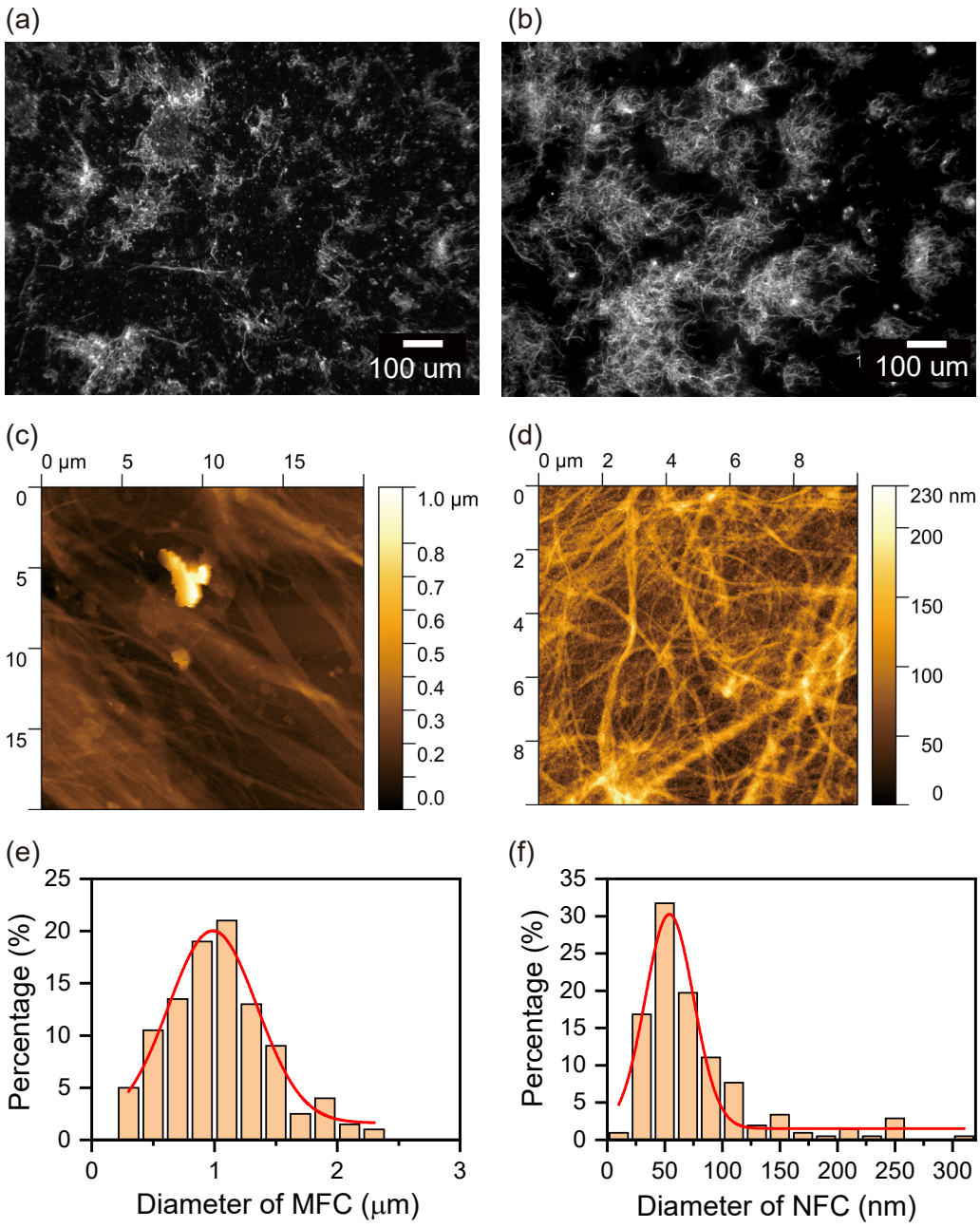

Figure 4.7: Microscopic morphology of (a, c) MFC and (b, d) NFC observed by (a, b) fluorescence microscope and (c, d) AFM. Fibre diameter distribution of (e) MFC and (f) NFC by analysing corresponding AFM images of samples.

The presence of intra- and intermolecular hydrogen bonds within the cellulose fibre structure

plays a pivotal role in preserving the structural stability of cellulose [421]. In industrial settings, various mechanical techniques such as high-pressure homogenization, microfluidization, and micro-grinding are employed to disrupt the hierarchical arrangement of raw fibres [422] and engineer them at the micro and nanoscale to obtain MFC and NFC mesh networks with excellent aspect ratios and large specific surface areas. In this work, MFC and NFC were homogenised before use. Based on the information provided in Figure 4.7, it is evident that MFC exhibits widths ranging from 0.3 to 2 µm, while NFC demonstrates a width distribution spanning from 30 to 100 nm. Fibrillated cellulose with high aspect ratios interconnects and entangles with each other, forming a densely packed network structure. The morphology of MFC and NFC in this project is consistent with previous reports [167, 423].

4.3.3 Synthesis of crosslinked hydrogels

Figure 4.8 illustrates the possible crosslinking mechanism of cellulose-composited ICE G/A hydrogels [264, 424, 425], during which the alkene functional group present in sample G undergoes crosslinking through the action of a photo-initiator upon exposure to UV irradiation, leading to the formation of a covalently crosslinked network (orange component shown in Figure 4.8). Sodium alginate is a chain-like polysaccharide composed of repeating units of guluronic acid (G block) and mannuronic acid (M block) residues [426] - it engages in a rapid ion exchange reaction when it encounters calcium ions (Figure 2.5) [427]. The guluronic acid residues within its structure coordinate with the calcium ions, causing the pattern of an "Egg-box" model [428] or an ionic crosslinked network (black component in Figure 4.8). During the formation process, the two networks entangle with each other, along with the inherent web-like structure of MFC or NFC (green component in Figure 4.8), resulting in the formation of MFC-composited or NFC-composited ICE G/A hydrogels.

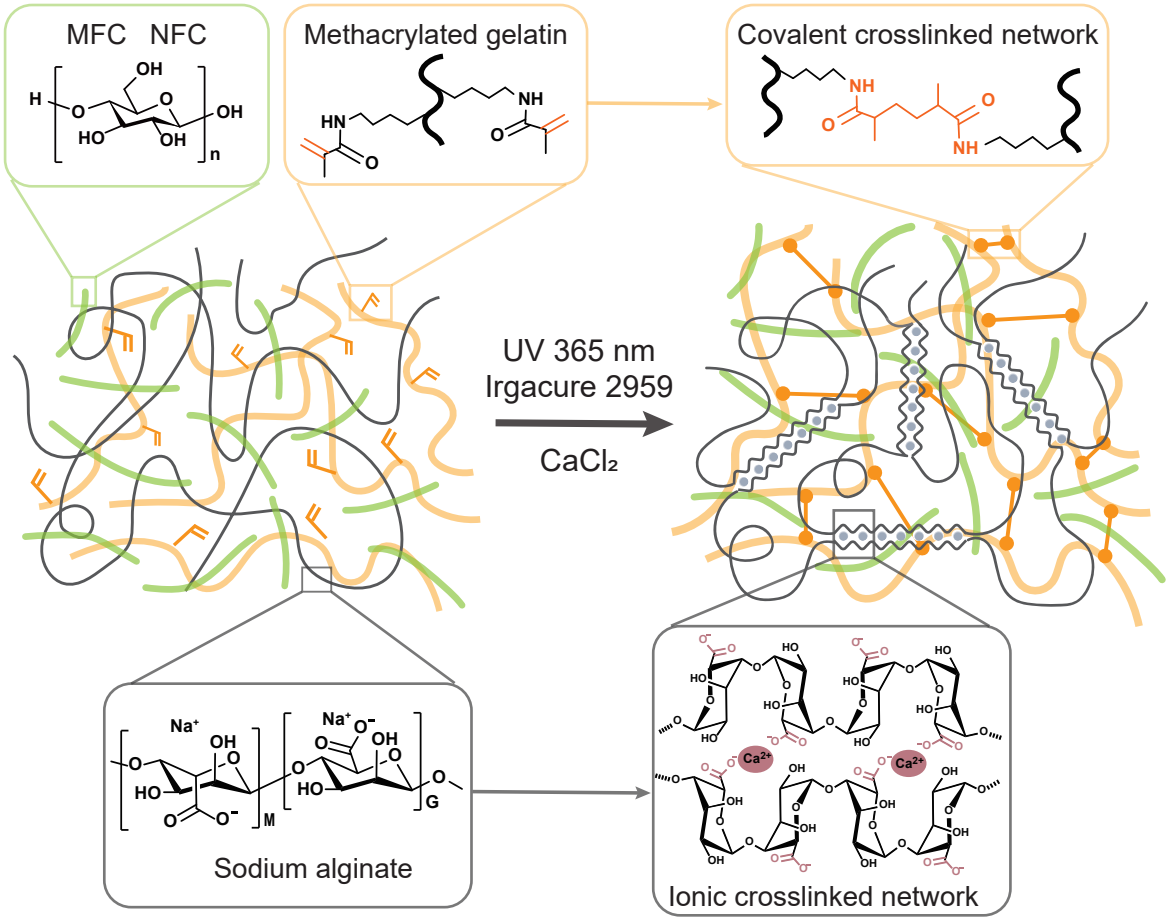

Figure 4.8: Schematic representation of the synthesis and structure of MFC-composited or NFC-composited ionic-covalent entanglement network hydrogel. Every single green line represents MFC or NFC fibre networks.

To verify the photo-crosslinking reaction that underpins the formation of the cellulose composited hydrogel, FTIR was employed to reveal the differences in chemical structure between various bioink formulations before and after crosslinking. As shown in Figure 4.9a, G/A bioink and G/A/MFC-0.7 bioink formulations display stretching vibration peaks of unsaturated carbon-hydrogen bonds (=C-H) within the alkenyl functional groups around 3073 cm^{-1}. However, after crosslinking, the peak intensity around 3073 cm^{-1} significantly decreases for both G/A hydrogel and G/A/MFC-0.7 hydrogel. Similarly, for both G/A and G/A/MFC-0.7 formulations, the stretching

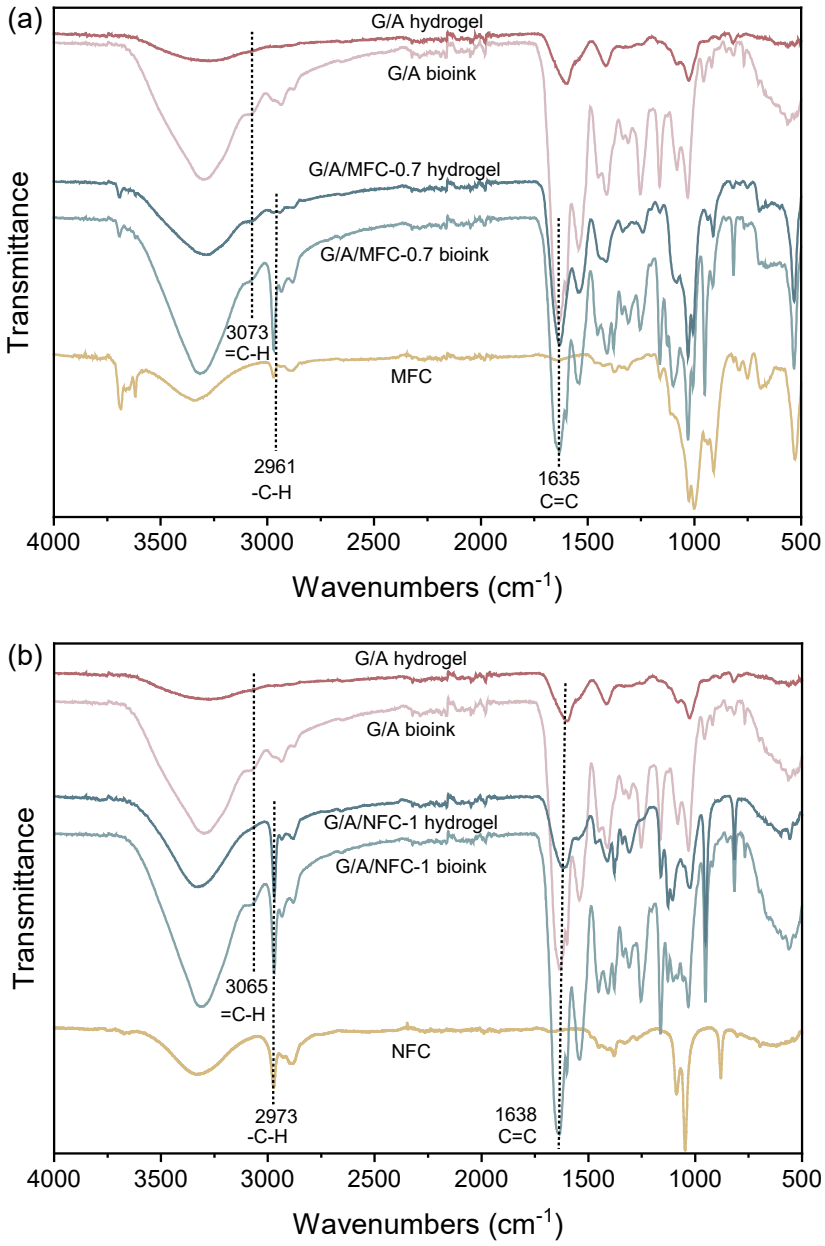

Figure 4.9: Representative FTIR spectra of (a) MFC-composited ICE bioink and crosslinked hydrogel and (b) NFC-composited ICE bioink and crosslinked hydrogel. Peak intensities at around 3073 cm^{-1} (stretching vibration of =C-H bond) and at about 1635 cm^{-1} (stretching vibration of C=C bond) all decrease after G/A, G/A/MFC-0.7, and G/A/NFC-1 bioink formulations are covalently crosslinked into corresponding hydrogels, respectively. Peaks at about 2961 cm^{-1}(stretching vibration of -C-H bond) and at around 3323 cm^{-1} (stretching vibration of hydrogen bonding) become strong, confirming the successful incorporation of MFC or NFC into G/A bioink formulation.

vibration peak at 1635 cm^{-1}, representing the unsaturated carbon bond (C=C), weakens significantly after the transformation of the bioink into hydrogel [429, 430]. All of the above supports the conclusion that a covalently crosslinked network was formed in the hydrogel.

In addition, FTIR spectrum of MFC exhibits a peak at 2961 cm^{-1}, representing the stretching vibration of saturated carbon-hydrogen bonds (-C-H). In the case of G/A/MFC-0.7 bioink and the resulting G/A/MFC-0.7 hydrogel, the peak at this region becomes sharper, indicating the successful incorporation of MFC into the formulation. Moreover, the peak representing the stretching vibration of hydrogen bonding at around 3323 cm^{-1} becomes strong after MFC is combined with G/A bioink and hydrogel, suggesting an interaction between G/A and MFC [431]. FTIR spectra of NFC-composite ICE network hydrogel in Figure 4.9b shows similar results due to the consistent structure of NFC and MFC. Therefore, NFC was also successfully incorporated into G/A bioink formulation and covalent crosslinking networks were also formed in G/A/NFC hydrogel.

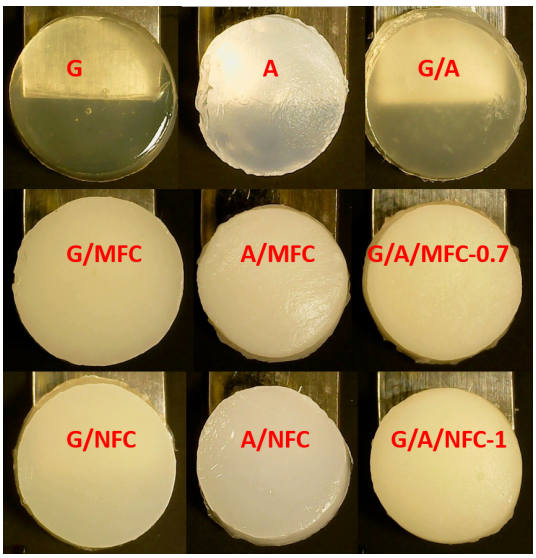

Figure 4.10: Images of crosslinked hydrogel discs captured by a regular camera. Samples G, A, and G/A hydrogels transfer from transparent to opaque after the addition of MFC or NFC to them. Macroscopic images of the samples further support the results of FTIR.

Images of the hydrogel discs prepared through homemade mould were acquired using an ordinary camera (Figure 4.10). It was found that the hydrogel discs, without incorporation of cellulose fibrils,

in the first row (G, A, G/A) are transparent. When white MFC or NFC aqueous slurry is incorporated into the formulation, whether the cellulose-composited single network (G/MFC, A/MFC, G/NFC, and A/NFC) or cellulose-composited ICE double network (G/A/MFC-0.7 and G/A/NFC-1), the final hydrogels become opaque. The above results provide additional corroborative evidence for the findings obtained through FTIR analysis.

4.4 Conclusions

This chapter explains the preparation process of MFC-composited and NFC-composited G/A bioink formulations, including the preparation of sample gelatin methacryloyl (G), homogenisation of MFC and NFC slurries, and crosslinking of bioink formulations.

The differences in FTIR spectra between sample gelatin and G provide evidence for the successful synthesis of sample G. This is corroborated by the diminished peak intensity at 3285 cm^{-1} representing the stretching vibration of the nitrogen-hydrogen bond (N-H) in the FTIR spectrum of sample gelatin and the emergence of a new peak at 3073 cm^{-1}, corresponding to the stretching vibration of unsaturated hydrocarbon bond (=C-H) in the FTIR spectrum of sample G. Furthermore, NMR results of sample gelatin and G were used to confirm the degree of modification (*DoM*) (54.8%) of G by analyzing the peak area associated with the methylene proton at 2.9 ppm.

Results of AFM illustrate the sizes of individual cellulose fibrils in MFC (width of 0.3 - 2 μm) and NFC (width of 30 - 100 nm). Fluorescence microscopy results show that fibrillated cellulose with high aspect ratios interconnects with each other and forms a densely packed network, which is consistent with previous reports [432].

The crosslinking mechanism of MFC-composited and NFC-composited ICE G/A hydrogels was proposed. The covalently crosslinked gelatin methacryloyl (G) network interpenetrates with the ionically crosslinked sodium alginate (A) network to form an ionic-covalent entanglement dual network. MFC or NFC network interacts with ICE network through hydrogen bonding

[431]. FTIR results support the crosslinking mechanism, of which FTIR spectra of G/A/MFC-0.7 and G/A/NFC-1 hydrogels prove the formation of a covalently crosslinked network by the decreased stretching vibration peaks of unsaturated carbon-hydrogen bond (=C-H) near 3073 cm^{-1} and unsaturated carbon bond (C=C) at about 1635 cm^{-1}. Moreover, the incorporation of MFC or NFC strengthens the stretching vibration peak of hydrogen bonds at around 3323 cm^{-1} in the FTIR spectra of G/A/MFC-0.7 and G/A/NFC-1. Finally, compared to transparent G/A hydrogel, macroscope images of opaque G/A/MFC-0.7 and G/A/NFC-1 hydrogels also back the fact of the successful addition of MFC or NFC to G/A hydrogel.

Chapter 5

EFFECTS OF CELLULOSE ON THE PRINTABILITIES OF G/A BIOINK FORMULATIONS

5.1 Introduction

The flow behaviour of bioinks is crucial for studying their printability. For nozzle-based extrusion printing, the viscosity of ideal hydrogel-based bioinks should range from 0.03 to 6×10^4 Pa.s [212, 433]. An ideal bioink maintains system stability before extrusion (first stage), undergoes shear thinning so as to smooth pass through the nozzle ranging 100 to 1500 µm inner diameter [212] at a printing speed of 1 to 40 mm/s [64] during extrusion (second stage), and quickly recover after extrusion to maintain the shape fidelity of the printed structure (third stage). Rheology, as a discipline that studies the flow, deformation, and recovery of fluids, plays a vital role in understanding and optimising the flow behaviour of bioink formulations in these three stages.

This chapter focuses on investigating the printabilities of cell-free bioinks and evaluating the effects of microfibrillated cellulose (MFC) and nanofibrillated cellulose (NFC) on the printability of

MFC-composited and NFC-composited gelatin methacryloyl (G)/sodium alginate (A) bioink formulations, using rheological properties as key characterisation parameters. The rheological findings obtained will serve as a guide for optimizing the extrusion printing process of bioink formulations. Subsequently, the bioinks will be loaded into a three-dimensional (3D) printer to explore their processability in three dimensions (one-dimensional (1D) filaments, two-dimensional (2D) scaffolds, and 3D constructs), thereby comprehensively investigating their potential for bioprinting applications.

5.2 Methods

5.2.1 Characterisation of rheological properties of bioinks

Measurements of the rheological properties of MFC-composited and NFC-composited G/A bioink formulations were carried out by using rheometers (Discovery HR-1 and Discovery HR-2, TA Instrument, UK). Different rheological properties of bioink are required at each printing stage, from the sample being loaded into the cartridge to being printed and then crosslinked. Therefore, different testing procedures were established.

To determine the yield stress that initiates flow in the formulation of bioink before printing, amplitude sweep in oscillation mode was conducted in the range of 0.1 to 1000 Pa at a frequency of 1 Hz [239]. The intersection of storage modulus (*G'*) and loss modulus (*G"*) represents the yield point, with the corresponding stress at this point being the yield stress. Before this point, *G'* is greater than *G"* and the material behaves as a gel, while after this point *G'* is less than *G"* and viscous flow dominates.

Furthermore, the shear thinning behaviour of bioink formulations determines that bioink formulations can be smoothly extruded out of the nozzle. Thus, shear rate sweep tests were conducted in rotation mode within the range of 0.01 to 100 s^{-1} to evaluate the relationship between viscosity of the sample and shear rate. The data was collected via the software Trios and analysed by fitting

with built-in power law flow model, with the model described in Table 3.1.

The rapid recoverability of the sample after extrusion was assessed by peak hold program in rotation mode and high-low strain cycle program in oscillation mode, respectively. In the peak hold program, the shear rate was initially set to 1 s^{-1} for 60 s, then ramped up to 300 s^{-1} for 5 s to simulate the moment when the bioink flows through the narrow nozzle, and finally decreased to 0.2 s^{-1} for 235 s to record the recoverable behaviour of bioink viscosity after extrusion. Additionally, the high-low strain cycle program tracked the recoverability of *G'* and *G"* under four cycles of high strain (100%) for 150 s and low strain (1%) for 150 s at a frequency of 1 Hz. Each transition between high and low strain was allowed to wait for 5 s to stabilise the sample. All tests above utilised a Peltier cone-plate measurement geometry (serial number of 109466, diameter of 40 mm, cone angle of 4°, truncation gap of 112 μm). After the geometry was installed each time, geometry calibrations, including inertia, bearing friction, and rotational mapping, were carried out in turn. The testing temperature was set at 25°C. Before each test, the sample was equilibrated on the geometry plate for 3 min to ensure a uniform temperature. Every type of measurements was repeated in triplicate.

The gelation kinetics of bioink formulations under the influence of $CaCl_2$ and UV radiation were studied separately via a time sweep procedure in oscillation mode at 25°C. Storage modulus was recorded at 1 Hz frequency and 0.1% strain to investigate the gelling kinetics of the ionically crosslinked network in the hydrogel. $CaCl_2$ of 2% was added to the sample surrounding the cone-plate geometry after 5 min of testing. Gelation kinetics of the covalently crosslinked network in the hydrogel was measured at 25 Hz frequency and 2% strain by parallel plate measurement geometry with transparent quartz bottom plate (serial number of 105147, diameter of 20 mm, truncation gap of 1000 μm). UV light guide accessory (365 nm of wavelength, Omnicure S2000) was installed on the Discovery HR-2 rheometer, and the light intensity was set to 100% iris.

5.2.2 Characterisation of printabilities for bioinks by extrusion printing

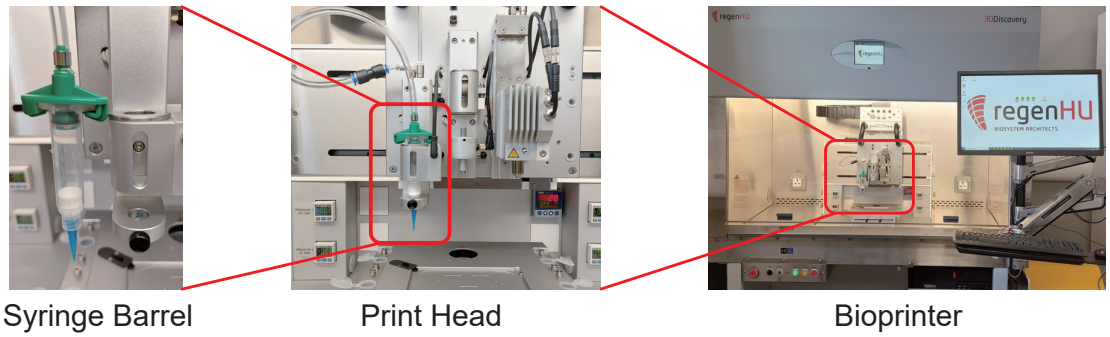

Figure 5.1: RegenHU bioprinter and extrusion print head used in this project.

Three-dimensional printing of cell-free bioink formulations was performed by RegenHU bioprinter (3D Discovery, Switzerland) with a direct dispension printhead (DD-135N). Bioink formulations were loaded into 5 mL syringe barrels (Nordson EFD, Bedfordshire, UK), as shown in Figure 5.1. Compressed air (0.6 bar) was used to extrude the specimen through a conical syringe nozzle with inner diameter of 410 µm (22 gauge) or 200 µm (27 gauge). BioCAD software was used to build and slice 3D models, passing G code to the printer control software 3D Discovery HMI.

For 1D printing, bioink formulations were dispensed according to the model in Figure 5.2a. The pressure valve opening and the subsequent build-up of pressure may cause a temporal gap between initiating the g-code and the effective extrusion of material in the pneumatic system [434]. Therefore, the time of start delay was set to 200 ms before printing. Dispensing pressure was adjusted in the range of 20 to 60 kPa. Printing speed was chosen from 2 to 74 mm/s. The filament exhibits a theoretical width of 0.47 mm and a theoretical height of 0.33 mm when utilising a 22-gauged nozzle, while the dimensions shift to 0.23 mm in width and 0.16 mm in height with the use of a 27-gauged nozzle. Images of filament printed at different printing pressures, print speeds, and nozzle sizes were captured using a USB digital microscope and analysed by Image J. At least ten different positions on the filament were selected to calculate the average width of the filament. The optimum printing conditions for bioink formulation G/A/MFC-0.7 to form a filament with the

highest print resolution and the lowest theoretical shear stress were determined based on parameter optimisation index (*POI*).

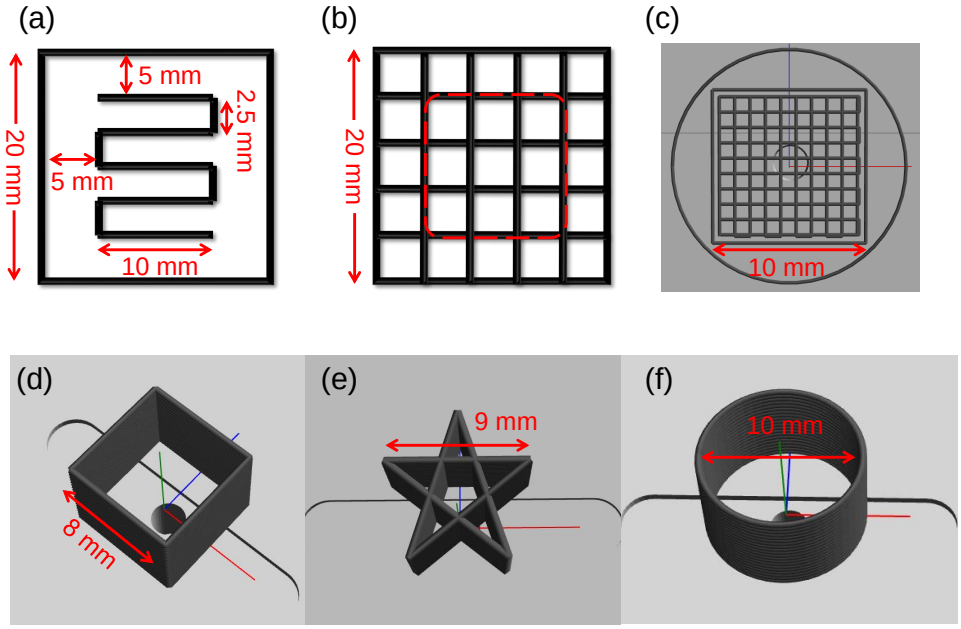

Figure 5.2: Models for different dimensional printing. (a) Model for 1D printing. The width of the printed filament in the central area of the square was measured for the calculation of parameter optimisation index (*POI*). A square with a side length of 20 mm was pre-printed. (b) Model for 2D printing. To obtain printability index (*Pr*), the area and perimeter of the nine squares within the red dashed box were the focus of this study. Based on the model (c), bioink was printed into 3D scaffolds with a 10 mm side containing 2, 4, 8, and 16 layers. Printing fidelity was explained by examining the relationship between the number of layers and thickness of the scaffold. Three 20-layer models with different shapes (square (d), pentagram (e), and circle (f)) for 3D stability studies.

The formulated bioink was subsequently printed to fabricate a 2D lattice with 5×5 grids to investigate and compare the 2D printability of the bioink using printability index (*Pr*). The lattice model had a side of 20 mm and line space of 4 mm, as shown in Figure 5.2b. The area and perimeter of every grid in the centre 3×3 grids (within the red dashed box in Figure 5.2b) were measured for calculation of *Pr*. As mentioned in Section 3.4, the *Pr* of 2D scaffold or roundness of the grid is affected by interlayer fusion. In the centre 3×3 grids region, the intersection between the two printed layers is the vertex of each grid. Therefore, in this region, the difference in grid

roundness caused by interlayer fusion comes only from the grid vertices. However, for the edge grid of the printed structure, in addition to the fusion at the grid vertices, more obviously, the outermost sides of the grid also overlap, which is caused by the rasterised printing method. Therefore, the difference in interlayer fusion between the edge grid and the internal grid prompted the author to select only the centre 3 × 3 grids for the calculation of the printability index. The printing process of formulations G/A, G/A/MFC-0.4, G/A/MFC-0.55, G/A/MFC-0.7, and G/A/NFC-1 was repeated three times using a 27-gauged nozzle at a printing speed of 2 mm/s and dispensing pressure of 30 kPa.

The shape fidelity of the 3D constructs was verified by establishing a relationship between the number of layers and thickness of the constructs. The print model is shown in Figure 5.2c. A single layer of a circle with a radius of 8 mm was first pre-printed. Then formulation G/A/MFC-0.7 was printed as a cube with a side length of 10 mm using a 27-gauged nozzle at a printing speed of 2 mm/s and dispensing pressure of 30 kPa. The filling offset was set to 0.45 mm and line space was 1 mm in every layer of the cube. Three-dimensional structures with 2, 4, 8, and 16 layers were constructed, followed by crosslinking at UV irradiation for 30, 60, 120, and 250 s respectively and then in $CaCl_2$ of 2% for 180 s. The thicknesses of cubes with different layers were measured triple by a digital calliper.

Finally, the print stability of formulation G/A/NFC-1 was evaluated by constructing 20-layer structures with 3 different shapes: a square with 8 mm side (Figure 5.2d), a pentagram with 9 mm (Figure 5.2e), and a circle structure with 10 mm diameter (Figure 5.2f). G/A/NFC-1 was dispensed by a 22-gauged nozzle at a printing speed of 22 mm/s and dispensing pressure of 25 kPa. These tubes were then UV-crosslinked for 3 min and immersed in 2% $CaCl_2$ for 3 min. These hollow structures were pressed with tweezers and the process of shape recovery of the tube was recorded.

It is worth noting that compared with the crosslinking process of hydrogel discs in silicone elastomer mold (Section 4.2.5), both the UV irradiation time and the calcium ion crosslinking time of the printed structures (Figure 5.2c,d,e,f) are significantly shortened. Also, photo-crosslinking

times are different for constructs with different layer numbers. Above can be explained by the fact that geometric differences in the constructs affect light penetration and calcium ion diffusion, thereby changing the crosslinking kinetics of the sample. Therefore, the crosslinking time of the construct in this part was further optimised. The time of sufficient photo-crosslinking for the construct was judged by whether it could be transferred from the printing platform to 12-wells cell culture plate for the next ionic crosslinking by tweezers. The construct that was not fully photo-crosslinked would partially stick to the printing platform and the tweezers could not pick up the complete scaffold. The fully photo-crosslinked scaffold was easily transferred because of its overall elasticity. Additionally, the time of ion crosslinking for the constructs was based on the previous report [435]. Thin alginate discs (1.5 µL) were surrounded by $CaCl_2$ and distance from the alginate disc edge to gel front position as a function of time were then tracked by *in situ* dark-field microscopy and confocal laser scanning microscopy to determine the crosslinking kinetics [435]. Meanwhile, a reaction-diffusion model of gelation that matched the experimental results well was developed to describe the diffusion of calcium ions within the hydrogel [435]. According to the report, 0.1 M $CaCl_2$ can fully diffuse into hydrogel discs with diameters of 0.5 and 0.85 mm in 20 and 180 seconds, respectively (corresponding to the gel front positions of 0.25 and 0.425 mm, separately) [435]. In the current work, G/A/MFC-0.7 and G/A/NFC-1 were printed as cylindrical filaments with diameters of 0.5 mm and 0.85 mm, respectively. Assuming that there is no interlayer fusion within the scaffold, 2% $CaCl_2$ (0.18 M) can fully crosslink the scaffold within 3 min.

5.2.3 Statistical analysis

The results from quantitative experiments were analysed in OriginPro 2022 and expressed as mean ± standard deviation ($n \geq 3$). Significant differences were determined using one-way analysis of variance (ANOVA) followed by Tukey's post hoc test for pairwise comparisons. Statistical significance was determined at the 0.05 level. The p-values labelled in all figures are $*p \leq 0.05$, $**p \leq 0.01$ and $***p \leq 0.001$, respectively.

5.3 Results and discussion

5.3.1 Fluidity of bioink formulations

Centrifuge tubes containing different bioink formulations were inverted for 1 hour at room temperature to observe the macroscopic fluidity, with all samples initially positioned at the bottom of the tube. Figure 5.3a displays the images of inverted MFC-composited G/A bioinks and their benchmarks. The yellow and red arrows represent the area where the sample is located. Samples MFC, G, and A all flow to the top of the tube after an hour of inversion. When MFC is added to pure G or A, samples G/MFC and A/MFC are also transferred to the top of the tube. Even formulation G/A flows to the top of the tube. It illustrates that these above samples are fluid like a sol. Only when MFC is mixed with G/A formulation, the resulting samples, including G/A/MFC-0.4, G/A/MFC-0.55, and G/A/MFC-0.7, remain in the bottom of the centrifuge tube, indicating that MFC-composited G/A bioinks lack of macroscale fluidity. The high viscosity of the MFC-composited G/A bioink formulation allows it to hold its shape like a gel, which confers significant advantages upon the bioink in preserving system stability prior to printing [436].

Figure 5.3b shows the macroscale flowing results of inverted NFC-composited G/A bioink formulations and their benchmarks. Consistent with the results of Figure 5.3a, only G/A/NFC-1 remains in the bottom of the tube like a gel. Specimens NFC, G/NFC, and A/NFC all move to the top area of the tube. In addition, Figure 5.3c shows that G/A/MFC25/NFC75, G/A/MFC50/NFC50, and G/A/MFC75/NFC25 all remain in the initial position without flow. Therefore, whether it is a single MFC or NFC, or a blend of MFC and NFC slurry, they are able to form a gel-like formulation when mixed with G/A [436]. The gel-like behaviour of bioink formulations is beneficial in maintaining the stability of the formulation before printing and the shape fidelity after printing [436].

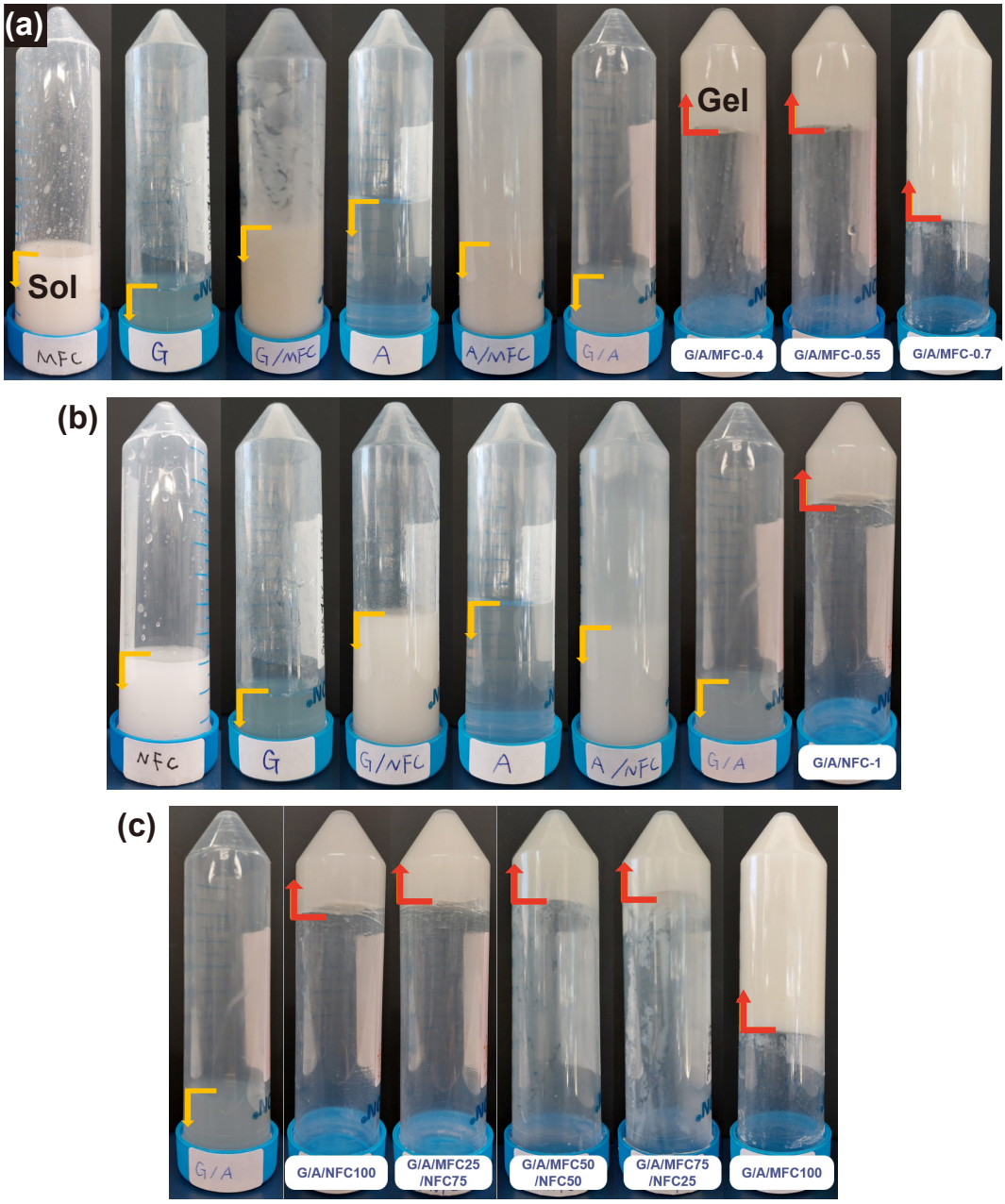

Figure 5.3: Images of cell-free (a) MFC-composited, (b) NFC-composited, and (c) hybrid cellulose-composited G/A bioink formulations and their corresponding benchmarks after inverting the tube for 1 hour. The yellow arrows show that bioink formulations can flow to the top zone of the tube, evidencing a sol state of formulations. However, the incorporations of MFC and/or NFC remain G/A formulations stable in the bottom of the tube (red arrows), akin to a non-flowing gel.

5.3.2 Rheological properties of bioink formulations

5.3.2.1 Yield before extrusion

The yield behaviour of MFC-composited G/A bioinks was investigated by comparing *G'* and *G"* upon an increasing oscillatory stress. Figure 5.4a presents tendencies of *G'* and *G"* for different MFC-composited G/A bioinks, while Figure 5.4b shows the yield stress of samples. In Figure 5.4a, as the oscillation stress increases, *G'* of sample G/A is always less than *G"*, indicating that G/A is a flowing sol without a yield point. This is consistent with the macro fluidity results for G/A shown in Figure 5.3. The sol-like flow state of G/A demonstrates that in this formulation, both G and A polymer chains exist independently in the system and there is no interaction between them to jointly resist the flow of the entire system.

However, when MFC is doped into G/A, the sample sequentially experiences linear viscoelastic (LVE) region, yield zone, yield point, and viscous flow. Also, the yield stress of the sample increases from 62.31 Pa to 491.42 Pa as the concentration of MFC rises from 0.4% to 0.7%. This phenomenon can be attributed to the hydrogen bonding interactions formed between MFC with a large aspect ratio and G/A. Also, the strength of the interaction is closely related to the concentration of MFC. Hydrogen bonding interactions increase the overall viscosity and hinder the flow of the formulation. At rest or when the stress is small enough (< 10 Pa), hydrogen bonding interactions can maintain the stability of the system. However, as the stress gradually increases, the hydrogen bonding interaction is gradually weakened, causing the sample to begin to enter the yield zone. When the hydrogen bonding interaction is completely broken by stress, the sample begins to flow.

Therefore, when MFC-composited G/A formulated bioink is loaded into a syringe barrel, hydrogen bonding interactions between MFC and G/A could effectively prevent deposition or uneven distribution of each component (G, A, MFC, cells if encapsulated) under their own weight in this formulation before printing [167]. To induce flow, it necessitates the application of a specific threshold of stress.

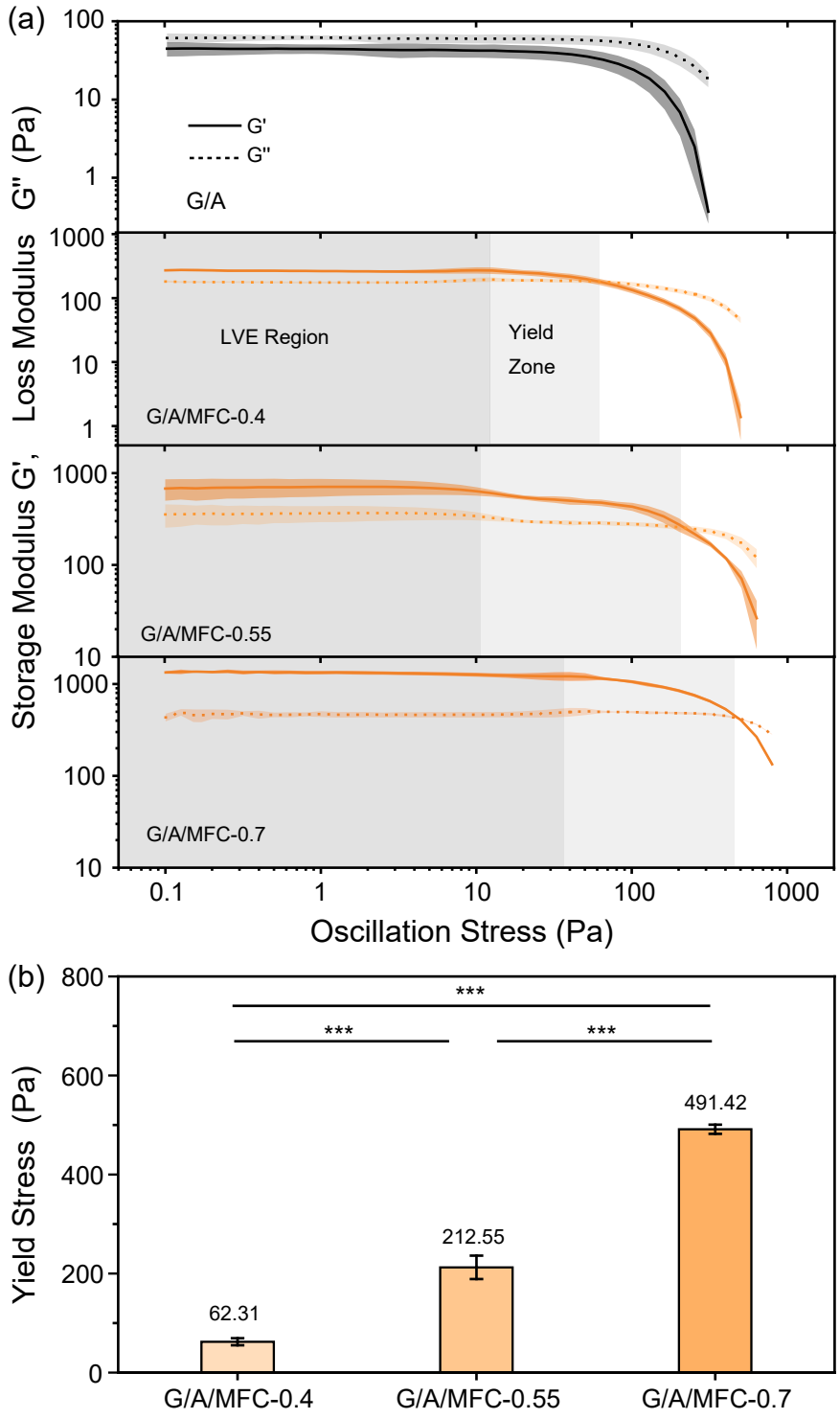

Figure 5.4: (a) Storage and loss moduli variations of MFC-composited G/A bioink formulations and benchmark with the increase of oscillation stress from 0.1 to 1000 Pa at a frequency of 1 Hz. (b) Yield stress of MFC-composited G/A bioinks.

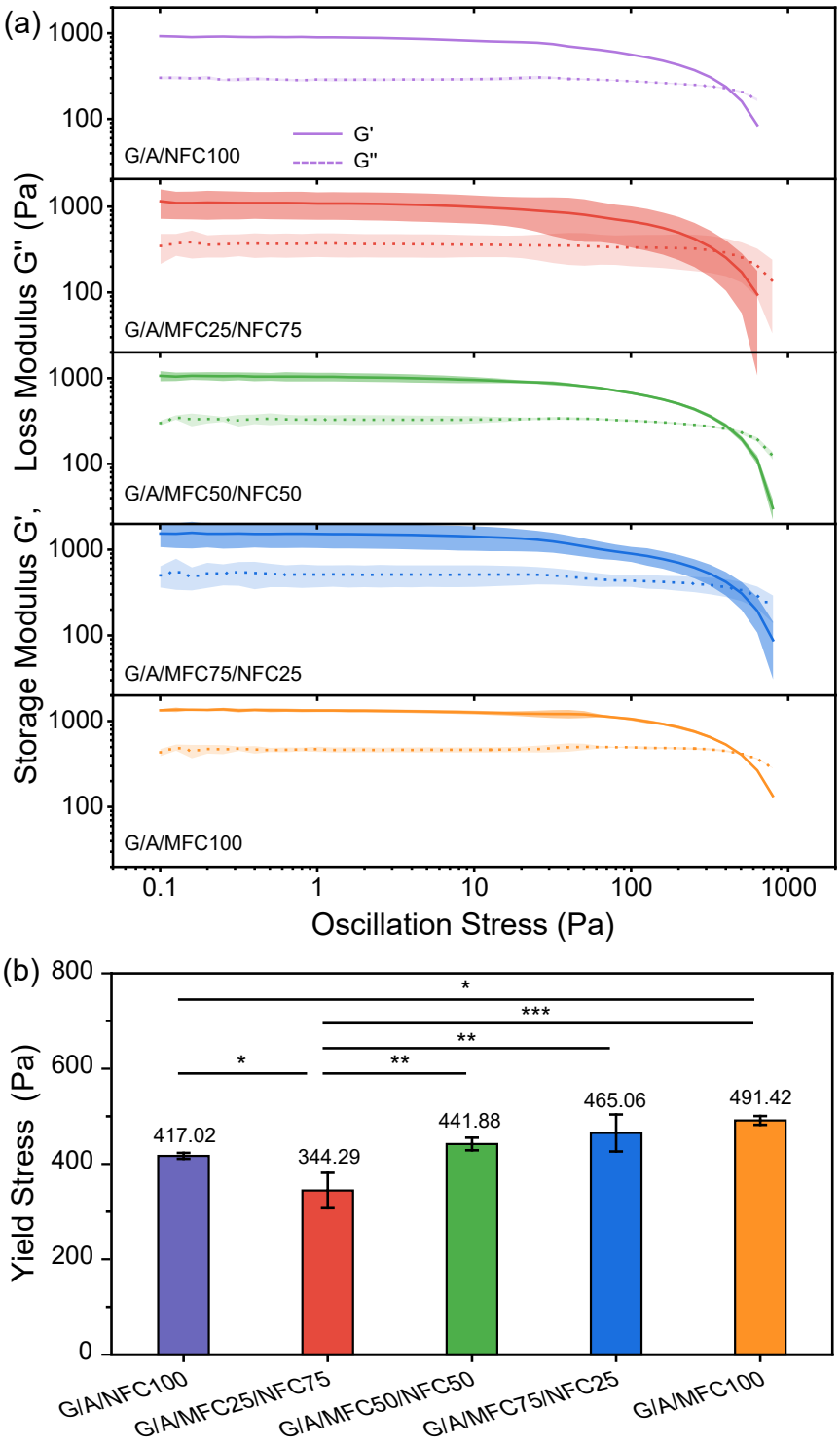

Figure 5.5: (a) Storage and loss moduli variations of hybrid cellulose-composited G/A bioinks with the increase of oscillation stress from 0.1 to 1000 Pa at a frequency of 1 Hz. (b) Yield stress of hybrid cellulose-composited G/A bioinks.

When MFC and NFC are incorporated into G/A formulation at different volume ratios, the yield behaviour of the samples changes. As shown in Figure 5.5, the yield stress of G/A/NFC100 (417.02 Pa) is lower than that of G/A/MFC100 (491.42 Pa). The yield stress increases with the rise of the proportion of MFC in the mixed cellulose, implying that MFC has greater advantages than NFC in maintaining the stability of the system. This can be explained by the size of the fibrils. The size of microfibrils (diameter of 1 to 3 µm) is larger than that of nanofibrils (diameter of 20 to 100 nm), making the MFC network more difficult to move.

5.3.2.2 Shear-thinning behaviour during extrusion

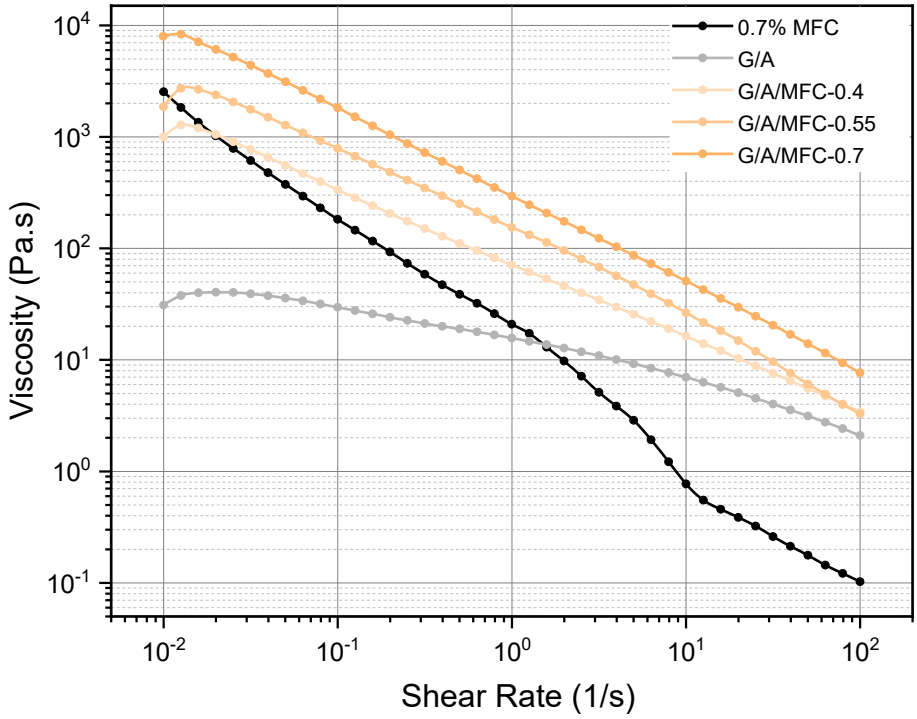

Figure 5.6: Viscosity variations of MFC-composited G/A bioink formulations compared to benchmark via shear rate sweep from 0.01 to 100 1/s. The viscosity span (2518.68 to 0.1 Pa.s) of 0.7% MFC is the largest among these samples. The shear thinning property of formulation G/A was improved after the incorporation of MFC.

Shear-thinning behaviour is critical for the bioink to pass smoothly through the narrow nozzle of the printhead. Figure 5.6 shows the change in viscosity of different MFC-composited G/A bioink

Table 5.1: Fitting results of Power Law model for MFC-composited G/A bioink formulations. Power law flow index and apparent viscosity (Pa.s) at 1 1/s shear rate are represented as n_f and k_{PL}, respectively.

Sample	n_f	k_{PL}	R^2 [1]
0.7% MFC	-0.12	22.04	0.72
G/A	0.52	20.16	>0.99
G/A/MFC-0.4	0.34	73.86	>0.99
G/A/MFC-0.55	0.2	149.09	0.95
G/A/MFC-0.7	0.22	300.3	>0.99

[1] R^2 is a goodness-of-fit measure for linear regression models. Higher R^2 represent smaller differences between the raw data and the fitted values. The maximum of R^2 is 1.

formulations under gradually increasing shear rates. The flow index (n_f) (Table 5.1) obtained by fitting a power law model explained in Table 3.1 was used to analyse the flow characteristics of the bioink formulation. The viscosity span (2518.68 to 0.1 Pa.s) of 0.7% MFC is the largest in Figure 5.6. This implies that shear induces the breakage of intra- and intermolecular hydrogen bonds in MFC structure, thereby orienting MFC in the direction of the shear force, ultimately manifesting as a significant decrease in viscosity. However n_f of MFC (-0.12) is negative, suggesting that the power law model may not be suitable for describing the flow behaviour of pure MFC.

The shear thinning behaviour of formulation G/A is not obvious, with the viscosity dropping only from 30 to 2 Pa.s. This is because simple entanglements between G and A polymer chains are broken by shear. Compared with G/A (n_f of 0.52), G/A/MFC is observed to have more significant shear thinning behaviour, as quantified by n_f of 0.34, 0.2, and 0.22 for 0.4%, 0.55%, and 0.7% MFC, respectively. This indicates that in MFC-composited G/A system, both the intrinsic hydrogen bonding of MFC and the complex hydrogen bonds between MFC and G/A are responsible for the high viscosity (7967.55 Pa.s) of the formulation (G/A/MFC-0.7) at a low shear rate of 0.01 1/s. With the increasing shear rate, hydrogen bonding interactions are disrupted. Polymer chains of G and A driven by MFC with a high aspect ratio, and like MFC, all rearrange along the shear direction [167, 437], causing the viscosity of the system to considerably decrease to 7.66 Pa.s at a shear

rate of 100 1/s. Therefore, the results evidence that the incorporation of MFC contributes to the shear-thinning behaviour of G/A bioink formulations.

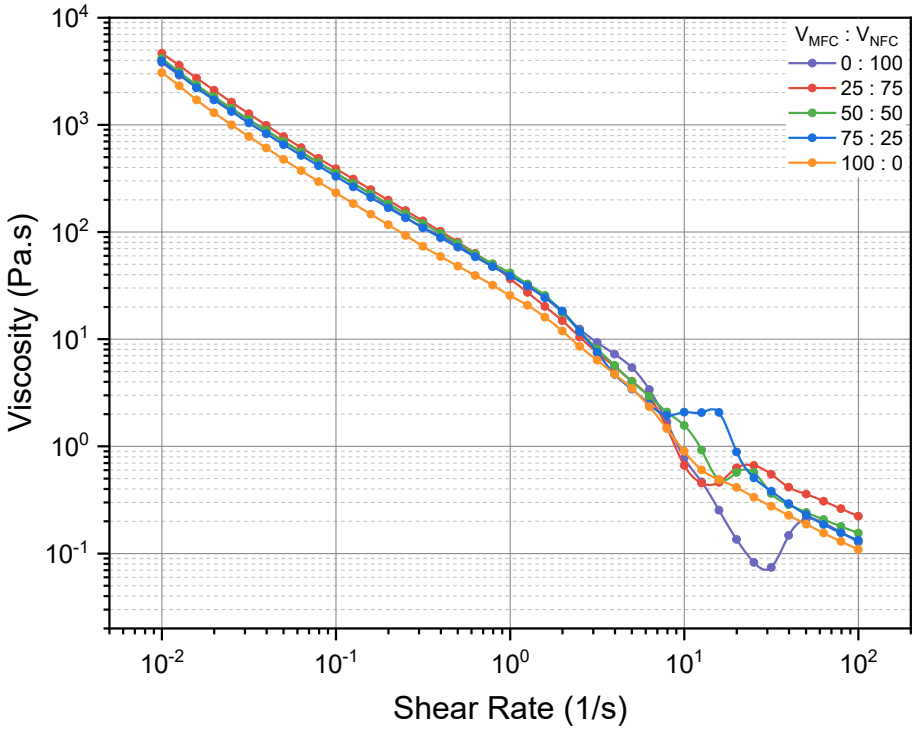

Figure 5.7: Viscosity variations of hybrid cellulose slurries in shear rate sweep from 0.01 to 100 1/s. The differences in the viscosity variation range of the samples are not obvious.

Before studying the effects of NFC and hybrid cellulose slurries on the shear-thinning characteristics of G/A bioink, the shear-thinning of the cellulose slurry itself was recorded. As shown in Figure 5.7, although the contents of MFC and NFC in the slurry are different, the gap in the viscosity variation range of the samples is not obvious. It is worth noting that the viscosity of the sample fluctuates significantly only when the shear rate increases from 7 to 60 1/s, which is consistent with the results reported by Schenker et al [438]. When the shear rate is less than 7 1/s and greater than 60 1/s, samples follow the power law model. Shear rates between 7 and 60 1/s are defined as the transition region, where the power law model no longer applies. Hence, if the entire curve of the sample is fitted using power law model, the goodness-of-fit (R^2) will be reduced and the resulting

Table 5.2: Fitting results of Power Law model for blended cellulose slurries.

V_{MFC} : V_{NFC}	n_f	k_{PL}	R^2
0 : 100	-0.11	25.74	0.55
25 : 75	-0.13	28.32	0.66
50 : 50	-0.11	27.58	0.49
75 : 25	-0.09	27.28	0.47
100 : 0	-0.12	22.04	0.72

n_f will behave abnormally, as shown in Table 5.2.

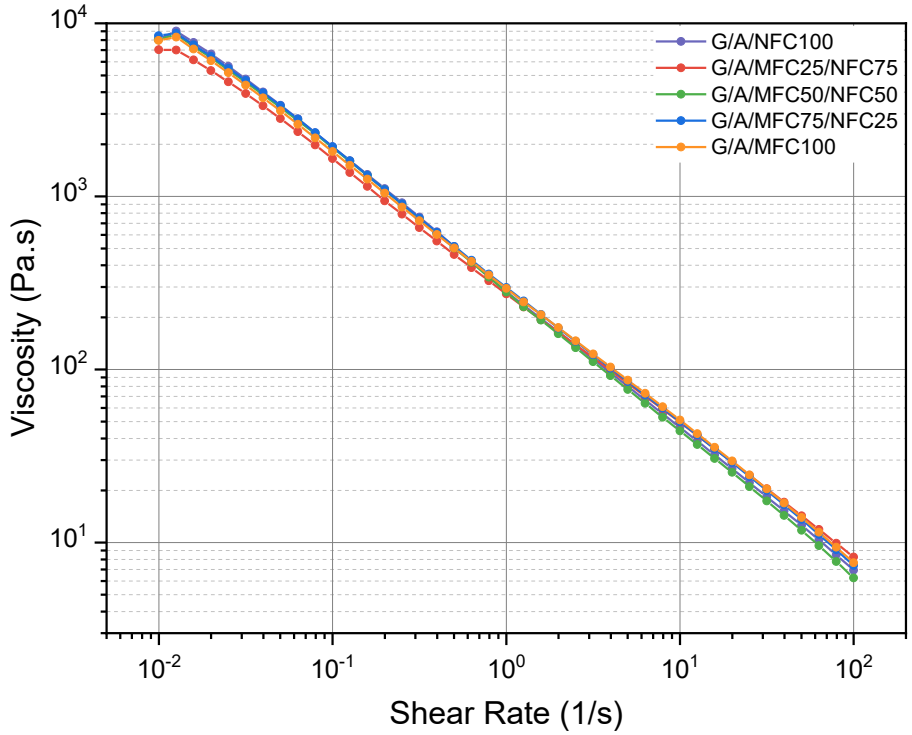

Figure 5.8: Viscosity Variations of five hybrid cellulose-composited G/A bioinks in shear rate sweep from 0.01 to 100 1/s.

When MFC, NFC, and hybrid cellulose are mixed with G/A, it can be seen from Figure 5.8 and Table 5.3 that, viscosities of these 5 samples decrease from about 8000 to 7 Pa.s with increasing shear rate from 0.01 to 100 1/s. Differences in fibre size in the slurry and the NFC/MFC ratios in bioink formulation do not significantly affect the shear-thinning behaviour of hybrid cellulose-composited G/A bioink. They all follow power law model with R^2 of more than 0.99 and have n_f

Table 5.3: Fitting results of Power Law model for hybrid cellulose-composited G/A formulations.

Sample	n_f	k_{PL}	R^2
G/A/NFC100	0.19	292.7	>0.99
G/A/MFC25/NFC75	0.24	280.2	>0.99
G/A/MFC50/NFC50	0.18	284.1	>0.99
G/A/MFC75/NFC25	0.21	303.7	>0.99
G/A/MFC100	0.22	300.3	>0.99

numbers of around 0.2. This is in good agreement with the shear thinning properties previously observed for nanocelluloses formulation [439–441].

5.3.2.3 Recovery post extrusion

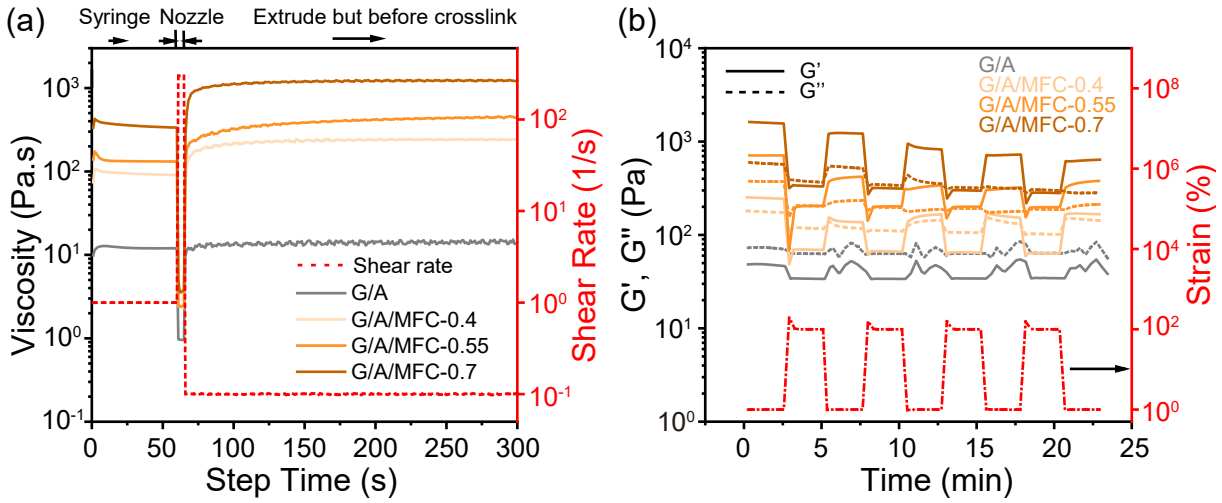

Figure 5.9: (a) The viscosity change process of MFC-composited G/A bioinks at shear rates of 1, 300, and 0.2 1/s for 60, 5, and 235 s, respectively. This peak hold mode was used to simulate the printing process. (b) The recoverabilities of G'and G" for MFC-composited G/A bioinks under four cycles of high strain (100%) for 150 s and low strain (1%) for 150 s at a frequency of 1 Hz.

After the bioink passes through the nozzle and is extruded onto the substrate, the bioink should be able to immediately return to the initial gel state, which is of great significance for building hydrogel scaffolds layer-by-layer while maintaining the shape fidelity of the scaffold. Therefore, the recoverabilities of the viscosity and modulus of the bioink formulations were evaluated.

As shown in Figure 5.9a, the shear rate is controlled at 1 1/s for 60 s to simulate the gradual movement of the bioink in the syringe under the action of external force. The shear rate is then ramped up to 300 1/s for just 5 s to replicate the moment the sample flows through the nozzle. It can be seen that the apparent viscosities of MFC-composited G/A formulations experience a substantial reduction by two orders of magnitude, while the viscosity of G/A only reduced from 10 to 1 Pa.s. As the shear rate drops sharply to 0.2 1/s, G/A/MFC-0.4, G/A/MFC-0.55, and G/A/MFC-0.7 rapidly fully recover within just about 5 seconds. Comparing apparent viscosities of G/A/MFC-0.4, G/A/MFC-0.55, and G/A/MFC-0.7 at a shear rate of 0.2 1/s in Figure 5.6 and at 300 s in Figure 5.9, viscosity recovery rates for G/A/MFC-0.4, G/A/MFC-0.55, and G/A/MFC-0.7 are 115%, 95%, and 92% respectively. However, the viscosity of G/A at a shear rate of 0.2 1/s is not fully restored with a viscosity recovery rate of only 58%. It suggests that MFC can improve the recoverability of G/A bioink viscosity. However, higher concentrations of MFC may be less conducive to complete recovery of formulation viscosity.

Figure 5.9b exhibits the trends of *G'* and *G"* for MFC-composited G/A bioink formulations under four cycles of high strain (100%) and low strain (1%). It can be seen that formulated G/A keeps a sol state because *G"* is always greater than *G'* regardless of high and low strain. It is hard for G/A to recover modulus immediately because *G'* and *G"* of G/A within 150 s of each low strain cannot level off but noticeably fluctuate. Hence, G/A formulation where viscous flow dominates is not suitable for extrusion printing. However, *G'* and *G"* of G/A/MFC-0.4, G/A/MFC-0.55, and G/A/MFC-0.7 experience a similar tendency. Under low strain, *G'* of samples are significantly greater than *G"*, while *G"* are significantly greater than *G'* when there is a sudden surge in strain. After each alternate strain, *G'* and *G"* of G/A/MFC can rapidly maintain stability, revealing the strong strain-responsiveness of MFC-composited G/A formulations. By comparing *G'* of samples at the first and last low strain, the recovery rates of modulus for G/A/MFC-0.4, G/A/MFC-0.55, and G/A/MFC-0.7 were determined to be 72%, 56%, and 43%, respectively, demonstrating that the recovery rate decreases with increasing MFC content although the addition of MFC significantly

improves the modulus recoverability of bioinks.

In summary, Figure 5.9 illustrates that the incorporation of MFC can significantly enhance the recoverability of G/A formulation. The limited recoverability of the pure G/A formulation is likely due to its inherent sol state, which results in increased fluidity when subjected to significant strain or shear forces. However, in MFC-composited G/A system, the hydrogen bonds disrupted by deformation can reversibly reform once the external force dissipates, thus causing the system to transition back from a sol state to a gel state [167]. The thixotropic properties of MFC-composited G/A system suggest its ability to be efficiently extruded from a nozzle. Moreover, the printed structure can retain its shape without flowing [167]. In addition, note that a high concentration of MFC does not favour the formulation reverting completely to its original state, possibly because the high concentration of MFC impedes its movement and results in fewer hydrogen bonds being reformed between MFC and G/A.

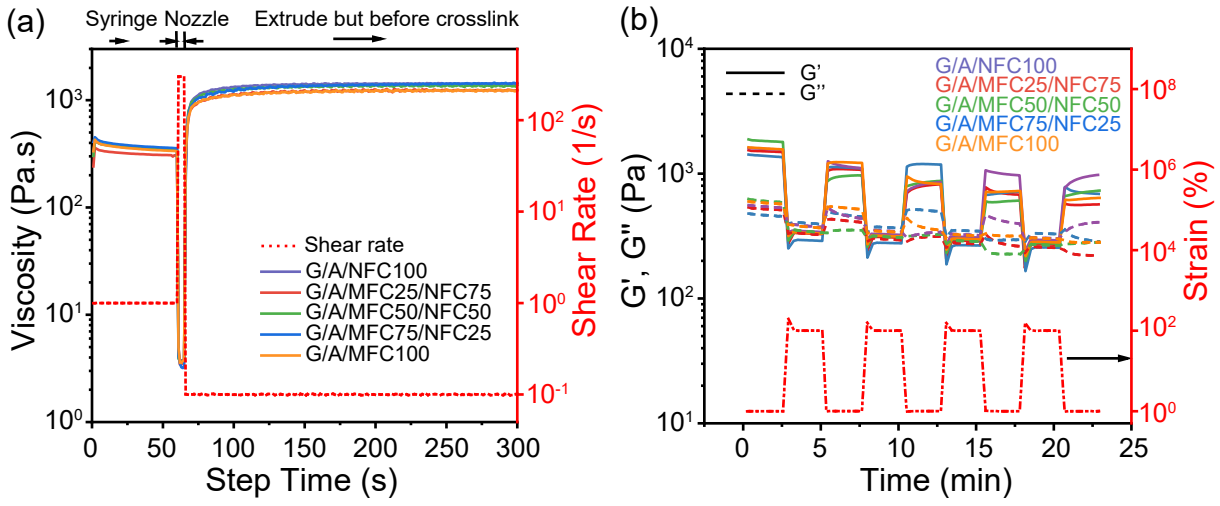

Figure 5.10: (a) The viscosity change process of hybrid cellulose-composited G/A bioinks in peak hold mode. (b) The recoverabilities of G'and G" for hybrid cellulose-composited G/A bioinks under four cycles of high strain (100%) for 150 s and low strain (1%) for 150 s at a frequency of 1 Hz.

When 1% NFC and hybrid cellulose are doped into G/A formulation, as shown in Figure 5.10a, viscosity trends of sample G/A/NFC100, G/A/MFC25/NFC75, G/A/MFC50/NFC50, and G/A/MFC75/NFC25 are almost the same as that of G/A/MFC100. The viscosity recovery rates of

G/A/NFC100, G/A/MFC25/NFC75, G/A/MFC50/NFC50, and G/A/MFC75/NFC25 all are approximately 100%. In Figure 5.10b, recovery rates of modulus for G/A/NFC100, G/A/MFC25/NFC75, G/A/MFC50/NFC50, and G/A/MFC75/NFC25 are 63%, 38%, 41%, and 51% respectively. The highest modulus recovery rate of G/A/NFC100 among five samples illustrates that the size advantage of NFC makes it easier to achieve the movement of polymer chain segments than MFC.

5.3.2.4 Gelation kinetics during crosslinking

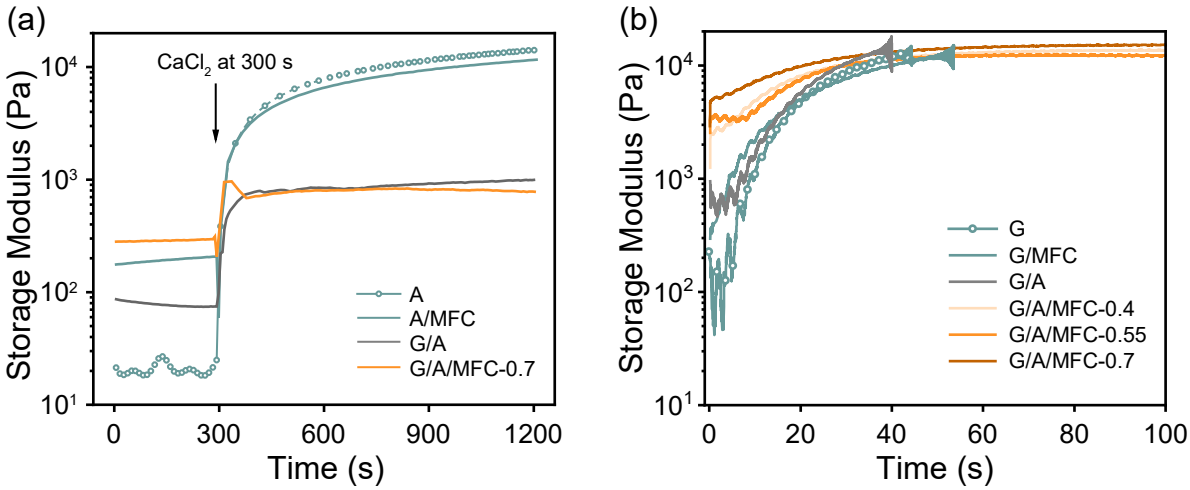

Figure 5.11: (a) Representative curves of storage moduli during addtion of 2% $CaCl_2$ to different bioinks. (b) Representative curves of storage moduli during irradiation of different bioinks with UV light (365 nm).

The rapid crosslinking behaviour of bioinks is effective in preventing scaffold collapse. Therefore, the study of gelation kinetics for MFC-composited G/A bioink formulations in the presence of $CaCl_2$ and UV light were carried out respectively. In Figure 5.11a, when $CaCl_2$ is added dropwise to the sample at 300 s, *G'* of all samples increased sharply and the storage modulus change rate dropped sharply, indicating that they were crosslinked with calcium ions. The times required for ion gelation of sample A, A/MFC, G/A, and G/A/MFC-0.7 were measured 900, 900, 486 and 389 s respectively, while storage modulus increments of A, A/MFC, G/A, and G/A/MFC-0.7 are 13778, 11330, 710, 493 Pa. It reveals that when G and MFC are mixed to A, the reaction site of A is

greatly shielded by G and MFC (mainly G), causing calcium ions to only crosslink with part of A. It is worth noting that in this experiment, the sample was located in the middle of the parallel plate geometry of the rheometer. Calcium ions can only gradually penetrate into the sample from the edges of the geometry. However, in the actual process of synthesising hydrogels, the samples were completely immersed in calcium ions for crosslinking. These two different operations will result in differences in ionic crosslinking times.

Figure 5.11b depicts the change in *G'* of samples during photo-crosslinking. The UV light with 100% iris was triggered at the beginning of the test. It can be seen that the time required for covalent cross-linking of all samples is approximately between 40 and 45 s. Compared to ionic crosslinking, covalent photo-crosslinking takes significantly less time. But when cells are encapsulated in bioink, the intensity of the UV light will be appropriately reduced to ensure cell viability. On the other hand, the modulus increments of G/A/MFC-0.4, G/A/MFC-0.55, and G/A/MFC-0.7 are significantly lower than that of G and G/MFC, which also verifies the shielding effect of A on the covalent crosslinking of G.

5.3.3 Printabilities of bioink formulations

A preliminary evaluation of the printability of bioink formulations was performed, guided by the results of the bioink's macroscopic fluidity and rheological properties testing. G/A and G/A/MFC-0.7 were loaded into the syringe cartridge. The dispensing pressure was adjusted so that the sample was just extruded from the 27-gauged nozzle (Figure 5.12). It can be found that G/A forms a droplet at the tip of the nozzle. As the extrusion proceeds, the droplet falls directly onto the substrate due to gravity, while G/A/MFC-0.7 appears in the shape of a droplet in the early stages of extrusion, and then forms continuous filaments. Thus, the bioink formulations containing the following rheological characteristics, such as a sol state, devoid of a yield point, and lacking recoverability, are recommended to be unprintable. However, the gel-like and shear-thinning bioinks can be continuously extruded in the form of filaments. The recoverability of the bioink allows it to

maintain shape fidelity. The strong self-supporting ability ensures the resolution of the final printed scaffold.

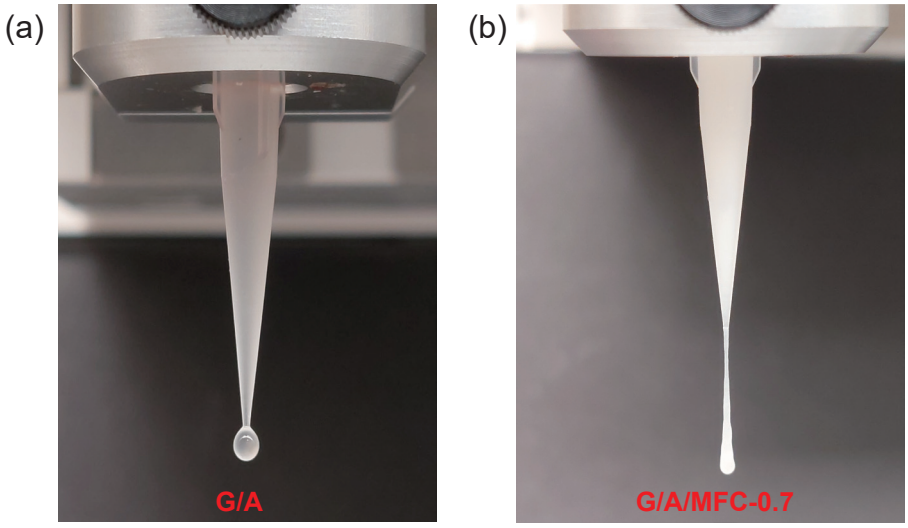

Figure 5.12: Extrusion results of sample G/A and G/A/MFC-0.7. G/A was in the form of droplets after extrusion, while G/A/MFC-0.7 can be dispensed in the form of continuous fine filaments.

5.3.3.1 The effects of printing parameters on the accuracy of 1D filaments

To determine the optimal printing conditions for printable formulations, the effects of dispensing pressure, printing speed, and nozzle size on the accuracy of 1D filaments were studied. Figure 5.13 shows the images and corresponding line widths of filaments formed by G/A/MFC-0.7 bioink formulation using a 27-gauged nozzle under different dispensing pressures and printing speeds. The gray area is the printable area. Combined with Figure 5.14a, it can be found that under constant dispensing pressure, the line width decreases exponentially as the printing speed increases. Figure 5.14b reveals that the line width increases linearly with the rise of dispensing pressure at a constant printing speed. Additionally, when the printing speed is 24 mm/s and the dispensing pressure is 55 kPa, the filament exhibits the thinnest line width of 0.49 mm. If the damage to the encapsulated cells caused by shear stress during the extrusion process and the accuracy of printing are taken into account at the same time, Figure 5.14c shows that *POI* has a maximum value when the printing

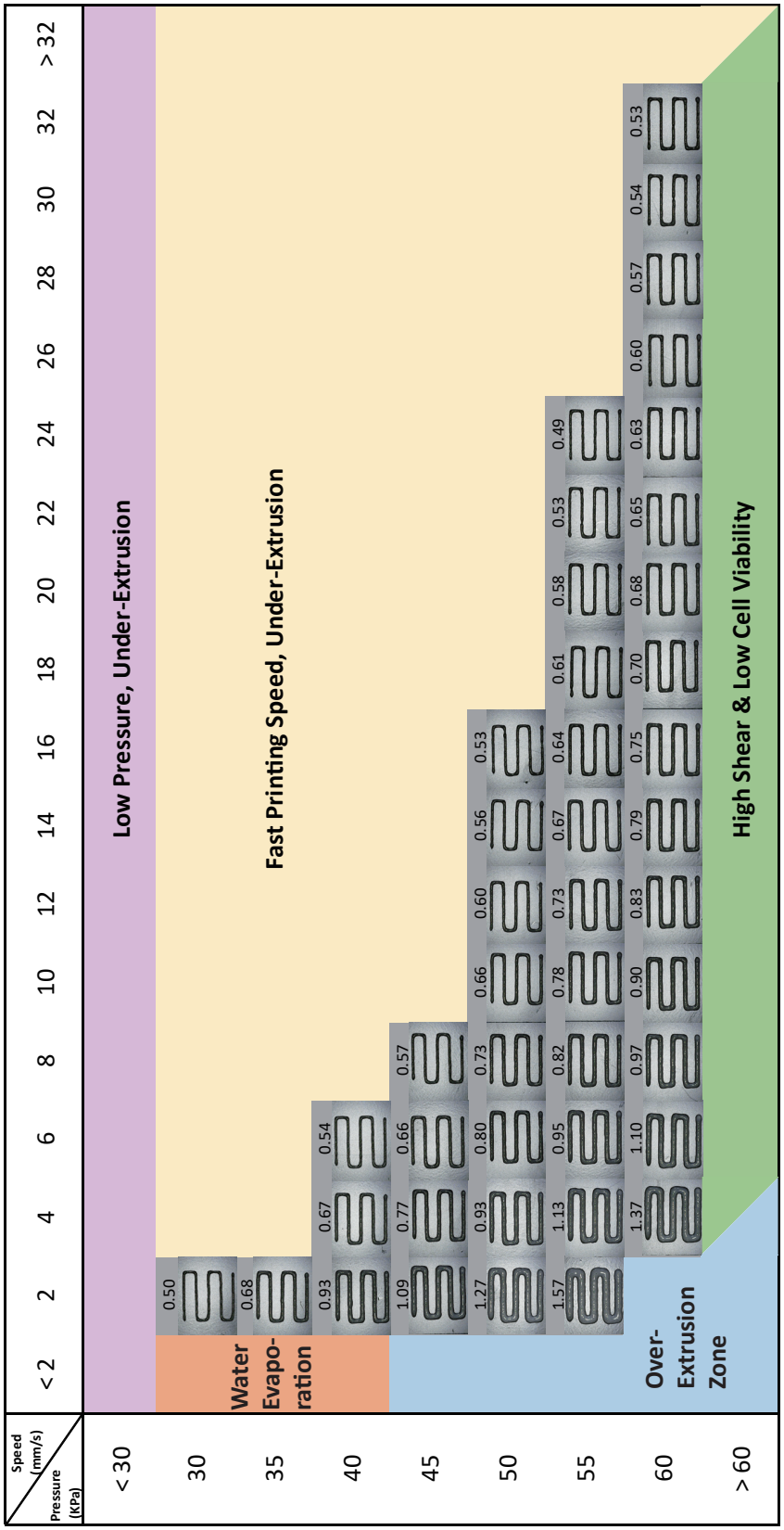

Figure 5.13: Line width (mm) of G/A/MFC-0.7 filaments extruded from a 27-gauged nozzle at different print speeds and dispensing pressures.

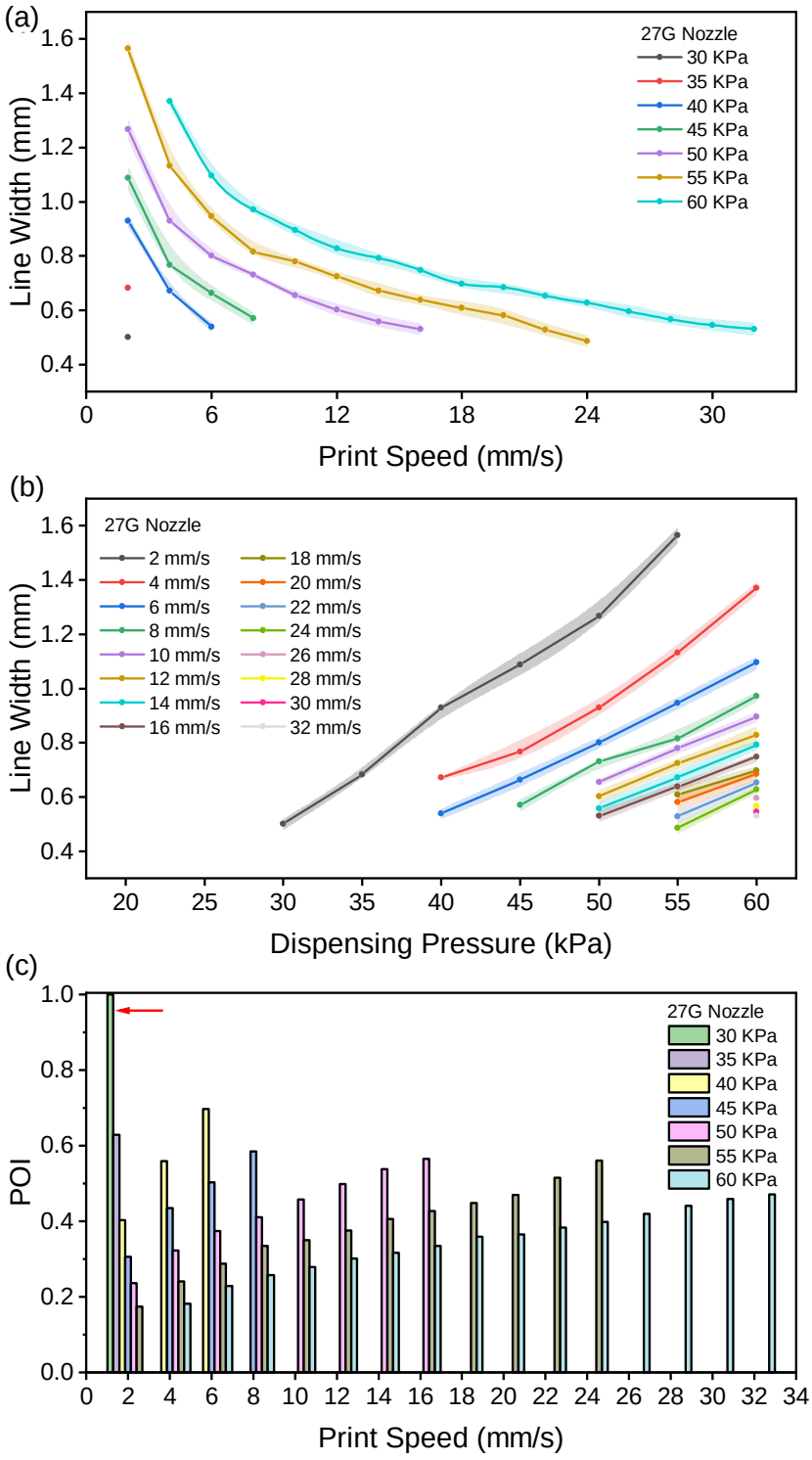

Figure 5.14: Trends of line width with (a) print speed and (b) dispensing pressure. Comparison of different POIs when G/A/MFC-0.7 was extruded from 27-gauged nozzle (c).

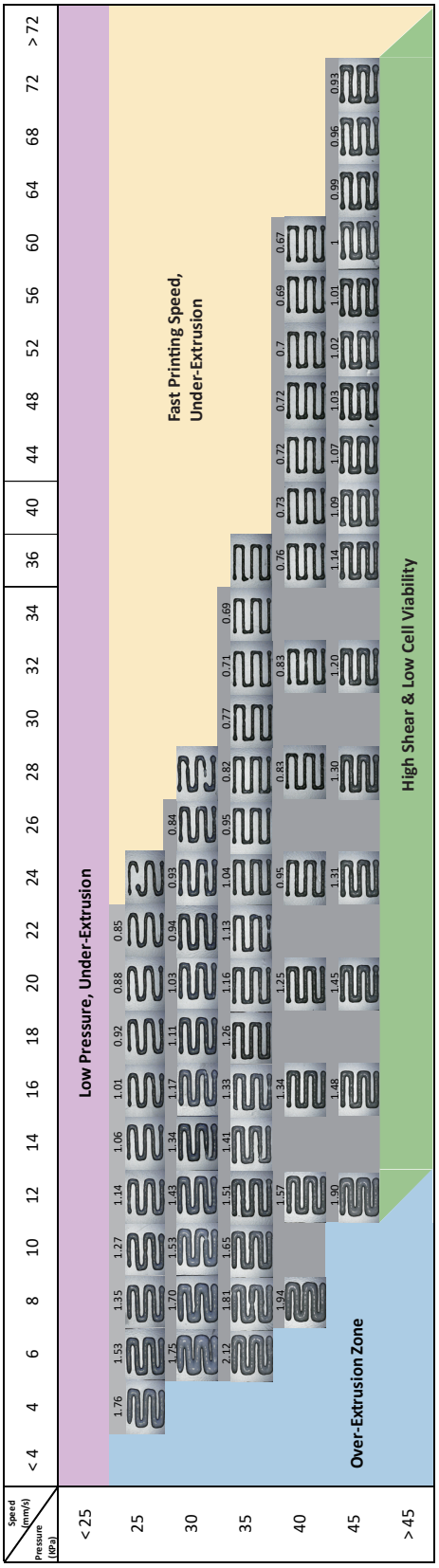

Figure 5.15: Line width (mm) of filaments extruded from a nozzle of 22 gauge at different print speeds and dispensing pressures.

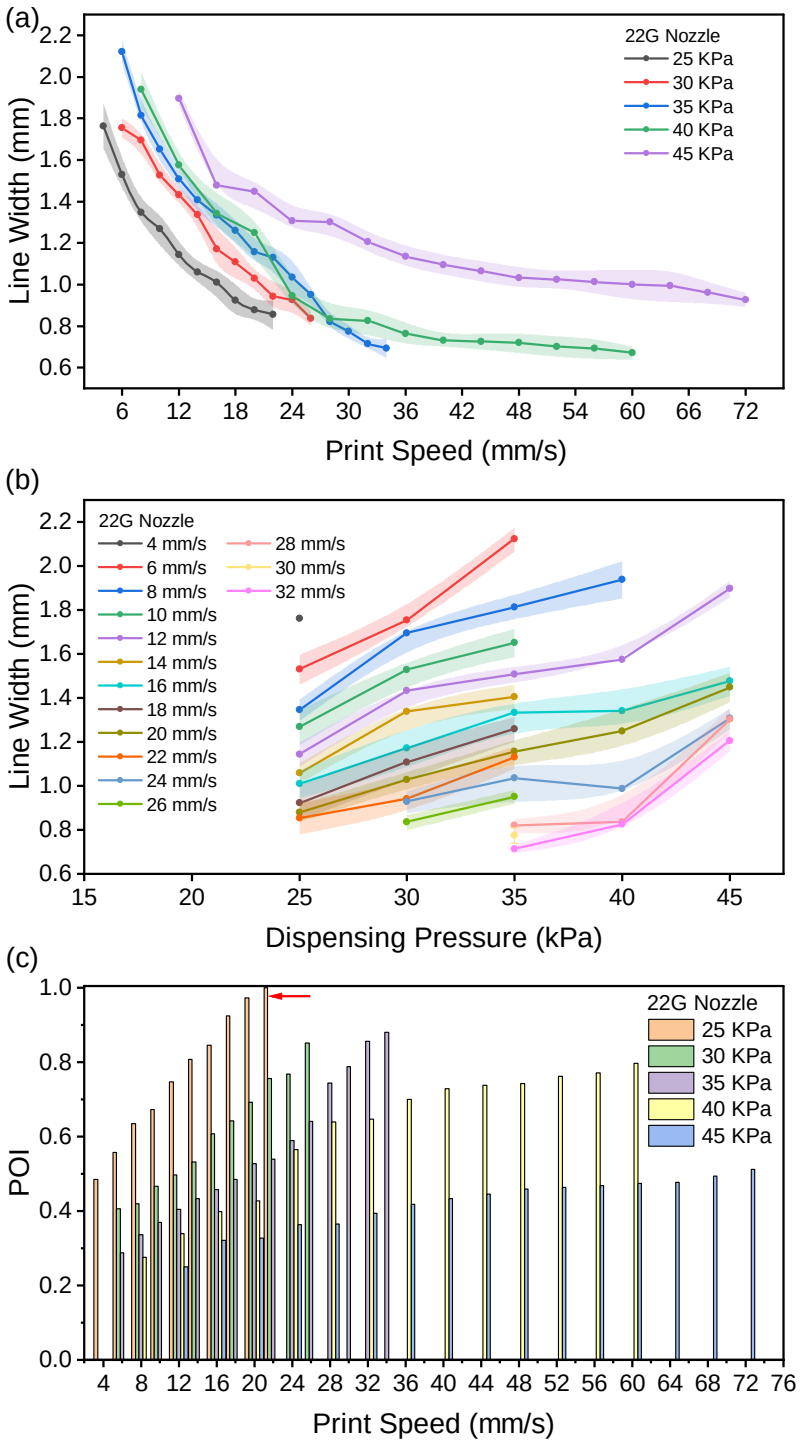

Figure 5.16: Trends of line width with (a) print speed and (b) dispensing pressure. (c) Comparison of different POIs when G/A/MFC-0.7 was extruded from a 22-gauged nozzle.

speed is 2 mm/s and the dispensing pressure is 30 kPa, thus shedding light on the optimal printing condition when using a 27-gauged nozzle. Under this optimal printing condition, the line width is 0.5 mm.

In addition, outside the grey printable area, if the dispensing pressure is less than 30 kPa (pink area in Figure 5.13), or the printing speed is too fast (yellow zone in Figure 5.13), the continuity of the filament will be seriously damaged. Thur, under-extrusion occurs. If the bioink is extruded at a printing speed of less than 2 mm/s at a dispensing pressure of 30 to 40 kPa, especially when constructing larger-sized scaffolds, excessive printing time will cause water evaporation in the scaffold and failure of material (orange region in Figure 5.13). When the printing speed is lower than 2 mm/s and the distribution pressure climbs higher than 45 kPa, the resolution of the filament drops sharply and over-extrusion occurs (blue area in Figure 5.13). In addition, it is not advisable to blindly increase the distribution pressure without considering the impact of shear force on cell viability (green zone in Figure 5.13).

When a 22-gauged nozzle was used to extrude G/A/MFC-0.7 formulation, gray printable area becomes larger than that when using a 27-gauged nozzle (Figure 5.15). The increase in the nozzle inner diameter from 200 to 410 μm allows the printer to dispense filament at faster printing speeds for high resolution. The influence of printing speed and dispensing pressure on line width (Figure 5.16) is consistent with the findings when using a 27-gauged nozzle. Figure 5.15 presents that the thinnest line width (0.67 mm) appears at a printing speed of 60 mm/s and a dispensing pressure of 40 kPa. However, in accordance with the maximum POI value, the optimal printing condition with line width of 0.85 mm is revealed when printing speed and dispensing pressure are set to 22 mm/s and 25 kPa separately.

5.3.3.2 Printability index of 2D scaffolds

After the optimal printing conditions for 1D filaments of G/A/MFC-0.7 were determined, different bioink formulations were deployed to construct 2D scaffolds with 2 layers under the printing

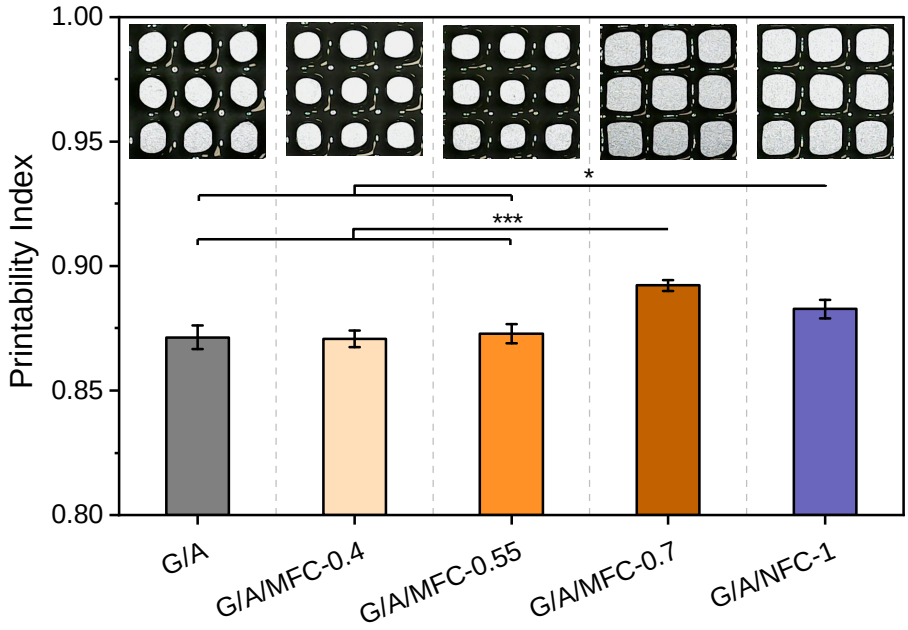

Figure 5.17: Printability indices for 2D scaffolds extruded with different bioinks under same printing conditions (printing speed of 2 mm/s, dispensing pressure of 30 kPa, and 27-gauged nozzle).

conditions (printing speed of 2 mm/s, dispensing pressure of 30 kPa, 27-gauged nozzle). Two-dimensional printability index (*Pr*) was used to compare the degree of interlayer fusion for different bioink formulations under the same printing conditions and thus evaluate the printability of different formulations under certain printing conditions. As explained in Section 3.4, the range of *Pr* is from $\pi/4$ (about 0.785) to 1. Sample with *Pr* of $\pi/4$ displays severe interlayer fusion while sample with *Pr* of 1 produces clear printing path and consistent filament structure. According to Figure 5.17, undoubtedly, the G/A/MFC-0.7 scaffold under its optimal printing conditions has obvious square-like lattices and thus keeps the minimised interlayer fusion and highest *Pr* of 0.892 among these five samples. The internal lattice of the scaffolds for G/A/NFC-1 also tends to be square, as quantified by *Pr* of 0.883, suggesting that G/A/MFC-0.7 and G/A/NFC-1 have very similar printabilities.

Furthermore, *Pr* of G/A/MFC-0.4 (0.87), and G/A/MFC-0.55 (0.873) are significantly lower than that of G/A/MFC-0.7 (*** $P \leq 0.001$), which is reasonable and can be explained by the rheological results: the yield stresses of G/A/MFC-0.4 (62.31 Pa) and G/A/MFC-0.55 (211.55

Pa) are lower than that of G/A/MFC-0.7 (491.42 Pa) (Figure 5.4). The apparent viscosities of G/A/MFC-0.4 (73.86 Pa.s) and G/A/MFC-0.55 (149.09 Pa.s) at shear rate of 1 1/s are also less than that of G/A/MFC-0.7 (300.3 Pa.s) (Table 5.1). All above suggests that the dispensing pressure (30 kPa) used in this measurement suitable for the G/A/MFC-0.7 formulation is too high for G/A/MFC-0.4 and G/A/MFC-0.55 formulations, causing over-extrusion. Appropriate decrease of dispensing pressure according to yield points and viscosities of G/A/MFC-0.4 and G/A/MFC-0.55 would improve the *Pr* of them.

5.3.3.3 Shape fidelity of 3D constructs

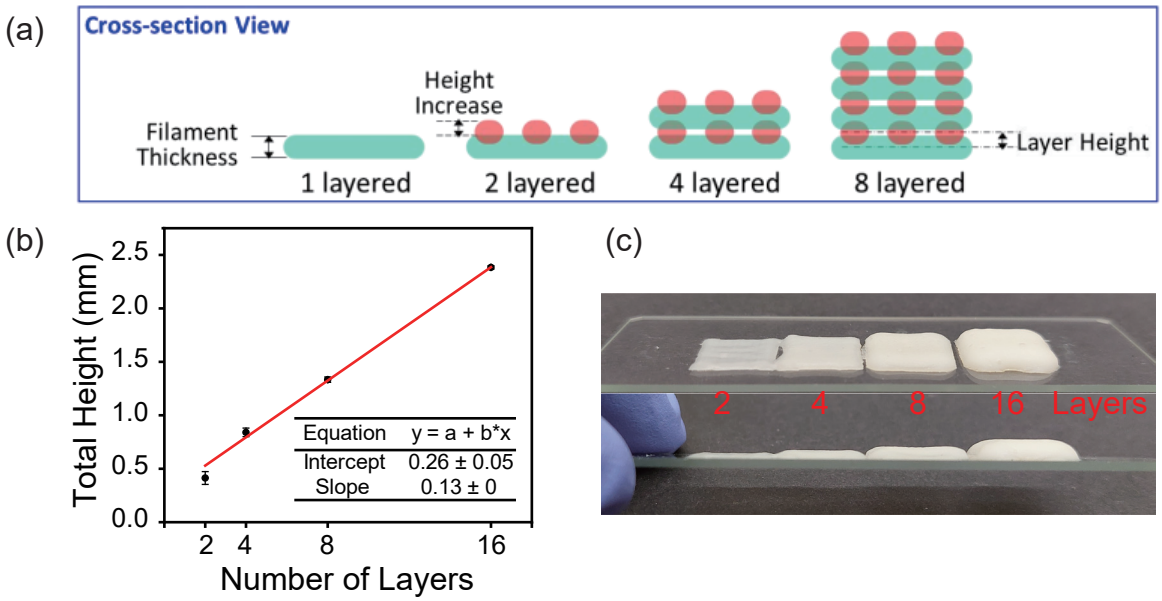

Figure 5.18: (a) Cross-section view of the scaffolds with multiple layers and schematic representation of the layer height [442]. (b) Relationship between the total height of the scaffold and the number of layers and linear fitting results. (c) Images of crosslinked constructs with different numbers of layers.

To verify the shape fidelity of multilayer constructs established by MFC-composited G/A formulations, G/A/MFC-0.7 formulation was printed into 2-, 4-, 8-, and 16-layer scaffolds under optimal printing conditions (printing speed of 2 mm/s, dispensing pressure of 30 kPa, 27-gauged nozzle), and then underwent covalent photo-crosslinking and ion crosslinking to synthesis MFC-composited

ICE G/A hydrogel constructs. As shown in Figure 5.18, the total heights of 2-, 4-, 8-, and 16-layer scaffolds are 0.41, 0.84, 1.33, and 2.38 mm, respectively. It was found that the total height of the construct does not double as the number of layers doubles. A clear linear relationship between the number of layers and the total height of the construct can be observed due to a blend between each layer (Figure 5.18b). This result is supported by previous reports [442]. The linear relationship between the number of layers and the total height of the construct allows us to precisely predict the height of complex constructs with multiple layers and achieve scheduled shape fidelity of 3D constructs.

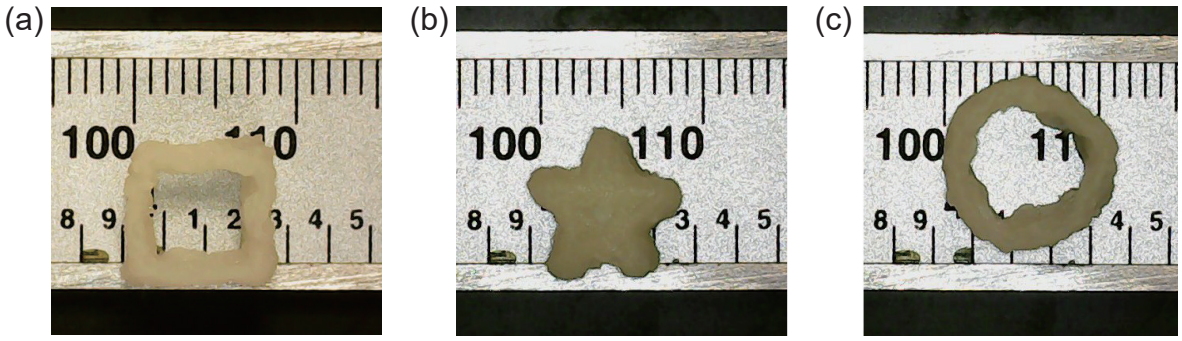

Figure 5.19: Printed constructs of G/A/NFC-1 according to different models at a printing speed of 22 mm/s and a dispensing pressure of 25 kPa using a 22-gauged nozzle.

The shape fidelity of multilayer constructs printed by NFC-composited G/A bioink formulation G/A/NFC-1 was also checked by building 20-layer constructs with different shapes. Since the difference in *Pr* index between G/A/NFC-1 and G/A/MFC-0.7 is not significant ($P > 0.05$) (Figure 5.17), the optimal printing conditions of G/A/MFC-0.7 (printing speed of 22 mm/s, dispensing pressure of 25 kPa, 22-gauged nozzle) was used to extrude G/A/NFC-1 layer by layer. Figure 5.19 depicts a top view of each construct. Obviously, the actual side lengths of the square (8 mm) (Figure 5.19a) and the true length between the two non-adjacent vertices of the five-pointed star (9 mm) (Figure 5.19b) are consistent with their corresponding theoretical lengths (Figure 5.2d,e). Only the true diameter of the circle is slightly larger than the theoretical length (10 mm) by about 1 mm (Figure 5.19c). This illustrates the excellent shape fidelity of NFC-composited ICE hydrogel. In

addition, by performing 3 consecutive press-relax cycles from the sides of these 3 constructs using a tweezer, the shape of the constructs changed accordingly and completely returned to the initial state after the last relax, revealing the mechanical stability of crosslinked interlayers and excellent elasticity of the crosslinked body.

5.4 Conclusions

In the present chapter, cellulose, including MFC, NFC, and hybrid cellulose containing MFC and NFC, was demonstrated to exert a significant effect on the macroscale fluidity, rheological properties, and printabilities of G/A bioink formulation.

The G/A formulation exhibits a low viscosity (20.16 Pa.s) and a sol state due to the lack of interactions among its constituents. However, the introduction of cellulose, regardless of MFC, NFC, and hybrid cellulose, enhances the overall viscosity of the cellulose-composited G/A formulations through hydrogen bond interactions between cellulose and G/A, transitioning the formulations from a sol to a gel state, and imparting a certain yield stress (such as 491.42 Pa for sample G/A/MFC-0.7). Moreover, the yield stress of MFC-composited G/A formulation increases from 62.31 to 491.42 Pa with the concentration of MFC from 0.4% to 0.7% in the formulation. Additionally, because large-sized MFC (diameter of 1 to 3 μm) is more difficult to deform than NFC (diameter of 20 to 100 nm), G/A/MFC-0.7 exhibits higher yield stress than G/A/NFC-1 (417.02 Pa). The gel-like cellulose-composited G/A formulations with yield stress effectively prevent the sedimentation and uneven distribution of components within the system, thereby enhancing its stability prior to printing.

In addition, both MFC and NFC can promote the shear-thinning behaviour of G/A formulation, which is strongly supported by the fitting results of the Power Law model because the flow index of G/A decreased from 0.52 to 0.22 and 0.19 after the incorporation of either 0.7% MFC or 1% NFC, separately. Furthermore, it was found that the shear-thinning behaviours of 0.7% MFC, 1%

NFC, and hybrid cellulose containing 0.7% MFC and 1% NFC are very similar. Therefore, flow indices of sample G/A/NFC100, G/A/MFC25/NFC75, G/A/MFC50/NFC50, G/A/MFC75/NFC25, and G/A/MFC100, are all around 0.2, suggesting that there is no significant difference between NFC and MFC in improving the shear-thinning characteristics of G/A bioink formulation. In summary, excellent shear-thinning behaviours of cellulose-composited G/A formulations can be attributed to the shear-induced orientation behaviours of cellulose fibrils by breaking hydrogen bonds. Components G and A in formulations are also driven by cellulose fibrils to reorient polymer chains along with shear force direction. Therefore, the shear thinning behaviours of cellulose-composited G/A bioink formulations indicate that they can be extruded smoothly through a narrow nozzle in 3D printing.

Recoverability tests of bioink formulations clarify that the incorporation of cellulose can significantly enhance the recoverability of G/A formulation. This is because the hydrogen bonds disrupted by shear deformation can reversibly re-establish once the external force disappears. The thixotropic properties of cellulose-composited G/A system enable it to transition back from a sol state to a gel state and retain its shape post-printing. However, the effect of MFC concentration on the recovery rates of MFC-composited G/A formulations is negative, possibly because the high concentration of MFC impedes its movement and results in fewer hydrogen bonds reformed between MFC and G/A. Additionally, in terms of the effect of cellulose fibrils size on the recovery rates of cellulose-composited G/A formulations, the size advantage of NFC makes it easier to achieve movement in the formulations than MFC, thus causing a higher recovery rate (63% of storage modulus for G/A/NFC100) of NFC-composited G/A formulations than MFC-composited ones (43% of storage modulus for G/A/MFC100).

The gelation kinetics study showed that in the formulated MFC-composited G/A system, G and MFC have a shielding effect on the ionic crosslinking of ingredient A. Similarly, components A and MFC also exert an adverse effect on the photo-crosslinking of G.

In printability measurements, the extruded form of G/A formulation changes from droplets

to continuous filaments after the addition of 0.7% MFC, confirming the printability of MFC-composited G/A formulations. In 1D printing, the optimal printing conditions for sample G/A/MFC-0.7 were determined by testing the width of 1D filament and comparing parameter optimisation index (*POI*) under different printing conditions. In 2D printing, MFC-composited G/A formulations containing varying concentrations of MFC yield scaffolds with differing printability index (*Pr*) under identical printing conditions. This variation in *Pr* can be attributed to differences in the yield points and viscosities of the formulations. Finally, for G/A/MFC-0.7 hydrogel constructs printed at the optimal printing conditions, the linear relationship between the number of layers and the total height of the construct provides a guide for establishing complex structures. Sample G/A/NFC-1 demonstrated the ability to build multilayer structures with high shape fidelity and mechanical stability.

Chapter 6

EFFECTS OF CELLULOSE ON THE MECHANICAL PROPERTIES OF ICE G/A HYDROGELS

6.1 Introduction

The initial mechanical properties of hydrogels after implantation in damaged tissues are significant for the tissue repair process. The mechanical properties of hydrogels, such as stiffness and elasticity, determine their ability to provide structural support to cells and tissues. The scaffold needs to be strong enough to withstand physiological forces and maintain its integrity during cell culture, while also being flexible and deformable to mimic the mechanical properties of native tissues. So, seamless integration of the scaffold with native tissues can effectively avoid mechanical mismatches, inflammation, and implant failure. Also, the mechanical properties of hydrogels can influence the behaviour of cells cultured within them. Because cells can sense and respond to mechanical cues from their surrounding environment, by tuning the stiffness of the hydrogel, it is possible to influence cell adhesion, migration, proliferation, and differentiation, thus guiding tissue development

and regeneration. Furthermore, the transport of nutrients, oxygen, and waste products within the tissue-engineered construct is also related to the mechanical properties of hydrogels. Hydrogels with appropriate mechanical properties can have interconnected pores and channels that facilitate efficient diffusion and transport of essential molecules, enabling cell survival and function within the scaffold. Overall, by understanding and controlling the mechanical properties of 3D printed hydrogels, tissue engineers can design scaffolds that mimic the mechanical environment of native tissues, thereby enhancing cellular behaviour, tissue regeneration, and integration with the host tissue.

In Chapter 4, cellulose-composited gelatin methacryloyl (G)/sodium alginate (A) bioink formulations were dual-crosslinked into cellulose-composited ionic-covalent entanglement (ICE) gelatin methacryloyl (G)/sodium alginate (A) hydrogels in rubber mould with calcium ions and UV light. The macroscopic and microscopic mechanical properties of microfibrillated cellulose (MFC)-composited, nanofibrillated cellulose (NFC)-composited, and hybrid cellulose-composited ICE G/A hydrogels will be investigated through coaxial macro-compression and micro-indentation. The mechanical enhancement mechanisms behind the hydrogels will be revealed by studying the morphology and pore structure of the hydrogel.

6.2 Methods

6.2.1 Macro coaxial compression

The macro-mechanical properties in compression of swelling-equilibrated hydrogel discs were characterised by Instron microtester 5848 equipped with a 2 kN load cell at room temperature. The constant compression rate was set to 0.6 mm/min. The dimension of each sample disc was measured by digital callipers and entered into the software Bluehill. Engineering stress-strain curves were obtained by Bluehill and Young's modulus was calculated at the initial linear elastic region of the engineering stress-strain curve (from 0 to 10% strain). The yield point was determined with the

0.2% offset method [267, 443]. A line was drawn parallel to the initial linear part of the engineering stress–strain curve, intersecting the "strain" axis at 0.002. The yield point was determined as the intersection of this line to the engineering stress–strain curve. Hydrogel samples were retrieved from PBS solution and excess moisture on the sample surface was gently removed with paper towels. Each sample was tested in triplicate.

6.2.2 Micro-indentation

6.2.2.1 Micro-indentation test setup

The micro-mechanical properties of MFC-composited, NFC-composited, and hybrid cellulose-composited ICE G/A hydrogel discs were carried out by using a NanoTest Vantage instrument (Micro Materials Ltd., Wrexham, UK) at room temperature of 19℃. The core of the instrument is a pendulum that exhibits rotational motion around a frictionless pivot. As shown in Figure 6.1, when an electric current flows through the copper coil mounted at the top end of the pendulum, the coil is attracted to a permanent magnet, causing the indenter to move toward the sample [444]. Built-in software Platform 5 was used to analyse the raw data according to the theory mentioned in Section 3.3.3.

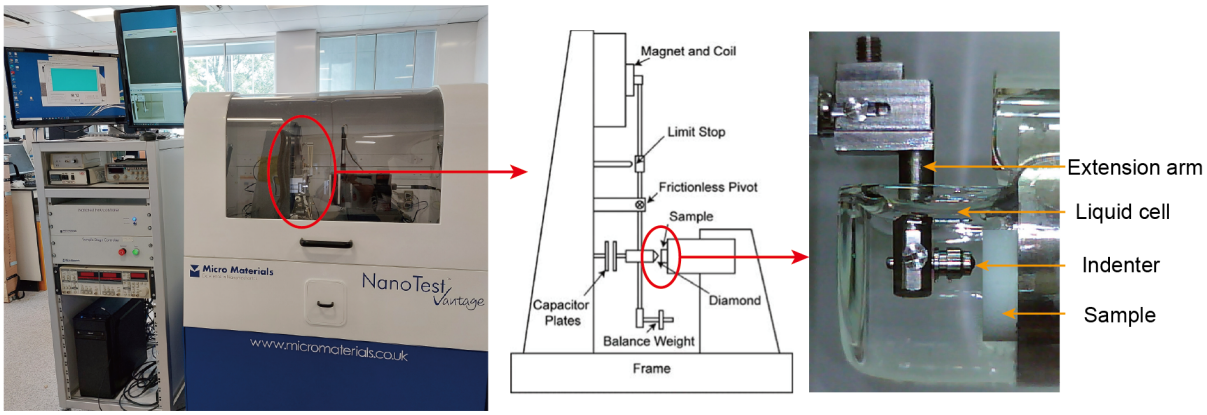

Figure 6.1: NanoTest Vantage instrument used in the study, amplified core pendulum, and instrumental adaptations for liquid environmental testing of hydrogels.

Because indentation was originally developed to evaluate the mechanical properties of hard materials, especially metals, some special considerations and corresponding experimental procedures were taken in this study for highly hydrated soft materials. Firstly, to avoid greater plastic deformation and sample damage caused by stress concentration, a spherical indenter with a large radius of 500 µm and a cone angle of 120° was used to contact the sample surface. The radius of the spherical indenter (R_i) was calibrated to 553 µm by SEM and white light interferometer (Figure 6.2). Secondly, because the hydration state of the hydrogel has a significant effect on the mechanical properties, a liquid cell was attached to the sample stub and the entire test was performed in deionized water. The indenter touched the sample in the liquid cell by attaching an extension arm (Figure 6.1). The hydrogel sample was fixed on the sample stub using Loctite Universal superglue. The testing of each sample was completed within 24 h after the sample reached a state of hydration equilibrium.

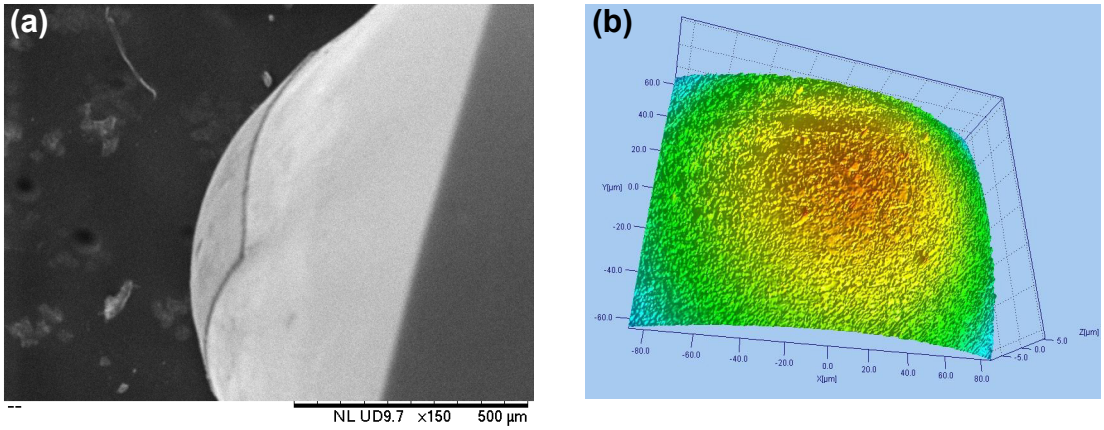

Figure 6.2: Surface morphology of spherical indenter used in this study obtained by (a) SEM and (b) white light interferometry. Image J was then used to measure the radius of the spherical indenter (553 µm).

6.2.2.2 Soft contact protocol

The conventional approach of detecting the surface contact is based on a 10 µN load threshold. The sample's surface is located by gently bringing the indenter into contact with it. NanoTest Vantage

spots the contact point when a load of 10 μN is detected. Once the contact point is found, the indenter and the sample are then moved to a predefined measurement position and the indentation test starts to proceed [380]. However, in situations where the material being tested has a low modulus in the kPa range, the method for finding surface of sample is not suitable. This is because the soft material can undergo significant deformation and penetration by the tip before reaching the 10 μN load threshold, leading to continuous contact between the tip and the surface even at the predefined measurement position. Therefore, a soft contact protocol was applied to find the real surface of hydrogel in this study.

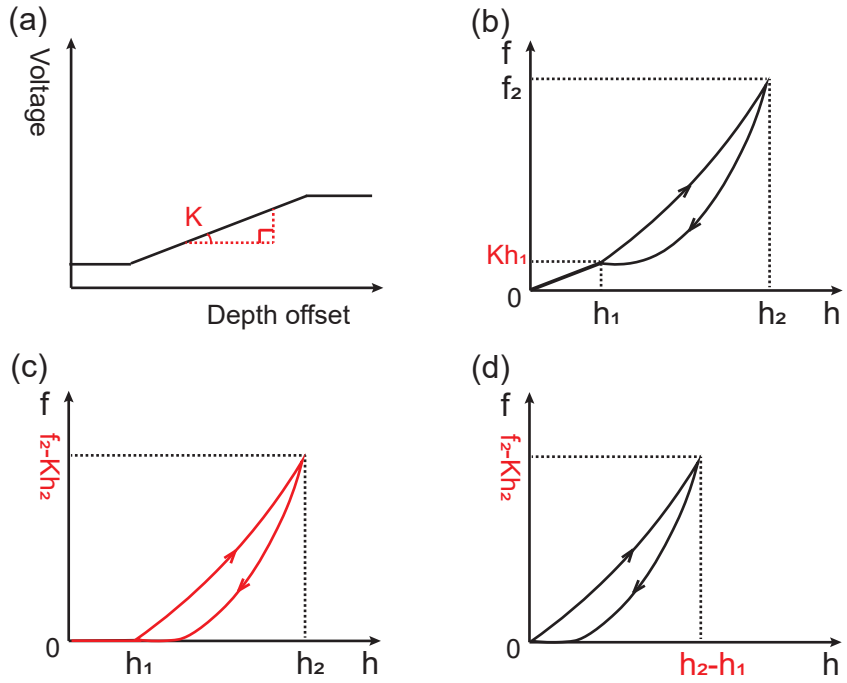

Figure 6.3: Schematic representation of raw data processing in soft contact protocol. (a) The system performs zero load calibration to characterise the flexural stiffness (K, the slope of the line connecting the two parallel lines) of the load head. (b) Real-time raw load-depth curve containing both out-of-contact and contact processes. (c) Load-depth curve after removing the flexural stiffness of the load head from the raw load-depth curve. (d) Real load-depth curve after defining the true contact point as the new zero point.

After the scheduled programme has been triggered, the first step in soft contact protocol is zero load calibration. At this point, the sample is not within the measurable range of the indenter. The

purpose of zero load correction is to characterise the flexural stiffness (K of the load head, which is shown as the slope of the line connecting the two parallel lines in Figure 6.3a. The sample then moves towards the indenter at a user-defined rate, typically 1 µm s^{-1} until contact with the indenter is detected in terms of a defined change in the indenter displacement signal. This process differs from the standard method in that the sensitivity to the contact event is as high as absolutely possible in order to minimise the deformation of the sample as it contacts the indenter. Once the contact even has been detected the indenter is moved away from the sample to the furthest limit of the measurable range. The sample is then moved to the optimal position in the measurable range, the exact movement required to place the sample in this position is determined via some trial tests. Once the sample is in the optimal position, the indentation load ramp commences. The optimal position is that which allows the indenter 5 - 10 µm of uninhibited motion of the indenter until it contacts the sample. This period of uninhibited motion allows the precise point of contact to be identified, thus giving great confidence that the measured indentation depth is true (i.e. zero depth point is truly exactly the point the indenter contacts the sample as opposed to some unknown depth into the sample). As shown in Figure 6.3b, real-time load-depth data is collected right from the moment the indenter begins to approach the sample surface. Due to the extremely small change in contact stiffness when the indenter contacts the sample it is not practically possible to use the conventional surface detection algorithm which is used when working with more 'conventional' engineering material samples, hence the point of contact is manually identified on the completion of data acquisition. It is important to consider that force is required not only to indent the sample but also to move the load head through any given displacement. Therefore, the load applied by instrument's load actuation system is not equal to the load on the sample. Thereby, the load required to move the indenter through the covered displacement range must be deducted. This correction process is achieved automatically using the load head flexural stiffness value determined during the Zero Load Calibration process at the beginning of the test process. So, the load–depth curve now has a flat region, 0 to h_1 in Figure 6.3c. (no load on sample as the indenter is approaching the sample)

followed by the indentation data. The exact contact point h_1 can be easily confirmed based on the start point of the continuous increase in the contact stiffness of the indenter-sample interaction. (Please note, the total measured stiffness is a sum of the flexural stiffness of the instrument load head and the contact stiffness of the indenter-sample interaction.) Finally, by defining h_1 as the new zero point, the true indentation data is shown in Figure 6.3d.

6.2.2.3 Experimental procedure

The indentation experiments were carried out in the load-controlled mode for all cases. Indentation measurements of each sample were conducted at 9 distinct positions of the sample surface. These measurements were performed within an area of 0.04 mm^2, with each measurement point being separated by a distance of 100 µm, forming a 3 x 3 grid pattern on the sample surface. The effects of indentation parameters on the mechanical properties of hydrogels were studied. The loading rate was adjusted from 0.006 to 0.15 mN/s. Creep time was regulated in a range of 0 to 300 s. Unloading rates were set to 0.016, 0.08, and 0.4 mN/s. On the other hand, to compare the moduli and hardness of hydrogel samples with different formulations, as shown in Figure 6.4, the loading rate was set to 0.03 mN/s, the maximum load was 0.5 mN, the dwelling time at maximum load was 300 s, and the unloading rate was 0.08 mN/s.

6.2.3 SEM

The morphology of hydrogel discs was visualised using a Philips XL-30 field emission SEM and a Zeiss EVO 10 SEM. Hydrogel samples were freeze-dried at -56°C for 24 h. To improve the conductivity of hydrogel, samples were gold-coated for 3 min to a thickness of about 20 nm using Emscope SC-650 series sputter coater. Carbon adhesive discs were then used to attach the sample to the SEM specimen stub. Most of the images were captured at an accelerating voltage of 20 KV, beam current of 50 pA, and spot size of 3.

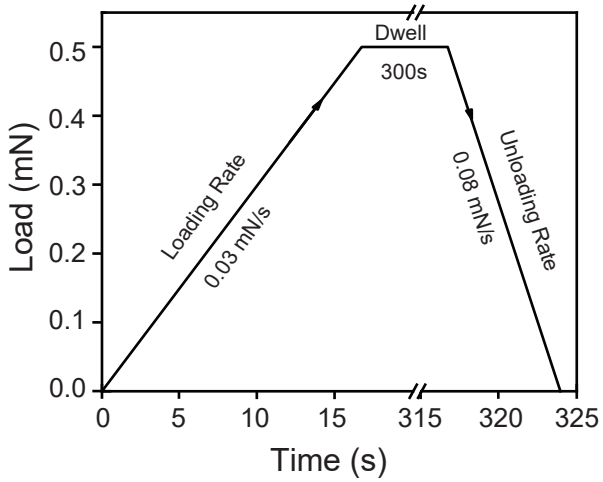

Figure 6.4: Micro-indentation experiment procedure used in this work for comparing the moduli and hardness of hydrogel samples with different formulations.

6.2.4 Micro-CT scan

The pore structure of dried hydrogel discs was scanned via micro-computed tomography (µCT) using SkyScan 1172 (Bruker, Germany). Samples were glued to the sample holder on the sample stage using blue tack. The flat-field correction was updated to eliminate ringing artefacts in the background due to pixel-to-pixel intensity variations. Pixel size was set to 11.2 ± 0.3 µm with medium magnification at middle pixel 2K resolution level. In most cases, the minimum, average, and maximum image intensities were optimised to about 30%, 61.5%, and 87.5% separately by adjusting the x-ray camera exposure time (ms). All images were collected at a rotation step of 0.4° for 360° scan with 4 frame averaging.

After the scan was completed, NRecon (Bruker) was applied to reconstruct these 2D projection images of specimens into cross-section images. Smoothing, misalignment compensation, ring artifacts reduction, and beam-hardening were finely tuned manually through a systematic trial-and-error approach. These cross-section images were organised to 3D images in ImageJ. Region-of-interest in the reconstructed 3D volume was further analysed in CTAn (Bruker) to obtain information on the porosity and pore size distribution of the sample.

6.3 Results and discussion

6.3.1 Compression moduli of hydrogels

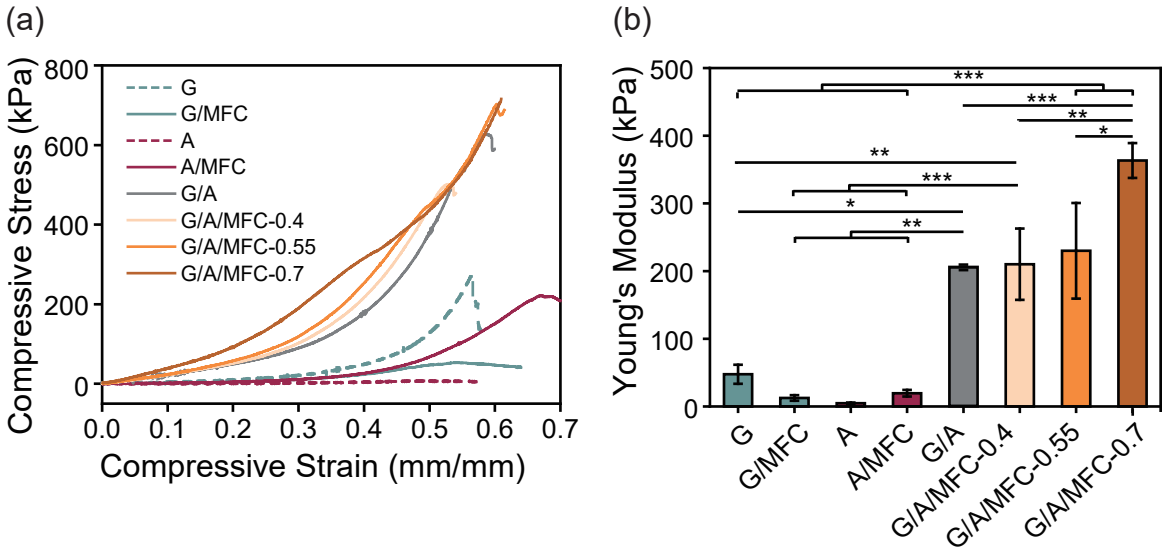

Figure 6.5: (a) Engineering stress-strain curves and (b) Young's moduli of MFC-composited ICE G/A hydrogel samples by macro-compression tests.

Figure 6.5a presents the engineering stress-strain curves of MFC-composited ICE G/A hydrogel discs and the benchmarks under macro-compression, of which sample G and G/A show the same trend: neither samples show a yield point, and the compression strains are all at around 0.58 mm/mm, although the compression strength (616.83 kPa) of G/A is much greater than that of G (259.27 kPa). On the contrary, the engineering stress-strain curve of sample A is almost a straight line, which indicates that the internal structure of G/A hydrogel is not a physical mixing of pure gelatin methacryloyl and sodium alginate. As shown in Figure 4.8, when photocrossliked G/A sample is treated with $CaCl_2$ solution, the α-L-guluronate (G) units of alginate polymer chains form 'egg-box' pattern with Ca^{2+}, which acts as junction points in ionically crosslinked alginate networks [426, 427]. The β-D-mannuronate (M) units of alginate chains move and arrange to entangle with gelatin methacryloyl covalent network, achieving the construction of ICE G/A hydrogel. When a load is applied to G/A, the ionically cross-linked alginate network with brittleness powerfully

dissipates energy by disrupting the physical 'egg-box' structure. The soft covalently crosslinked gelatin methacryloyl network enhances the ductility of the system. When the external force is removed, the 'egg-box' structure of alginate is reversibly restored, thus ensuring the integrity of the whole hydrogel system [45]. Therefore, the synergy of double networks in ICE G/A hydrogel ultimately causes a significant increase in the compression strength of the ICE G/A hydrogel. Likewise, due to the internal synergy of ICE G/A hydrogel, in Figure 6.5b, G/A (211.90 kPa) has a 45-fold higher Young's modulus than A alone (4.80 kPa) (**p-value $\leq$ 0.01) and 4-fold greater Young's modulus than individual G (47.63 kPa) (*p-value $\leq$ 0.05). Although gelation kinetic studies in Section 5.3.2.4 show that both G and A have a shielding effect on the formation of each other's single crosslinked network, when G/A undergoes covalent crosslinking and ionic crosslinking sequentially, synergistic effect from ICE network makes G/A more excellent mechanical strength than sample G or A.

When MFC is mixed with G/A , the enhancement of the G/A sample's Young's modulus by adding 0.4% and 0.55% MFC is not significant in the macroscale (p-value > 0.05 in Figure 6.5b). However, the addition of 0.7% MFC significantly increases macro-Young's modulus of G/A to 363.43 kPa (***p-value $\leq$ 0.001 in Figure 6.5b), implying that there is a concentration threshold for the macro-mechanical enhancement of ICE hydrogels by MFC though MFC has the potential to further enhance toughness and elasticity of ICE hydrogels.

In Figure 6.6a, when different contents of MFC and/or NFC are incorporated into ICE G/A hydrogels, the overall characteristics of these stress-strain curves change. The cellulose-composited ICE hydrogels exhibit yield in the strain region of 0.16 to 0.2 mm/mm beyond their elastic limit, followed by plastic deformation where polymer chains and water molecules realign within the hydrogels. Large deformations occur with relatively small increases in stress. Finally, the hydrogel samples show no compression fracture point but densification when the compressive strain exceeds around 0.45 mm/mm. The macroscopic mechanical results emphasize that MFC and/or NFC incorporated in ICE G/A hydrogels can significantly improve the macroscopic toughness and

compression resistance of the specimen. The results also imply the presence of a more complicated reinforcement mechanism in cellulose-composited ICE G/A hydrogel than in pure ICE G/A hydrogel. Meanwhile, when the volume fraction of MFC in the mixed cellulose slurry increased from 0 to 100%, the yield stress of the hydrogel increased from 41.43 kPa to 54.1 kPa. Therefore, MFC can significantly improve the yield strength of ICE hydrogels compared to NFC, which probably is because large-sized microfibrils establish a stronger fibril network than nanofibrils.

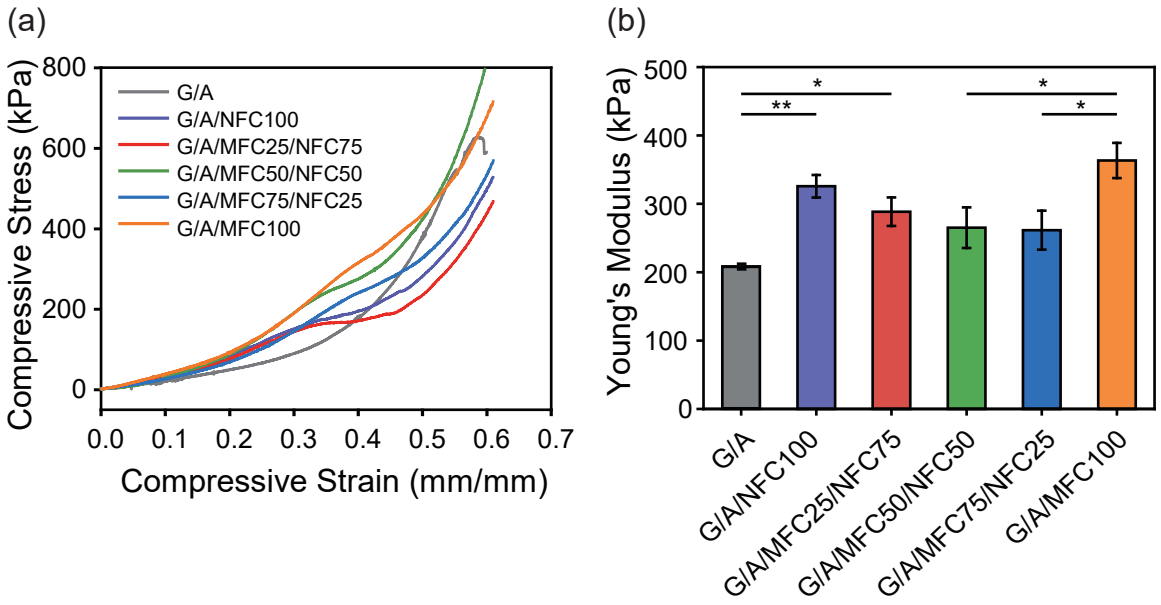

Figure 6.6: (a) Engineering stress-strain curves and (b) Young's moduli of hybrid cellulose-composited ICE G/A hydrogel samples by macro-compression tests.

In addition, when MFC and/or NFC with different contents are incorporated into G/A ICE hydrogels, macroscopic Young's moduli of cellulose-composited ICE hydrogels all increase by varied extent compared to sample G/A (6.6b), indicating that there is a synergistic enhancement between MFC/NFC and the ICE G/A double networks, although the synergy between cellulose and ICE is not as strong as the synergy within ICE itself. Synergistic enhancement between ICE and cellulose can be attributed to the formation of hydrogen bonds between them. Hydrogen bonds ensure that cellulose is not simply physically incorporated into the ICE hydrogel, but cellulose interacts with ICE to build a highly entangled integrated hydrogel network. Furthermore, MFC

or NFC alone could produce ICE hydrogels with slightly greater Young's moduli than mixed MFC/NFC, which implies that the homogeneity of the fibril network can affect the synergistic interaction between cellulose and ICE. A homogeneous NFC or MFC fibril network can generate more hydrogen bonds with G/A than mixed MFC/NFC fibril networks, which contributes to the overall structural integrity of the hydrogel. In particular, when 0.7% MFC is individually added to the ICE hydrogel, the system has the highest Young's modulus (363.43 kPa), which is far superior to Young's modulus (11.22 kPa) of 3% cellulose nanocrystals composited ICE hydrogel containing 5% gelatin methacryloyl and 1% alginate reported previously [445]. In conclusion, either MFC or NFC can act as a reinforcement material in complex polymer networks to improve the macroscopic mechanical properties of hydrogels by forming hydrogen bonding interactions with the hydrogel components. A strong MFC network can produce more excellent reinforcement effects on ICE hydrogel than NFC.

6.3.2 Effects of micro-indentation parameters on the mechanical properties of hydrogels

Prior to the characterisation of the microscale mechanical properties i.e. Young's modulus, hardness, and creep behaviour of hydrogels using micro-indentation technique, the effect of three key indentation parameters on the mechanical properties of hydrogels during testing was investigated to assess the applicability of the method to hydrogels.

6.3.2.1 Loading rate

Firstly, maintaining the same creep time (180 s) and unloading rate (0.08 mN/s), hydrogels were subjected to an indentation test at three different loading rates. Load-depth curves of G/A/NFC100, G/A/MFC50/NFC50, G/A/MFC100 at different loading rates of 0.006, 0.03 and 0.15 mN/s are shown in Figure 6.7a, c, e, separately. Correspondingly, the creep depths of the above three samples

Table 6.1: Creep results of micro-indentation tests for hybrid cellulose-composited ICE hydrogels at different loading rates of 0.006, 0.03 and 0.15 mN/s. F_{max} was held for 180 s. The unloading rate was 0.08 mN/s.

Samples	h_0 (μm)			h_{max} (μm)			Δh (μm)			C (%)		
	0.006	0.03	0.15	0.006	0.03	0.15	0.006	0.03	0.15	0.006	0.03	0.15
G/A/NFC100	15.03	13.69	11.42	17.16	17.00	15.94	2.13	3.31	4.52	14.14	24.18	39.62
G/A/MFC25/NFC75	14.84	12.49	10.46	16.54	15.29	14.83	1.69	2.80	4.37	11.40	22.38	41.81
G/A/MFC50/NFC50	15.86	13.82	11.92	17.77	17.09	16.14	1.91	3.27	4.22	12.08	23.67	35.39
G/A/MFC75/NFC25	16.68	14.80	12.86	19.11	18.45	17.85	2.43	3.66	4.99	14.58	24.72	38.81
G/A/MFC100	16.98	14.24	11.30	19.57	18.21	17.04	2.58	3.97	5.74	15.22	27.86	50.82

as a function of time are represented in Figure 6.7b, d, f. Table 6.1 summarises the creep results of micro-indentation at different loading rates of 0.006, 0.03 and 0.15 mN/s. Despite the different ratios of MFC and NFC content in G/A, all cellulose-composited hydrogels reveal almost the same phenomenon.

During the loading stage, the slower the loading rate, the greater the initial depth (h_0), the poorer the hydrogel's penetration resistance, and the softer the hydrogel behaves. This highlights that the time-dependent deformation of the hydrogel results in the mechanical properties of the hydrogel being affected by the time scale of the measurement. When the hydrogel is subjected to time-dependent load, it exhibits both an instantaneous elastic response and a slow time-dependent viscous response [446]. Slow loading rates allow the polymer chains in the hydrogel to rearrange over time and viscous deformation to increase. Whereas a fast loading rate is detrimental to the viscous flow of the polymer chains, thus the overall resistance to deformation of the hydrogel increases and the material behaves stiffly.

Upon entering the load-holding stage of 180 s, compared with the rapidly loaded hydrogel, depth variation (Δh) and creep rate (C) of the slowly loaded hydrogel is lower and the material exhibits higher creep resistance, which is because the hydrogel has already dissipated some energy through viscous deformation during the slow loading stage. Therefore, the initial fast creep is not obvious and the steady-state creep dominates. Finally, the deformation and recovery of the polymer chains are in equilibrium. However, due to the local stress concentration in rapidly loaded hydrogels,

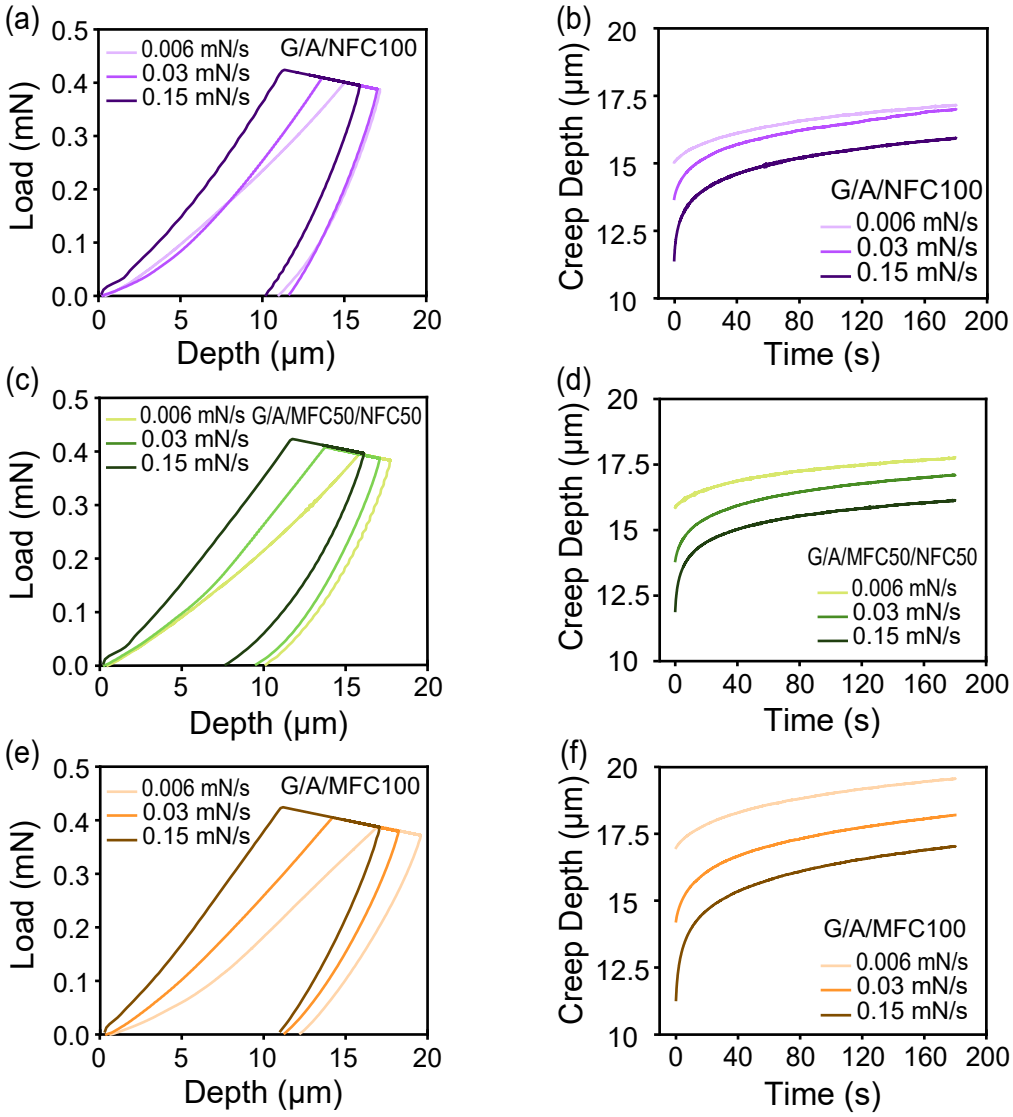

Figure 6.7: Load-depth curves of samples (a) G/A/NFC100, (c) G/A/MFC50/NFC50, (e) G/A/MFC100 at different loading rates of 0.006, 0.03 and 0.15 mN/s. Maximum load (F_{max}) was held for 180 s for creep. The unloading rate was 0.08 mN/s. The changes of creep depth from initial depth (h_0) to maximum depth (h_{max}) within 180 s for (b) G/A/NFC100, (d) G/A/MFC50/NFC50, (f) G/A/MFC100. Time scale of the measurement affects the mechanical properties of samples due to the time-dependent deformation of the hydrogel. Compared to fast loading rate of 0.15 mN/s, slow loading rate of 0.006 mN/s yields a greater indentation depth, leading to a softer sample. The loading rate can also affect the creep results of samples to some extent, which is manifested by the slow loading rate weakening the initial fast creep of the sample.

the initial fast creep becomes significant and the polymer chain shows a transient elastic response through stretching and reorientation, and then gradually enters the steady-state creep. In conclusion, the stiffness and creep resistance of hydrogels are closely related to the time scale of testing.

6.3.2.2 Creep time at maximum load and unloading rate

According to the "Oliver and Pharr" method, the slope of the initial unloading curve is a significant factor for the calculation of reduced modulus (E_r) of the material [447]. The effect of the unloading rate on E_r of hydrogel G/A/NFC100 (purple in Figure 6.8) and G/A/MFC100 (orange in Figure 6.8) after different creep times was studied. During the measurement, the loading rate was always kept at 0.03 mN/s. Maximum load of 0.5 mN starts to unload after being held at 0 s (Figure 6.8a, d) and 180 s (Figure 6.8b, e). The unloading rates are set to 0.016, 0.08, and 0.4 mN/s in sequence. Taking G/A/NFC100 as an example, as shown in Figure 6.8a, when F_{max} is directly unloaded, the unloading rate significantly affects the trend of the unloading curve. When the unloading rate is 0.016 mN/s, the unloading curve exhibits 'nose effect', i.e. an increase in depth in the early stages of unloading. The reason for the nose effect can be attributed to the ongoing time dependent deformation of the hydrogel samples under load. The key to reliable modulus testing is that the initial part of the unloading curve is as purely elastic as possible. However, with materials such as hydrogels, this is practically challenging to achieve as the ongoing rates of plastic deformation can be sufficiently high. Therefore, depending on the severity of 'nose effect', the implications on measurement results range from over-estimation contact stiffness and thus elastic modulus. However, when the unloading rate increases to 0.08 mN/s, the "nose" disappears. After the unloading rate rises to 0.4 mN/s, the unloading curve shows another phenomenon at the initial stage. The load decreases sharply and the depth remains unchanged. This problem also leads to measurement error of E_r. It may be helpful for this problem to use a higher data acquisition rate.

When the hydrogel is allowed to creep for 180 s at F_{max} (Figure 6.8b), the effect of unloading rate on reduced modulus changes. When the unloading rates are 0.016 and 0.08 mN/s, respectively, the

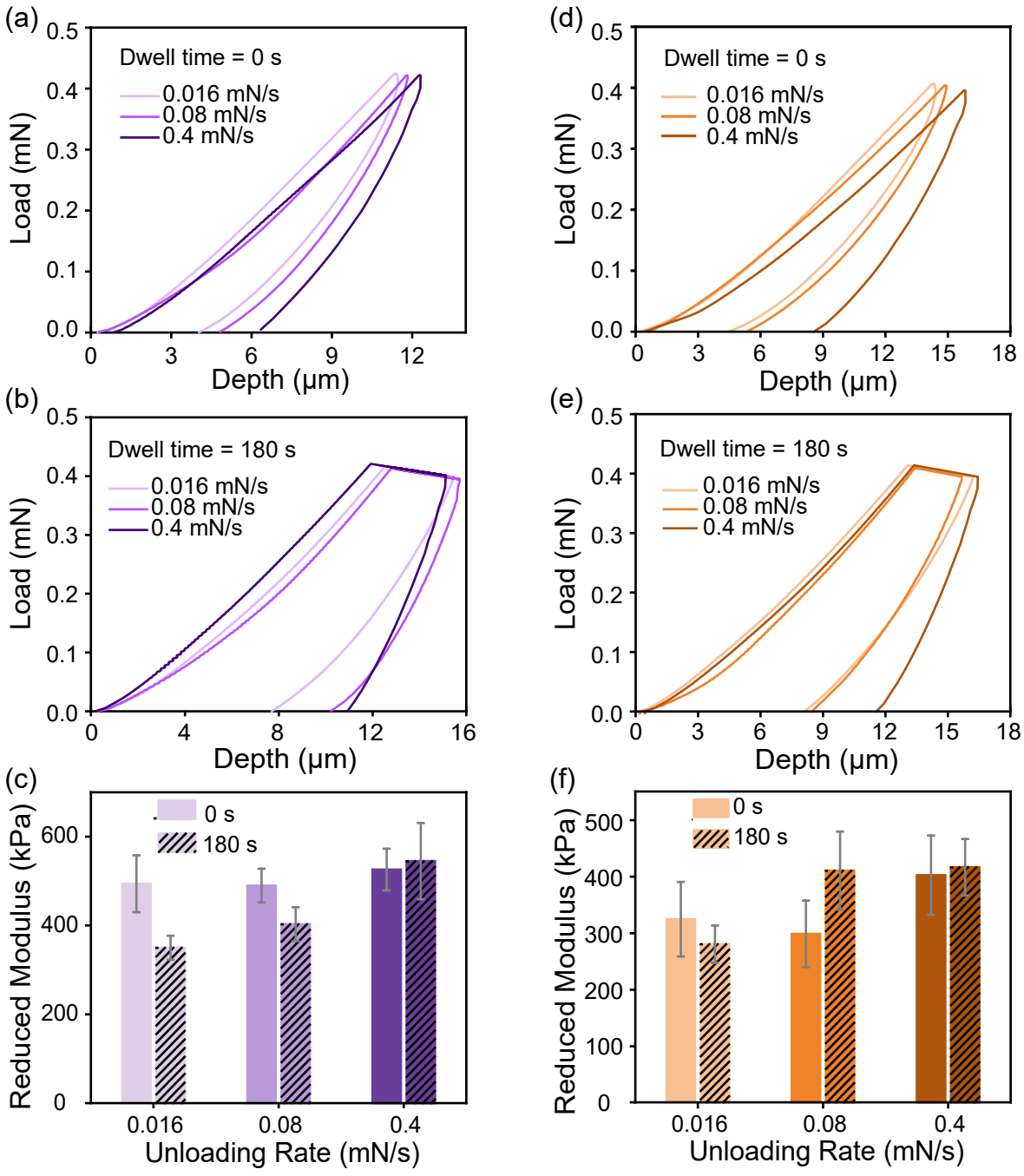

Figure 6.8: Purple and orange figures are represented sample G/A/NFC100 and G/A/MFC100, respectively. (a)(d) Load-depth curves without dwell time at the F_{max}. When there is not enough time for the hydrogel to creep, slow unloading rate of 0.016 mN/s causes a slight increase of depth at the beginning of unloading, thus resulting in abnormally high modulus for soft materials. (b)(e) Load-depth curves for dwelling time of 180 s at the F_{max}. When unloading occurs after the hydrogel is in steady-state creep, reduced modulus (E_r) of the hydrogels increases with the rise of unloading rates. (c)(f) Comparison of $E_r$of hydrogels at different unloading rates and different creep times.

unloading curves are normal. Also, the higher the unloading rate, the steeper the unloading curve and the higher the reduced modulus (Figure 6.8c). However, when the unloading rate increases to 0.4 mN/s, the sudden reduction of load in the very early stage of unloading still exists, which suggests that in the indentation experiment, unloading should be introduced after the hydrogel is in steady-state creep and the unloading rate should be significantly faster than the loading rate. This protocol ensures that the unloading process is completely dominated by the elastic response, thereby improving the accuracy of the experiment. Measurements obtained from the sample G/A/MFC100 demonstrate a high degree of congruence with those derived from the G/A/NFC100, reinforcing the reliability of the observed outcomes.

6.3.3 Micro-mechanical properties of cellulose-composited ICE hydrogels

6.3.3.1 Effect of MFC concentration on micro-mechanical properties of MFC-composited ICE hydrogels

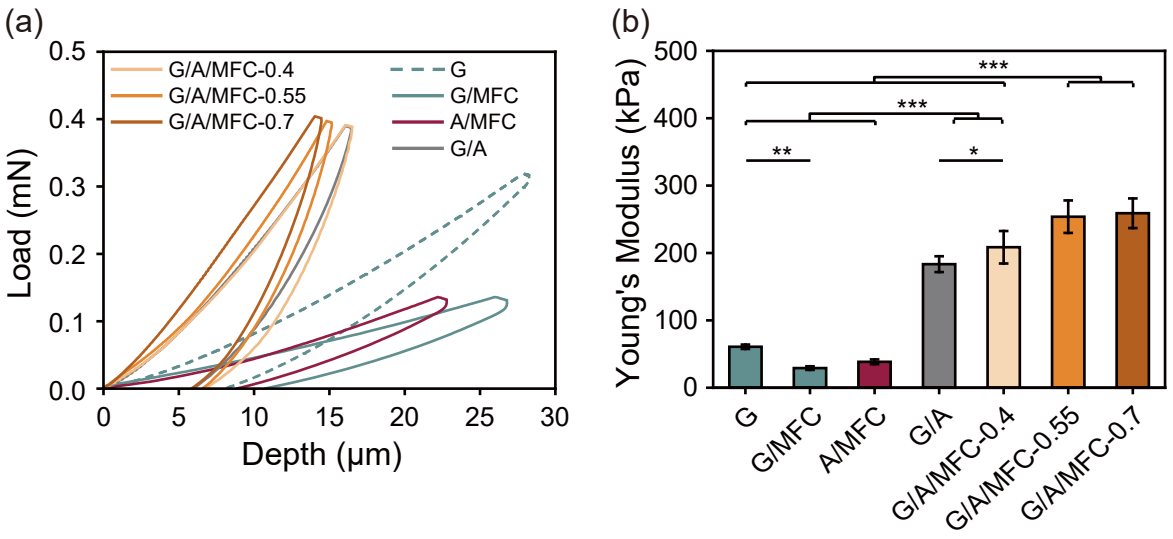

Figure 6.9: (a) Load-depth curves and (b) microscopic averaged Young's moduli of MFC-composited ICE hydrogels in a localised area by micro-indentation. Loading and unloading rates were 0.03 and 0.08 mm/s. Maximum load of 0.5 mN was dwelled for 1 s before unloading.

By performing microindentations at multiple locations on the hydrogel surface, it is possible to

evaluate the distribution of the mechanical strength of the hydrogel from a microscopic perspective and analyze the effect of cellulose on the mechanical properties of ICE hydrogels. Figure 6.9a depicts load-depth curves of MFC-composited ICE G/A hydrogels obtained by microindentation. (It is worth noting that the load-depth curve of sample A is not shown in this figure. As sample A is too soft to define the true contact point from the curve of A. The indentation experiment fails for sample A.) The single network hydrogels containing MFC or not, such as G, G/MFC, and A/MFC, exhibit a more pronounced 'nose effect' at the initial unloading stage due to strong time-dependent deformation behaviour compared to the sample G/A. Also, maximum depth (h_{max}) of single network hydrogels (28.25 μm for G) is significantly deeper than that of ICE double network hydrogels (16.51 μm for G/A), which illustrates the effectiveness of the ICE enhancement strategy in enhancing the anti-deformation ability of hydrogels. Additionally, 0.7% MFC decreases h_{max} of G/A to 14.42 μm, proving the further strengthening effect of MFC on ICE hydrogel.

By analysing the unloading part of the load-depth curve, the microscopic averaged Young's moduli of samples in a localised area are presented in Figure 6.9b, where the results are in the same order of magnitude as Young's modulus measured by the macroscopic overall compression method (Figure 6.5b) and thus the effectiveness of microindentation for testing the mechanical properties of soft materials is demonstrated. Moreover, the enhancement effects of the internally synergistic ICE network on modulus (183.82 kPa for G/A) and the further collaborative enhancement between MFC and ICE (260.18 kPa for G/A/MFC-0.7) are also clearly demonstrated in the microscale. However, the MFC concentration threshold for enhancement ICE in the microscale is not notably evident. As the MFC content increases from 0.4% to 0.7%, there is a corresponding decrease in the h_{max} and an increase in the micro-indentation Young's modulus of the samples.

Microscopic variations of Young's modulus in a localised area for hydrogels with different concentrations of MFC are visualised in Figure 6.10. ICE hydrogel (G/A) has a broader Young's modulus distribution (167.25 to 194.25 kPa) than single covalent network hydrogels G (55.5 to 64.5 kPa). Furthermore, the Young's modulus distribution of G/A/MFC-0.7 (232.7 to 276 kPa) is wider

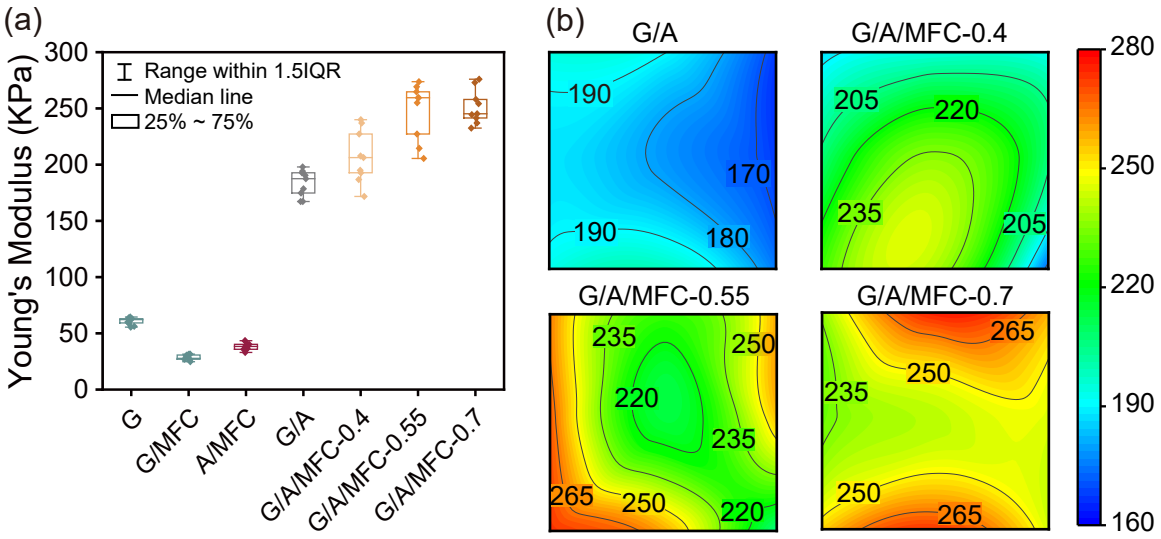

Figure 6.10: Young's modulus distribution variation of MFC-composited ICE hydrogels in a localised area visualized by (a) boxplot and (b) contour plot within an area of 200 × 200 μm^2. Loading and unloading rates were 0.03 and 0.08 mm/s. Maximum load of 0.5 mN was dwelled for 1 s before unloading.

than that of G/A. It illustrates that the different synergies between components in a multi-component hydrogel lead to differences in the local Young's modulus of the material. The microscopic local modulus gap is conducive to the formation of an effective energy dissipation mechanism in the hydrogel, thereby enhancing both the microscopic averaged Young's modulus and macroscopic overall modulus of the material. The microscopic difference in localised Young's modulus of G/A can be attributed to the difference in mechanical properties of the two heterogeneous networks in ICE. Energy is dissipated through the reversible breaking of ionic bonds in the mechanically weak alginate network.

In addition, the differences in the microscopic Young's moduli within MFC-composited ICE G/A hydrogels can be explained by examining three types of reinforcement. Firstly, the cellulose fibril network can distribute energy uniformly across the hydrogel. Secondly, synergistic ICE network dissipate energy by the cleavage of ionic bonds. Lastly, the interaction between MFC and G/A, primarily through hydrogen bonds, also contributes to energy dissipation. Each of these reinforcements has a unique way of influencing the hydrogel's mechanical properties, leading to the

observed variations in localised Young's moduli. On the other hand, the increase of MFC contents in the system can reinforce the strength of cellulose fibril network and interactions between MFC and ICE. Therefore, the microscopic averaged Young's moduli of MFC-composited ICE hydrogels rise with the increasing MFC content. The above results also indirectly reflect that micro-indentation is able to identify various synergies by touching different areas of the sample on a micro-scale.

6.3.3.2 Effects of cellulose fibril size on micro-mechanical properties of cellulose-composited ICE hydrogels

The microscale Young's moduli calculated from the representative load-depth curves of hybrid cellulose-composited ICE hydrogels are shown in Figure 6.11. Table 6.2 lists the data and results of microindentation tests for samples G/A, G/A/NFC100, G/A/MFC25/NFC75, G/A/MFC50/NFC50, G/A/MFC75/NFC25, and G/A/MFC100.

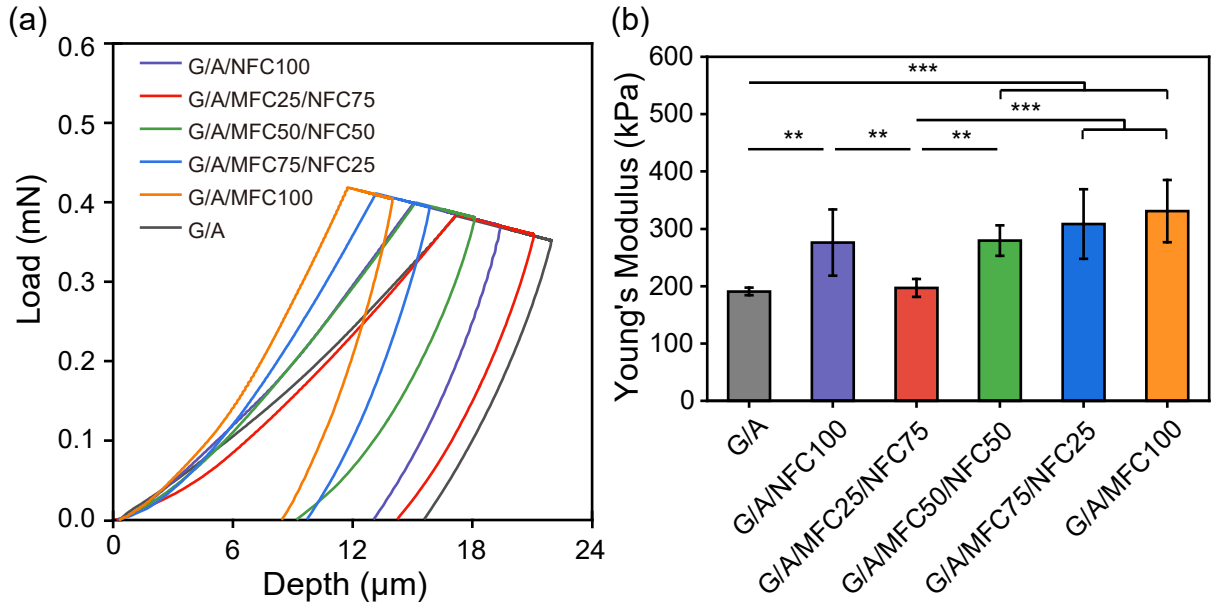

Figure 6.11: (a) Load-depth curves and (b) Young's moduli of hybrid cellulose-composited ICE hydrogels by micro-indentation. Loading and unloading rates were 0.03 and 0.08 mm/s. A maximum load of 0.5 mN was dwelled for 300 s before unloading.

It can be seen that G/A has the highest initial depth (h_0) of 17.26 μm. After holding F_{max} for

Table 6.2: Data and results of indentation tests for hybrid cellulose-composited ICE hydrogels. The loading rate and unloading rate were 0.03 and 0.08 mN/s. The maximum load was held for 300 s.

Experimental Data		**G/A**	**G/A/NFC100**	**G/A/MFC25/NFC75**	**G/A/MFC50/NFC50**	**G/A/MFC75/NFC25**	**G/A/MFC100**
Initial depth	h_0 (μm)	17.26	15.09	17.26	15.20	13.21	11.82
Creep displacement	Δh (μm)	4.3	3.97	3.81	2.97	2.63	2.17
Maximum indentation depth	h_{max} (μm)	21.54	19.06	21.07	18.17	15.84	13.99
Maximum load	F_{max} (mN)	0.36	0.37	0.36	0.41	0.42	0.40
Elastic displacement	h_e (μm)	7.64	5.9	8.88	6.42	6.22	5.58
Residual impression of depth	h_r (μm)	13.92	13.16	12.19	11.75	9.62	8.41
Contact depth	h_c (μm)	17.74	16.11	16.63	14.96	13.88	13.36
Contact stiffness	S ($\times 10^{-2}$ mN/μm)	7.07	9.47	7.13	9.59	10.2	10.82
Experimental Results							
Contact area	Ac ($\times 10^4$ μm^2)	6.16	5.59	5.78	5.2	4.82	4.64
Indentation hardness	H_1 (kPa)	5.86	6.91	4.72	9.3	8.86	7.74
Reduced Modulus	E_r (kPa)	254.33	368.11	262.78	372.67	411.33	441.33
Young's Modulus	E_s (kPa)	190.75	276.08	197.08	279.5	308.5	331
Creep rate	C (%)	24.91	26.31	22.07	19.54	19.91	18.36

300 s, G/A exhibits the largest creep displacement (Δh of 4.3 μm). Without a doubt, maximum depth (h_{max}) (21.56 μm) is also the largest among the 6 samples. After unloading, the surface of G/A leaves the deepest residual impression (h_r of 13.92 μm), indicating the most significant time-dependent deformation among all specimens. When pure NFC is added to G/A, the values of h_0 (15.09 μm), Δh (3.97 μm), h_{max} (19.06 μm), and h_r (13.16 μm) all decrease compared with G/A. With the increase of MFC from 25% to 100% in the mixed cellulose slurry, h_0, Δh, h_{max}, and h_r of G/A/MFC/NFC all show a decreasing trend. Therefore, G/A/MFC100 has the lowest h_0 (11.82 μm), Δh (2.17 μm), h_{max} (13.99 μm), and h_r (8.41 μm) among cellulose-composited ICE G/A hydrogels when MFC with 100% volume fraction is incorporated into G/A. Consistent with the results obtained from macroscopic compression (Figure 6.6a), all the above indicate that incorporating cellulose improves the microscopic deformation resistance of G/A hydrogel. Compared with NFC, hydrogen bonds between higher-strength MFC network and ICE reduce the time-dependent deformation of cellulose-composited ICE hydrogels, further resulting in a stiffer cellulose-composited ICE hydrogel.

Figure 6.11b presents microscopic averaged Young's moduli of hydrogels obtained by micro-indentation. G/A (190.75 kPa) has a very similar Young's modulus to G/A/MFC25/NFC75 (197.08 kPa). With an increased content of MFC in the mixed cellulose slurry, microscopic averaged Young's moduli of hybrid cellulose-composited ICE hydrogels gradually increase (Figure 6.11b,

Table 6.2). The results illustrate that compared with NFC, hydrogen bonds between a higher-strength MFC network and ICE increase the elasticities of cellulose-composited ICE hydrogels, which is achieved by the reversible breaking and reforming of hydrogen bonds to effectively dissipate and store energy.

In addition, micro-indentation also provided microscopic Young's modulus distributions of the hydrogels in an area of 0.04 mm^2, which are visualised in the forms of boxing plots (Figure 6.12a) and contour plots (Figure 6.12b). It can be seen that Young's modulus of G/A is concentrated in the vicinity of 190 kPa and the range within 1.5IQR (Interquartile range) is very narrow. After cellulose incorporation, regardless of pure MFC, NFC, and hybrid cellulose, the ranges within 1.5IQR of all hydrogel samples become significantly broader than that of pure G/A hydrogel. For example, Young's modulus of G/A/NFC100 is distributed in the range of 230 to 350 kPa, and G/A/MFC100 ranges from 270 to 400 kPa. For three different reinforcement types (cellulose fibril network, synergistic ICE network, and hydrogen bond interactions between MFC and ICE) in cellulose-composited ICE hydrogels revealed by Figure 6.10, cellulose fibril size can affect both cellulose fibril network and hydrogen bond interactions between MFC and ICE. Thereby, MFC displays more excellent reinforcement effects in cellulose-composited ICE hydrogels than NFC.

Indentation experiments also recorded indentation hardness (H_I) of hybrid cellulose-composited ICE hydrogels in the area of 0.04 mm^2. Figure 6.13a shows the average H_I of samples, while Figure 6.13b displays the microscopic distribution of H_I at different tested locations. In comparison to G/A (5.86 ± 0.41 kPa), the hardness distributions of G/A/NFC100 and G/A/MFC100 are particularly broad although H_I of G/A/NFC100 (6.91 ± 1.67 kPa) and G/A/MFC100 (7.74 ± 2.31 kPa) just increased by 1.05 kPa and 1.88 kPa. G/A only has a range within 1.5IQR of 5.26 to 6.30 kPa. Whereas G/A/NFC100 and G/A/MFC100 have a range within 1.5IQR of 4.84 to 10.08 kPa and 4.79 to 10.86 kPa, respectively. Remarkably, the microscopic hardness distributions of samples G/A/MFC25/NFC75 and G/A/MFC75/NFC25 are the most concentrated and dispersed among all samples, respectively. In terms of three different reinforcement types (cellulose fibril network,

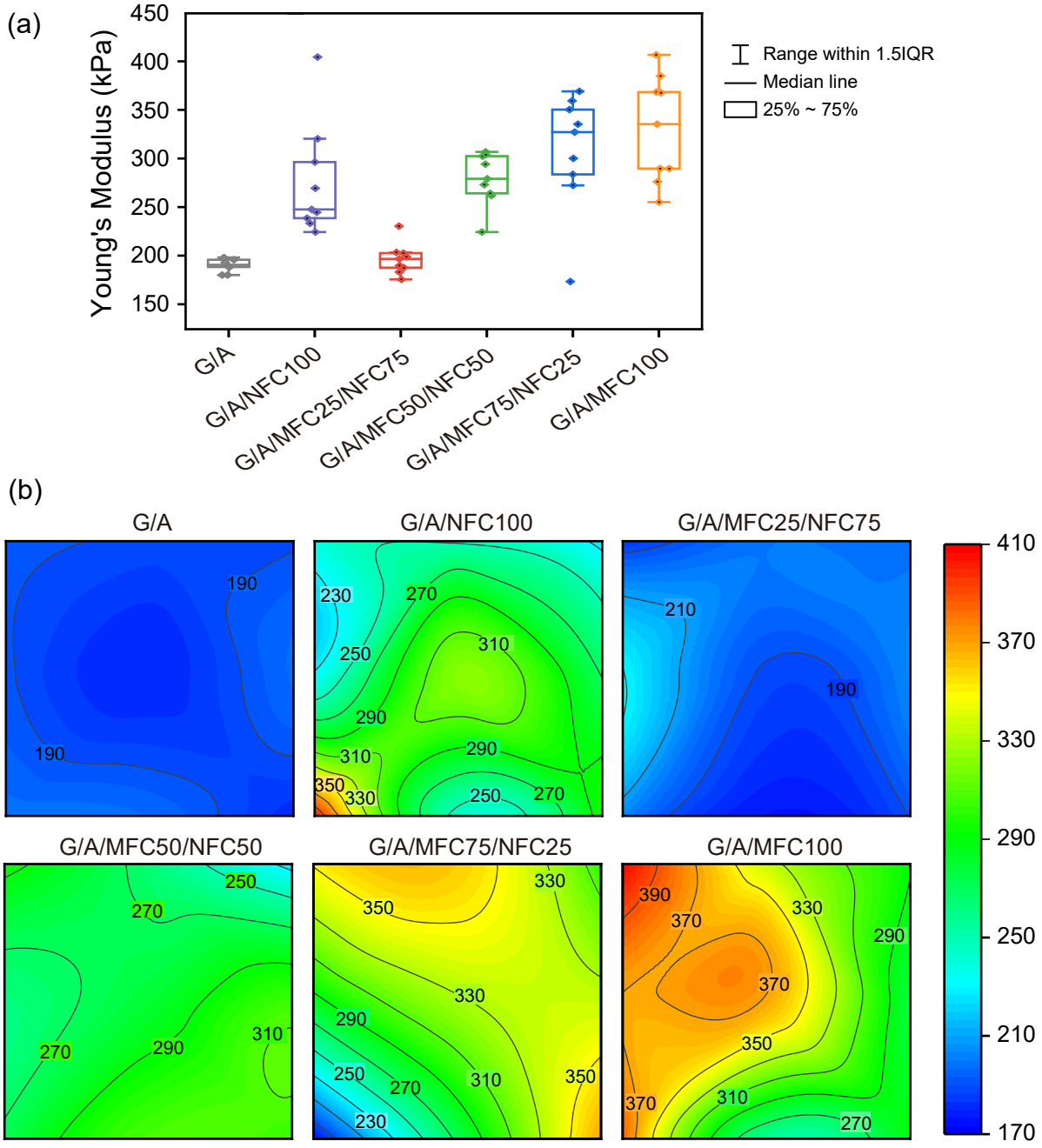

Figure 6.12: The Young's modulus distribution variation of hybrid cellulose-composited ICE hydrogels visualized by (a) boxplot and (b) contour plot. The scale of the tested area in contour plot is 200 × 200 μm^2. Loading and unloading rates were 0.03 and 0.08 mm/s. Maximum load of 0.5 mN was dwelled for 300 s before unloading.

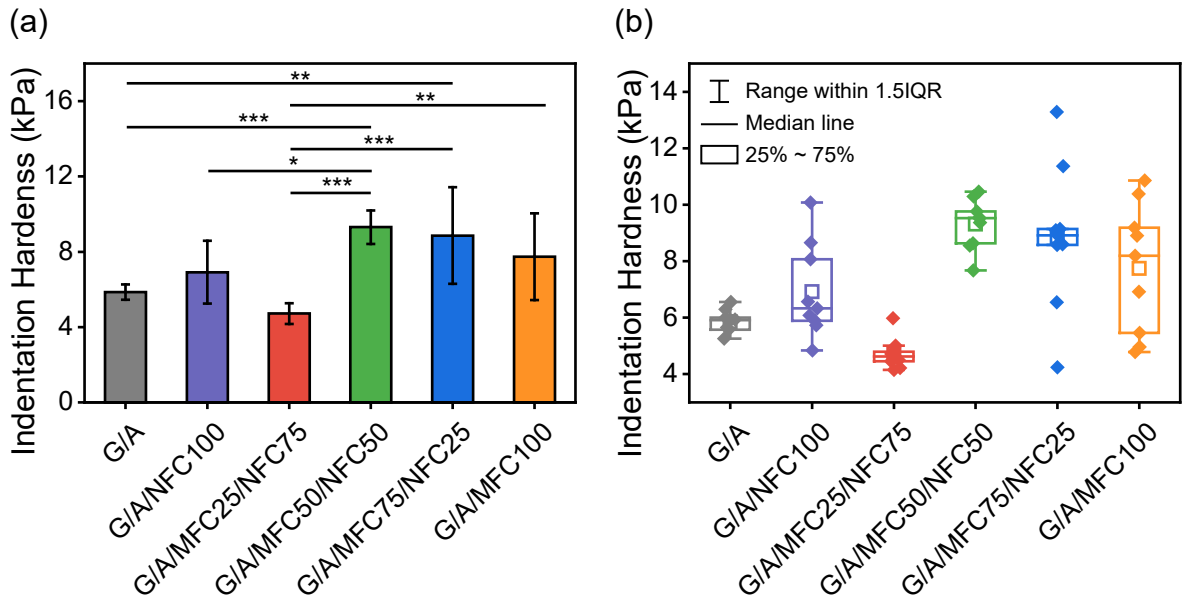

Figure 6.13: (a) Microscopic averaged indentation hardness and (b) microscopic hardness distribution of hybrid cellulose-composited ICE hydrogels. Loading and unloading rates were 0.03 and 0.08 mm/s. Maximum load of 0.5 mN was dwelled for 300 s before unloading.

synergistic ICE network, and hydrogen bond interactions between MFC and ICE) in cellulose-composited ICE hydrogels, if the hardness at a certain point in the cellulose-composited ICE hydrogel is lower than the microscopic hardness of the pure ICE G/A hydrogel, this test point is inferred to be located in an area of cellulose fibre networks. Yet if the hardness at a certain point in the cellulose composite ICE hydrogel is higher than the microscopic hardness of the pure ICE G/A hydrogel, this point may be characterised by the synergistic interaction between ICE and fibre networks. Therefore, it is inferred that the test areas of G/A/MFC25/NFC75 may all be located in the mixed cellulose fibre network, while the test locations of G/A/MFC75/NFC25 involve the above three different reinforcement areas. In conclusion, when MFC or NFC is incorporated into ICE hydrogels, differences in the local micromechanical properties of hydrogel samples reflect the presence of three different reinforcement types. Moreover, hydrogen bond interactions between MFC and ICE play a dominant role in enhancing the overall macroscopic mechanical strength of the cellulose-composited ICE hydrogel. This finding is consistent with the results previously

published by Chalmers University of Technology [448], of which the high reinforcing effect of CNC in nanocomposite CNC/poly(ethylene-stat-sodium acrylate) and stress transfer within the nanocomposite primarily occurs through strong interactions between the cellulose and the polymer, with cellulose/cellulose interactions playing a relatively minor role [448].

In terms of the methods used to study the multi-scale mechanical properties of cellulose-composited G/A ICE hydrogels, compared to macro-compression, indentation demonstrates its potential as a powerful analytical tool for evaluating the modulus distribution of multi-component hybrid systems from micro-scale with mapping capability. The modulus distribution can directly reflect the distribution of various mechanical reinforcement types present in the hybrid hydrogel system, thus further obtaining information about the distribution of each component in the multi-component hydrogel. In the case of hybrid cellulose- composited ICE hydrogels, micro-indentation can map the distribution of G/A dual networks and mixed MFC/NFC clusters.

6.3.4 Creep behaviour of cellulose-composited ICE hydrogels

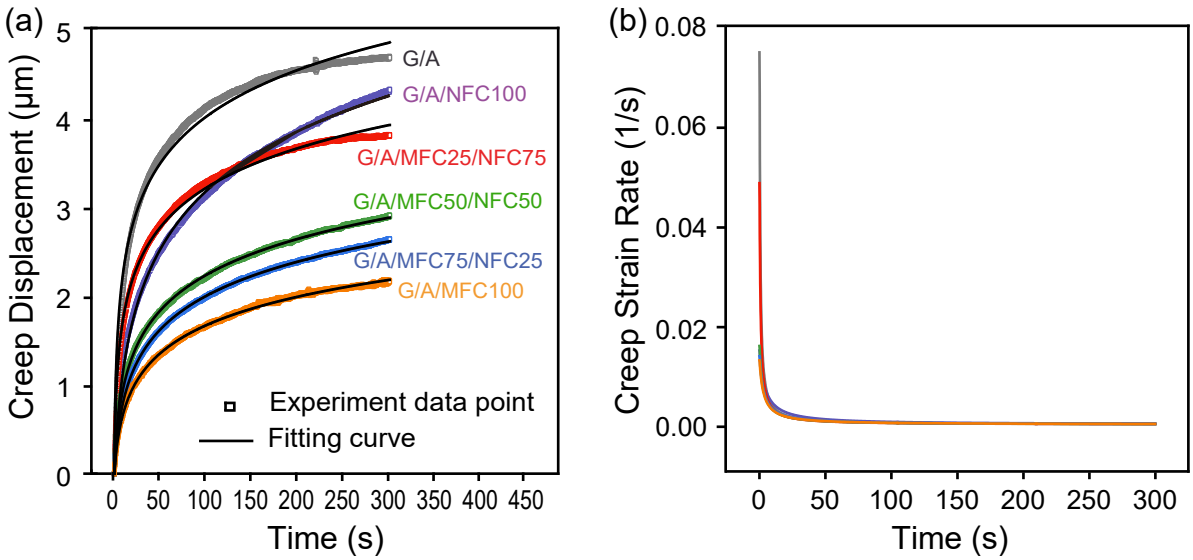

Figure 6.14: (a) Creep displacement of hybrid cellulose-composited ICE hydrogels as a function of time and fitting curves. (b) Representative curves of creep strain rate with time for hybrid cellulose-composited ICE hydrogels.

Table 6.3: Creep fitting equations of hybrid cellulose-composited ICE hydrogels.

Sample	Creep fitting curve	A (μm)	h_0 (μm)	A/h_0
G/A	$\Delta h(t) = 0.76 \cdot ln(1.93 \cdot t + 1)$	0.76	17.26	0.044
G/A/NFC100	$\Delta h(t) = 1.01 \cdot ln(0.23 \cdot t + 1)$	1.01	15.1	0.067
G/A/MFC25/NFC75	$\Delta h(t) = 0.65 \cdot ln(1.43 \cdot t + 1)$	0.65	17.26	0.038
G/A/MFC50/NFC50	$\Delta h(t) = 0.6 \cdot ln(0.41 \cdot t + 1)$	0.6	15.2	0.039
G/A/MFC75/NFC25	$\Delta h(t) = 0.57 \cdot ln(0.32 \cdot t + 1)$	0.57	13.2	0.043
G/A/MFC100	$\Delta h(t) = 0.47 \cdot ln(0.33 \cdot t + 1)$	0.47	11.82	0.04

The creep behaviour of soft materials is a time-dependent deformation characteristic. In the indentation experiment, maximum load (F_{max}) was maintained at initial depth (h_0) position for 300 s and the displacement change of the indenter with time was recorded and fitted by Eq.3.5, as shown in Figure 6.14a. The differences in creep rate of the samples can be found in Table 6.2. The fitting curves and creep strain rate sensitivity (A/h_0) are listed in Table 6.3. By deriving the fitted curves, the creep strain rates as a function of creep time are shown in Figure 6.14b.

The creep displacement (Δh of 4.3 μm) of G/A with time is the largest among all samples and the creep rate is 24.91%. Creep displacements all decrease after MFC/NFC slurry incorporation, which confirms the synergistic effect of cellulose and ICE hydrogel again and the creep resistance of cellulose. However, the creep rate of G/A/NFC100 (26.31%) increases slightly and A/h_0 of G/A/NFC100 (0.067) is the highest among samples. However, with the increase of MFC in the mixed slurries, creep rates begin to decrease gradually. The final creep rate of G/A/MFC100 is only 18.32%. Also, A/h_0 of all MFC-containing ICE hydrogels had little difference and were all lower than G/A (0.044) and G/A/NFC100 (0.067). It interprets that the difference in the size of MFC (width of 1 to 3 μm) and NFC (width of 20 to 100 nm) causes the difference in creep resistance behaviour of hybrid hydrogels. Compared with MFC, under constant F_{max}, NFC with low molecular chain rigidity is more likely to change the spatial micro-conformation in the system, and the hydrogel entanglement network can be adjusted easily. High chain rigidity of MFC promotes the excellent creep resistance of G/A/MFC100. In other words, the confinement effect of MFC network is better

than that of NFC network. When subjected to external indentation force, MFC acts as a site that effectively blocks the movement of the ICE networks [449–451]. In Figure 6.14b, the creep strain rates of all samples exhibit extremely similar trends. Creep strain rates decrease rapidly during the first 10 s and levelled off after about 50 s, revealing that hydrogel has the most obvious diffusional creep in the first 10 seconds, and then gradually transforms into steady-state creep.

6.3.5 Mechanical enhancement mechanism of hydrogels

In the analysis of macro- and micro-scale mechanical properties for cellulose-composited ICE G/A hydrogels, it was found that three types of reinforcement effect (cellulose fibril network, synergistic ICE network, hydrogen bond interactions between MFC and ICE) contribute to mechanical properties of the hydrogel. In this section, the author attempts to reveal the mechanical enhancement mechanism of the above reinforcement effects by examining the micromorphology and pore structure of hydrogels.

Figure 6.15 and Figure 6.16 are SEM images of MFC-composited and NFC-composited ICE hydrogels and their benchmarks. Figure 6.17 and Figure 6.18 are cross-sectional images and 3D views of reconnected samples by μCT, respectively. Figure 6.19 and Table 6.4 provide the overall pore size distribution curve and porosity of each sample after reconstruction, respectively.

SEM and μCT images show that all samples have interconnected porous structures, as described in previous reports [452, 453]. Sample G and A hydrogels have a single crosslinked network with porosities of 79.31% and 72.31% respectively. Also, most of their pore sizes are around 100 microns. However, the synergy of covalently crosslinked network and ionically crosslinked network reduces the porosity of G/A to 64.24%. The pore size distribution width of G/A does not change much, but a new peak appears in the pore size distribution curve of G/A between 25 and 50 μm. Therefore, the reason why the synergy of the dual network within the ICE improves the mechanical strengthening of the hydrogel is the reduced porosity and pore size from 100 microns to a range of 25 to 50 microns.

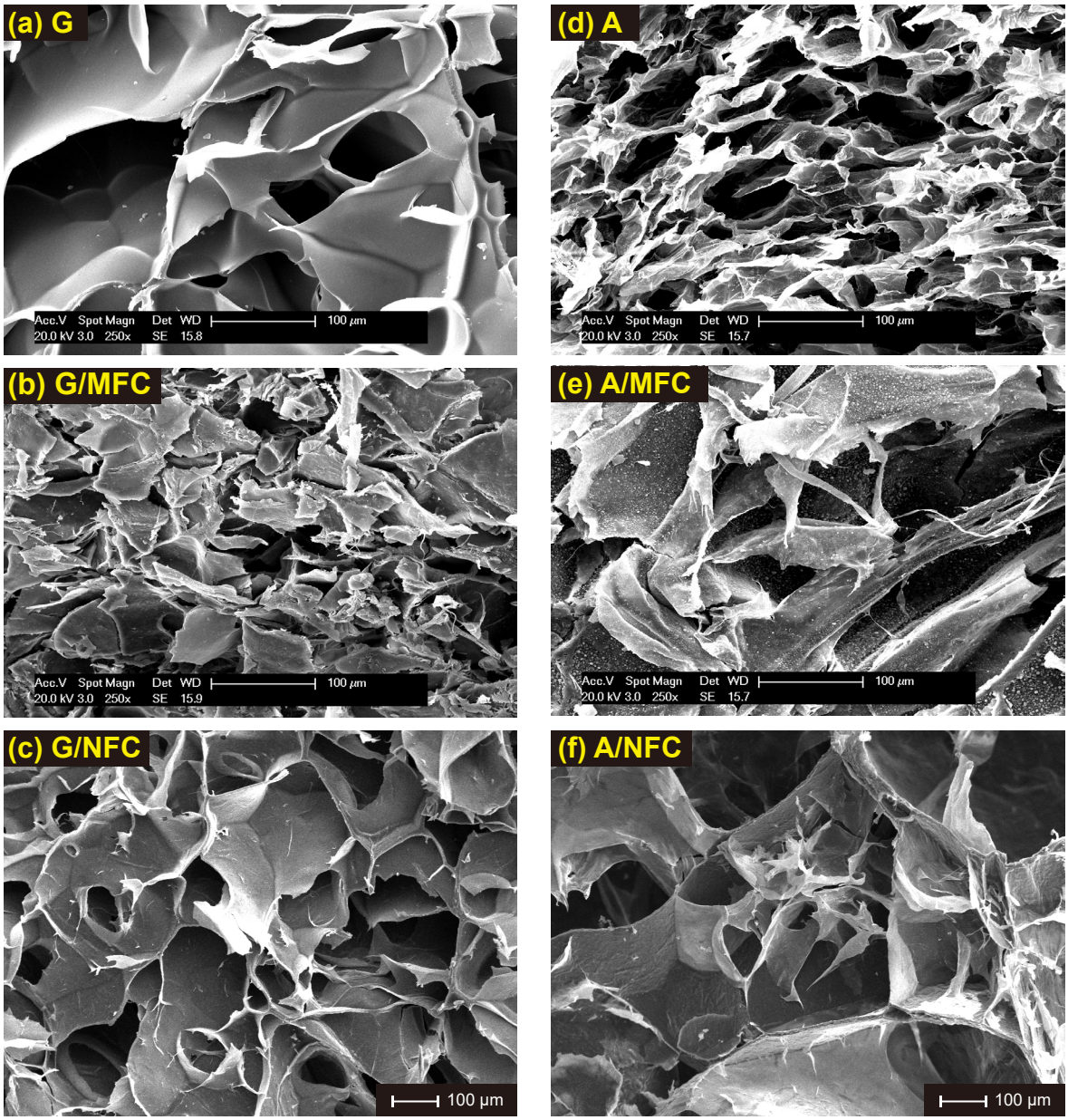

Figure 6.15: SEM images of (a) pure sample G, (b) MFC-composited G, (c) NFC-composited G, (d) pure sample A, (e) MFC-composited A, (f) NFC-composited A.

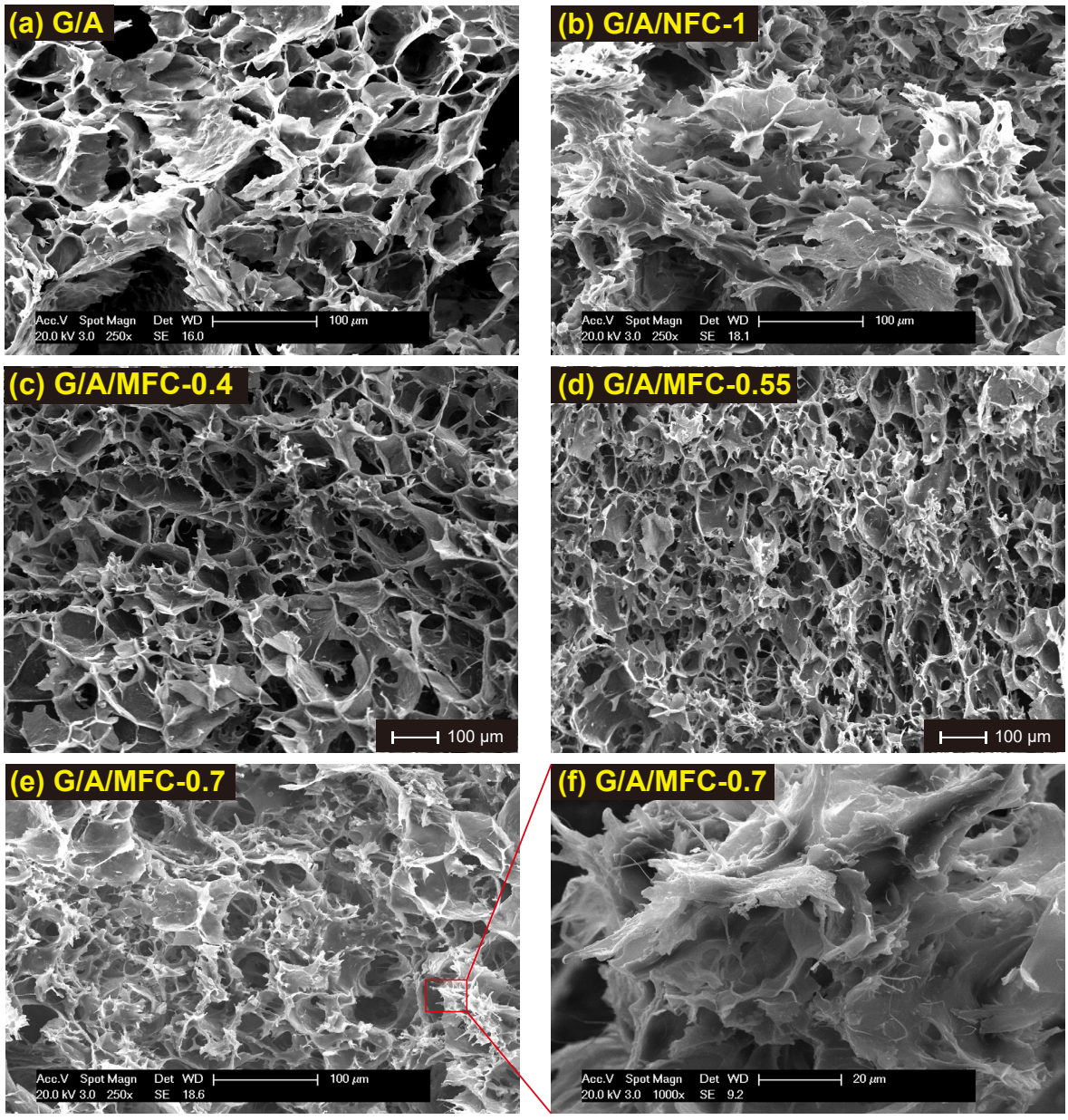

Figure 6.16: SEM images of (a) ICE hydrogel G/A, (b) NFC-composited ICE hydrogel G/A/NFC-1, (c) (d) (e) MFC-composited ICE hydrogel with different MFC contents, and (f) partially magnified G/A/MFC-0.7.

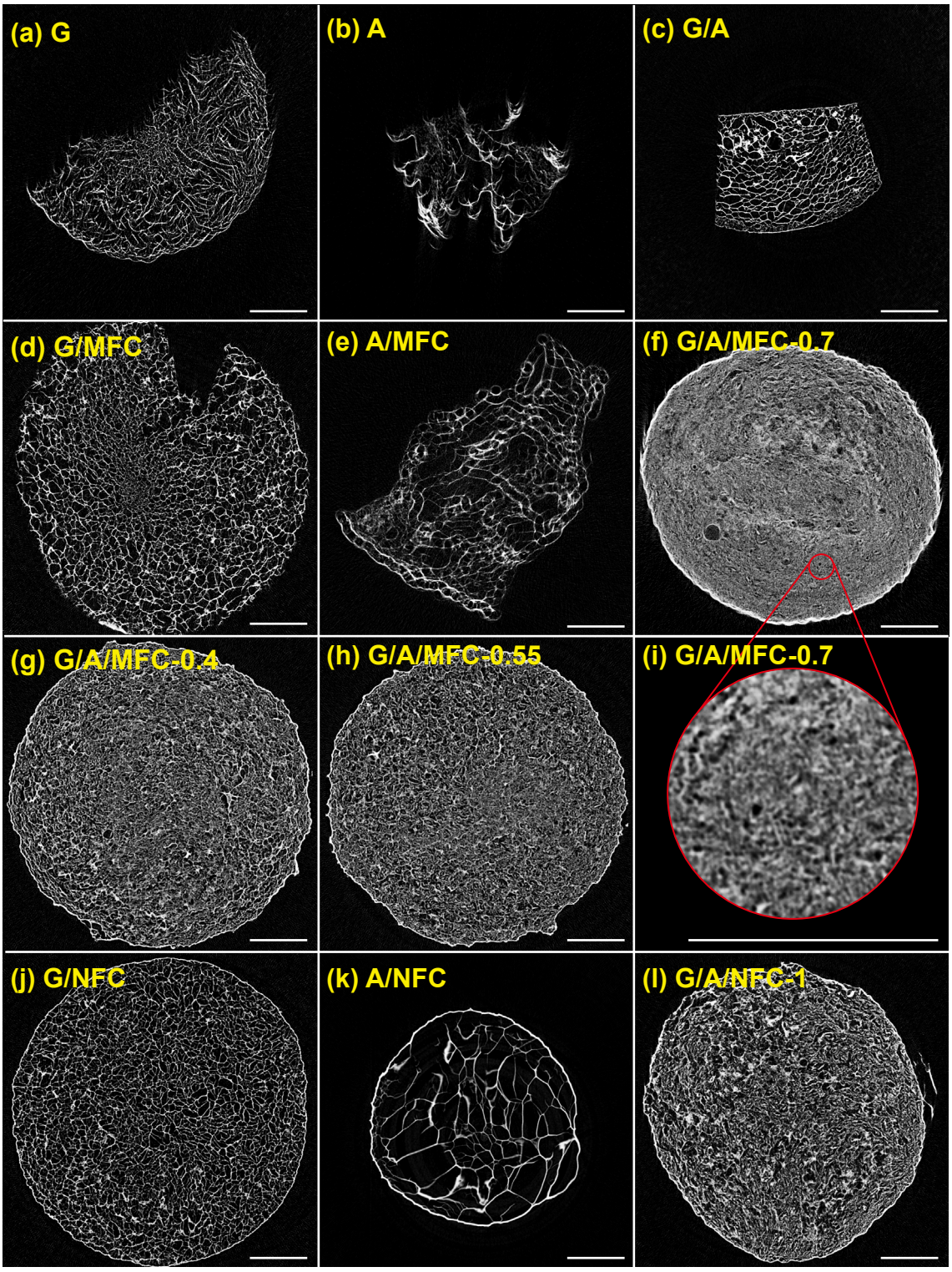

Figure 6.17: Cross-sectional images reconstructed by μCT of MFC-composited ICE hydrogels with different MFC contents, NFC-composited ICE hydrogels, and their benchmarks. The scale bar is 2 mm.

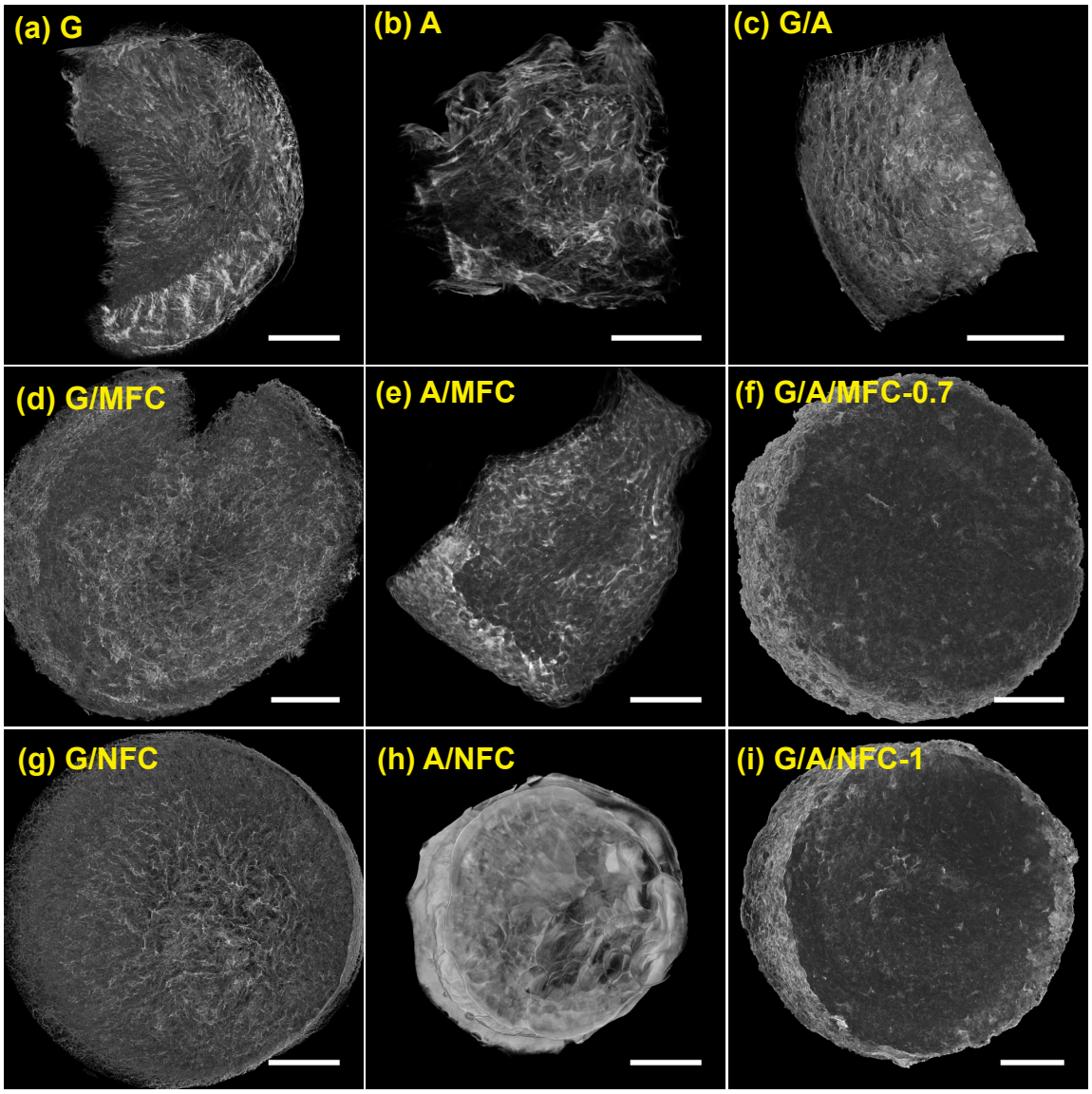

Figure 6.18: Three-dimensional images of MFC-composited ICE hydrogel G/A/MFC-0.7, NFC-composited ICE hydrogel G/A/NFC-1, and their benchmarks reconstructed by ImageJ. The scale bar is 2 mm.

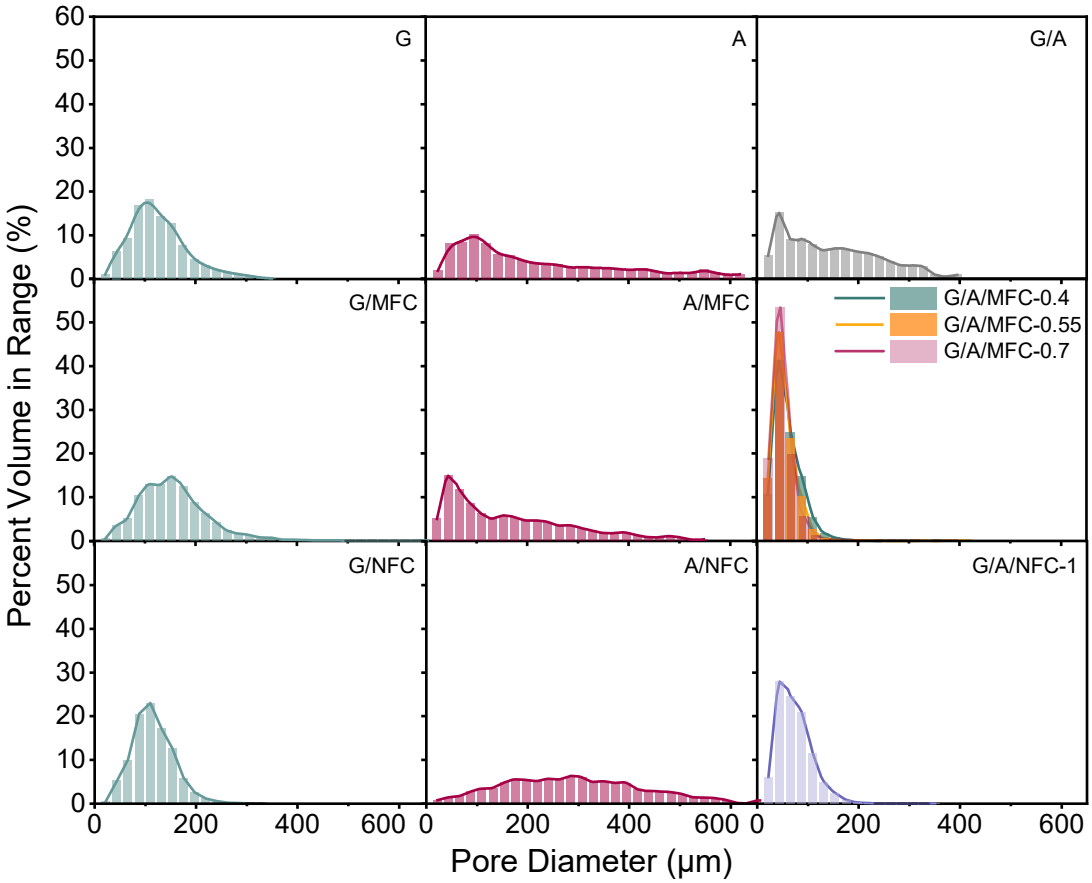

Figure 6.19: Pore size distributions of ICE G/A hydrogel, MFC-composited ICE G/A hydrogels with different MFC contents, NFC-composited ICE G/A hydrogel G/A/NFC-1, and corresponding benchmark samples.

Table 6.4: Mean pore sizes and porosities of MFC-composited ICE G/A hydrogels, NFC-composited ICE G/A hydrogels, and their benchmarks by μCT.

Sample	**Porosity (%)**
G	79.31
G/MFC	82.52
G/NFC	79.833
A	72.31
A/MFC	60.79
A/NFC	85.59
G/A	64.24
G/A/MFC-0.4	55.47
G/A/MFC-0.55	50.74
G/A/MFC-0.7	51.61
G/A/NFC-1	64.05

Table 6.5: Mean pore sizes and porosities of hybrid cellulose-composited ICE hydrogels by μCT.

Sample	Porosity (%)
G/A	64.24
G/A/NFC100	64.05
G/A/MFC25/NFC75	59.55
G/A/MFC50/NFC50	54.61
G/A/MFC75/NFC25	57.26
G/A/MFC100	51.61

The incorporation of MFC into ICE significantly narrows the pore size distribution curve of G/A, with more pore diameters concentrated in the range of 25 to 50 μm. Further, the higher the content of MFC in the MFC-composited ICE hydrogel, the higher percent volume of the sample's pore size between 25 and 50 microns, and the sharper the pore size distribution curve. The pores with a diameter greater than 100 microns basically disappear in MFC-composited ICE hydrogels. In particular, G/A/MFC-0.7 has more than 50% of the pores concentrated in the range of 25 to 50 μm and only 1.16% of the pore sizes are above 100 μm. The concentration of MFC has little effect on the porosity of MFC-composited ICE hydrogels, because the porosities of G/A/MFC-0.4, G/A/MFC-0.55, G/A/MFC-0.7 are between 50% and 55%. The above results reveal that the G/A hydrogel enhancement by MFC is by reducing the pore size distribution. By making up for the large pores (more than 100 μm) in ICE, MFC makes the overall pore size of the hydrogel tend to be the pore size formed by the synergy of the dual networks inside the ICE. Uniformly concentrated small pores can effectively avoid stress concentration, improving the structural integrity of the material and therefore strengthening the mechanical properties of hydrogels.

Compared with G/A, the pore size distribution curve of G/A/NFC-1 becomes narrower (Figure 6.19 and Figure 6.22), and the porosity of G/A/NFC-1 (64.05%) is almost the same as that of G/A (64.24%) (Table 6.4 and Table 6.5). However, the pore size distribution of G/A/NFC-1 is less concentrated than that of G/A/MFC (Figure 6.19). For example, there are still 20.2% of pores with more than 100 μm in pore size. This demonstrates that although both NFC and MFC

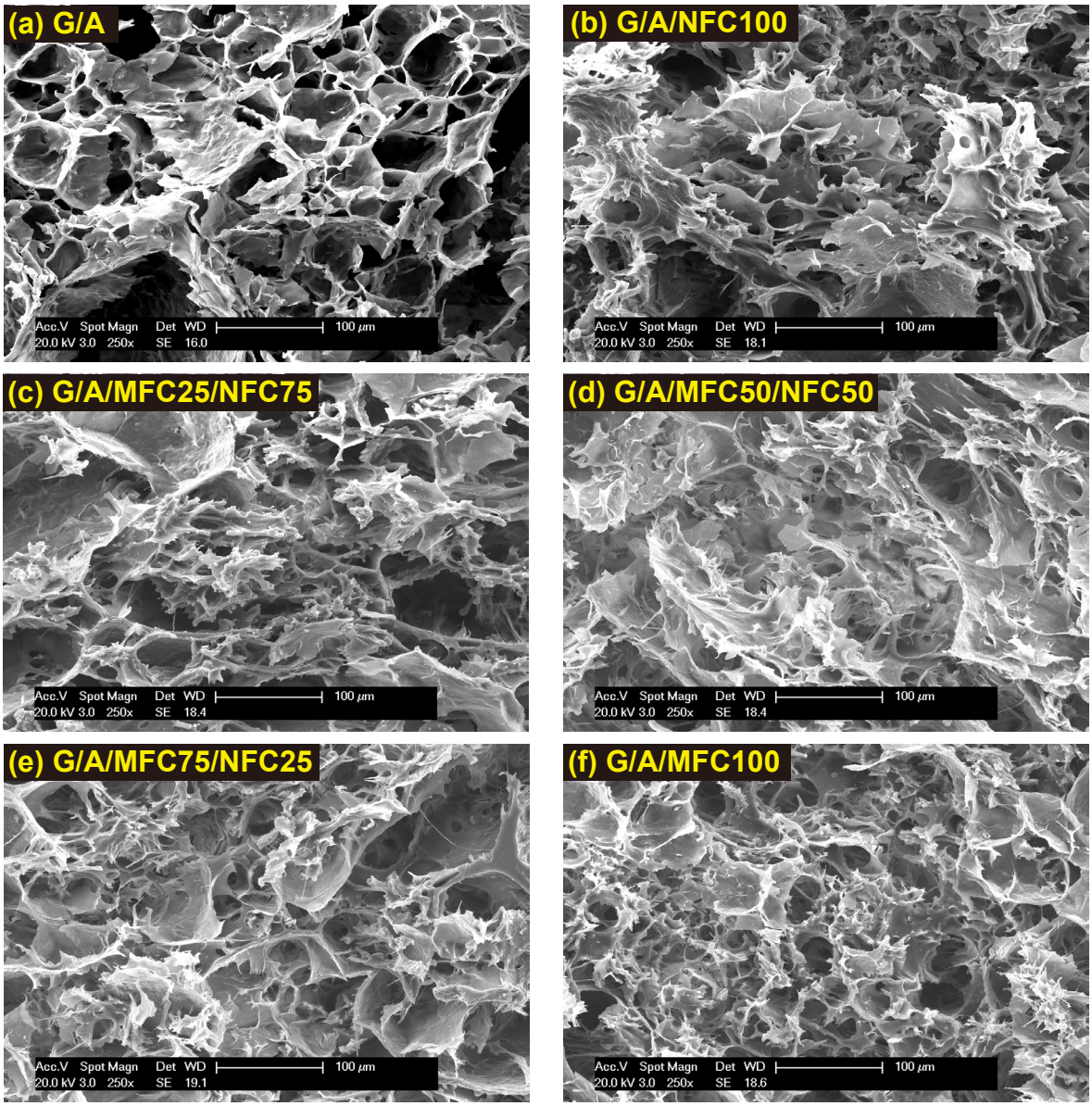

Figure 6.20: SEM images of (a) ICE hydrogel G/A and (b-f) hybrid cellulose-composited ICE hydrogels.

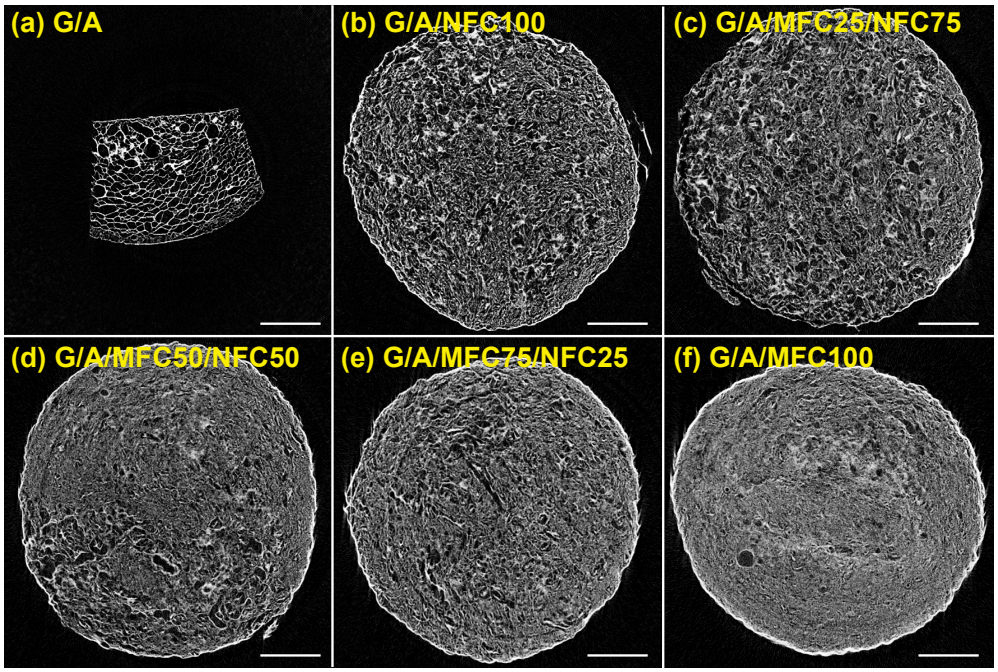

Figure 6.21: Cross-sectional images reconstructed by μCT of (a) ICE hydrogel G/A and (b-f) hybrid cellulose-composited ICE hydrogels. The scale bar is 2 mm.

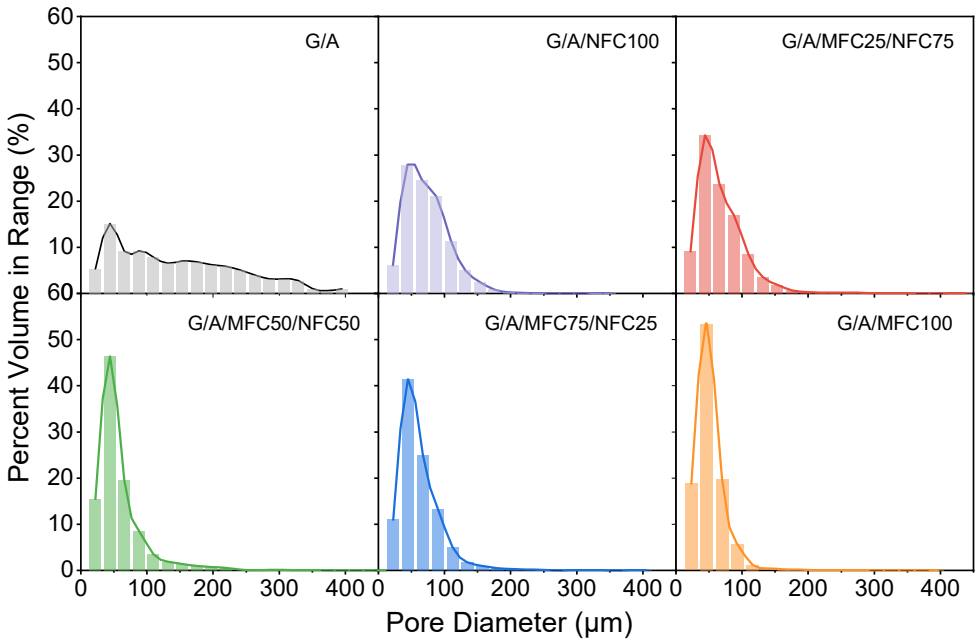

Figure 6.22: Pore size distributions of ICE hydrogel G/A and hybrid cellulose-composited ICE hydrogels.

can synergistically enhance hydrogels with ICE by hydrogen bonds, MFC is better than NFC in narrowing the pore size distribution. Therefore, in the hybrid cellulose-composite ICE hydrogels, as the content of MFC in the hybrid cellulose increases, the uniformity of the pore structure of the sample gradually increases (Figure 6.20 and Figure 6.21) and the pore size distribution curve of the sample gradually narrows (Figure 6.22).

In conclusion, cellulose forms a homogeneous fibril network in ICE hydrogels and interacts with ICE through hydrogen bonding, resulting in a more concentrated pore size distribution of the material in the range of 25 to 50 μm. The small and uniform pore structure significantly enhances the mechanical properties of the hydrogel. The increase in concentration of MFC and the size of microfibrils both contribute to the concentrated distribution of pore sizes.

6.4 Conclusions

In this chapter, the effects of microfibrillated cellulose (MFC), nanofibrillated cellulose (NFC), and hybrid cellulose on the mechanical properties of ionic-covalent entanglement (ICE) gelatin methacryloyl (G)/sodium alginate (A) hydrogels were investigated. Macroscopic Young's moduli and microscopic modulus distributes of hydrogels were evaluated through macro-compression and microindentation, respectively. The viscoelastic behaviour (creep) of hydrogels was studied by microindentation as well. By analysing the morphology and pore structure of the material, the mechanical enhancement mechanism of cellulose to ICE hydrogels was revealed.

The synergistic action of the internal dual networks of ICE G/A hydrogels results in a higher macroscopic Young's modulus of G/A (211.9 kPa) than a single G (47.63 kPa) or A network (4.8 kPa). Also, ICE G/A hydrogel has a broader microscopic Young's modulus distribution (167.25 to 194.25 kPa) than single covalent network hydrogels G (55.5 to 64.5). In ICE G/A hydrogel, the ionically crosslinked alginate network with brittleness dissipates energy by reversibly disrupting the physical 'egg-box' structure. The soft covalently crosslinked gelatin methacryloyl network

enhances the ductility of the system. Morphology and pore structure characterisations evidence that hydrogel enhancement by synergistic ICE network is due to the reduced porosity (64.24%) and pore size from 100 microns to a range of 25 to 50 microns.

The incorporation of cellulose fibril network into ICE hydrogels further enhances the mechanical properties of ICE G/A hydrogel. On the macroscopic scale, regardless of MFC, NFC, and mixed cellulose fibril network, they all improve the compression resistance, yield stress, and Young's modulus of ICE G/A hydrogel, which implies that the hydrogen bonding interaction between cellulose fibril network and ICE contributes to the synergistic enhancement between cellulose and ICE. Also, the homogeneity of cellulose fibril network can affect the synergy between cellulose and ICE. A homogeneous NFC or MFC fibril network can generate more hydrogen bonds with G/A than mixed MFC/NFC fibril networks, thus increasing the overall structural integrity of the hydrogel. Additionally, the increase of size in cellulose fibril from nano- to micro-scale improves the strength of cellulose fibril network. Therefore, MFC (363.43 kPa of macroscopic Young's modulus for G/A/MFC100) displays a more excellent macroscopic reinforcement effect than NFC (325.75 kPa of macroscopic Young's modulus for G/A/N100) in cellulose-composited ICE G/A hydrogel.

On the microscopic scale, regardless of MFC, NFC, and mixed cellulose fibril network, they all decrease the time-dependent deformation of ICE G/A hydrogel and enhance the microscopic averaged Young's modulus of ICE G/A hydrogel. More importantly, the incorporation of cellulose fibril network significantly broadens the microscopic distributions of Young's modulus and hardness for ICE G/A hydrogel in a localised area. The differences in the microscopic Young's moduli and hardness within cellulose-composited ICE G/A hydrogels can be explained by three types of reinforcement. Firstly, the cellulose fibril network can distribute energy uniformly across the hydrogel. Secondly, synergistic ICE network dissipate energy by the cleavage of ionic bonds. Lastly, the interaction between MFC and G/A, primarily through hydrogen bonds, also contributes to energy dissipation. Each of these reinforcement effects has a unique way of influencing the hydrogel's mechanical properties. Furthermore, the increases in MFC concentration and fibril size

from nano- to micro-scale are all conducive to the strength of cellulose fibril network and the interaction between cellulose and G/A.

The study of creep behaviour for cellulose-composited ICE hydrogels shows that G/A/MFC100 has lower creep displacement (2.17 μm), creep rate (18.36%), and creep strain rate sensitivity (0.04) than G/A/NFC100 (3.97 μm, 26.31%, and 0.067, respectively), indicating the increase of fibril size from nano- to micro-scale improves the creep resistance of cellulose-composited ICE G/A. This can be attributed to the greater confinement effect of MFC network than NFC network. Under external indentation force, MFC acts as a site that effectively blocks the movement of the ICE networks.

Results of micromorphology and pore structure of hydrogels evidence that homogeneous cellulose fibril networks and interactions with cellulose and ICE can make up for the large pores (more than 100 μm) in ICE hydrogel and thus concentrate pore structure in a small range of 25 to 50 micros. Such Uniformly and concentrated pores can effectively avoid stress concentration, strengthening the mechanical properties of cellulose-composited ICE G/A hydrogels. The increases in MFC concentration and fibril size from nano- to micro-scale can both narrow the pore size distribution. In conclusion, the integration of cellulose into ICE G/A hydrogels substantially regularises the micromorphology and pore structure of hydrogels, thereby enhancing their multi-scale mechanical properties.

Chapter 7

EFFECTS OF CELLULOSE ON THE BIOLOGICAL PROPERTIES OF ICE G/A HYDROGELS

7.1 Introduction

The biological properties of bioprintable hydrogels represent a cornerstone in advancing tissue regeneration strategies [66]. Water retention capacity, a fundamental characteristic of hydrogels, is paramount for maintaining a hydrated microenvironment reminiscent of the native extracellular matrix. This property enables nutrient diffusion and waste removal, fostering an environment essential for cell survival and function. In the context of tissue regeneration, the ability of hydrogels to imbibe and retain biological fluids ensures a nourishing milieu for cells, thereby promoting tissue repair and growth [454]. Biodegradation is another pivotal characteristic of hydrogels once tissue regeneration reaches a satisfactory extent. These hydrogels should ideally provide structural support during the early phases of tissue development and gradually degrade as the native tissue matures [455]. Controlled biodegradability is crucial for maintaining tissue integrity and avoiding complications

associated with long-term implant presence [456]. Furthermore, cytocompatibility is indispensable to ensure that formulations of the hydrogel do not elicit adverse cellular responses, inflammation, or cytotoxicity [457]. Maintaining a favorable microenvironment through cytocompatible hydrogels is essential for promoting cell adhesion, proliferation, and differentiation, ultimately driving successful tissue regeneration. In the realm of tissue engineering, the controlled release of bioactive molecules from hydrogels, known as drug delivery, becomes a powerful tool for modulating tissue regeneration processes [458]. This feature enables the localized administration of growth factors or therapeutic agents, orchestrating the regenerative response and enhancing tissue repair [459]. Additionally, the antimicrobial properties of some hydrogel formulations contribute to safeguarding the regenerating tissue from potential infections, a critical consideration in the context of open wounds or implantable medical devices [460, 461]. Collectively, these biological properties make bioprinted hydrogels invaluable assets in the pursuit of effective tissue regeneration strategies.

In the preceding chapters, the benefits of cellulose in enhancing both the extrusion printability of ICE bioinks and the mechanical strength of ionic-covalent entanglement (ICE) hydrogels have been evidenced. In light of these advancements, and with the ultimate goal of facilitating seamless post-transplantation functionality of cellulose-composited ICE hydrogels in the context of tissue repair, this chapter will explore the effects of cellulose on the multifaceted biological properties of ICE hydrogels, including swelling behaviour, degradation kinetics, cell viability, controlled drug release, and antimicrobial properties.

7.2 Materials and methods

7.2.1 Materials

Mouse preosteoblasts MC3T3-E1 Subclone 4 cells (ATCC-2593) were purchased from LGC standards (Middlesex, UK). Alpha Minimum Essential Medium (αMEM) with L-glutamine, fetal bovine serum (FBS), penicillin-streptomycin (10,000 U/mL), trypsin-EDTA (0.05%), trypan blue (0.4%),

1 × Dulbecco's phosphate-buffered saline (dPBS) with and without calcium and magnesium, and collagenase type II were ordered from Gibco, Thermo Fisher Scientific (UK). LIVE/DEAD Viability/Cytotoxicity Kit for mammalian cells was obtained from Invitrogen, Thermo Fisher Scientific (UK). Dimethyl sulfoxide (≥ 99.7%) and ampicillin sodium salt was bought from Sigma-Aldrich (UK).

Basal culture media of MC3T3-E1 cells comprised αMEM, 10% FBS, and 1% penicillin-streptomycin. Cryopreservation reagent for MC3T3-E1 was prepared using 90% FBS and 10% dimethyl sulfoxide. Collagenase Type II was dissolved in 1 × dPBS to prepare a stock solution (50000 U/mL), followed by sterilisation using 0.2 µm PES syringe filter (Whatman, UK). The stock solution of collagenase type II was stored at -18°C until use.

Strains of *Escherichia coli* (*E. Coli*) (MG1655) and *Staphylococcus aureus* (*S. Aureus*) (ATCC-29213) were obtained from the University of Birmingham. Nutrient agar (Oxoid) and PBS tablets (Oxoid) were ordered from Thermo Fisher Scientific (UK). Luria-Bertani (LB) broth (Miller) and Tryptic Soy Broth (TSB) were purchased from Merck, Sigma-Aldrich (UK). Nutrient agar, PBS, LB broth, and TSB broth were all dissolved in deionised water with appropriate concentrations and sterilised by autoclave at 121°C for 20 min following the manufacturer's protocol.

7.2.2 Physiological stability

7.2.2.1 Swelling and degradation

Dry hydrogel discs were weighted first to record the initial mass (W_{dry}). The hydrogel samples were then placed in tissue culture-treated 6 well plates filled with 2 mL deionised water per well at room temperature. The deionised water was refreshed every 2 days until the study was completed. At different times, swollen samples were carefully taken out. The surface water of hydrogels was removed using precision wipes (Kimberly-Clark). Hydrated samples were weighed and the wet mass at a different time n was expressed as $W_{wet,n}$. Swelling ratio at a different time (SR_n) was calculated

based on Equation 7.1. Equilibrium hydration degree (*EHD*) of the hydrogel was estimated using $W_{\text{wet,48h}}$ based on the trend of SR_n.

$$SR_n = \frac{W_{wet,n} - W_{dry}}{W_{dry}} \tag{7.1}$$

$$EHD(\%) = \frac{W_{wet,48h} - W_{dry}}{W_{wet,48h}} \cdot 100 \tag{7.2}$$

After immersing in deionised water for 50 days, the hydrogel was carefully extracted from the container. Uniaxial compression test was conducted to investigate the changes in the mechanical properties of the hydrogel due to its degradation. Unless otherwise specified, the measurement and analysis of compression used here were the same as the methods mentioned in 6.2.1.

7.2.2.2 Enzymatic biodegradation

The enzymatic biodegradation behaviour of hydrogels was investigated in 1× dPBS with collagenase type II. Hydrogel discs in an equilibrium state were freeze-dried and their initial dry weights (W_0) were recorded. The stock solution of collagenase type II was diluted to 5 U/mL for the research. Each hydrogel disc was immersed in 1 mL of 1× dPBS with 5 U/mL collagenase type II and incubated at 37°C. The enzymatic biodegradation solution was replaced every 2 days until complete degradation of samples or the experiment was concluded. After 1, 3, 7, and 10 days, all enzymatic biodegradation solution was carefully extracted out of tissue culture-treated 24 well plates. The remaining hydrogel disc in the container was lyophilised at -56°C and the remaining dry masses (W_n) of samples after 1, 3, 7, and 10 days were collected and marked as W_1, W_3, W_7, and W_{10}, respectively. The biodegradation rate (*BDR*) was calculated following the equation below:

$$BDR(\%) = \frac{W_0 - W_n}{W_0} \cdot 100. \tag{7.3}$$

To track the enzymatic biodegradation process of hydrogels, morphology and pore size distri-

bution of dry hydrogels biodegraded for 3 and 7 days were measured by SEM and μCT. Unless otherwise specified, the parameters used for SEM and μCT were consistent with the experiments mentioned in 6.2.3 and 6.2.4.

7.2.3 Cytocompatibility

7.2.3.1 Cell thawing

A cryovial of frozen cells was transferred rapidly from the liquid nitrogen storage tank to 37°C water bath. After 3 min of gentle agitation, frozen cells changed colour from yellow to pink, indicating that the cells were mostly thawed. The cells were subsequently transferred slowly to a 15 mL centrifuge tube under the sterile conditions of the cell culture hood. Pre-cultured basal culture medium of 6 mL was added dropwise to the tube. The cell suspension was then centrifuged at 125 × g (Megafuge 8R Small Benchtop Centrifuge with a rotor radius of 11 cm, Thermo Fisher Scientific, UK) for 5 min and the supernatant was thrown away. The cell pellet was resuspended by adding 1 ml basal culture media. Pre-warmed basal culture media of 9 mL and cell resuspension of 1 mL were all added to a T-150 tissue culture-treated cell culture flask and cultured in an incubator (95% air and 5% CO_2) at 37°C. The cell culture medium was refreshed after 24 h.

7.2.3.2 Cell passaging and counting

EVOS XL Core imaging system (Invitrogen, Thermo Fisher Scientific, UK) was applied to assess the confluence of MC3T3-E1. When the confluence reached 80-90%, subcultivation was initiated in a cell culture hood. The growth medium was carefully aspirated from T-150 culture flask. Adhesive cells were washed twice using 6 mL dPBS without calcium and magnesium. Pre-warmed 0.05% trypsin-EDTA solution of 7 mL was added to the culture flask for cell dissociation. After being cultured in a 37°C incubator for 5 min, complete detachment of cells in the culture flask was inspected by EVOS XL Core imaging system. Trypsinization was then terminated by adding

8 mL of pre-warmed basal culture medium to the flask. All cell suspension was aspirated to a 15 mL centrifuge tube and spun down for 5 min at 250 × g. The cell pellet was resuspended using 7 mL warm basal culture medium following discarding the supernatant. Only cell re-suspension of 1 mL was added to a new T-150 culture flask containing 20 mL pre-cultured basal culture medium (passaging ratio of 1:7). After incubating at 37°C for 3 days, the culture was inspected and next passaging based on cell confluence. In this study, Passages 1 to 5 were used to obtain cell stocks. Passages 6 to 9 were applied to the cytocompatibility experiment.

Regarding cell counting, cell re-suspension was thoroughly mixed with 0.4% trypan blue in equal parts. The mixture of 10 µL was pipetted into a chamber on the cell counting slide (Bio-rad, Watford, UK). Cell counting was performed immediately by inserting the slide into TC20 automated cell counter (Bio-rad, Watford, UK).

7.2.3.3 Cell freezing and storage

The cryopreservation reagent of cells was on-demand prepared and utilised. In cell passaging, after cell pellet was collected, cryopreservation reagent of 1 mL was used to suspense it. The suspension was transferred to 1 mL cryovial, followed by freezing using Mr. Frosty Freezing Container at -80°C for 24 h and moving to liquid nitrogen for long-term storage.

7.2.3.4 Bioprinting and *in vitro* culture

Building upon the physico-chemical properties established, sterilised bioink formulations G/A/MFC-0.7, and G/A/NFC-1 were selected in the present work. MFC (0.7%) in PBS and 1% NFC in PBS were sterilised by autoclaving at 121°C for 20 min. Samples G, A, and Irgacure 2959 were all dissolved in 0.7% MFC in PBS and 1% NFC in PBS under the sterile environment of the biological safety cabinet to prepare bioink formulations G/A/MFC-0.7 and G/A/NFC-1, respectively.

Syringe barrels of 5 mL, syringe pistons, and conical nozzles with 200 µm inner diameter were all autoclaved in advance. Bioink formulation and cell resuspension were loaded into a cartridge

that was connected to another empty cartridge by a syringe adaptor. A homogeneous blend of the bioink formulation and cell resuspension was facilitated by gently pushing syringe pistons back and forth. The final number of cells in bioink formulation was 1.56×10^6 /mL.

Bioprinting was conducted based on the model in Figure 5.2c at a printing speed of 2 mm/s and dispensing pressure of 25 kPa. The resulting scaffolds with 4 and 6 layers were crosslinked under UV radiation (20% iris and 365 nm wavelength) for 10 and 15 s, respectively. Then they were immersed in 2% $CaCl_2$ for 5 min. Each cell-encapsulated bioink was bioprinted twice at room temperature.

Scaffolds were immersed in warm dPBS for 3 min to remove unreacted chemicals within them before being cultured for 2, 4, 7,10, 14, and 21 days in a humidified incubator at 37°C with 5% CO_2. Cell culture medium was changed every 2 days.

7.2.3.5 Live/dead assay by confocal laser scanning microscopy

Live/dead assay was employed to evaluate cell viability following the manufacturer's protocol. Briefly, calcein-AM for live cells and ethidium homodimer-1 for dead cells were diluted in sterile dPBS, vortexing to ensure thorough mixing. At each time point, each scaffold was dyed and incubated in a cell imaging μ-dish with a glass bottom (Ibidi, UK) using 1 mL staining solution with 1 $\mu L\,mL^{-1}$ calcein-AM and 4 $\mu L\,mL^{-1}$ ethidium homodimer-1 at 37°C with 5% CO_2 for 20 min. Then live/dead assay reagents were gently aspirated out and the scaffold was washed once by dPBS to minimise background signal. The cell-loaded scaffolds were imaged with a confocal laser scanning microscope (Zeiss LSM780, Carl Zeiss Microscopy, US). Three randomly selected areas of $850 \times 850\ \mu m^2$ in XY coordination system were scanned. Scanning depths of samples depend, ranging from 126 to 312 microns. ImageJ was then utilised for processing the Z-stack images of cells, building 3D projections of confocal Z-stack images, and conducting cell counting within each 3D section of the construct to distinguish living and dead cells.

7.2.4 Structural changes of scaffolds with incubation time

The structure of cell-loaded scaffolds G/A/MFC-0.7 and G/A/NFC-1 with 4 and 6 layers were imaged by SEM after they were incubated for 7 and 21 days. Once the live/dead assay was completed by confocal laser scanning microscopy, staining solution was removed from the cell imaging μ-dish. These scaffolds were frozen at -80°C and dried under vacuum at -56°C. Unless otherwise specified, gold-coating of sample surface and imaging parameters used in SEM were consistent with the experiments mentioned in 6.2.3.

7.2.5 Controlled drug release

7.2.5.1 UV/Vis spectroscopy

Ampicillin in this work was used as a drug model to study the controlled drug release behaviour of hydrogels. Initially, the standard stock solution of ampicillin (100 $\mu g\,mL^{-1}$) was prepared in sterile PBS. The standard solution was scanned within a wavelength range of 200 to 400 nm by UV/Vis spectrometer (Biochrom Libra S12, Cambridge, UK) at room temperature. Therefore, the maximum absorbance wavelength for ampicillin was found to be at 220 nm. To build the relationship between absorbance and concentration of ampicillin, the absorbance of ampicillin solutions with a range of different concentrations (5 to 1000 $\mu g\,mL^{-1}$) was measured three times at 220 nm. Finally, the standard calibration curve was graphed against absorbance at 220 nm vs concentration for different ampicillin solutions.

7.2.5.2 Isothermal absorption of ampicillin

Ampicillin was loaded into hydrogel discs using a previously reported method [462–466]. Specifically, pre-weighted dry hydrogel discs were immersed in 50 mL of 100 $\mu g\,mL^{-1}$ standard solution of ampicillin. They were incubated at 20°C with continuous agitation at 100 rpm. To determine the time required for the hydrogel to reach the absorption equilibrium of ampicillin, at scheduled

time intervals within 28 h, free ampicillin of 1 mL was aspirated and the absorbance was read immediately by UV/Vis spectrometer. The withdrawn liquid was replaced with an equal volume of fresh sterile PBS. The drug loading capacity (*LC*) [462, 464] and encapsulation efficiency (*EE*) [465, 466] was determined following the equations below. Each test was repeated triple from which the mean value was calculated.

$$A_{Amp,L} = A_{Amp,T} - A_{Amp,F} \tag{7.4}$$

$$LC(\frac{mg}{g}) = \frac{A_{Amp,L}}{A_{Hydrogel}} \tag{7.5}$$

$$EE(\%) = \frac{A_{Amp,L}}{A_{Amp,T}} \cdot 100 \tag{7.6}$$

where $A_{\mathrm{Amp,T}}$ (mg) shows the total amount of ampicillin before absorption, $A_{\mathrm{Amp,F}}$ (mg) represents free amount of ampicillin after absorption. Hence, the gap between $A_{\mathrm{Amp,T}}$ and $A_{\mathrm{Amp,F}}$ is the amount of loaded ampicillin within the hydrogel ($A_{\mathrm{Amp,L}}$, mg). A_{Hydrogel} (g) describes the amount of initial dry hydrogel disc. The hydrogel loaded with ampicillin was named in this study as G/A-AMP, G/A/MFC-0.4-AMP, G/A/MFC-0.55-AMP, G/A/MFC-0.7-AMP, and G/A/NFC-1-AMP.

7.2.5.3 Controlled release of ampicillin

The drug release method was also based on previous reports [462–466]. Once hydrogels reached the absorption equilibrium of ampicillin, the ampicillin-loaded hydrogel was immediately transferred to 50 mL of sterile PBS and incubated at 20°C with 80 rpm shaking. At predetermined time intervals, 1 mL of release medium was pipetted and replaced with same amount of fresh PBS solution. The amount of drug released was then analysed spectrometrically. The cumulative release (*CR*) of ampicillin was estimated by Equation 7.7 [462]. The test for drug release was performed until the absorbance of the release medium remained nearly constant.

$$CR(\%) = \frac{A_{Amp,R}}{A_{Amp,L}} \cdot 100 \tag{7.7}$$

where $A_{Amp,R}$ (mg) depicts the amount of the cumulative released ampicillin from the hydrogel at every time point. $A_{Amp,L}$ can be calculated according to Equation 7.4.

7.2.5.4 Release mechanism analysis

The logarithmic fit to the first 60% of the release in the cumulative release profile for ampicillin was performed using Equation 3.13. The release mechanisms of G/A-AMP, G/A/MFC-0.4-AMP, G/A/MFC-0.55-AMP, G/A/MFC-0.7-AMP, and G/A/NFC-1-AMP were analysed based on the release indices of the cylindrical polymer release systems in Table 3.2.

7.2.6 *In vitro* antimicrobial test of drug-loaded hydrogels

7.2.6.1 Isolating bacteria

A sterile inoculation loop was dipped in the original glycerol bacterial stock and streaked onto an agar plate using the streak plate technique. The agar plate was put into a 37°C microbiological static incubator (30°C if growing *E. Coli*) overnight to allow colonies to grow. The agar plate was taken out the morning after, and abudant single colonies (white dots) can be observed. Bacterial agar plates were stored in the 4°C fridge for a maximum of 6 weeks.

7.2.6.2 Preparing bacterial glycerol stocks for long-term storage

A colony was selected from a bacterial agar plate and inoculated into 10 mL broth (LB broth for *E. Coli* and TSB broth for *S. Aureus*). Bacteria was thoroughly suspended in broth by vortexing. Bacterial cultures were incubated at 37°C with shaking at 150 rpm overnight. The overnight bacterial culture of 500 µL was aspirated and mixed with 500 µL of 50% glycerol in a screw top vial. Bacterial glycerol stocks were frozen at -80°C and can be stored for years.

7.2.6.3 Agar disc diffusion assay

An isolated colony was picked and grown overnight in 10 ml broth medium (LB for *E. Coli* and TSB broth for *S. Aureus*) at 37°C with shaking at 150 rpm. Overnight cultures were pelleted at 3900 rpm for 10 min using Eppendorf Centrifuge 5810 and washed twice with broth medium. Cultures were resuspended in broth medium and the concentration of the strain was adjusted to approximately 10^8 CFU/mL by measuring the optical density of the bacterial culture at 600 nm to 0.5 AU with a visible spectrometer (Jenway 6300, Cole Parmer, UK).

A sterilised cork-borer was used to extract three wells of the same size as the hydrogel disc on a clean agar plate. These wells were then filled with ampicillin-loaded hydrogel discs. Cultures of 150 µL were spread evenly throughout the agar plate and incubated inverted for 1 day in a static incubator(30°C for *E. Coli* and 37°C for *S. Aureus*). The areas of zones of inhibition for bacterial growth were then recorded. All hydrogel discs were transferred from the day-1 plates into freshly inoculated agar plates and allowed to incubate for an additional 24 h. The same measurements were performed on the day-2 plates. This procedure was then repeated and the inhibitory results were observed after a total incubation period of 3 days.

Test group includes G/A-AMP, G/A/MFC-0.4-AMP, G/A/MFC-0.55-AMP, G/A/MFC-0.7-AMP, and G/A/NFC-1-AMP. For positive control, 50 µL of ampicillin solution (100 µg mL^{-1}) was dropped to a sterile filter paper disc with 13 mm diameter (Whatman, UK) and dried in a laminar flow hood for 30 min. Ampicillin-loaded filter paper discs were put on the inoculated agar plate. The same incubation process as in the test group was applied. For negative control, hydrogel discs without ampicillin, including G/A, G/A/MFC-0.7, and G/A/NFC-1 followed the completely same protocol as the test group. Every sample and bacterial strain was tested three times independently.

7.3 Results and discussion

7.3.1 Water retention capacities of hydrogels

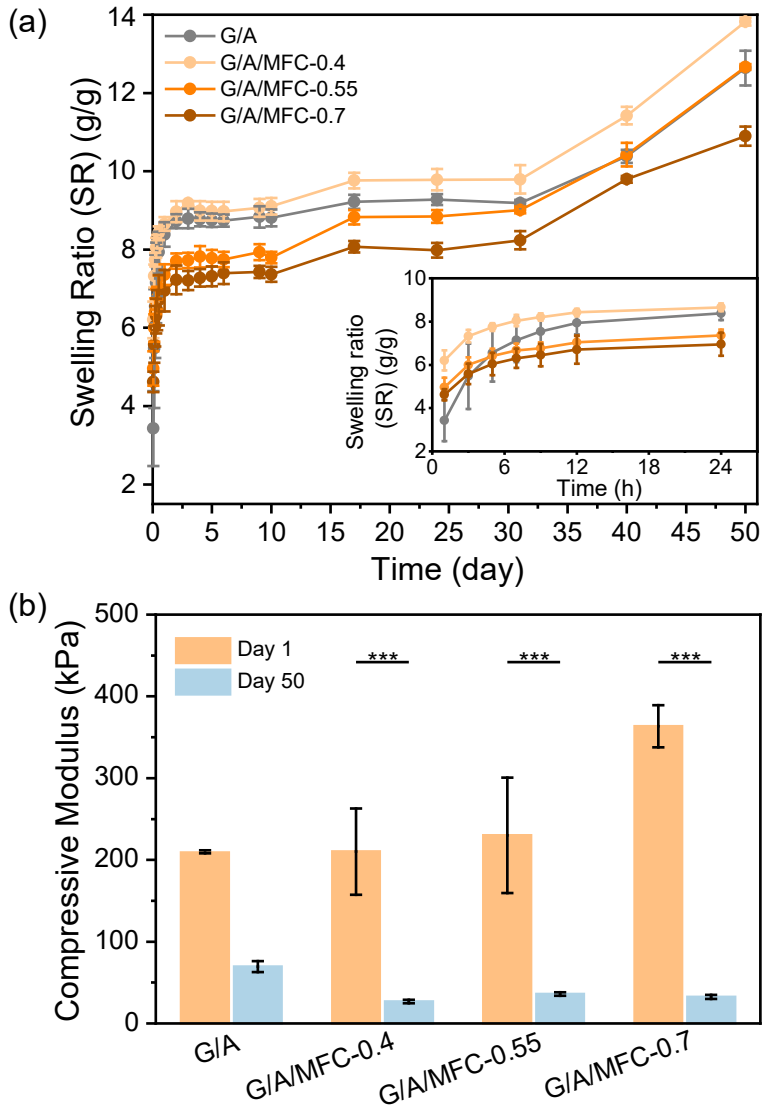

Figure 7.1: (a) Swelling ratio of MFC-composited ICE hydrogels over 50 days and enlarged view of swelling ratio in the initial first day. (b) Compressive moduli of hydrogels after 1 day and after 50 days of immersion in deionised water.

Figure 7.1a shows the change in swelling ratio of dry ICE hydrogel G/A and MFC-composited ICE hydrogels G/A/MFC-0.4, G/A/MFC-0.55, and G/A/MFC-0.7 in deionised water over 50 days.

The swelling ratio of all samples shows an increase in three stages over the 50 days. The first stage of ascent is expected when the dried hydrogel samples were immersed in water. Hydrophilic functional groups in structures of ingredients G, A, and MFC form hydrogen bonds with H_2O, causing the swelling ratio of the hydrogels to reach approximately 7 g/g within 12 hours. The first stage of increase in the swelling ratio reaches an equilibrium 1 day after the hydrogel is immersed in water.

The second rise in swelling ratio occurs after 10 days. During this stage, G/A/MFC-0.4, G/A/MFC-0.55, and G/A/MFC-0.7 show a greater increment in swelling ratio than G/A, suggesting that not only is the synergy within the ICE dual-network diminished across all samples, but the synergistic effect between MFC and ICE is also reduced in MFC-composited ICE hydrogels. As discussed in Figure 6.19 of Section 6.3.5, the above two synergistic effects are beneficial to the pore diameter of the hydrogel sample being concentrated in the range of 25 to 50 microns. Therefore, the increase in swelling ratio in the second stage can be attributed to the enlargement of the pores in the range of 25 to 50 μm.

The third stage of accelerated rise in swelling ratio happened after day 31, with all samples swelling at almost the same rate, which can be attributed to the degradation of the ionically crosslinked network of alginate with calcium ions. Ionic crosslinking is a physical crosslinking with low bond energy. The phenomenon of the leaching of calcium ions in hydrogels has been shown in some reports [467, 468]. Failure of ionic crosslinking leads to a significant reduction in the crosslinking density and an increase in the pore size of the hydrogel. Hence, the third rise in swelling ratio is much more significant than the second.

Furthermore, for different samples, the swelling ratio of G/A/MFC-0.4 is always above that of G/A, which is contra-intuitive. However, when MFC is mixed with ICE at concentrations of 0.55% and 0.7%, the swelling ratios of the resulting samples are lower than that of G/A at every time point, which is related to the concentrated distribution of the pore sizes of MFC-composited ICE hydrogels between 25 and 50 microns. Without affecting the hydration degree of the hydrogel, the

actual size of the samples with a small swelling rate more closely fit the pre-determined size of the hydrogel, which is important for the seamless connection of the hydrogel to the damaged tissue after implantation.

By characterising Young's moduli of the hydrogel samples after 50 days of swelling (Figure 7.1b), it is found that Young's moduli of MFC-containing samples all drop significantly to 36 kPa or lower (p-value ≤ 0.001), while Young's modulus of G/A only decreases from 176.37 to 69.41 kPa. It evidences that MFC-composited ICE hydrogels have the ability to provide strong mechanical support to the damaged tissues at the initial stage of implantation, whereas, at the later stage of implantation, its degradation frees up space for the remodelling of the new tissues.

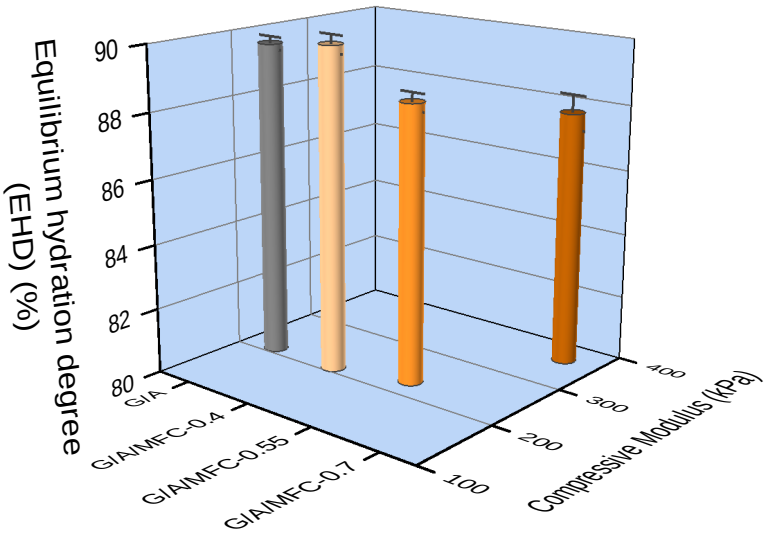

Figure 7.2: Relationship between equilibrium hydration degree and compressive modulus of MFC-composited ICE hydrogels.

Because the swelling ratio of the dried hydrogel essentially reaches equilibrium after one day of immersion in water and remains constant for the first 10 days, *EHD* of samples were calculated during this time and are presented in Figure 7.2. It can be seen that the 0.7% MFC only slightly reduced *EHD* of ICE hydrogels from 89.71 to 87.83%. Equilibrium hydration degree of MFC-composited ICE G/A hydrogels still align well with the standard hydration spectrum observed in various body tissues [264]. Thus, the effect of MFC on *EHD* of ICE hydrogels is insignificant.

In conclusion, MFC can increase Young's modulus of ICE hydrogel from 211.9 kPa to 363.43 kPa (G/A/MFC-0.7) while maintaining high hydration of the hydrogel by centralising pore size distribution, which is of great significance for hydrogels to maintain a balance between mechanical and biological functions.

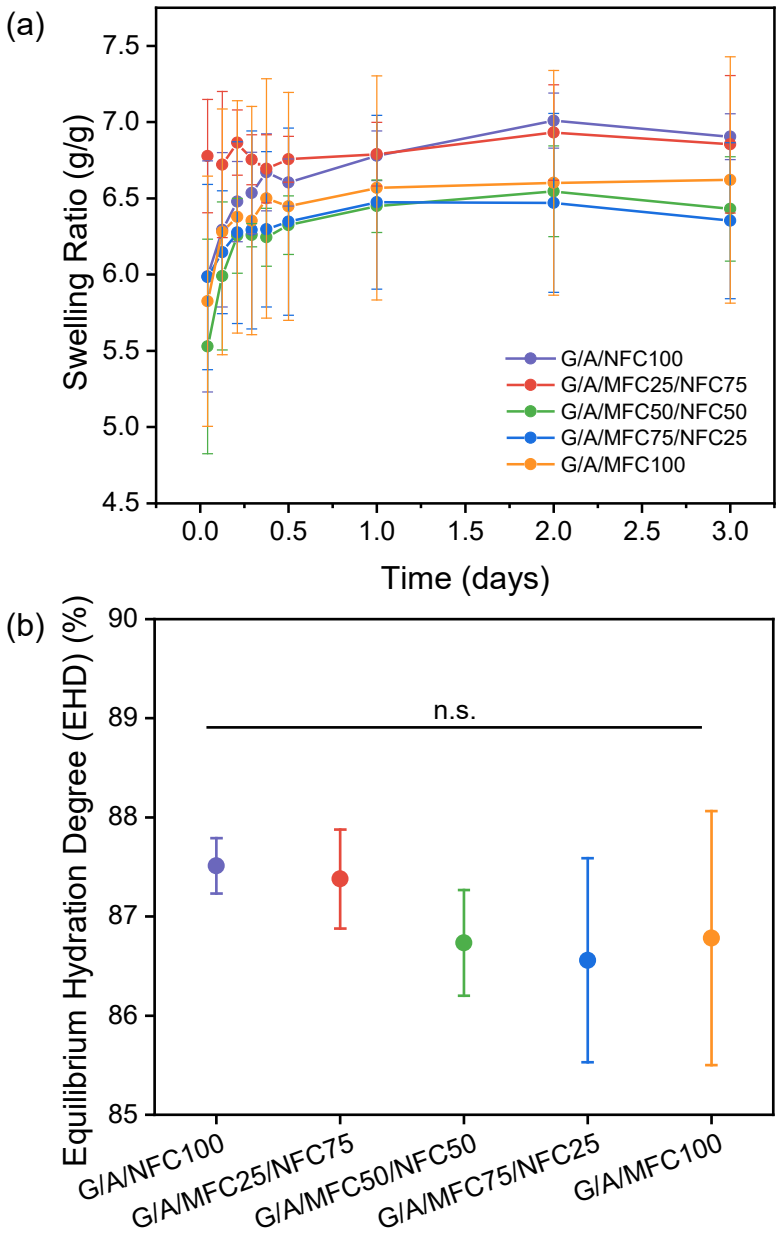

Figure 7.3: (a) Swelling ratio of hybrid ICE hydrogels over 3 days. (b) Equilibrium hydration degree of hybrid ICE hydrogels after 48 h.

The effects of NFC and hybrid cellulose on *EHD* of ICE hydrogels were also evaluated and the results are shown in Figure 7.3. For swelling ratio curves, samples with high NFC content, such as G/A/NFC100 and G/A/MFC25/NFC75, are slightly greater than samples with high MFC content, e.g. G/A/MFC100 and G/A/MFC75/NFC25. Also, all the samples have no significant differences of *EHD* (p-value > 0.05) and remain around 87%, indicating that the size of fibrillated fibre does not have much effect on the water content of the hydrogel.

7.3.2 Enzymatic biodegradation

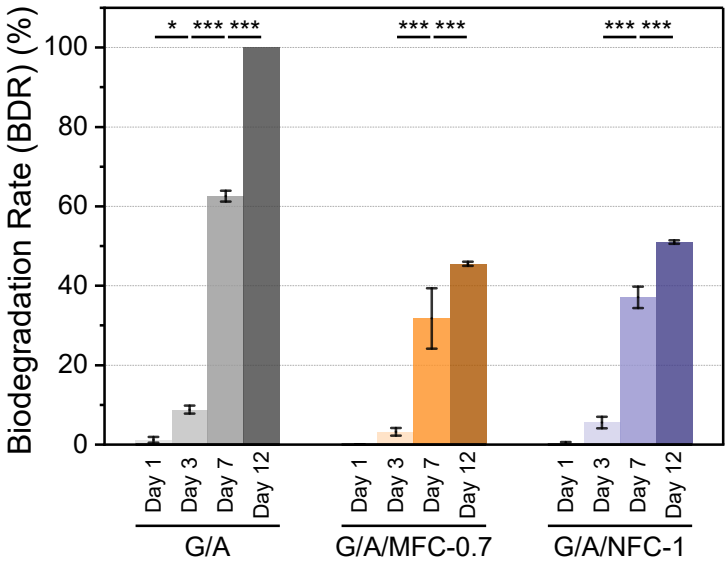

Figure 7.4: Biodegradation rates of G/A, G/A/MFC-0.7, and G/A/NFC-1 after 1, 3, 7, and 12 days of immersion in 1 × dPBS with 5 U/mL collagenase type II. Either MFC or NFC significantly prolongs the biodegradation half-life of ICE hydrogels from less than 7 days to around 12 days.

Collagenase type II is an enzyme that primarily cleaves peptide bonds within the collagen protein [469]. Gelatin, a partially hydrolyzed form of collagen, has a characteristic repeating sequence of Glycine-Proline-X (where X can be any amino acid) [470]. Collagenase type II can cleave the peptide bond between glycine and the X amino acid in this sequence [471, 472]. Hence, the effects of cellulose on enzymatic biodegradability of ICE hydrogels were investigated. Figure 7.4 presents biodegradation rate (*BDR*) of G/A, G/A/MFC-0.7, and G/A/NFC-1 over 12 days. If *BDR* reaches

50% as an indicator, the half-life of G/A is obviously less than 7 days. The half-life of G/A/MFC-0.7 and G/A/NFC-1 is basically around 12 days. G/A has been completely biodegraded at the 12th day. It indicates that MFC and NFC significantly prolong the biodegradation of ICE hydrogels.

Meanwhile, by characterising the morphology and pore size of these three samples during enzymatic biodegradation, it can be concluded from Figure 7.5 that the pores of 25 to 50 µm formed within G/A due to the synergistic action of the dual network disappear after 3 days of biodegradation. A large number of pores enlarges to 175 µm and the percent volume of these pores gradually increases during 7 days. Figure 7.5c further indicates that the internal connectivity of the pores of G/A was broken by collagenase type II after 7 days.

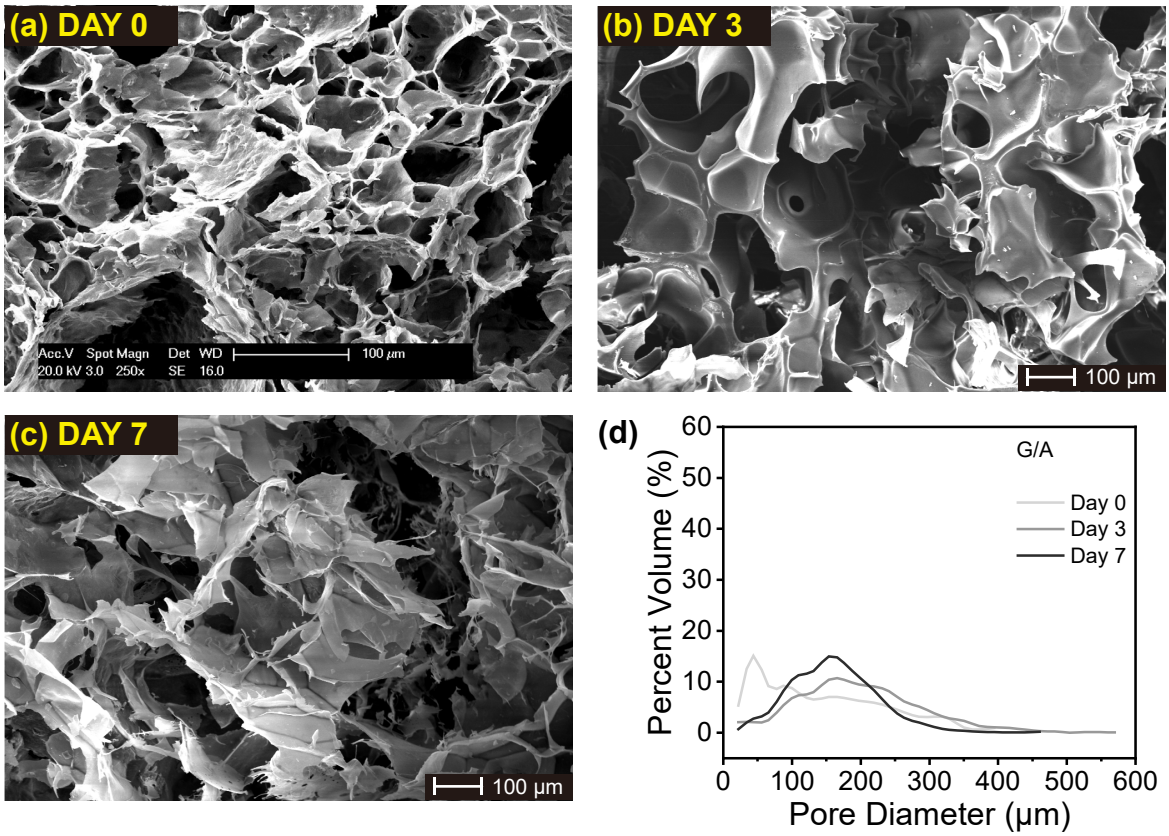

Figure 7.5: SEM images of G/A after (a) 0, (b) 3, and (c) 7 days of biodegradation. (d) Pore size distributions of G/A after 0, 3, and 7 days of biodegradation. A large number of pores enlarges to 175 µm after 3 days of biodegradation. The internally connected porous structure of G/A was broken by collagenase type II after 7 days.

However, the pore size of G/A/MFC-0.7 does not change much after 3 days of biodegradation (Figure 7.6b) and remains concentrated in the range of 25 to 50 microns (Figure 7.6d), though the percent volume of these pores decreases from 53.44 to 38.2%. After 7 days of biodegradation, the hydrogel is still interconnected porous structure (Figure 7.6c), though the pore size distribution widens slightly and the pore size rises to the range of 50 to 100 μm (Figure 7.6d). The results indicate that hydrogen bonding interactions between components MFC and ICE G/A network can slow down the biodegradation process of gelatin methacryloyl network in MFC-composited ICE system [473].

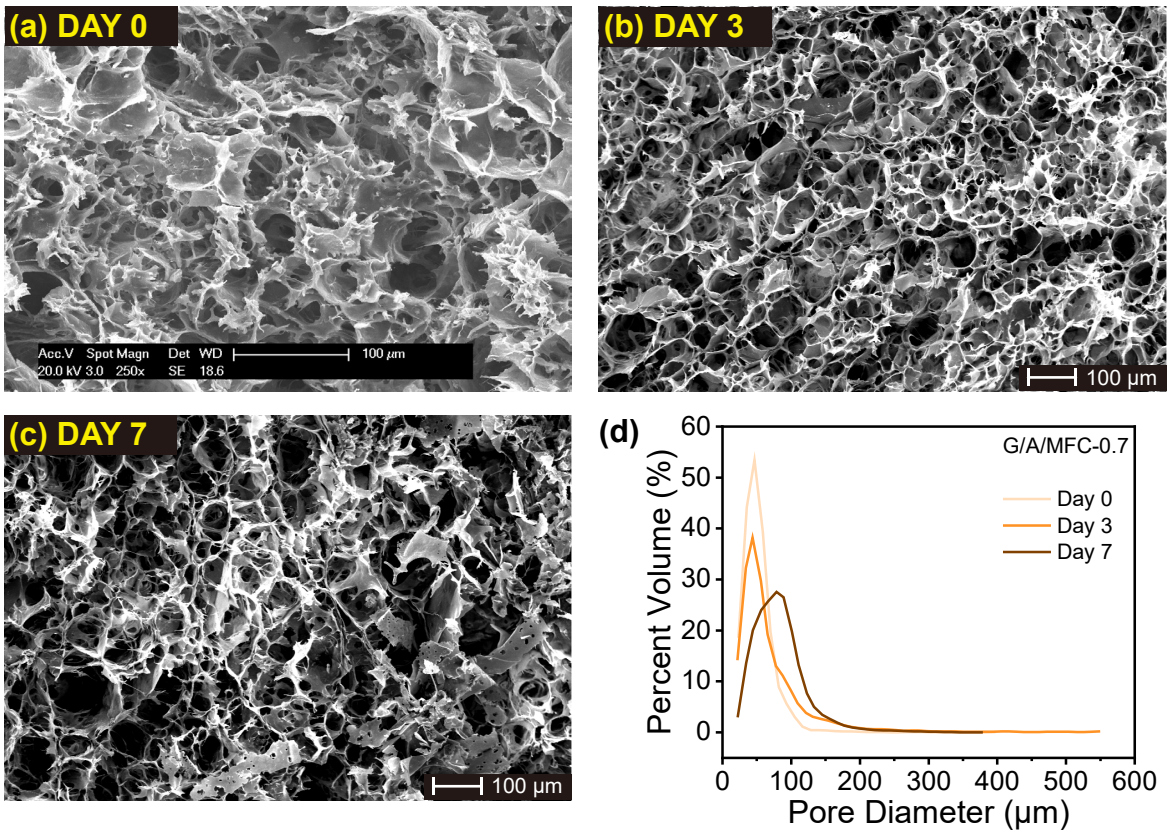

Figure 7.6: SEM images of G/A/MFC-0.7 after (a) 0, (b) 3, and (c) 7 days of biodegradation. (d) Pore size distributions of G/A/MFC-0.7 after 0, 3, and 7 days of biodegradation. Pores still remain concentrated in the range of 25 to 50 microns after 3 days and maintain internal connectivity after 7 days of biodegradation. Adding MFC can slow down the biodegradation process of ICE G/A hydrogels.

The morphological changes of G/A/NFC-1 during biodegradation (Figure 7.7a, b, c) are very similar to those of G/A/MFC-0.7. However, the proportion of pores in the range of 25 to 50 µm after 3 days of biodegradation is more than that in the undegraded state, which is very strange. The retention of internal connectivity and the expansion of the pore size to 50 to 100 µm after 7 days are expected [474, 475].

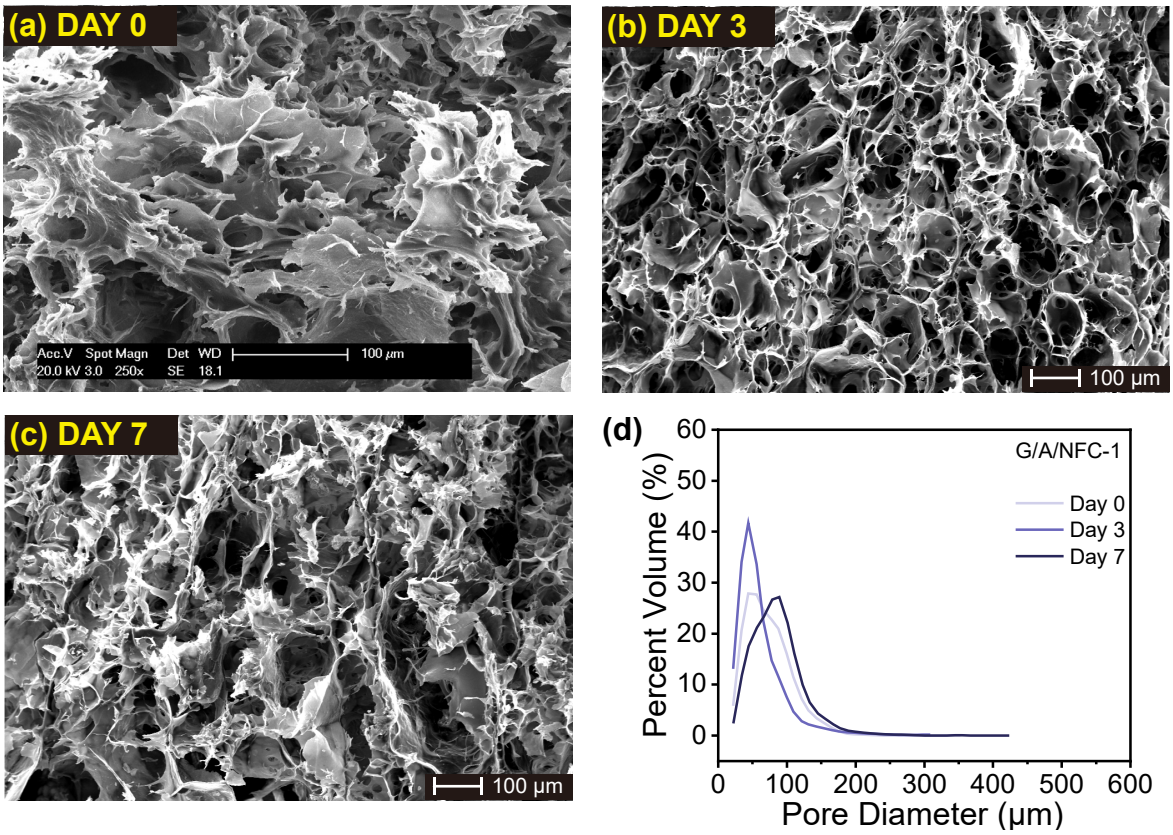

Figure 7.7: SEM images of G/A/NFC-1 after (a) 0, (b) 3, and (c) 7 days of biodegradation. (d) Pore size distributions of G/A/NFC-1 after 0, 3, and 7 days of biodegradation. Pores are concentrated in the range of 25 to 50 microns after 3 days and maintain internal connectivity after 7 days of biodegradation.

In conclusion, collagenase type II weakens hydrogels G/A, G/A/MFC-0.7, and G/A/NFC-1 by degrading gelatin methacryloyl network. However, MFC and NFC can delay the enzymatic biodegradation reaction of hydrogels by hydrogen bonding interactions between components MFC and ICE G/A network and thus improve the physiological stability of ICE hydrogels. The slow

biodegradation process of cellulose-composited ICE hydrogels plays a vital role in the maintenance of the initial modulus of the hydrogel and in the growth and proliferation of the cells in the hydrogel.

7.3.3 Cell viability in printed hydrogels

Cell adhesion of gelatin methacryloyl is widely recognized, attributed to the preservation of bioactive motifs in its structure, notably the arginine-glycine-aspartic acid (RGD) sequences [476–478]. To assess the effect of cellulose incorporation on the cytocompatibility of component G in hydrogels, formulated G/A/MFC-0.7 and G/A/NFC-1 encapsulated with mouse preosteoblasts MC3T3-E1 were bioprinted into 4- and 6-layer scaffolds, respectively. Cell distribution and viability within the scaffolds were tracked over a 21-day period. Figure 7.8 and Figure 7.9 display confocal Z-stack images of dead, live, and merged cells in 4-layer G/A/MFC-0.7 scaffolds, while Figure 7.10 and Figure 7.11 show cell images in 6-layer G/A/MFC-0.7 scaffolds over 21 days. Also, Figure 7.12 plus Figure 7.13, Figure 7.14 plus Figure 7.15 demonstrate the cell survival in G/A/NFC-1 scaffolds with 4 and 6 layers, respectively. Cell distributions in 3D scaffolds G/A/MFC-0.7 and G/A/NFC-1 over 21 days are exhibited in Figure 7.16.

Within the first 2 days, cells are found evenly and irregularly distributed in G/A/MFC-0.7 and G/A/NFC-1 scaffold with 4 and 6 layers, suggesting that the adhesion behaviour of cells to gelatin methacryloyl in the scaffold is not obvious. It is worth noting that cell activity is low and cell viabilities are all only about 78% (Figure 7.17) in the first 2 days, likely because cells on the surface of the hydrogel scaffolds can gain sufficient energy supply but cells located inside the hydrogel scaffolds could not take up the nutrients in time. However, with the gradual penetration of nutrients, the number of dead cells decreases significantly and the cell density gradually increases. Therefore, cell viabilities for all samples increase to about 90% after 7 days of culture (Figure 7.17). Also, the distribution of cells in the 3D scaffold is found to be regional after 7 days (Figure 7.16), implying that cell adhesion to the scaffold occurs [479]. The results are in good agreement with previous reports published by Chalmers University of Technology [441, 480]. As reported by Henriksson

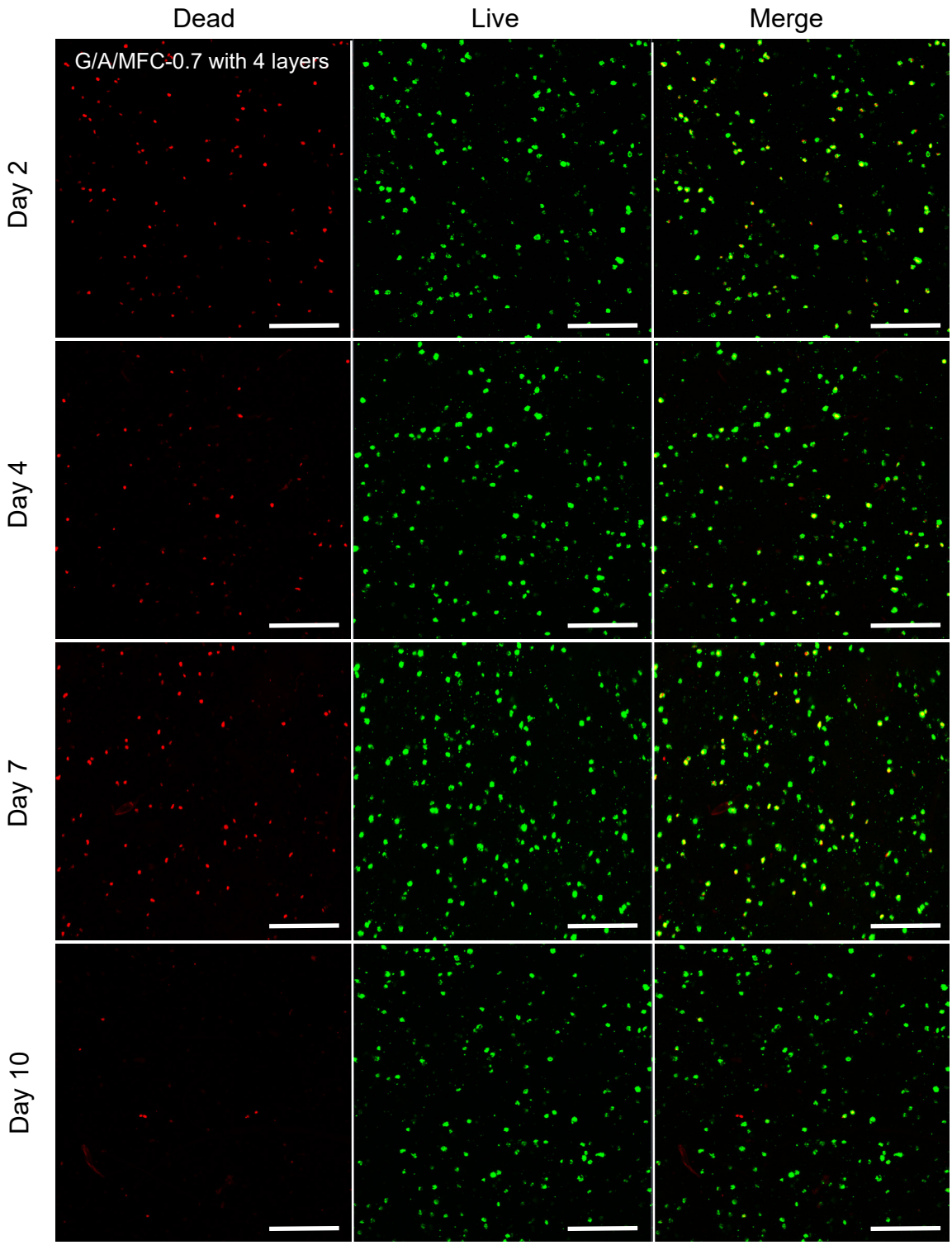

Figure 7.8: Confocal Z-stack images of dead, live, and merged cells for G/A/MFC-0.7 scaffolds with 4 layers at Day 2, 4, 7, and 10. Scale bar is 200 μm.

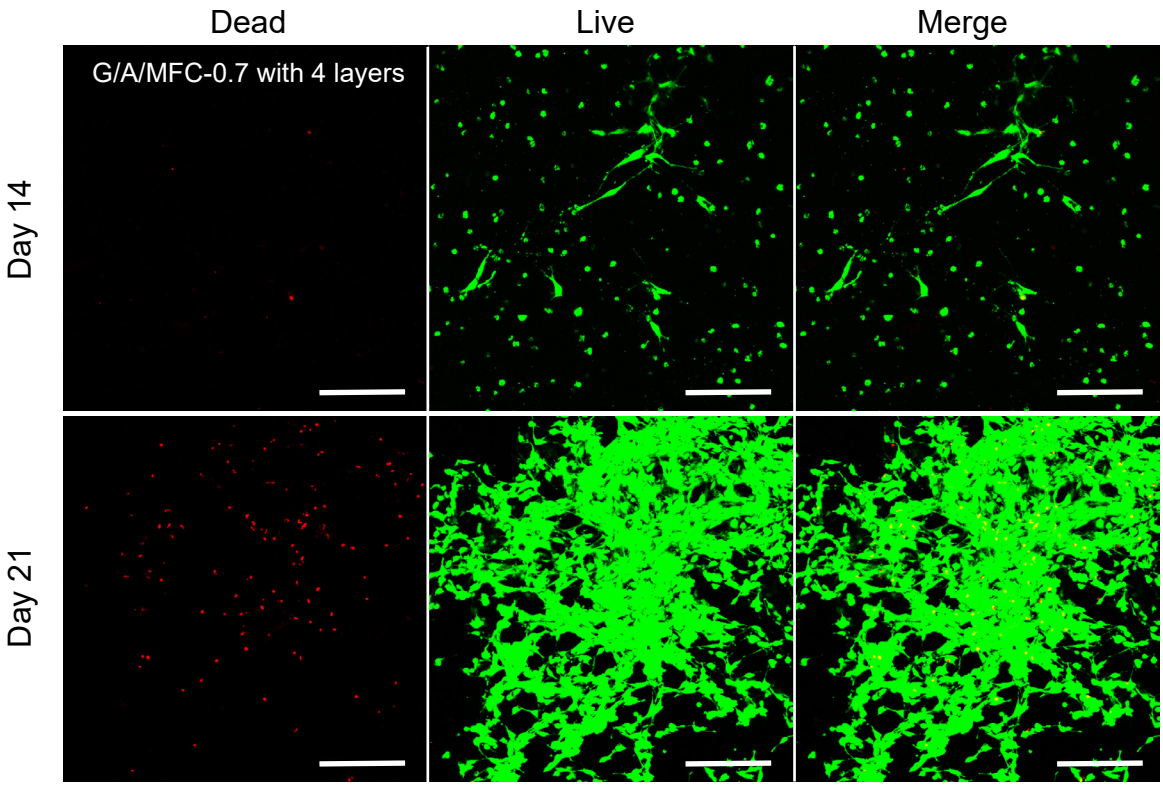

Figure 7.9: Confocal Z-stack images of dead, live, and merged cells for G/A/MFC-0.7 scaffolds with 4 layers at Day 14 and 21. Scale bar is 200 μm.

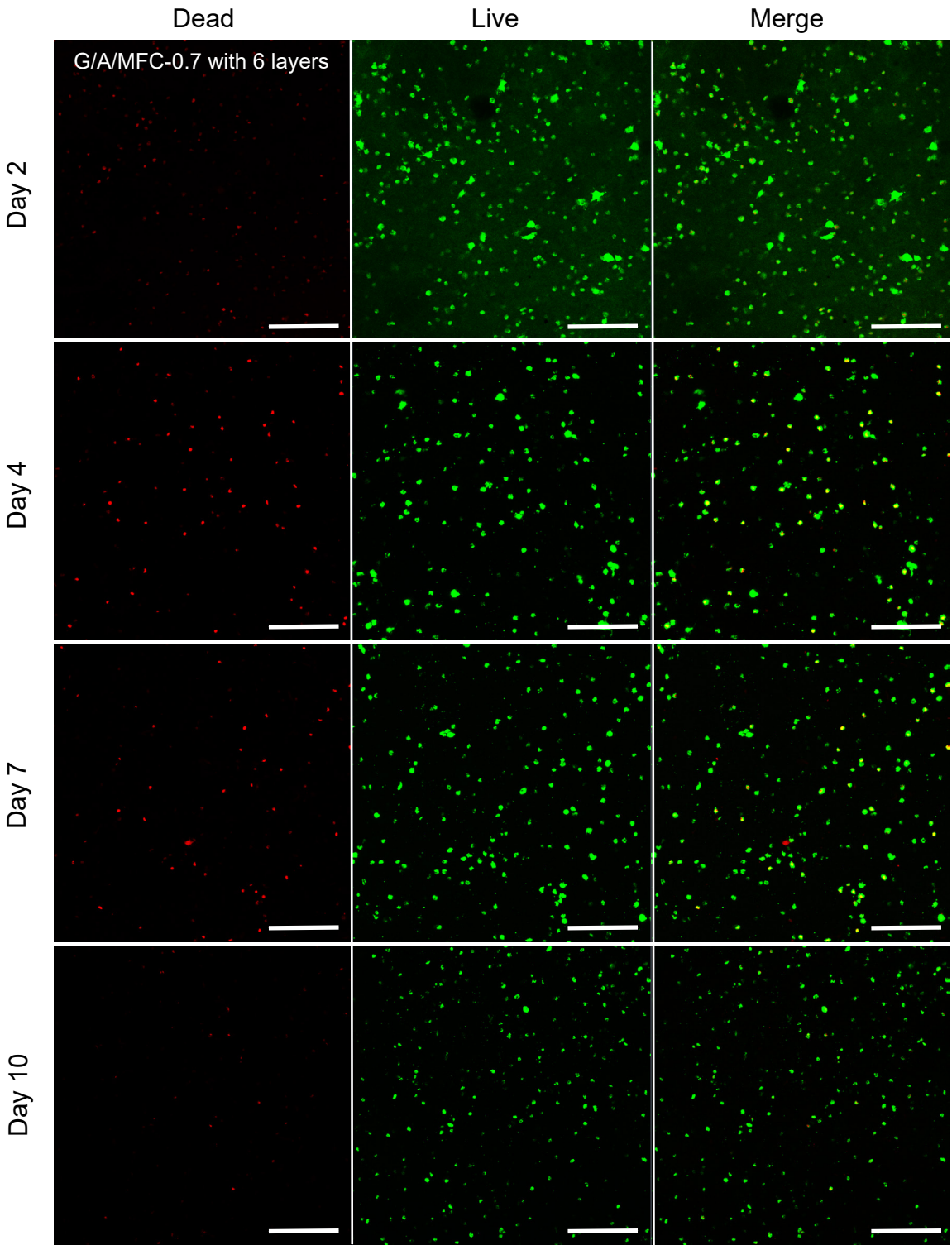

Figure 7.10: Confocal Z-stack images of dead, live, and merged cells for G/A/MFC-0.7 scaffolds with 6 layers at Day 2, 4, 7, and 10. Scale bar is 200 μm.

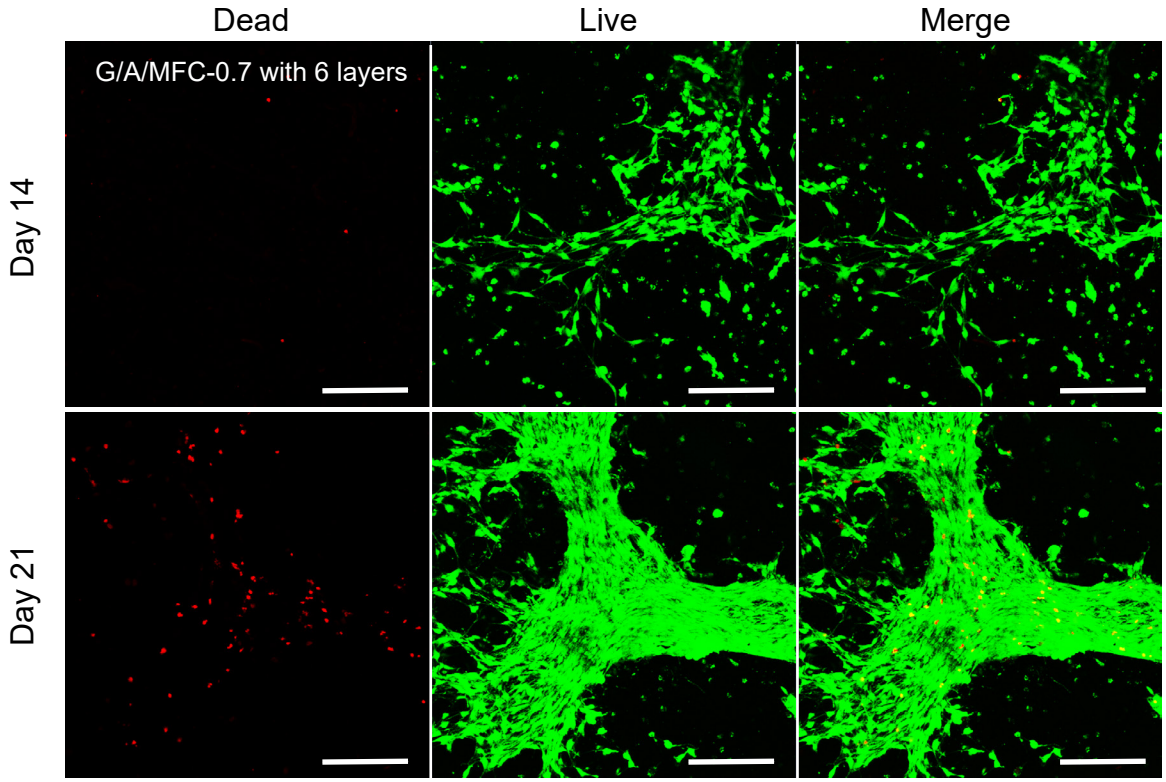

Figure 7.11: Confocal Z-stack images of dead, live, and merged cells for G/A/MFC-0.7 scaffolds with 6 layers at Day 14 and 21. Scale bar is 200 μm.

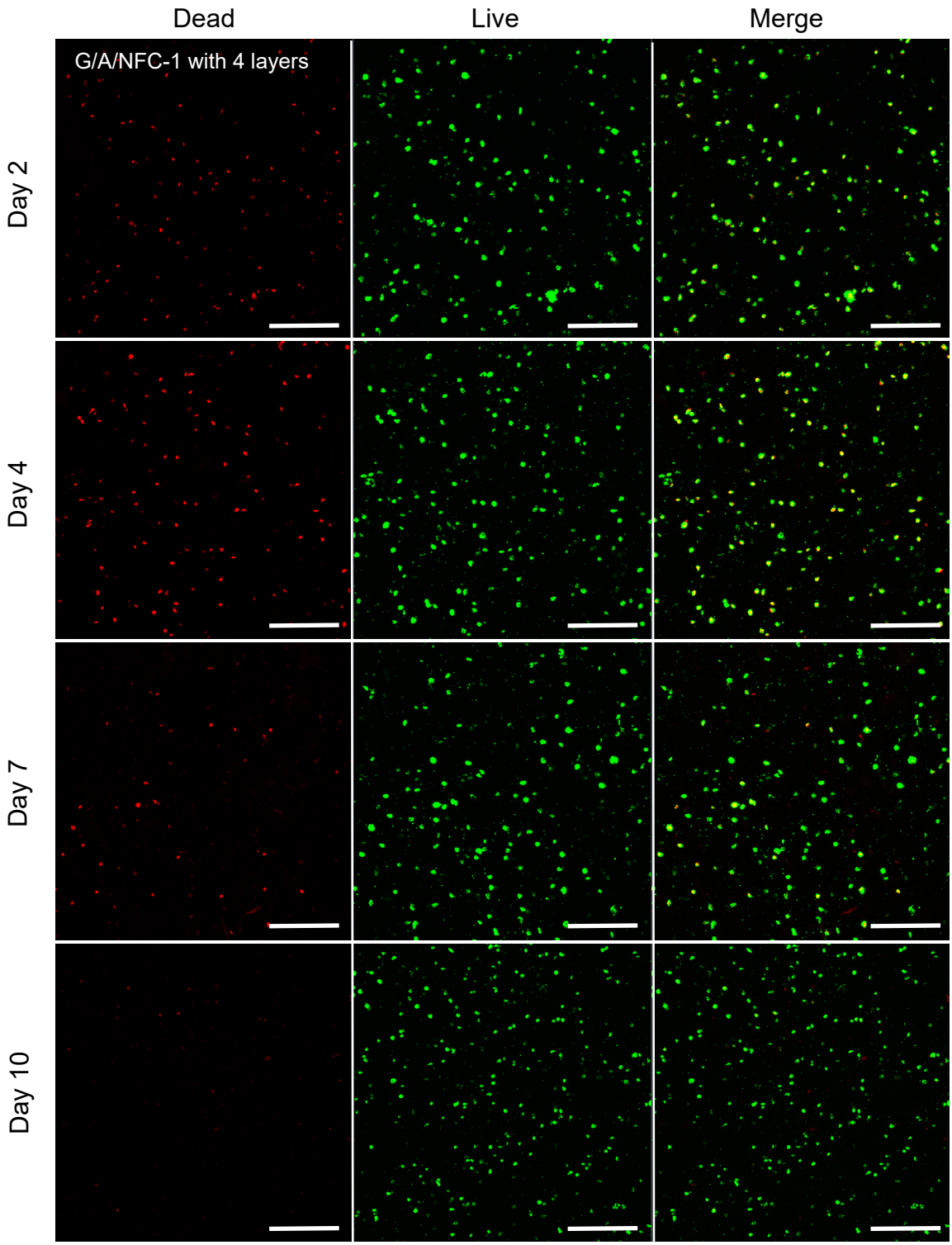

Figure 7.12: Confocal Z-stack images of dead, live, and merged cells for G/A/NFC-1 scaffolds with 4 layers at Day 2, 4, 7, and 10. Scale bar is 200 μm.

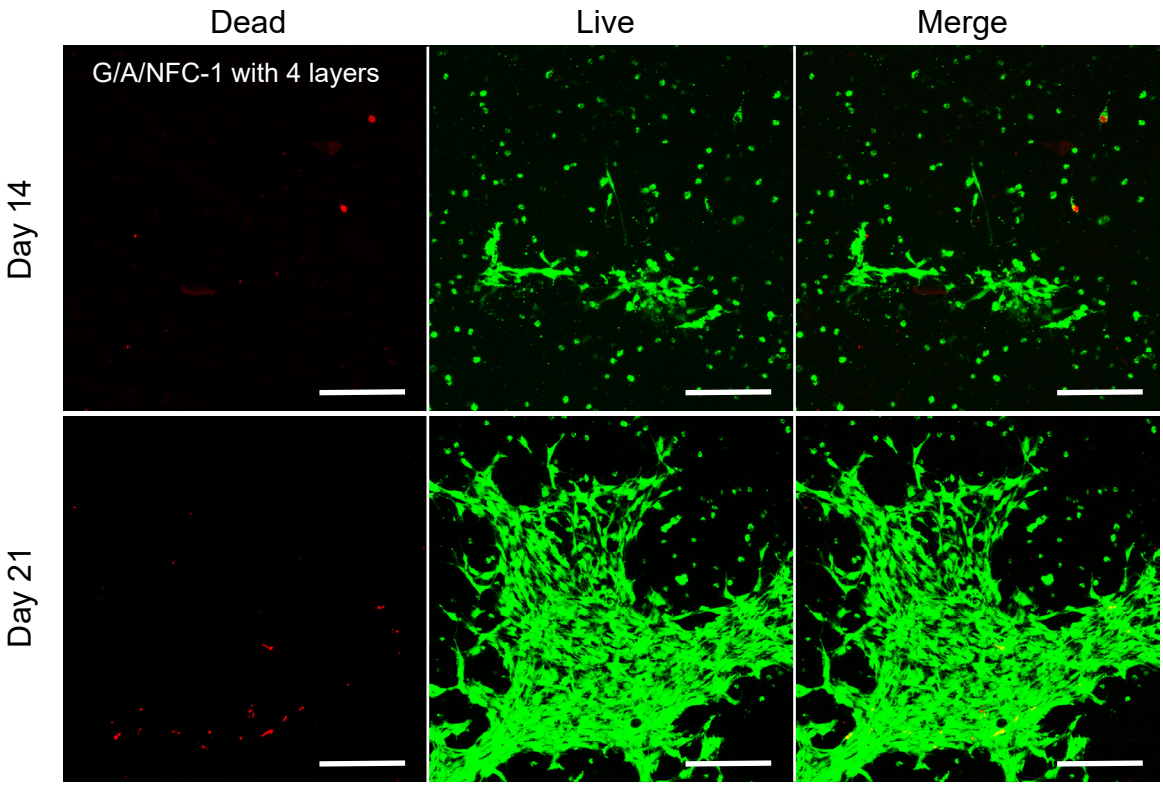

Figure 7.13: Confocal Z-stack images of dead, live, and merged cells for G/A/NFC-1 scaffolds with 4 layers at Day 14 and 21. Scale bar is 200 μm.

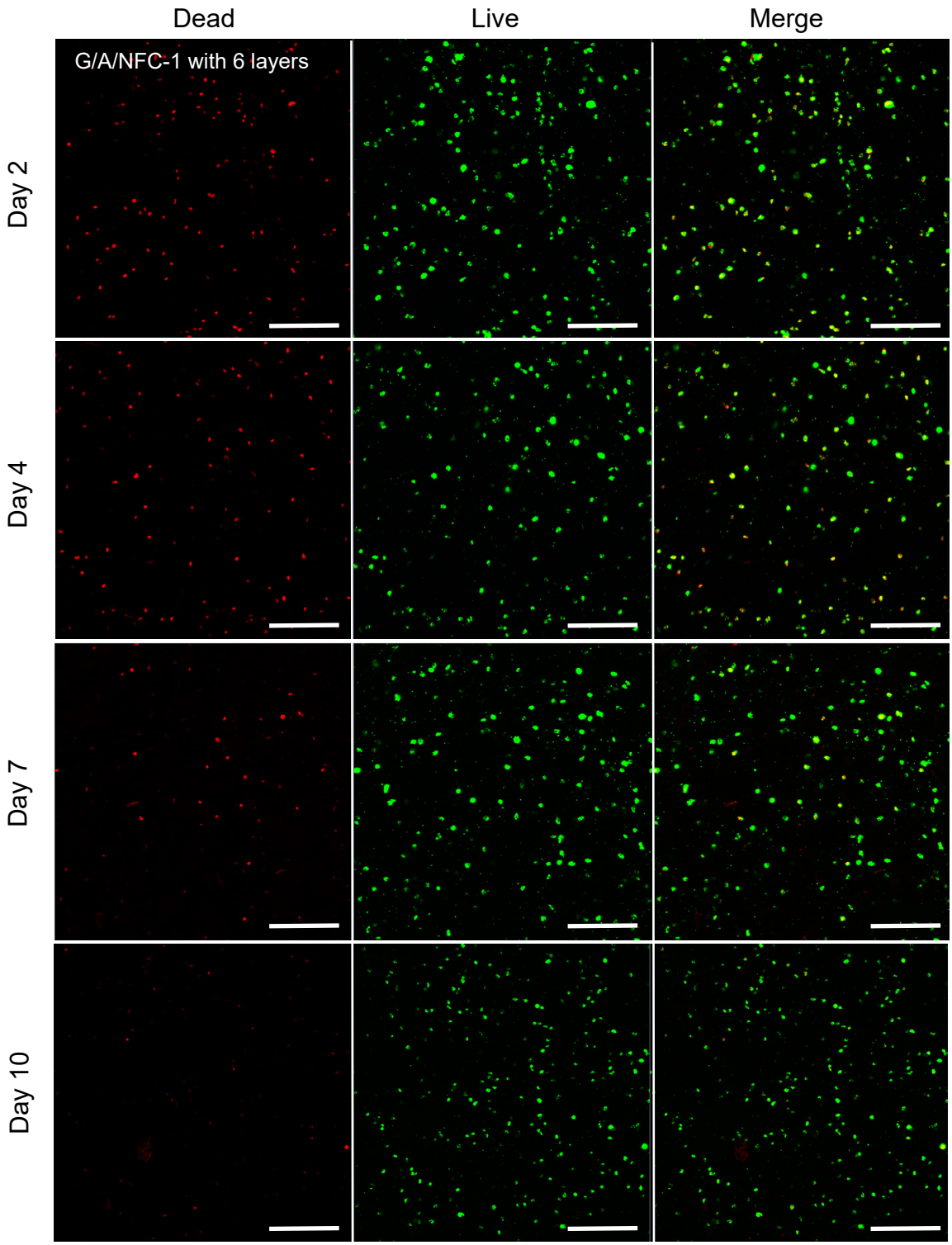

Figure 7.14: Confocal Z-stack images of dead, live, and merged cells for G/A/NFC-1 scaffolds with 6 layers at Day 2, 4, 7, and 10. Scale bar is 200 μm.

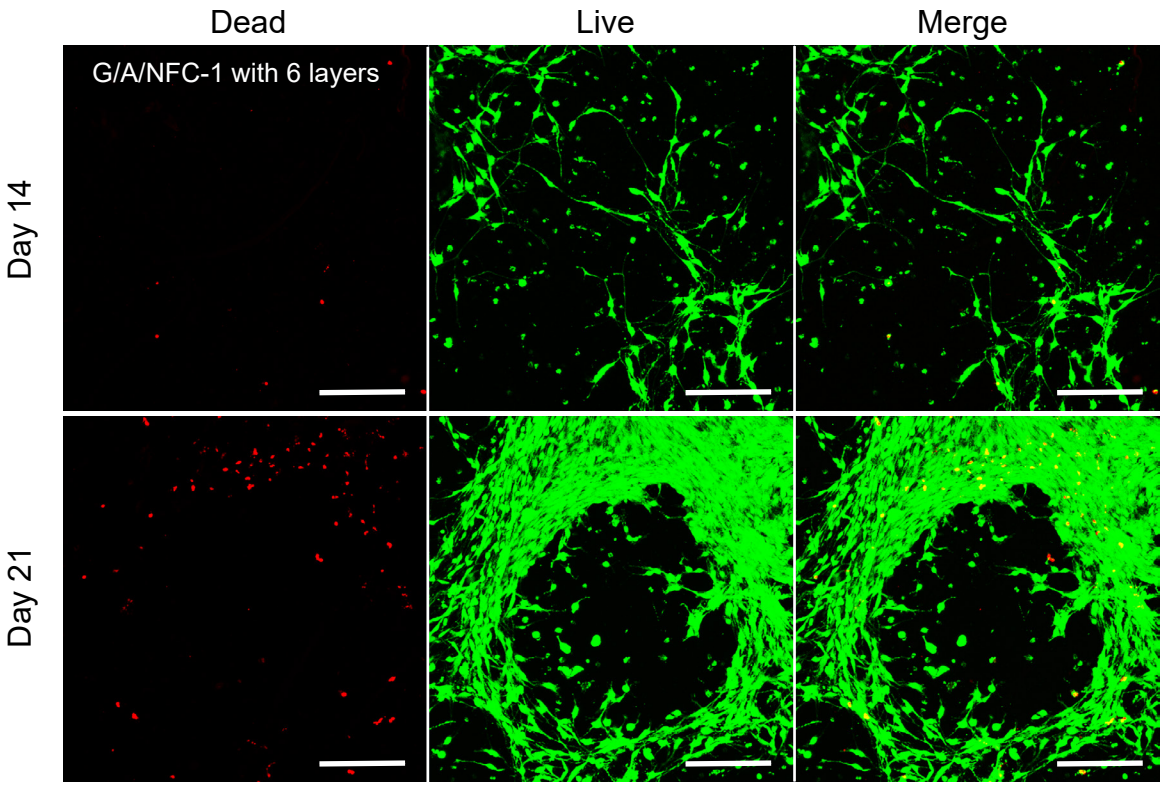

Figure 7.15: Confocal Z-stack images of dead, live, and merged cells for G/A/NFC-1 scaffolds with 6 layers at Day 14 and 21. Scale bar is 200 μm.

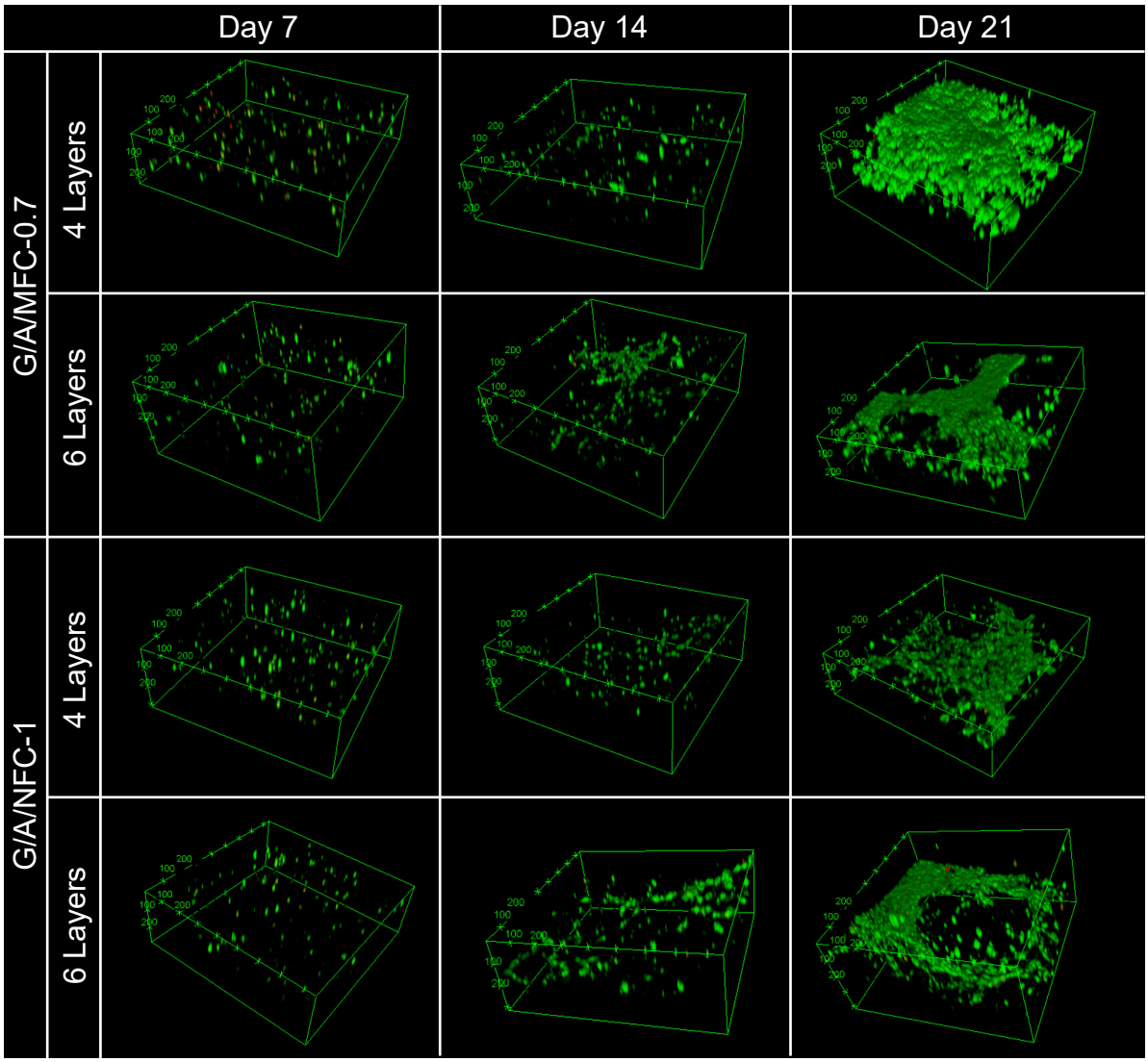

Figure 7.16: Three-dimensional projections of the confocal Z-stack cell images in G/A/MFC-0.7 and G/A/NFC-1 scaffolds with 4 and 6 layers after incubating 7, 14, and 21 days.

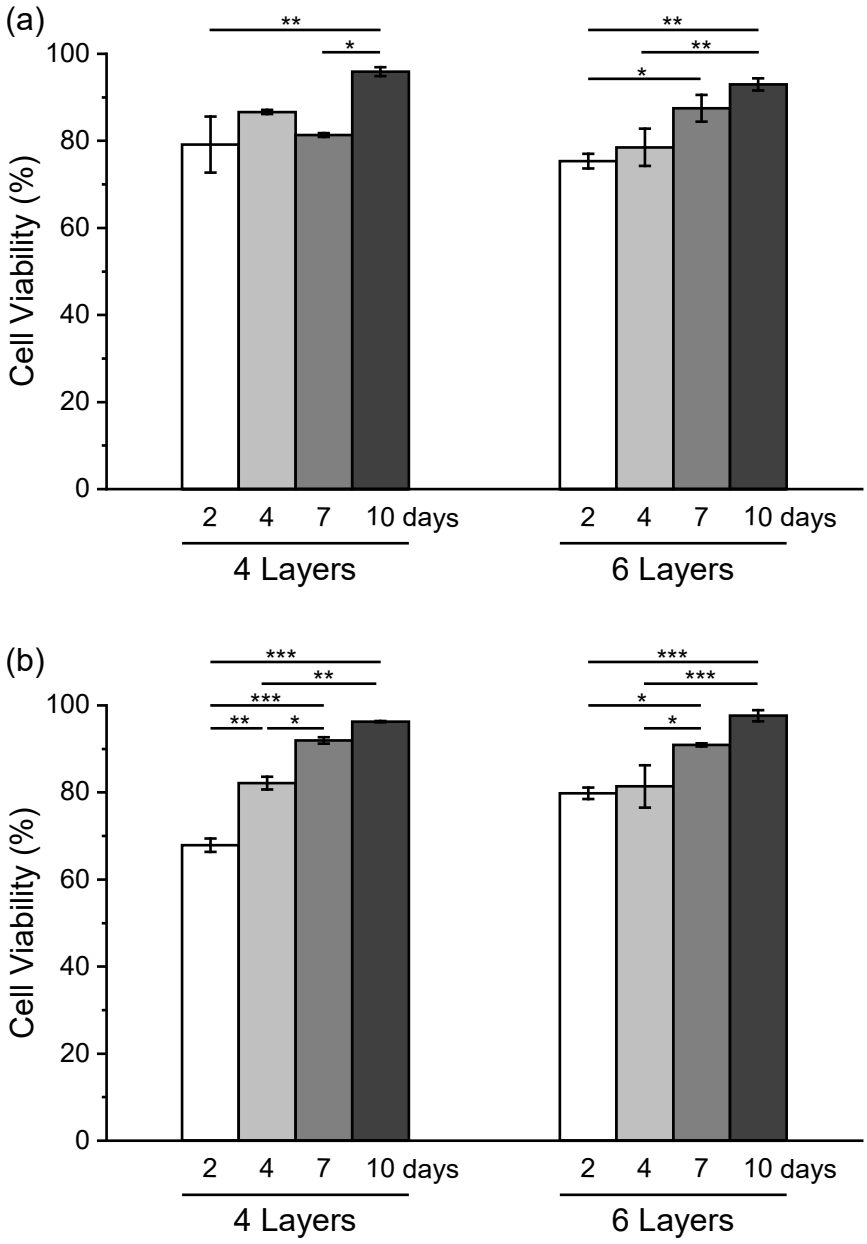

Figure 7.17: Cell viabilities in bioprinted (a) G/A/MFC-0.7 and (b) G/A/NFC-1 scaffolds with 4 and 6 layers after incubating 2, 4, 7, and 10 days.

et al, mouse mesenchymal stem cell line C3H10T1/2 were encapsulated in nanocellulose/alginate formulation (Cellink) and printed in gridded structures [480]. Live/Dead staining also shows that after 7 days in the expansion medium, cell viability significantly increased from 64% to 95%, evidence that the printed structures are compatible with culturing of these cells [480]. In addition, in the present work, no significant effects of cellulose fibril size and number of scaffold layers on cell viability are observed.

After 14 days of culture, cells within all samples begin to elongate along the shape of the scaffold. Notably, the growth rates of cells within the 6-layer hydrogel scaffolds (Figure 7.11, Figure 7.15) are higher than that of the 4-layer hydrogel scaffolds (Figure 7.9, Figure 7.13, Figure 7.16), which can be attributed to the fact that the 6-layer scaffolds contain more ingredient G and thus more bioactive sites than the 4-layer scaffolds to induce cell adhesion and growth along the inner texture of the hydrogel scaffold.

After 21 days of culture, live cells have divided and proliferated extensively with high cell densities. Even the saturation of cells within the 6-layer hydrogel scaffolds is higher than that within the 4-layer hydrogel scaffolds. In particular, for 6-layered G/A/MFC-0.7 and G/A/NFC-1, MC3T3-E1 cells are significantly distributed along the printed paths inside the scaffold (Figure 7.11, Figure 7.15, and Figure 7.16). In conclusion, the results confirm that MFC and NFC do not hinder the cell-attachment behaviour of component G. MFC-composited and NFC-composited ICE G/A hydrogels have superior cytocompatibility and are suitable for long-term cell culture and remodelling.

Enzymatic biodegradation of MFC-composited and NFC-composited ICE hydrogels in 5 U/mL collagenase type II after 12 days has been demonstrated to be approximately 50% (Figure 7.4). However, in *in vivo* environment, fibroblasts are regulated by physiological and pathological conditions to secrete collagenase type II to ensure that this enzyme is involved in collagen breakdown and tissue repair when necessary [481, 482]. Therefore, the active concentration of collagenase type II *in vivo* may be lower than 5 U/ml used in this experiment. Further, the *in vivo* biodegradation process of

cell-encapsulated MFC-composited and NFC-composited ICE hydrogels should be slower than the enzymatic biodegradation process depicted in Figure 7.4.

To assess whether there is a matched kinetics between tissue remodelling and degradation process of cell-containing MFC-composited and NFC-composited ICE hydrogel scaffolds, the morphological changes of cell-loaded G/A/MFC-0.7 and G/A/NFC-1 were observed after 7 and 21 days of incubation without the addition of collagenase type II. As can be seen from Figure 7.18a, c, e, g and Figure 7.19a, c, e, g, cell-containing G/A/MFC-0.7 and G/A/NFC-1 hydrogel scaffolds maintain their structural integrity after 7 and even 21 days of incubation and the path of bioprinted scaffolds is still clearly visible. When morphology of these scaffolds was amplified, it can be noticed that the porosities of cell-containing G/A/MFC-0.7 and G/A/NFC-1 scaffolds with 4 and 6 layers incubated for 21 days are larger than that of the scaffolds incubated for 7 days (Figure 7.18b, d, f, h, and Figure 7.19b, d, f, h). However, the intrinsic connectivity of the pores for cell-containing G/A/MFC-0.7 and G/A/NFC-1 scaffolds remains intact after 21 days of incubation (Figure 7.18f, h, and Figure 7.19f, h).

The above results suggest that the structural integrity of cell-encapsulated MFC-composited and NFC-composited ICE hydrogel scaffolds allows them to provide support to the damaged tissue area during the 21-day incubation period, despite the presence of two types of degradation in the hydrogels: one is natural degradation in the hydrogel resulted from the weakening of the ICE dual network synergy and cellulose-ICE synergism (Figure 7.1); another one is enzymatic biodegradation caused by a small number of lytic enzymes secreted by the cells within the hydrogel. Moreover, the increase in porosities of cell-containing hydrogels due to the above two degradations provides a favourable space for cells to proliferate significantly and produce new extracellular matrix within 21 days. In conclusion, the slow degradation behaviour of the cell-encapsulated MFC-composited and NFC-composited ICE hydrogel scaffolds is well-matched to the tissue restoration process.

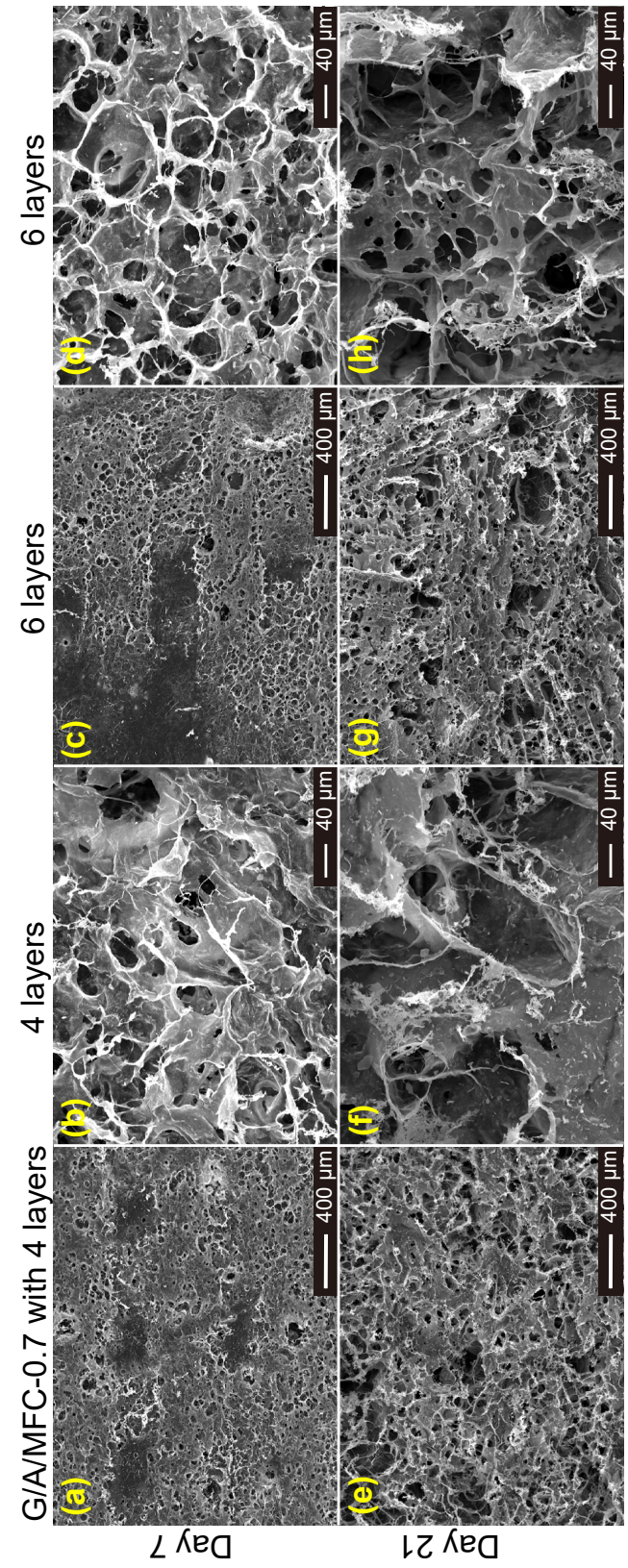

Figure 7.18: SEM images of cell-loaded G/A/MFC-0.7 scaffolds with 4 and 6 layers after incubation of (a, b, c, d) 7 and (e, f, g, h) 21 days.

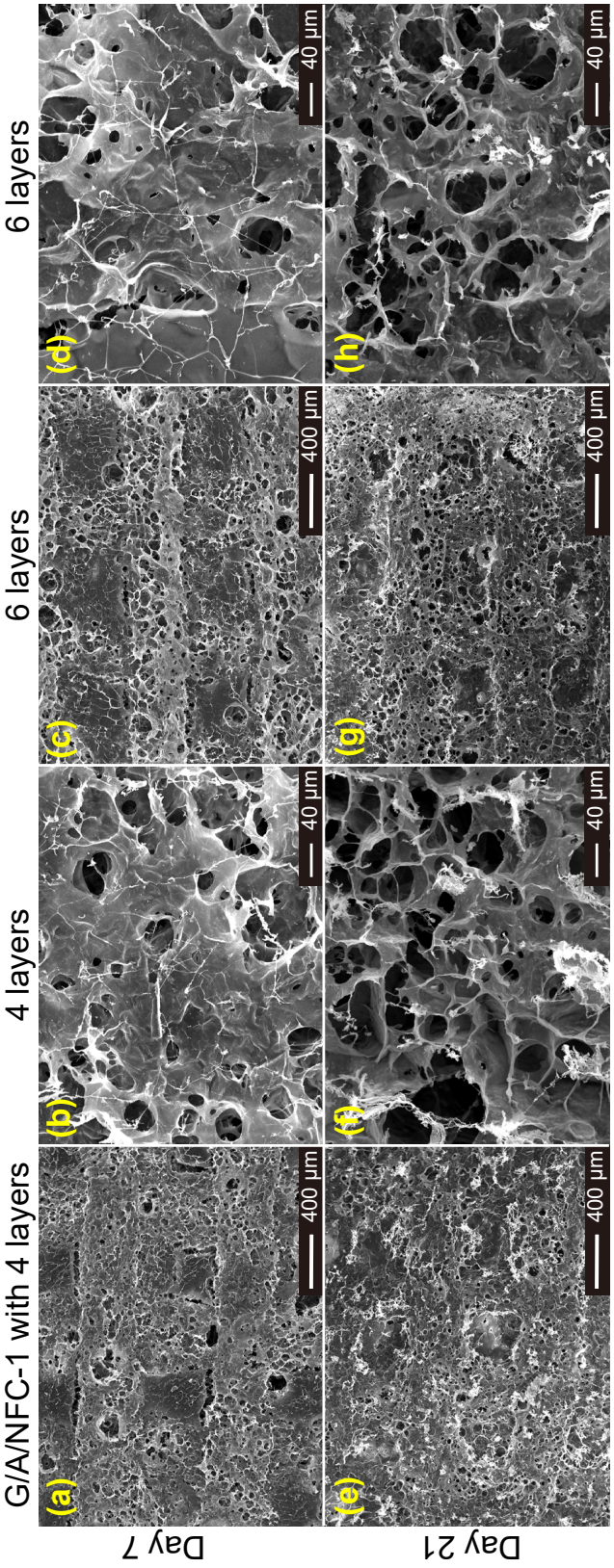

Figure 7.19: SEM images of cell-loaded G/A/NFC-1 scaffolds with 4 and 6 layers after incubation of (a, b, c, d) 7 and (e, f, g, h) 21 days.

7.3.4 Controlled release of ampicillin

The relationship between concentrations of ampicillin and absorbance at 220 nm is shown in Figure 7.20a. When concentrations of ampicillin are below 150 μg mL^{-1}, a linear relationship between concentration and absorbance can be observed. However, when the concentration exceeds 250 μg mL^{-1}, the absorbance at 220 nm tends to be saturated. Since Beer's law (Equation 3.12) is valid for very dilute solutions, to improve accuracy, a linear fit is performed on all data points with absorbance below 1. The final standard calibration curve of ampicillin is shown in Figure 7.20b.

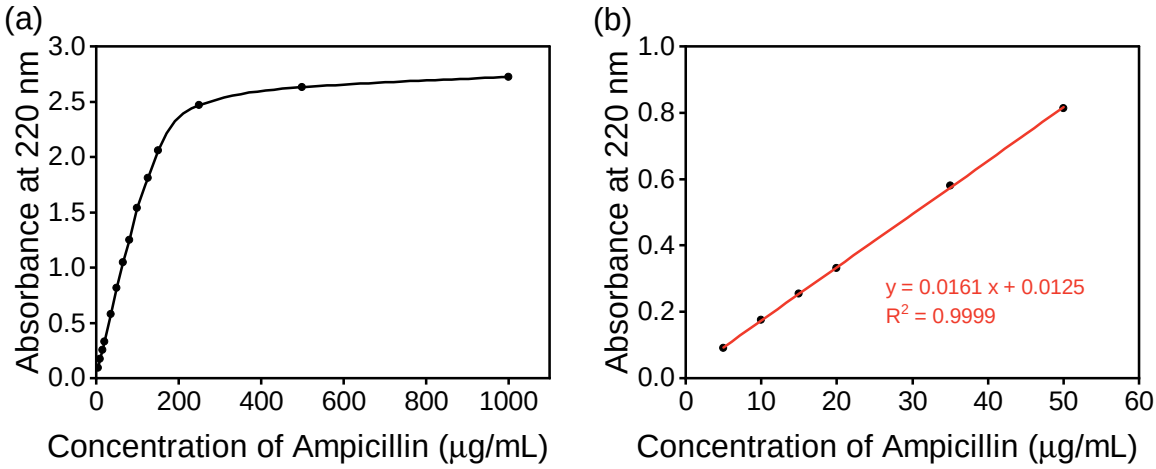

Figure 7.20: (a) Representative curve of concentration of ampicillin versus absorbance at 220 nm within the concentration range of 5 to 1000 μg mL^{-1}. (b) Standard calibration curve of ampicillin within the concentration range of 5 to 50 μg mL^{-1}.

Figure 7.21 depicts the embedding of ampicillin into the hydrogel via post-loading. The drug loading capacity (*LC*) of all samples gradually increases with the increase in loading time. After 21 h, *LC* of the samples level off. Eventually, at saturation loading (at 24 h), *LC* of the hydrogels and encapsulation efficiency (*EE*) of ampicillin in samples are listed in Table 7.1.

It can be seen that *LC* of G/A for water-soluble ampicillin is higher than G/A/MFC-0.4 and G/A/MFC-0.55. After saturation loading, *LC* and *EE* of G/A are 7.34 mg/g and 7.5%, respectively. From the perspective of pore structures (Figure 6.19) and swelling behaviours ((Figure 7.1)) of G/A, G/A/MFC-0.4, and G/A/MFC-0.55, G/A has a broader pore size distribution and a faster swelling

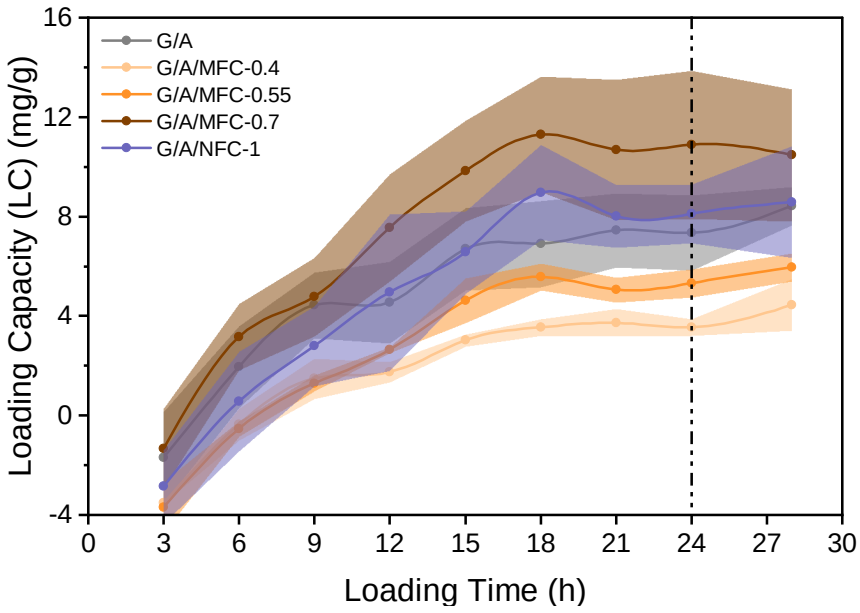

Figure 7.21: Drug loading capacity curves of hydrogel discs over time.

Table 7.1: Table of drug loading capacities and encapsulation efficiencies of ICE G/A hydrogel, MFC-composited ICE G/A hydrogels with different MFC content, and NFC-composited ICE G/A hydrogel after 24 h of post-loading.

Sample	**Loading capacity at 24 h (mg/g)**	**Encapsulation efficiency at 24 h (%)**
G/A	7.34 ± 1.51	7.5 ± 1.52
G/A/MFC-0.4	3.55 ± 0.33	4.2 ± 0.38
G/A/MFC-0.55	5.33 ± 0.56	6.41 ± 0.66
G/A/MFC-0.7	10.9 ± 2.98	11.47 ± 2.98
G/A/NFC-1	8.12 ± 1.17	9.38 ± 1.44

process than MFC-composited G/A hydrogels, hence resulting in higher loading capacities for drugs in the same period.

However, as the content of MFC in ICE hydrogels gradually increases from 0.4% to 0.7%, *LC* of MFC-composited G/A hydrogels for ampicillin enhance progressively even though MFC causes a decrease in swelling ratios of ICE hydrogels. The saturated *LC* and *EE* of G/A/MFC-0.7 surpass that of G/A, reaching 10.9 mg/g and 11.47%, respectively. This indicates the interactions between MFC and ampicillin, favourable for ampicillin encapsulation [483, 484]. Cellulose can be used as a drug carrier to achieve high drug loading within hydrogel matrices. Meanwhile, loading capacity

of such hydrogels for ampicillin is affected by both swelling ratio of the hydrogel and cellulose. The *LC* profile of G/A/NFC-1 is almost consistent with G/A, which can be attributed that the impact of hydrogel swelling on drug encapsulation and the competitive influence of cellulose-drug interactions on drug encapsulation exhibit a balanced interplay.

Figure 7.22a shows the cumulative release percentage of ampicillin from the hydrogels over time and Figure 7.22b is a linear fit to the first 60% cumulative release data of the samples. The slope of the linear fit, i.e. the release index (n_r) in the power law model (Equation 3.13), is shown in Table 7.2.

The release of ampicillin from sample G/A-AMP is rapid, with a half-life for release of 4.92 h. After 15 h, ampicillin is fully released. The release curve of G/A-AMP has a turning point near the half-life. The release index (0.27) of G/A-AMP is less than 0.45, indicating a Fickian diffusion-controlled release mechanism. Although the half-life of ampicillin release from G/A/MFC-0.4-AMP (4.57) is near that of G/A-AMP and the complete release time is also about 15 h, the cumulative release curve of G/A/MFC-0.4-AMP is significantly different from that of G/A-AMP. Moreover, n_r (0.95) for G/A/MFC-0.4-AMP demonstrates that the release mechanism of AMP from sample G/A/MFC-0.4-AMP is Super case II transport. The results suggest that MFC significantly changes the drug release kinetics of ICE hydrogels.

Further, when the content of MFC in ICE increased to 0.55%, the release half-life of ampicillin is extended to 12 h. After the half-life, the release rate decreases significantly. It is not until 72 hours that ampicillin is completely released from G/A/MFC-0.55-AMP. More obviously, 0.7% MFC extends the half-life of drug release from ICE hydrogels beyond 72 h, because percent cumulative release of AMP at 72 h is only 43.75%. Release indexes of both G/A/MFC-0.55-AMP and G/A/MFC-0.7-AMP are in a range of 0.45 to 0.89, proving an anomalous transport mechanism of ampicillin from such hydrogel system [485–488], possibly induced by both ampicillin diffusion and MFC incorporation. Moreover, compared with G/A-AMP, G/A/NFC-1-AMP system also delays ampicillin release process, as quantified by the half-life (24 to 48 h), complete release time (more

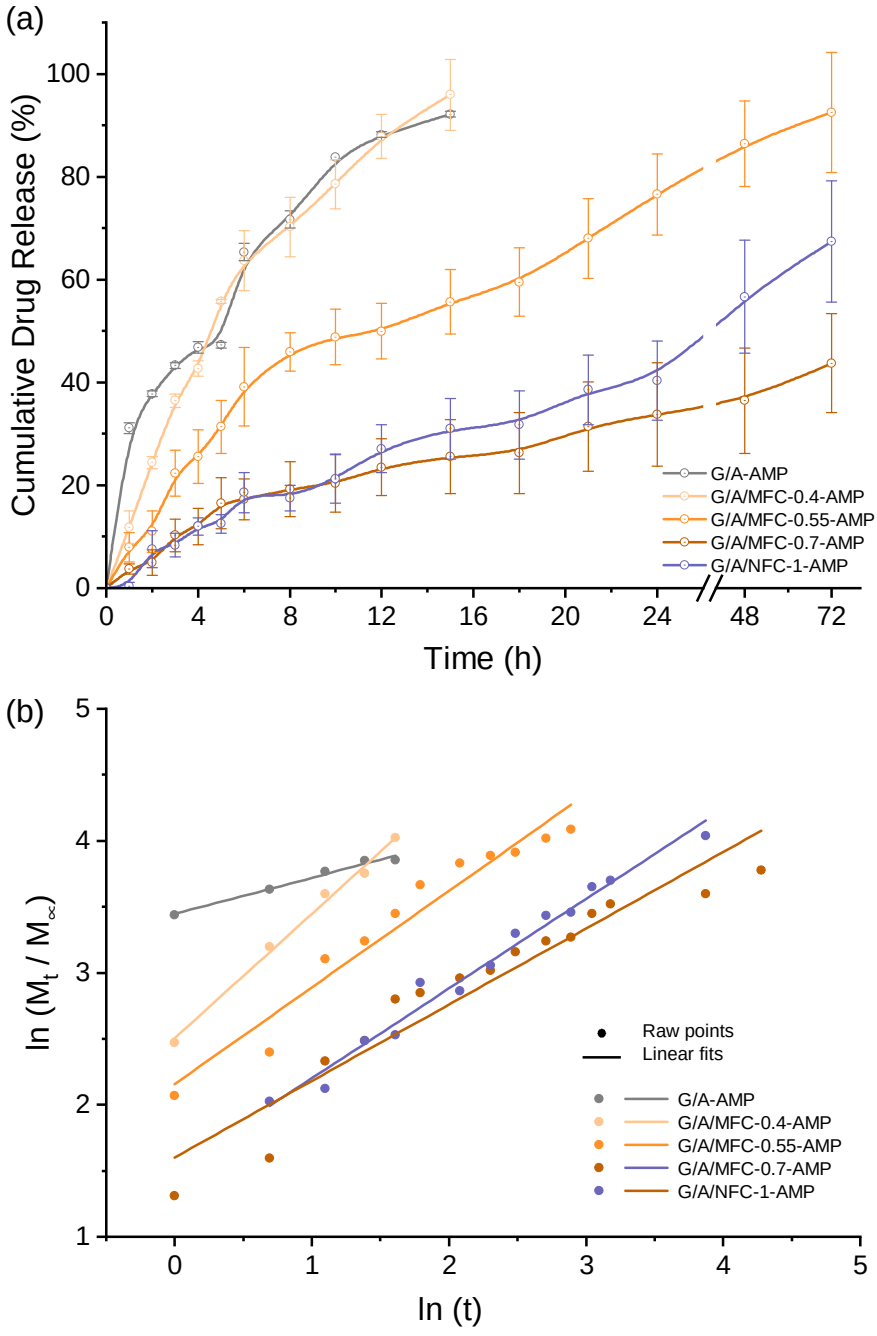

Figure 7.22: (a) Percentages of cumulative drug released from ampicillin-loaded hydrogel discs over time. (b) Fitting of the first 60% cumulative drug release according to the power law model (Equation 3.13). Dots represent raw data. The straight lines are the results of linear fits.

than 72 h), and release index (0.68).

In summary, the incorporation of cellulose into ICE hydrogel system alters the drug release

Table 7.2: Fitting results of cumulative ampicillin release using power-law model introduced by Peppas and co-workers [409].

Sample	release index , n_r	R^2
G/A-AMP	0.27 ± 0.02	0.98
G/A/MFC-0.4-AMP	0.95 ± 0.04	0.99
G/A/MFC-0.55 -AMP	0.73 ± 0.06	0.95
G/A/MFC-0.7-AMP	0.58 ± 0.05	0.92
G/A/NFC-1-AMP	0.68 ± 0.03	0.98

kinetics, shifting the release mechanism from Fickian diffusion-controlled release to anomalous transport determined by both diffusion and MFC doping. Combined with the interaction between cellulose and drugs during the drug encapsulation process, cellulose may act as a barrier for drug diffusion in ICE hydrogel systems, contributing to a controlled and sustained release of drugs. Such release behaviour is of significance for drug-loaded hydrogel scaffolds to achieve several days of drug delivery and long-term therapeutic interventions in damaged tissues.

7.3.5 Antimicrobial properties of drug-loaded hydrogels

Ampicillin, as a conventional antibiotic medicine, has been extensively utilised for the treatment of bacterial infections, demonstrating efficacy against both Gram-negative and Gram-positive bacteria [489]. The effect of cellulose addition on the antibacterial properties of drug-loaded ICE hydrogels was studied by agar diffusion technique. Figure 7.23 illustrates the inhibition of Gram-negative bacteria (*E. Coli*) growth by ampicillin-loaded hydrogels, alongside corresponding negative and positive control groups over a span of three consecutive days, while Figure 7.24 shows the inhibitory effect of these samples on Gram-positive bacteria *S. Aureus*. The centre of the agar plate is the embedded hydrogel disc. The outer ring of the sample delineates the zone where bacterial proliferation is effectively suppressed, and the other areas are zones where bacteria multiply.

The positive control group represented by ampicillin exhibits noticeable inhibition of both *E. Coli* and *S. Aureus* strains after the initial day of cultivation. However, after day-2, ampicillin has

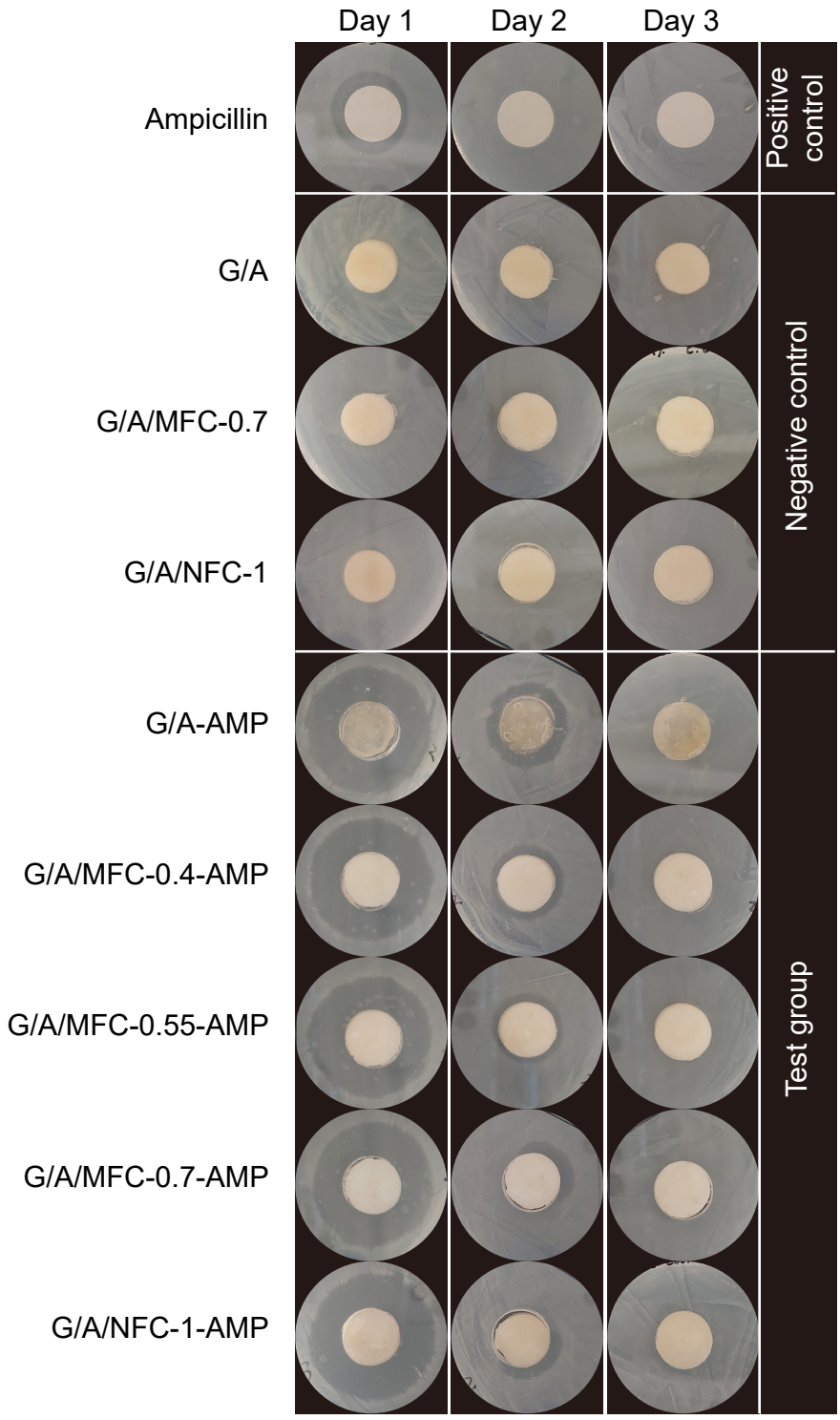

Figure 7.23: Inhibition zone images of antimicrobial ampicillin-loaded hydrogels, positive control, and negative controls using *E. Coli* on agar plates after incubating 1, 2, and 3 days.

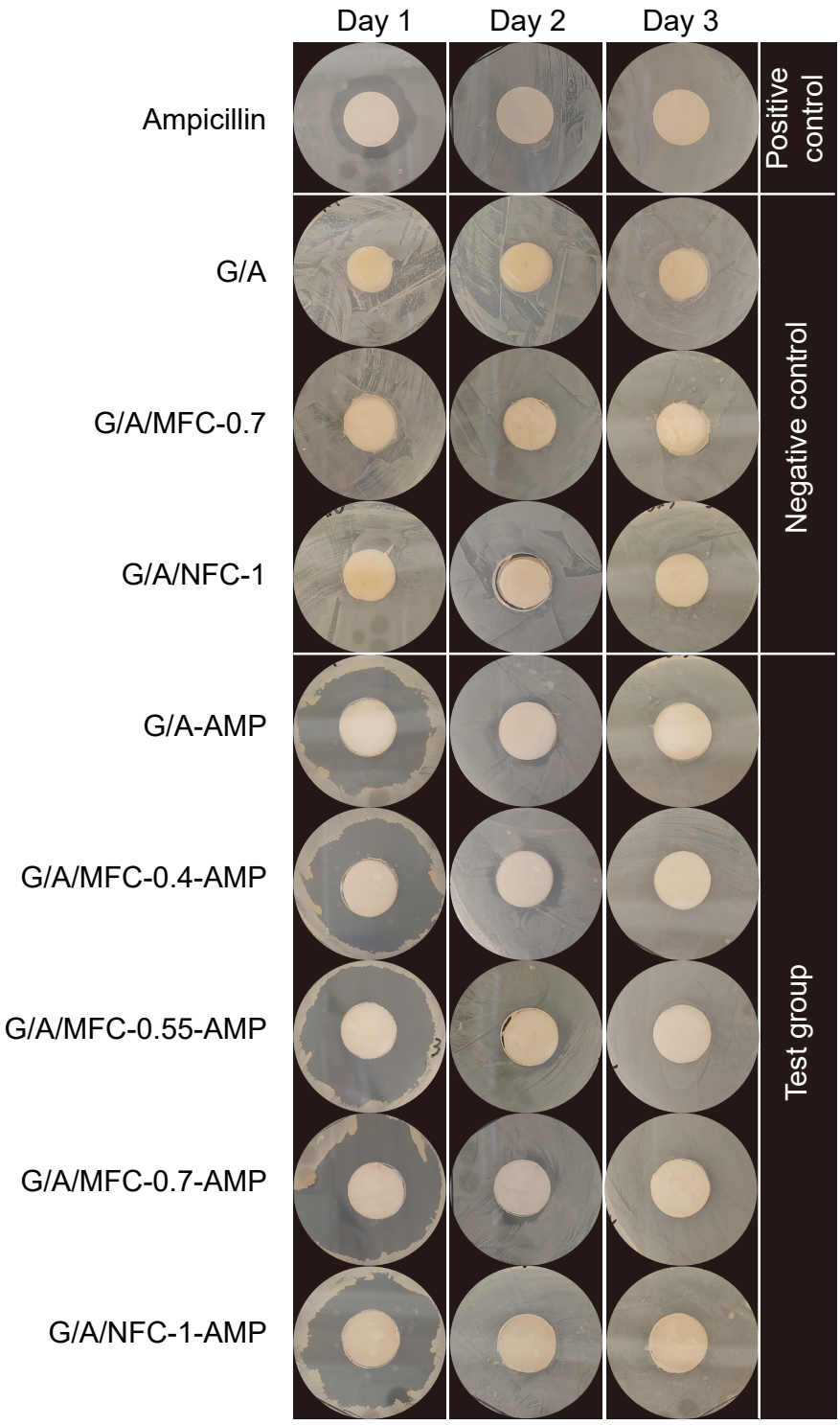

Figure 7.24: Inhibition zone images of antimicrobial ampicillin-loaded hydrogels, positive control, and negative controls using *S. Aureus* on agar plates after incubating 1, 2, and 3 days.

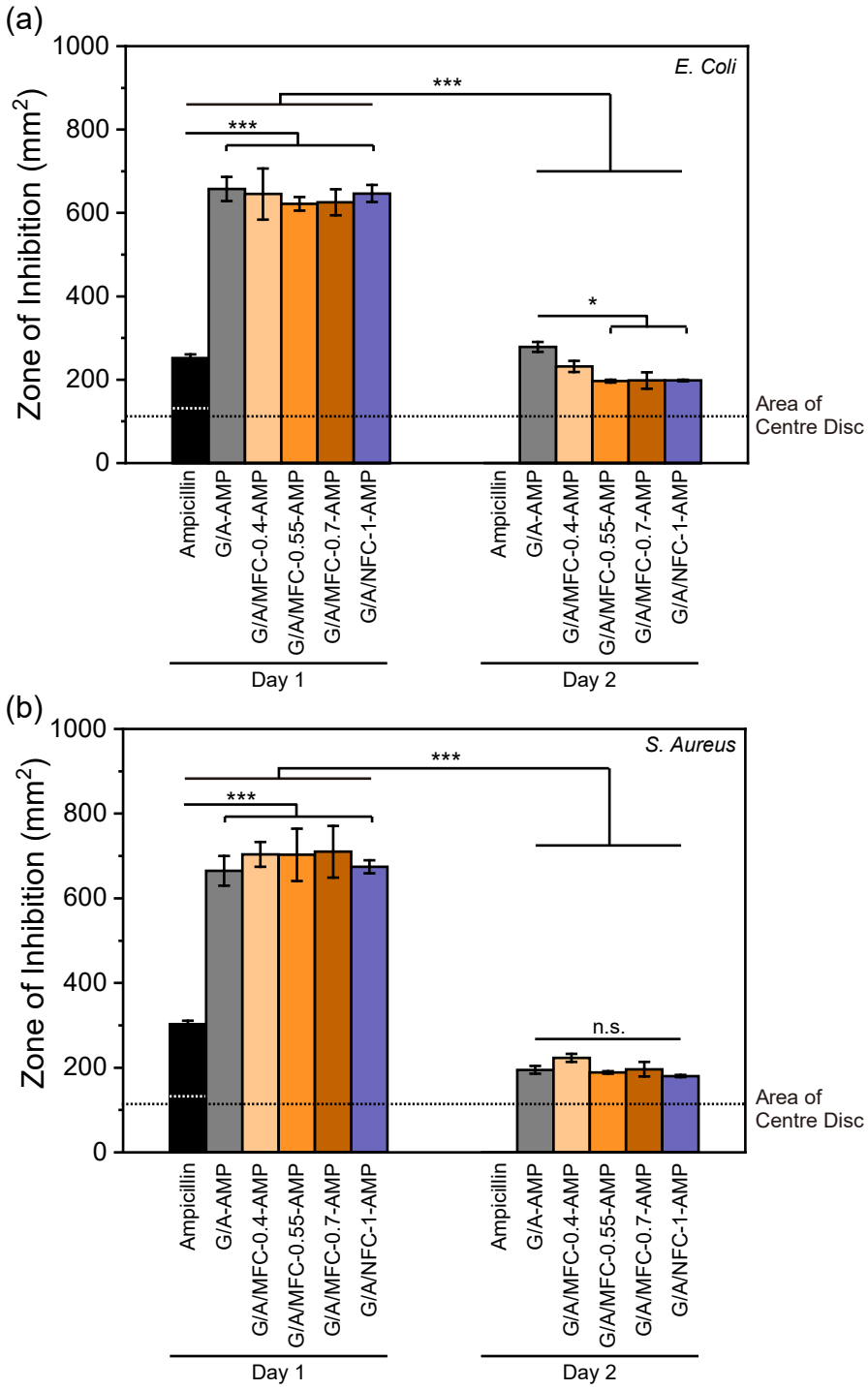

Figure 7.25: Zone of inhibition of ampicillin-loaded hydrogels and negative control against (a) *E. Coli* and (b) *S. Aureus* after incubating 1 and 2 days.

been entirely released from the filter paper, rendering it ineffective against any bacterial strains. In contrast, the negative control groups, encompassing G/A, G/A/MFC-0.7, and G/A/NFC-1, do not demonstrate bacterial inhibitory effects during three days. Therefore, none of the components of the hydrogels, including cellulose, G, and A, possess inherent antibacterial properties.

Ampicillin-loaded hydrogels, including G/A-AMP, G/A/MFC-0.4-AMP, G/A/MFC-0.55-AMP, G/A/MFC-0.7-AMP, and G/A/NFC-1-AMP, exhibit a pronounced bacterial inhibition zone after a single day of cultivation. Upon quantifying the inhibition area, it is discerned that there is no notable disparity in the inhibition zone areas among all ampicillin-loaded hydrogel samples after the initial day (p-value > 0.05), with all areas measured approximately 600 mm^2 (Figure 7.25). Subsequently, on the second day, despite a considerable reduction (p-value $\leq$ 0.001) in the inhibition zone areas of all samples to around 200 mm^2, there remains little difference in their efficacy against *S. Aureus* (Figure 7.25b). Only the antibacterial area produced by G/A-AMP against *E. Coli* is slightly larger than that of G/A/MFC-0.55-AMP, G/A/MFC-0.7-AMP, and G/A/NFC-1-AMP (Figure 7.25a). By the third day, none of the drug-loaded hydrogels exhibit antimicrobial properties.

These findings suggest that the inclusion of cellulose within ampicillin-loaded ICE hydrogels does not exert a notable influence on their antibacterial characteristics. Cellulose primarily functions as a vehicle for drug delivery within the ICE hydrogel matrix, regulating the controlled release of the drug, while it does not participate in the functional expression of drug molecules.

7.4 Conclusions

The effects of cellulose on the biological properties of hydrogels, including water-holding capability, enzymatic biodegradation, cell compatibility, drug loading and release, and antibacterial properties, were comprehensively investigated in this chapter.

Cellulose fibril network reduces swelling ratios of ICE hydrogels and increase its mechanical strength due to narrowing the pore size distribution range of ICE hydrogels, while maintaining the

equilibrium hydration degree of the sample in the range of 87.83 to 89.71%. It demonstrates that cellulose makes ICE hydrogels more similar to the extracellular matrix. Mechanical elasticity and high hydration degree of cellulose-composited ICE hydrogels provide a suitable environment for cells to function normally within the hydrogel.

The long-term swelling process of ICE hydrogel within 50 days is accompanied by the natural degradation of the hydrogel system due to the weakening of ICE itself synergy and the outflow of calcium ions. MFC can accelerate the long-term natural degradation process of ICE hydrogel, which was mainly manifested in the significant reduction of Young's modulus of G/A/MFC-0.7 from 363.43 kPa to about 36 kPa. This can be attributed to the failure of the synergistic reinforcing effect of cellulose and ICE. However, in the environment containing collagenase type II, MFC and NFC slow down the enzymatic biodegradation of ICE hydrogels, extending the half-life of ICE hydrogel from less than 7 days to 12 days. Moreover, cellulose allows ICE hydrogels to maintain a porous structure after biodegradation for 7 days. This means that cellulose can not only improve the biostability and mechanical modulus of ICE hydrogel in the early stages of implantation, but also cause the hydrogel to degrade naturally in the later stages of implantation, creating space for tissue remodelling. Furthermore, when cells were encapsulated in G/A/MFC-0.7 and G/A/NFC-1 scaffolds and cultured *in vitro*, cell viabilities gradually increase with the transfer of nutrients. Cells elongated obviously after 14 days and proliferated significantly after 21 days. Due to the coexistence of natural degradation and biodegradation of the system, porosities of G/A/MFC-0.7 and G/A/NFC-1 scaffolds increase after 21 days, elucidating that the degradation process of MFC-composited and NFC-composited hydrogel scaffolds has an excellent match with the growth process of cells.

In terms of ampicillin loading capacity of ICE hydrogels, although the addition of cellulose decreases the swelling ratio of ICE hydrogels and is unfavourable for drug loading, the beneficial interaction between cellulose and ampicillin can counteract the above-mentioned adverse effects as cellulose concentration increases. Additionally, cellulose also significantly improves ampicillin controlled sustained-release behaviour of ICE hydrogels. The half-life of drug release for sam-

ple G/A-AMP is extended from 4.92 h to more than 72 h, after incorporating 0.7% MFC into G/A hydrogel. Ampicillin release mechanism changes from diffusion-controlled in G/A to anomalous transport in G/A/MFC-0.7 and G/A/NFC-1, which has important implications for the use of therapeutic agents to assist the tissue regeneration process. Antibacterial testing further shows that cellulose only affects the drug release kinetics but has no adverse effect on the antibacterial properties of ampicillin.

In summary, cellulose-composited ICE hydrogels can provide a highly hydrated environment conducive to the survival and proliferation of encapsulated cells. The biodegradation process of cellulose-composited ICE hydrogels can align well with the tissue remodelling process. Moreover, cellulose fibrils aid ICE hydrogel in achieving controlled and sustained release of ampicillin without interfering with the antimicrobial properties of ampicillin.

Chapter 8

CONCLUSIONS AND FUTURE WORK

8.1 Conclusions

In the present project, cellulose-composited, including microfibrillated cellulose (MFC) and nanofibrillated cellulose (NFC), gelatin methacryloyl (G)/sodium alginate (A) bioink formulations with high printability during 3D extrusion were prepared. Corresponding tissue-engineered cellulose-composited ionic-covalent entanglement (ICE) G/A hydrogel scaffolds with strong mechanical properties and superior biological characteristics were developed for tissue restoration.

The integration of MFC or NFC into G/A bioink formulation is shown to enhance the printability of G/A bioink formulation, the mechanical properties, and the biological characteristics of ICE G/A hydrogel. The principal findings and their implications, as presented in Chapters 5, 6, and 7, are summarised as follows:

Enhancement of printability of G/A bioink formulation by cellulose

1. The extensive hydrogen bond interactions between high-aspect ratio cellulose and G/A significantly enhance the viscosities of the cellulose-composited G/A bioink formulations and impart specific yield points of formulations (491.42 Pa for G/A/MFC-0.7). The shear-induced orientation behaviours of cellulose fibrils by hydrogen bonding cleavage can enhance the shear-thinning

of G/A formulation, as quantified by the flow index of G/A (0.52), G/A/MFC-0.7 (0.22), and G/A/NFC-1 (0.19). The reversible breakage-formation of hydrogen bonds within the fibrillar network and between cellulose and G/A under shear stimuli introduces excellent thixotropic properties into formulations, mainly reflected in the high recovery rates of the viscosity and storage modulus of cellulose-composited G/A formulations after shear deformation. These findings are consistent with previous reports [167, 177].

2. The increases in MFC content from 0.4 to 0.7% and fibrillated cellulose size from nano- to micro-scale in G/A formulation enhance the yield stress and shear-thinning of formulations, yet treat unfavourably the recoverability of formulations. This is because the high content and large size of cellulose hinder the movement of the fibrils after the removal of shear stimuli, resulting in reduced hydrogen bonding interactions for reconstruction.

3. The addition of 0.7% MFC shifts the extrusion geometry of G/A formulation from droplets to continuous filaments, demonstrating the printability of MFC-composited G/A formulations. When G/A/MFC-0.7 formulation is printed at the optimal printing condition (2 mm/s printing speed and 30 kPa dispensing pressure when using a 27-gauged nozzle), the good linear relationship between the layer numbers and the total height of the 3D construct provides a guide for establishing complex structures. Formulated G/A/NFC-1 showcases remarkable capabilities in constructing multilayer structures with both exceptional shape fidelity and mechanical stability.

Reinforcement of mechanical properties of ICE G/A hydrogel by cellulose

1. Multiscale mechanical properties and enhancement mechanism of cellulose-composited ICE G/A hydrogels are investigated. The effects of cellulose fibril concentration and size on the multiscale mechanical properties of hydrogel are revealed.

2. The macroscopic increases in the compression resistance, yield stress, and Young's modulus of ICE G/A hydrogel due to either MFC, NFC, or mixed cellulose fibril network incorporation imply

that the hydrogen bonding interaction between cellulose fibril network and ICE results in the synergistic enhancement between cellulose and ICE. Homogeneous NFC or MFC networks can increase the overall structural integrity of the hydrogels than mixed MFC/NFC fibril networks, demonstrating that the homogeneity of cellulose fibril network can affect interactions between cellulose and ICE. Additionally, because the increase in cellulose fibril size from nano- to micro-scale improves the strength of the fibrillated network, hydrogel G/A/MFC100 has greater elasticity than G/A/NFC100.

3. Micro-indentation can map the modulus distribution of cellulose-composited ICE G/A hydrogels. Compared to ICE G/A hydrogel, wider microscopic distributions of Young's modulus and hardness for cellulose-composited ICE G/A hydrogels are observed, attributing to three types of reinforcement effects in such system: (1) Cellulose fibril network that distributes energy evenly across the hydrogel; (2) Synergistic ICE network dissipating energy by ionic bonds breaking; (3) Synergy of fibril network and ICE G/A by hydrogen bonds. Among the three reinforcement types, the third one plays a dominant role in significantly enhancing the microscopic averaged Young's modulus of the system, aligning with a previous report [448]. Moreover, the increases in MFC concentration and fibril size from nano- to micro-scale are all beneficial to the strength of cellulose fibril network and synergy of fibril network and ICE G/A.

4. Cellulose-composited ICE G/A hydrogels have interconnected porous structure. Cellulose fibril networks fill large pores (more than 100 microns) in ICE hydrogel and concentrate pores in a small range of 25 to 50 micros. Small and even pore structures can avoid stress concentration, strengthening the mechanical properties of cellulose-composited ICE G/A hydrogels. The rises in MFC concentration and fibril size from nano- to micro-scale are conducive to the centralised distribution of pore sizes.

Improvement of biological properties of ICE G/A hydrogel by cellulose

1. In a gradual nature degradation of MFC-composited ICE G/A hydrogel within 50 days, decreased

synergy within ICE network and weakened interactions between cellulose and ICE take place after 10 days of swelling and failure of ionically crosslinked alginate happen after 31 days of swelling. Moreover, MFC and NFC slow down the enzymatic biodegradation of ICE hydrogels, extending the half-life of ICE hydrogel from less than 7 days to 12 days. Thus, MFC and NFC promote the biostability of hydrogels for performing mechanical support functions in the initial stage.

2. Cell compatibility of bioprinted G/A/MFC-0.7 and G/A/NFC-1 scaffolds is confirmed: cells elongate after 14 days and proliferate significantly after 21 days. Meanwhile, porosities of G/A/MFC-0.7 and G/A/NFC-1 scaffolds increase after 21 days due to degradation of hydrogel. Thus, the degradation rate of cellulose-composited ICE hydrogel scaffolds aligns exceptionally well with the cellular growth process.

3. The increase in MFC content for MFC-composited ICE hydrogels leads to a decrease in the hydrogel's swelling ratio yet an increase in the interaction between MFC and ampicillin, which is favorable for drug loading.

4. Ampicillin release mechanism shifts from diffusion-controlled in G/A to anomalous transport in G/A/MFC-0.7 and G/A/NFC-1, clarifying that fibrillated cellulose network facilitates the controlled, gradual release of drugs within hydrogel systems. Further antibacterial tests reveal that while cellulose affects the drug release kinetics, it does not negatively impact the antimicrobial effectiveness of ampicillin.

In summary, both MFC and NFC have shown the potential to comprehensively improve traditional G/A hydrogel formulations. The effects of MFC content and cellulose fibril size changes on the above three properties of G/A hydrogels are scheduled to be published separately. In addition, the micromechanical properties and reinforcement mechanism of hybrid cellulose-composited G/A ICE hydrogel revealed by microindentation are also planned to be published.

8.2 Future work

The present thesis has demonstrated the potential of cellulose, mainly micro- and nano-fibrillated cellulose in developing 3D printable bioink formulation and constructing tissue-engineered hydrogel scaffolds with excellent mechanical strength and biological functions. To enhance the seamless integration of cellulose-composited ICE hydrogel scaffolds with damaged tissue and to achieve the goal of tissue regeneration as comprehensively as possible, future work is recommended as follows:

- **Smart bioink formulations/hydrogel scaffolds for 4D bioprinting:**

  Flexible chemical modifications of cellulose can imbue its natural form with new characteristics, such as responsiveness to stimuli such as temperature, pH changes, light, and electrical signals, paving the way for the development of smart cellulose-based bioink formulations/hydrogel scaffolds for 4D bioprinting. This responsiveness enables the scaffolds to change their shape, stiffness, or biochemical characteristics dynamically, closely replicating the behaviour of natural tissues. For instance, thermoresponsive cellulose can adapt its properties in response to body temperature variations, making it ideal for implantable grafts that need to integrate seamlessly with human tissue. Light-responsive cellulose can be manipulated with specific wavelengths to control scaffold degradation or drug release, tailoring treatments to the precise needs of healing tissues. Similarly, incorporating conductive materials can create scaffolds that respond to electrical stimuli, offering new therapies for nerve or muscle damage [160].

- **Comprehensive evaluation system for cell-scaffold interactions:**

  The Live/Dead assay used in this project is a useful tool for initial assessments of cell viability and distribution. However, to avoid potential biases associated with a single method (e.g., limited quantitative data, potential for non-specific staining) and to establish a comprehensive and reliable evaluation system for cell-scaffold interactions, the following improvements are suggested: fluorescent labelling of the scaffold material, metabolic assays (alamarBlue,

MTT, and XTT assays), proliferation assays (ki67, and BrdU assays), and histological and immunohistofluorescent evaluation of *in vivo* biocompatibility.

- **Vascularised tissue-engineered constructs:**

  The development of vascularized tissue-engineered constructs is critical for advancing the functionality and integration of bioprinted tissues, particularly for complex organs requiring robust blood supply. To address the challenges of nutrient and oxygen delivery within these constructs, one promising strategy involves the incorporation of fugitive bioink components into the bioprinting process. These materials, designed to be easily removed post-printing, create perfusable microchannels that mimic the intricate vascular networks found in natural tissues. This approach not only enhances cell viability and tissue remodeling by ensuring adequate perfusion but also supports the growth of endothelial cells along the channel walls, encouraging natural vasculogenesis.

- **Spatial heterogeneity of active bionic tissues:**

  The development of multi-component heterogeneous bioinks, utilizing various enhancement strategies, is critical for mimicking the complex architectural and functional gradients of natural tissues. Advanced bioprinting technologies allow for the precise arrangement of these bioinks, reflecting the anatomical and functional heterogeneity of target tissues. This process involves not only the selection of materials that can provide the necessary mechanical support and biocompatibility but also those that can facilitate specific biological functions, such as angiogenesis or nerve growth. Incorporating factors such as growth factor gradients, cell type variation, and mechanical properties tailored to mimic the natural tissue environment is important.

References

1. Lanza, R., Langer, R., Vacanti, J. P. & Atala, A. *Principles of tissue engineering* (Academic press, 2020).

2. Murphy, S. V. & Atala, A. 3D bioprinting of tissues and organs. *Nature biotechnology* **32,** 773–785 (2014).

3. Vacanti, J. P. & Langer, R. Tissue engineering: the design and fabrication of living replacement devices for surgical reconstruction and transplantation. *The lancet* **354,** S32–S34 (1999).

4. Fernandez de Grado, G. *et al.* Bone substitutes: a review of their characteristics, clinical use, and perspectives for large bone defects management. *Journal of tissue engineering* **9,** 2041731418776819 (2018).

5. Murphy, S. V., De Coppi, P. & Atala, A. Opportunities and challenges of translational 3D bioprinting. *Nature biomedical engineering* **4,** 370–380 (2020).

6. Atala, A., Kasper, F. K. & Mikos, A. G. Engineering complex tissues. *Science translational medicine* **4,** 160rv12–160rv12 (2012).

7. Colazo, J. M. *et al.* Applied bioengineering in tissue reconstruction, replacement, and regeneration. *Tissue Engineering Part B: Reviews* **25,** 259–290 (2019).

8. Chen, F.-M. & Liu, X. Advancing biomaterials of human origin for tissue engineering. *Progress in polymer science* **53,** 86–168 (2016).

9. Echeverria Molina, M. I., Malollari, K. G. & Komvopoulos, K. Design challenges in polymeric scaffolds for tissue engineering. *Frontiers in Bioengineering and Biotechnology* **9,** 617141 (2021).

10. Novosel, E. C., Kleinhans, C. & Kluger, P. J. Vascularization is the key challenge in tissue engineering. *Advanced drug delivery reviews* **63,** 300–311 (2011).

11. Nomi, M., Atala, A., De Coppi, P. & Soker, S. Principals of neovascularization for tissue engineering. *Molecular aspects of medicine* **23,** 463–483 (2002).

12. Webb, B. & Doyle, B. J. Parameter optimization for 3D bioprinting of hydrogels. *Bioprinting* **8,** 8–12 (2017).

13. Moysidou, C.-M., Barberio, C. & Owens, R. M. Advances in engineering human tissue models. *Frontiers in bioengineering and biotechnology* **8,** 620962 (2021).

14. Heinrich, M. A. *et al.* 3D bioprinting: from benches to translational applications. *Small* **15,** 1805510 (2019).

15. Morgan, F. L., Moroni, L. & Baker, M. B. Dynamic bioinks to advance bioprinting. *Advanced healthcare materials* **9,** 1901798 (2020).

16. Ashammakhi, N. *et al.* Bioinks and bioprinting technologies to make heterogeneous and biomimetic tissue constructs. *Materials Today Bio* **1,** 100008 (2019).

17. Kang, H.-W. *et al.* A 3D bioprinting system to produce human-scale tissue constructs with structural integrity. *Nature biotechnology* **34,** 312–319 (2016).

18. Langer, R. Perspectives and challenges in tissue engineering and regenerative medicine. *Advanced materials* **21,** 3235–3236 (2009).

19. Stanco, D., Urbán, P., Tirendi, S., Ciardelli, G. & Barrero, J. 3D bioprinting for orthopaedic applications: Current advances, challenges and regulatory considerations. *Bioprinting* **20,** e00103 (2020).

20. Xu, H.-Q., Liu, J.-C., Zhang, Z.-Y. & Xu, C.-X. A review on cell damage, viability, and functionality during 3D bioprinting. *Military Medical Research* **9,** 70 (2022).

21. Bracaglia, L. G. *et al.* 3D printing for the design and fabrication of polymer-based gradient scaffolds. *Acta biomaterialia* **56,** 3–13 (2017).

22. Zandrini, T., Florczak, S., Levato, R. & Ovsianikov, A. Breaking the resolution limits of 3D bioprinting: future opportunities and present challenges. *Trends in Biotechnology* **41,** 604–614 (2023).

23. Ravanbakhsh, H. *et al.* Emerging technologies in multi-material bioprinting. *Advanced Materials* **33,** 2104730 (2021).

24. Pössl, A., Hartzke, D., Schlupp, P. & Runkel, F. E. Optimized Cell Mixing Facilitates the Reproducible Bioprinting of Constructs with High Cell Viability. *Applied Sciences* **12,** 326 (2021).

25. Ramos, T. & Moroni, L. Tissue engineering and regenerative medicine 2019: the role of biofabrication—a year in review. *Tissue Engineering Part C: Methods* **26,** 91–106 (2020).

26. Berthiaume, F., Maguire, T. J. & Yarmush, M. L. Tissue engineering and regenerative medicine: history, progress, and challenges. *Annual review of chemical and biomolecular engineering* **2,** 403–430 (2011).

27. Seddiqi, H. *et al.* Cellulose and its derivatives: Towards biomedical applications. *Cellulose* **28,** 1893–1931 (2021).

28. Li, R. *et al.* Design and construction of fluorescent cellulose nanocrystals for biomedical applications. *Advanced Materials Interfaces* **9,** 2101293 (2022).

29. Hickey, R. J. & Pelling, A. E. Cellulose biomaterials for tissue engineering. *Frontiers in bioengineering and biotechnology* **7,** 45 (2019).

30. Novotna, K. *et al.* Cellulose-based materials as scaffolds for tissue engineering. *Cellulose* **20,** 2263–2278 (2013).

31. Jiang, J., Oguzlu, H. & Jiang, F. 3D printing of lightweight, super-strong yet flexible all-cellulose structure. *Chemical Engineering Journal* **405,** 126668 (2021).

32. Firmanda, A. *et al.* 3D printed cellulose based product applications. *Materials Chemistry Frontiers* **6,** 254–279 (2022).

33. Courtenay, J. C., Sharma, R. I. & Scott, J. L. Recent advances in modified cellulose for tissue culture applications. *Molecules* **23,** 654 (2018).

34. Müller, F. A. *et al.* Cellulose-based scaffold materials for cartilage tissue engineering. *Biomaterials* **27,** 3955–3963 (2006).

35. Habibi, Y. Key advances in the chemical modification of nanocelluloses. *Chemical Society Reviews* **43,** 1519–1542 (2014).

36. Rol, F., Belgacem, M. N., Gandini, A. & Bras, J. Recent advances in surface-modified cellulose nanofibrils. *Progress in Polymer Science* **88,** 241–264 (2019).

37. Chiarello, E. *et al.* Autograft, allograft and bone substitutes in reconstructive orthopedic surgery. *Aging clinical and experimental research* **25,** 101–103 (2013).

38. Van de Vijfeijken, S. E. *et al.* Autologous bone is inferior to alloplastic cranioplasties: safety of autograft and allograft materials for cranioplasties, a systematic review. *World neurosurgery* **117,** 443–452 (2018).

39. Vidal, L., Kampleitner, C., Brennan, M. Á., Hoornaert, A. & Layrolle, P. Reconstruction of large skeletal defects: current clinical therapeutic strategies and future directions using 3D printing. *Frontiers in bioengineering and biotechnology* **8,** 61 (2020).

40. Langer, R. & Vacanti, J. P. Tissue Engineering. *Science* **260,** 920–926 (1993).

41. Qu, H., Fu, H., Han, Z. & Sun, Y. Biomaterials for bone tissue engineering scaffolds: A review. *RSC advances* **9,** 26252–26262 (2019).

42. Jakus, A. E., Rutz, A. L. & Shah, R. N. Advancing the field of 3D biomaterial printing. *Biomedical Materials* **11,** 014102 (2016).

43. Rosales, A. M. & Anseth, K. S. The design of reversible hydrogels to capture extracellular matrix dynamics. *Nature Reviews Materials* **1,** 1–15 (2016).

44. Nicolas, J. *et al.* 3D extracellular matrix mimics: fundamental concepts and role of materials chemistry to influence stem cell fate. *Biomacromolecules* **21,** 1968–1994 (2020).

45. Fuchs, S., Shariati, K. & Ma, M. Specialty tough hydrogels and their biomedical applications. *Advanced healthcare materials* **9,** 1901396 (2020).

46. Raeisdasteh Hokmabad, V., Davaran, S., Ramazani, A. & Salehi, R. Design and fabrication of porous biodegradable scaffolds: a strategy for tissue engineering. *Journal of biomaterials science, polymer edition* **28,** 1797–1825 (2017).

47. Chocholata, P., Kulda, V. & Babuska, V. Fabrication of scaffolds for bone-tissue regeneration. *Materials* **12,** 568 (2019).

48. Haider, A. *et al.* Advances in the scaffolds fabrication techniques using biocompatible polymers and their biomedical application: A technical and statistical review. *Journal of saudi chemical society* **24,** 186–215 (2020).

49. Bailey, B. M., Fei, R., Munoz-Pinto, D., Hahn, M. S. & Grunlan, M. A. PDMSstar–PEG hydrogels prepared via solvent-induced phase separation (SIPS) and their potential utility as tissue engineering scaffolds. *Acta biomaterialia* **8,** 4324–4333 (2012).

50. Thorvaldsson, A. *et al.* Development of nanofiber-reinforced hydrogel scaffolds for nucleus pulposus regeneration by a combination of electrospinning and spraying technique. *Journal of applied polymer science* **128,** 1158–1163 (2013).

51. Wu, X. *et al.* Preparation of aligned porous gelatin scaffolds by unidirectional freeze-drying method. *Acta biomaterialia* **6,** 1167–1177 (2010).

52. Chiu, Y.-C., Larson, J. C., Isom Jr, A. & Brey, E. M. Generation of porous poly (ethylene glycol) hydrogels by salt leaching. *Tissue Engineering Part C: Methods* **16,** 905–912 (2010).

53. Zhang, L., Morsi, Y., Wang, Y., Li, Y. & Ramakrishna, S. Review scaffold design and stem cells for tooth regeneration. *Japanese Dental Science Review* **49,** 14–26 (2013).

54. Bedell, M. L., Navara, A. M., Du, Y., Zhang, S. & Mikos, A. G. Polymeric systems for bioprinting. *Chemical reviews* **120,** 10744–10792 (2020).

55. Jakus, A. Chapter 1: An Introduction to 3D Printing—Past. *Present, and Future Promise. 3D Printing in Orthopaedic Surgery,* 1–15 (2019).

56. Ventola, C. L. Medical applications for 3D printing: current and projected uses. *Pharmacy and Therapeutics* **39,** 704 (2014).

57. Kim, S. S. *et al.* Survival and function of hepatocytes on a novel three-dimensional synthetic biodegradable polymer scaffold with an intrinsic network of channels. *Annals of surgery* **228,** 8 (1998).

58. Morales, P. A. *et al.* Thermal inkjet bioprinting drastically alters cell phenotype. *Biofabrication* **15,** 031001 (2023).

59. Wilson Jr, W. C. & Boland, T. Cell and organ printing 1: protein and cell printers. *The Anatomical Record Part A: discoveries in molecular, cellular, and evolutionary biology* **272,** 491–496 (2003).

60. Correia Carreira, S., Begum, R. & Perriman, A. W. 3D bioprinting: the emergence of programmable biodesign. *Advanced healthcare materials* **9,** 1900554 (2020).

61. Valot, L., Martinez, J., Mehdi, A. & Subra, G. Chemical insights into bioinks for 3D printing. *Chemical Society Reviews* **48,** 4049–4086 (2019).

62. Fu, Z., Ouyang, L., Xu, R., Yang, Y. & Sun, W. Responsive biomaterials for 3D bioprinting: A review. *Materials Today* **52,** 112–132 (2022).

63. Li, N., Guo, R. & Zhang, Z. J. Bioink formulations for bone tissue regeneration. *Frontiers in Bioengineering and Biotechnology* **9,** 630488 (2021).

64. Paxton, N. *et al.* Proposal to assess printability of bioinks for extrusion-based bioprinting and evaluation of rheological properties governing bioprintability. *Biofabrication* **9,** 044107 (2017).

65. Schwab, A. *et al.* Printability and shape fidelity of bioinks in 3D bioprinting. *Chemical reviews* **120,** 11028–11055 (2020).

66. Levato, R. *et al.* From shape to function: the next step in bioprinting. *Advanced Materials* **32,** 1906423 (2020).

67. Dong, Z., Li, Y. & Zou, Q. Degradation and biocompatibility of porous nano-hydroxyapatite/polyurethane composite scaffold for bone tissue engineering. *Applied Surface Science* **255,** 6087–6091 (2009).

68. Williams, D. F. On the mechanisms of biocompatibility. *Biomaterials* **29,** 2941–2953 (2008).

69. Zhang, X.-Y., Fang, G. & Zhou, J. Additively manufactured scaffolds for bone tissue engineering and the prediction of their mechanical behavior: A review. *Materials* **10,** 50 (2017).

70. Rana, M. M. & De la Hoz Siegler, H. Tuning the properties of PNIPAm-based hydrogel scaffolds for cartilage tissue engineering. *Polymers* **13,** 3154 (2021).

71. Xu, J. *et al.* A 3D bioprinted decellularized extracellular matrix/gelatin/quaternized chitosan scaffold assembling with poly (ionic liquid) s for skin tissue engineering. *International Journal of Biological Macromolecules* **220,** 1253–1266 (2022).

72. Yuan, B. *et al.* A self-degradable supramolecular photosensitizer with high photodynamic therapeutic efficiency and improved safety. *Angewandte Chemie* **133,** 716–720 (2021).

73. Sabir, M. I., Xu, X. & Li, L. A review on biodegradable polymeric materials for bone tissue engineering applications. *Journal of materials science* **44,** 5713–5724 (2009).

74. Rouwkema, J., Rivron, N. C. & van Blitterswijk, C. A. Vascularization in tissue engineering. *Trends in biotechnology* **26,** 434–441 (2008).

75. Murphy, C. M., Haugh, M. G. & O'Brien, F. J. The effect of mean pore size on cell attachment, proliferation and migration in collagen–glycosaminoglycan scaffolds for bone tissue engineering. *Biomaterials* **31,** 461–466 (2010).

76. Neumann, M. *et al.* Stimuli-Responsive Hydrogels: The Dynamic Smart Biomaterials of Tomorrow. *Macromolecules* **56,** 8377–8392 (2023).

77. Wen, H. *et al.* Hierarchical patterning via dynamic sacrificial printing of stimuli-responsive hydrogels. *Biofabrication* **12,** 035007 (2020).

78. Lui, Y. S. *et al.* 4D printing and stimuli-responsive materials in biomedical aspects. *Acta Biomaterialia* **92,** 19–36. ISSN: 1742-7061 (2019).

79. Naniz, M. A., Askari, M., Zolfagharian, A., Naniz, M. A. & Bodaghi, M. 4D printing: A cutting-edge platform for biomedical applications. *Biomedical Materials* **17,** 062001 (2022).

80. Bittner, S. M., Guo, J. L., Melchiorri, A. & Mikos, A. G. Three-dimensional printing of multilayered tissue engineering scaffolds. *Materials Today* **21,** 861–874 (2018).

81. Dogan, E., Bhusal, A., Cecen, B. & Miri, A. K. 3D Printing metamaterials towards tissue engineering. *Applied materials today* **20,** 100752 (2020).

82. Vishwakarma, A., Sharpe, P., Shi, S. & Ramalingam, M. *Stem cell biology and tissue engineering in dental sciences* (Academic Press, 2014).

83. Joyce, K., Fabra, G. T., Bozkurt, Y. & Pandit, A. Bioactive potential of natural biomaterials: Identification, retention and assessment of biological properties. *Signal Transduction and Targeted Therapy* **6,** 122 (2021).

84. Yu, J. *et al.* Current advances in 3D bioprinting technology and its applications for tissue engineering. *Polymers* **12,** 2958 (2020).

85. Jirofti, N., Hashemi, M., Moradi, A. & Kalalinia, F. Fabrication and characterization of 3D printing biocompatible crocin-loaded chitosan/collagen/hydroxyapatite-based scaffolds for bone tissue engineering applications. *International Journal of Biological Macromolecules* **252,** 126279 (2023).

86. Montalbano, G., Calore, A. R. & Vitale-Brovarone, C. Extrusion 3D printing of a multiphase collagen-based material: An optimized strategy to obtain biomimetic scaffolds with high shape fidelity. *Journal of Applied Polymer Science* **140,** e53593 (2023).

87. Pei, M., Hwangbo, H. & Kim, G. Hierarchical fibrous collagen/poly (ε-caprolactone) structure fabricated with a 3D-printing process for tissue engineering applications. *Composites Part B: Engineering* **259,** 110730 (2023).

88. Maihemuti, A. *et al.* 3D-printed fish gelatin scaffolds for cartilage tissue engineering. *Bioactive Materials* **26,** 77–87 (2023).

89. Kang, D. *et al.* 3D bioprinting of a gelatin-alginate hydrogel for tissue-engineered hair follicle regeneration. *Acta biomaterialia* **165,** 19–30 (2023).

90. Liu, C. *et al.* 3D bioprinting of cell-laden nano-attapulgite/gelatin methacrylate composite hydrogel scaffolds for bone tissue repair. *Journal of Materials Science & Technology* **135,** 111–125 (2023).

91. De Melo, B. A. *et al.* Strategies to use fibrinogen as bioink for 3D bioprinting fibrin-based soft and hard tissues. *Acta Biomaterialia* **117,** 60–76 (2020).

92. Restan Perez, M., Sharma, R., Masri, N. Z. & Willerth, S. M. 3D Bioprinting mesenchymal stem cell-derived neural tissues using a fibrin-based bioink. *Biomolecules* **11,** 1250 (2021).

93. Oliveira, J. M. Current and future trends of silk fibroin-based bioinks in 3D printing. *Journal of 3D printing in medicine* **4,** 69–73 (2020).

94. Kim, S. H. *et al.* 3D bioprinted silk fibroin hydrogels for tissue engineering. *Nature protocols* **16,** 5484–5532 (2021).

95. Sangkert, S., Kamolmatyakul, S., Gelinsky, M. & Meesane, J. 3D printed scaffolds of alginate/polyvinylalcohol with silk fibroin based on mimicked extracellular matrix for bone tissue engineering in maxillofacial surgery. *Materials Today Communications* **26,** 102140 (2021).

96. Olate-Moya, F. *et al.* Chondroinductive alginate-based hydrogels having graphene oxide for 3D printed scaffold fabrication. *ACS applied materials & interfaces* **12,** 4343–4357 (2020).

97. Wei, Q. *et al.* Modification, 3D printing process and application of sodium alginate based hydrogels in soft tissue engineering: A review. *International Journal of Biological Macromolecules,* 123450 (2023).

98. Dravid, A. *et al.* Development of agarose–gelatin bioinks for extrusion-based bioprinting and cell encapsulation. *Biomedical Materials* **17,** 055001 (2022).

99. López-Marcial, G. R. *et al.* Agarose-based hydrogels as suitable bioprinting materials for tissue engineering. *ACS Biomaterials Science & Engineering* **4,** 3610–3616 (2018).

100. Nadernezhad, A. *et al.* Nanocomposite bioinks based on agarose and 2D nanosilicates with tunable flow properties and bioactivity for 3D bioprinting. *ACS Applied Bio Materials* **2,** 796–806 (2019).

101. Taghizadeh, M. *et al.* Chitosan-based inks for 3D printing and bioprinting. *Green Chemistry* **24,** 62–101 (2022).

102. He, Y. *et al.* A photocurable hybrid chitosan/acrylamide bioink for DLP based 3D bioprinting. *Materials & Design* **202,** 109588 (2021).

103. Butler, H. M., Naseri, E., MacDonald, D. S., Tasker, R. A. & Ahmadi, A. Optimization of starch-and chitosan-based bio-inks for 3D bioprinting of scaffolds for neural cell growth. *Materialia* **12,** 100737 (2020).

104. Lafuente-Merchan, M. *et al.* Development, characterization and sterilisation of Nanocellulose-alginate-(hyaluronic acid)-bioinks and 3D bioprinted scaffolds for tissue engineering. *Materials Science and Engineering: C* **126,** 112160 (2021).

105. Sekar, M. P., Suresh, S., Zennifer, A., Sethuraman, S. & Sundaramurthi, D. Hyaluronic Acid as Bioink and Hydrogel Scaffolds for Tissue Engineering Applications. *ACS Biomaterials Science & Engineering* **9,** 3134–3159 (2023).

106. Mörö, A. *et al.* Hyaluronic acid based next generation bioink for 3D bioprinting of human stem cell derived corneal stromal model with innervation. *Biofabrication* **15,** 015020 (2022).

107. Zhao, C., Xiao, Y., Ling, S., Pei, Y. & Ren, J. Structure of collagen. *Fibrous Proteins: Design, Synthesis, and Assembly,* 17–25 (2021).

108. Gómez-Guillén, M., Giménez, B., López-Caballero, M. a. & Montero, M. Functional and bioactive properties of collagen and gelatin from alternative sources: A review. *Food hydrocolloids* **25,** 1813–1827 (2011).

109. Alipal, J. *et al.* A review of gelatin: Properties, sources, process, applications, and commercialisation. *Materials Today: Proceedings* **42,** 240–250 (2021).

110. Li, J.-W. *et al.* Water-Soluble and degradable Gelatin/Polyaniline assemblies with a high photothermal conversion efficiency for pH-Switchable precise photothermal therapy. *ACS Applied Materials & Interfaces* **14,** 52670–52683 (2022).

111. Giorleo, L., Tegazzini, F. & Sartore, L. 3D printing of gelatin/chitosan biodegradable hybrid hydrogel: Critical issues due to the crosslinking reaction, degradation phenomena and process parameters. *Bioprinting* **24,** e00170 (2021).

112. Wang, L. *et al.* A physically cross-linked sodium alginate–gelatin hydrogel with high mechanical strength. *ACS Applied Polymer Materials* **3,** 3197–3205 (2021).

113. Asim, S., Tabish, T. A., Liaqat, U., Ozbolat, I. T. & Rizwan, M. Advances in Gelatin Bioinks to Optimize Bioprinted Cell Functions. *Advanced Healthcare Materials,* 2203148 (2023).

114. Litvinov, R. I., Pieters, M., de Lange-Loots, Z. & Weisel, J. W. Fibrinogen and fibrin. *Macromolecular Protein Complexes III: Structure and Function,* 471–501 (2021).

115. Ozbolat, I. T. & Hospodiuk, M. Current advances and future perspectives in extrusion-based bioprinting. *Biomaterials* **76,** 321–343 (2016).

116. Ahmed, T. A., Griffith, M. & Hincke, M. Characterization and inhibition of fibrin hydrogel–degrading enzymes during development of tissue engineering scaffolds. *Tissue engineering* **13,** 1469–1477 (2007).

117. Lee, H.-R. *et al.* Immobilization of planktonic algal spores by inkjet printing. *Scientific reports* **9,** 12357 (2019).

118. Wong, T. Y., Preston, L. A. & Schiller, N. L. Alginate lyase: review of major sources and enzyme characteristics, structure-function analysis, biological roles, and applications. *Annual Reviews in Microbiology* **54,** 289–340 (2000).

119. Law, N. *et al.* Characterisation of hyaluronic acid methylcellulose hydrogels for 3D bioprinting. *Journal of the mechanical behavior of biomedical materials* **77,** 389–399 (2018).

120. Hauptstein, J. *et al.* Hyaluronic acid-based bioink composition enabling 3D bioprinting and improving quality of deposited cartilaginous extracellular matrix. *Advanced Healthcare Materials* **9,** 2000737 (2020).

121. Zarrintaj, P. *et al.* Agarose-based biomaterials for tissue engineering. *Carbohydrate polymers* **187,** 66–84 (2018).

122. Yazdi, M. K. *et al.* Agarose-based biomaterials for advanced drug delivery. *Journal of Controlled Release* **326,** 523–543 (2020).

123. Irastorza-Lorenzo, A. *et al.* Evaluation of marine agarose biomaterials for tissue engineering applications. *International Journal of Molecular Sciences* **22,** 1923 (2021).

124. Lazaridou, M., Bikiaris, D. N. & Lamprou, D. A. 3D bioprinted chitosan-based hydrogel scaffolds in tissue engineering and localised drug delivery. *Pharmaceutics* **14,** 1978 (2022).

125. Yan, D. *et al.* Antimicrobial properties of chitosan and chitosan derivatives in the treatment of enteric infections. *Molecules* **26,** 7136 (2021).

126. Sahariah, P. & Másson, M. Antimicrobial chitosan and chitosan derivatives: A review of the structure–activity relationship. *Biomacromolecules* **18,** 3846–3868 (2017).

127. Wang, J. *et al.* Recent progress on synthesis, property and application of modified chitosan: an overview. *International Journal of Biological Macromolecules* **88,** 333–344 (2016).

128. Jayakumar, R., Prabaharan, M. & Muzzarelli, R. A. *Chitosan for biomaterials I* (Springer, 2011).

129. Carrow, J. K., Kerativitayanan, P., Jaiswal, M. K., Lokhande, G. & Gaharwar, A. K. in *Essentials of 3D biofabrication and translation* 229–248 (Elsevier, 2015).

130. Amini, S., Salehi, H., Setayeshmehr, M. & Ghorbani, M. Natural and synthetic polymeric scaffolds used in peripheral nerve tissue engineering: Advantages and disadvantages. *Polymers for Advanced Technologies* **32,** 2267–2289 (2021).

131. Lopes, M. S., Jardini, A. & Maciel Filho, R. Poly (lactic acid) production for tissue engineering applications. *Procedia engineering* **42,** 1402–1413 (2012).

132. Gioffredi, E. *et al.* Pluronic F127 hydrogel characterization and biofabrication in cellularized constructs for tissue engineering applications. *Procedia Cirp* **49,** 125–132 (2016).

133. Wang, S., Lee, J. M. & Yeong, W. Y. Smart hydrogels for 3D bioprinting. *International Journal of Bioprinting* **1** (2015).

134. Jeong, B., Kim, S. W. & Bae, Y. H. Thermosensitive sol–gel reversible hydrogels. *Advanced drug delivery reviews* **64,** 154–162 (2012).

135. De Vries, R. *et al.* in *Transplantation, Bioengineering, and Regeneration of the Endocrine Pancreas* 461–486 (Elsevier, 2020).

136. Wu, W., DeConinck, A. & Lewis, J. A. Omnidirectional printing of 3D microvascular networks. *Advanced materials* **23,** H178–H183 (2011).

137. Heinze, T. Cellulose: structure and properties. *Cellulose chemistry and properties: fibers, nanocelluloses and advanced materials,* 1–52 (2016).

138. Michelin, M., Gomes, D. G., Romaní, A., Polizeli, M. d. L. T. & Teixeira, J. A. Nanocellulose production: exploring the enzymatic route and residues of pulp and paper industry. *Molecules* **25,** 3411 (2020).

139. Iglesias, M. C., Gomez-Maldonado, D., Via, B. K., Jiang, Z. & Peresin, M. S. Pulping processes and their effects on cellulose fibers and nanofibrillated cellulose properties: a review. *Forest Products Journal* **70,** 10–21 (2020).

140. Toren, K. & Blanc, P. D. The history of pulp and paper bleaching: respiratory-health effects. *The Lancet* **349,** 1316–1318 (1997).

141. Mboowa, D. A review of the traditional pulping methods and the recent improvements in the pulping processes. *Biomass Conversion and Biorefinery,* 1–12 (2021).

142. Sixta, H., Potthast, A. & Krotschek, A. W. Chemical pulping processes. *Handbook of pulp* **1** (2006).

143. Parthasarathi, R. *et al.* Insights into hydrogen bonding and stacking interactions in cellulose. *The Journal of Physical Chemistry A* **115,** 14191–14202 (2011).

144. Habibi, Y., Lucia, L. A. & Rojas, O. J. Cellulose nanocrystals: chemistry, self-assembly, and applications. *Chemical reviews* **110,** 3479–3500 (2010).

145. Phanthong, P. *et al.* Nanocellulose: Extraction and application. *Carbon Resources Conversion* **1,** 32–43 (2018).

146. Beltramino, F., Roncero, M. B., Torres, A. L., Vidal, T. & Valls, C. Optimization of sulfuric acid hydrolysis conditions for preparation of nanocrystalline cellulose from enzymatically pretreated fibers. *Cellulose* **23,** 1777–1789 (2016).

147. Khalil, H. A. *et al.* Production and modification of nanofibrillated cellulose using various mechanical processes: a review. *Carbohydrate polymers* **99,** 649–665 (2014).

148. Saedi, S., Garcia, C. V., Kim, J. T. & Shin, G. H. Physical and chemical modifications of cellulose fibers for food packaging applications. *Cellulose* **28,** 8877–8897 (2021).

149. D'Amora, U. *et al.* Advances in the physico-chemical, antimicrobial and angiogenic properties of graphene-oxide/cellulose nanocomposites for wound healing. *Pharmaceutics* **15,** 338 (2023).

150. Wei, D. W. *et al.* Superhydrophobic modification of cellulose and cotton textiles: Methodologies and applications. *Journal of Bioresources and Bioproducts* **5,** 1–15 (2020).

151. Zhang, Y., Carbonell, R. G. & Rojas, O. J. Bioactive cellulose nanofibrils for specific human IgG binding. *Biomacromolecules* **14,** 4161–4168 (2013).

152. Credou, J. & Berthelot, T. Cellulose: from biocompatible to bioactive material. *Journal of Materials Chemistry B* **2,** 4767–4788 (2014).

153. Roy, D., Semsarilar, M., Guthrie, J. T. & Perrier, S. Cellulose modification by polymer grafting: a review. *Chemical Society Reviews* **38,** 2046–2064 (2009).

154. Yue, Y. *et al.* Interactions between pea protein isolate and carboxymethylcellulose in neutral and acid aqueous systems. *Foods* **10,** 1560 (2021).

155. Chen, Y. *et al.* Influence of carboxymethylcellulose on the interaction between ovalbumin and tannic acid via noncovalent bonds and its effects on emulsifying properties. *Lwt* **118,** 108778 (2020).

156. Nouri-Felekori, M., Nezafati, N., Moraveji, M., Hesaraki, S. & Ramezani, T. Bioorthogonal hydroxyethyl cellulose-based scaffold crosslinked via click chemistry for cartilage tissue engineering applications. *International Journal of Biological Macromolecules* **183,** 2030–2043 (2021).

157. Wu, M. *et al.* Biomimetic mineralization of novel hydroxyethyl cellulose/soy protein isolate scaffolds promote bone regeneration in vitro and in vivo. *International Journal of Biological Macromolecules* **162,** 1627–1641 (2020).

158. Liyanage, S., Acharya, S., Parajuli, P., Shamshina, J. L. & Abidi, N. Production and surface modification of cellulose bioproducts. *Polymers* **13,** 3433 (2021).

159. Emre Oz, Y., Keskin-Erdogan, Z., Safa, N. & Esin Hames Tuna, E. A review of functionalised bacterial cellulose for targeted biomedical fields. *Journal of Biomaterials Applications* **36,** 648–681 (2021).

160. Kuzmenko, V., Karabulut, E., Pernevik, E., Enoksson, P. & Gatenholm, P. Tailor-made conductive inks from cellulose nanofibrils for 3D printing of neural guidelines. *Carbohydrate polymers* **189,** 22–30 (2018).

161. Alizadeh, N., Akbari, V., Nurani, M. & Taheri, A. Preparation of an injectable doxorubicin surface modified cellulose nanofiber gel and evaluation of its anti-tumor and anti-metastasis activity in melanoma. *Biotechnology progress* **34,** 537–545 (2018).

162. Nurani, M., Akbari, V. & Taheri, A. Preparation and characterization of metformin surface modified cellulose nanofiber gel and evaluation of its anti-metastatic potentials. *Carbohydrate polymers* **165,** 322–333 (2017).

163. Brown, E. E., Hu, D., Abu Lail, N. & Zhang, X. Potential of nanocrystalline cellulose–fibrin nanocomposites for artificial vascular graft applications. *Biomacromolecules* **14,** 1063–1071 (2013).

164. Ávila, H. M., Schwarz, S., Rotter, N. & Gatenholm, P. 3D bioprinting of human chondrocyte-laden nanocellulose hydrogels for patient-specific auricular cartilage regeneration. *Bioprinting* **1,** 22–35 (2016).

165. Bhattacharya, M. *et al.* Nanofibrillar cellulose hydrogel promotes three-dimensional liver cell culture. *Journal of controlled release* **164,** 291–298 (2012).

166. Athukoralalage, S. S., Balu, R., Dutta, N. K. & Roy Choudhury, N. 3D bioprinted nanocellulose-based hydrogels for tissue engineering applications: A brief review. *Polymers* **11,** 898 (2019).

167. Li, M.-C., Wu, Q., Moon, R. J., Hubbe, M. A. & Bortner, M. J. Rheological aspects of cellulose nanomaterials: Governing factors and emerging applications. *Advanced Materials* **33,** 2006052 (2021).

168. Ebeling, T. *et al.* Shear-induced orientation phenomena in suspensions of cellulose microcrystals, revealed by small angle X-ray scattering. *Langmuir* **15,** 6123–6126 (1999).

169. Yoshiharu, N., Shigenori, K., Masahisa, W. & Takeshi, O. Cellulose microcrystal film of high uniaxial orientation. *Macromolecules* **30,** 6395–6397 (1997).

170. Shafiei-Sabet, S., Hamad, W. Y. & Hatzikiriakos, S. G. Rheology of nanocrystalline cellulose aqueous suspensions. *Langmuir* **28,** 17124–17133 (2012).

171. Im, S. *et al.* An osteogenic bioink composed of alginate, cellulose nanofibrils, and polydopamine nanoparticles for 3D bioprinting and bone tissue engineering. *International Journal of Biological Macromolecules* **205,** 520–529 (2022).

172. Patel, D. K., Dutta, S. D., Shin, W.-C., Ganguly, K. & Lim, K.-T. Fabrication and characterization of 3D printable nanocellulose-based hydrogels for tissue engineering. *RSC advances* **11,** 7466–7478 (2021).

173. Wang, X. *et al.* Printability of hybridized composite from maleic acid-treated bacterial cellulose with gelatin for bone tissue regeneration. *Advanced Composites and Hybrid Materials* **6,** 134 (2023).

174. Jiang, Y. *et al.* Rheological behavior, 3D printability and the formation of scaffolds with cellulose nanocrystals/gelatin hydrogels. *Journal of Materials Science* **55,** 15709–15725 (2020).

175. Jessop, Z. M. *et al.* Printability of pulp derived crystal, fibril and blend nanocellulose-alginate bioinks for extrusion 3D bioprinting. *Biofabrication* **11,** 045006 (2019).

176. Shin, S. & Hyun, J. Rheological properties of cellulose nanofiber hydrogel for high-fidelity 3D printing. *Carbohydrate Polymers* **263,** 117976 (2021).

177. Kumar, A., Matari, I. A. I. & Han, S. S. 3D printable carboxylated cellulose nanocrystal-reinforced hydrogel inks for tissue engineering. *Biofabrication* **12,** 025029 (2020).

178. Badhe, R. V. & Nipate, S. S. in *Advanced 3D-Printed Systems and Nanosystems for Drug Delivery and Tissue Engineering* 109–137 (Elsevier, 2020).

179. Shin, S. *et al.* Cellulose nanofibers for the enhancement of printability of low viscosity gelatin derivatives. *BioResources* **12,** 2941–2954 (2017).

180. Cui, Y. *et al.* Cellulose nanocrystal-enhanced thermal-sensitive hydrogels of block copolymers for 3D bioprinting. *International journal of bioprinting* **7** (2021).

181. Zennifer, A., Senthilvelan, P., Sethuraman, S. & Sundaramurthi, D. Key advances of carboxymethyl cellulose in tissue engineering & 3D bioprinting applications. *Carbohydrate Polymers* **256,** 117561 (2021).

182. Monfared, M., Mawad, D., Rnjak-Kovacina, J. & Stenzel, M. H. 3D bioprinting of dual-crosslinked nanocellulose hydrogels for tissue engineering applications. *Journal of Materials Chemistry B* **9,** 6163–6175 (2021).

183. Fan, Y., Yue, Z., Lucarelli, E. & Wallace, G. G. Hybrid printing using cellulose nanocrystals reinforced GelMA/HAMA hydrogels for improved structural integration. *Advanced Healthcare Materials* **9,** 2001410 (2020).

184. Kamdem Tamo, A. *et al.* Development of bioinspired functional chitosan/cellulose nanofiber 3D hydrogel constructs by 3D printing for application in the engineering of mechanically demanding tissues. *Polymers* **13,** 1663 (2021).

185. Jiang, Y. *et al.* Preparation of cellulose nanofiber-reinforced gelatin hydrogel and optimization for 3D printing applications. *BioResources* **13,** 5909–5924 (2018).

186. Wu, C.-Y., Suen, S.-Y., Chen, S.-C. & Tzeng, J.-H. Analysis of protein adsorption on regenerated cellulose-based immobilized copper ion affinity membranes. *Journal of Chromatography A* **996,** 53–70 (2003).

187. Feldmann, E. *et al.* Novel bilayer bacterial nanocellulose scaffold supports neocartilage formation in vitro and in vivo. *Biomaterials* **44,** 122–133 (2015).

188. Courtenay, J. C. *et al.* Surface modified cellulose scaffolds for tissue engineering. *Cellulose* **24,** 253–267 (2017).

189. Torres-Rendon, J. G. *et al.* Bioactive gyroid scaffolds formed by sacrificial templating of nanocellulose and nanochitin hydrogels as instructive platforms for biomimetic tissue engineering. *Adv. Mater* **27,** 2989–2995 (2015).

190. Ullah, M. W. *et al.* Impact of structural features of acetylated bacterial cellulose on cell-scaffold and scaffold-blood interactions in vitro. *Cellulose* **30,** 10373–10399 (2023).

191. Brackmann, C., Bodin, A., Åkeson, M., Gatenholm, P. & Enejder, A. Visualization of the cellulose biosynthesis and cell integration into cellulose scaffolds. *Biomacromolecules* **11,** 542–548 (2010).

192. Ozbolat, I. & Gudapati, H. A review on design for bioprinting. *Bioprinting* **3,** 1–14 (2016).

193. Park, J. Y. *et al.* A comparative study on collagen type I and hyaluronic acid dependent cell behavior for osteochondral tissue bioprinting. *Biofabrication* **6,** 035004 (2014).

194. Murphy, C. *et al.* 3D bioprinting of stem cells and polymer/bioactive glass composite scaffolds for bone tissue engineering. *International Journal of Bioprinting* **3** (2017).

195. Ahlfeld, T. *et al.* Bioprinting of mineralized constructs utilizing multichannel plotting of a self-setting calcium phosphate cement and a cell-laden bioink. *Biofabrication* **10,** 045002 (2018).

196. Pati, F. *et al.* Printing three-dimensional tissue analogues with decellularized extracellular matrix bioink. *Nature communications* **5,** 3935 (2014).

197. Cui, X., Dean, D., Ruggeri, Z. M. & Boland, T. Cell damage evaluation of thermal inkjet printed Chinese hamster ovary cells. *Biotechnology and bioengineering* **106,** 963–969 (2010).

198. Cui, X., Boland, T., DD'Lima, D. & K Lotz, M. Thermal inkjet printing in tissue engineering and regenerative medicine. *Recent patents on drug delivery & formulation* **6,** 149–155 (2012).

199. Xu, T., Kincaid, H., Atala, A. & Yoo, J. J. High-throughput production of single-cell microparticles using an inkjet printing technology. *Journal of manufacturing science and engineering* **130** (2008).

200. Fang, Y. *et al.* Rapid generation of multiplexed cell cocultures using acoustic droplet ejection followed by aqueous two-phase exclusion patterning. *Tissue Engineering Part C: Methods* **18,** 647–657 (2012).

201. Gomes, T., Constantino, C., Lopes, E., Job, A. E. & Alves, N. Thermal inkjet printing of polyaniline on paper. *Thin Solid Films* **520,** 7200–7204 (2012).

202. De Jong, J. *et al.* Air entrapment in piezo-driven inkjet printheads. *The Journal of the Acoustical Society of America* **120,** 1257–1265 (2006).

203. Nakamura, M. *et al.* Biocompatible inkjet printing technique for designed seeding of individual living cells. *Tissue engineering* **11,** 1658–1666 (2005).

204. Saunders, R. E., Gough, J. E. & Derby, B. Delivery of human fibroblast cells by piezoelectric drop-on-demand inkjet printing. *Biomaterials* **29,** 193–203 (2008).

205. Kyle, S., Jessop, Z. M., Al-Sabah, A. & Whitaker, I. S. 'Printability'of candidate biomaterials for extrusion based 3D printing: state-of-the-art. *Advanced healthcare materials* **6,** 1700264 (2017).

206. Jones, N. Science in three dimensions: the print revolution. *Nature* **487,** 22–23 (2012).

207. Chang, C. C., Boland, E. D., Williams, S. K. & Hoying, J. B. Direct-write bioprinting three-dimensional biohybrid systems for future regenerative therapies. *Journal of Biomedical Materials Research Part B: Applied Biomaterials* **98,** 160–170 (2011).

208. Jakab, K., Damon, B., Neagu, A., Kachurin, A. & Forgacs, G. Three-dimensional tissue constructs built by bioprinting. *Biorheology* **43,** 509–513 (2006).

209. Visser, J. *et al.* Biofabrication of multi-material anatomically shaped tissue constructs. *Biofabrication* **5,** 035007 (2013).

210. Shin, M., Galarraga, J. H., Kwon, M. Y., Lee, H. & Burdick, J. A. Gallol-derived ECM-mimetic adhesive bioinks exhibiting temporal shear-thinning and stabilization behavior. *Acta biomaterialia* **95,** 165–175 (2019).

211. Ning, L. & Chen, X. A brief review of extrusion-based tissue scaffold bio-printing. *Biotechnology journal* **12,** 1600671 (2017).

212. Hölzl, K. *et al.* Bioink properties before, during and after 3D bioprinting. *Biofabrication* **8,** 032002 (2016).

213. Guillemot, F. *et al.* Laser-assisted bioprinting to deal with tissue complexity in regenerative medicine. *Mrs Bulletin* **36,** 1015–1019 (2011).

214. Guillemot, F. *et al.* High-throughput laser printing of cells and biomaterials for tissue engineering. *Acta biomaterialia* **6,** 2494–2500 (2010).

215. Chimene, D., Kaunas, R. & Gaharwar, A. K. Hydrogel bioink reinforcement for additive manufacturing: a focused review of emerging strategies. *Advanced materials* **32,** 1902026 (2020).

216. Creton, C. 50th anniversary perspective: Networks and gels: Soft but dynamic and tough. *Macromolecules* **50,** 8297–8316 (2017).

217. Zhang, S. *et al.* Directly probing the fracture behavior of ultrathin polymeric films. *ACS Polymers Au* **1,** 16–29 (2021).

218. Costa, A. M. & Mano, J. F. Extremely strong and tough hydrogels as prospective candidates for tissue repair–A review. *European Polymer Journal* **72,** 344–364 (2015).

219. Maugis, D. & Barquins, M. Fracture mechanics and the adherence of viscoelastic bodies. *Journal of Physics D: Applied Physics* **11,** 1989 (1978).

220. Vega, S. L., Kwon, M. Y. & Burdick, J. A. Recent advances in hydrogels for cartilage tissue engineering. *European cells & materials* **33,** 59 (2017).

221. Taylor, D. L. & in het Panhuis, M. Self-healing hydrogels. *Advanced Materials* **28,** 9060–9093 (2016).

222. Rastogi, P. & Kandasubramanian, B. Review of alginate-based hydrogel bioprinting for application in tissue engineering. *Biofabrication* **11,** 042001 (2019).

223. Sakai, T. *et al.* Design and fabrication of a high-strength hydrogel with ideally homogeneous network structure from tetrahedron-like macromonomers. *Macromolecules* **41,** 5379–5384 (2008).

224. Boere, K. W. *et al.* Covalent attachment of a three-dimensionally printed thermoplast to a gelatin hydrogel for mechanically enhanced cartilage constructs. *Acta biomaterialia* **10,** 2602–2611 (2014).

225. Yin, J., Yan, M., Wang, Y., Fu, J. & Suo, H. 3D bioprinting of low-concentration cell-laden gelatin methacrylate (GelMA) bioinks with a two-step cross-linking strategy. *ACS applied materials & interfaces* **10,** 6849–6857 (2018).

226. Liu, Y. *et al.* ZIF-8 modified multifunctional injectable photopolymerizable GelMA hydrogel for the treatment of periodontitis. *Acta Biomaterialia* **146,** 37–48 (2022).

227. Guo, A., Zhang, S., Yang, R. & Sui, C. Enhancing the mechanical strength of 3D printed GelMA for soft tissue engineering applications. *Materials Today Bio,* 100939 (2023).

228. Gao, Y. & Jin, X. Dual crosslinked methacrylated alginate hydrogel micron fibers and tissue constructs for cell biology. *Marine drugs* **17,** 557 (2019).

229. Hasany, M. *et al.* Synthesis, properties, and biomedical applications of alginate methacrylate (ALMA)-based hydrogels: Current advances and challenges. *Applied Materials Today* **24,** 101150 (2021).

230. Skardal, A. *et al.* Photocrosslinkable hyaluronan-gelatin hydrogels for two-step bioprinting. *Tissue Engineering Part A* **16,** 2675–2685 (2010).

231. Wang, D. *et al.* Hyaluronic acid methacrylate/pancreatic extracellular matrix as a potential 3D printing bioink for constructing islet organoids. *Acta biomaterialia* **165,** 86–101 (2023).

232. Jongprasitkul, H., Parihar, V. S., Turunen, S. & Kellomäki, M. pH-Responsive Gallol-Functionalized Hyaluronic Acid-Based Tissue Adhesive Hydrogels for Injection and Three-Dimensional Bioprinting. *ACS Applied Materials & Interfaces* **15,** 33972–33984 (2023).

233. Chen, L. *et al.* Biomineralized hydrogel with enhanced toughness by chemical bonding of alkaline phosphatase and vinylphosphonic acid in collagen framework. *ACS Biomaterials Science & Engineering* **5,** 1405–1415 (2019).

234. Lee, J. M., Suen, S. K. Q., Ng, W. L., Ma, W. C. & Yeong, W. Y. Bioprinting of collagen: considerations, potentials, and applications. *Macromolecular Bioscience* **21,** 2000280 (2021).

235. Kajave, N. S., Schmitt, T., Nguyen, T.-U., Gaharwar, A. K. & Kishore, V. Bioglass incorporated methacrylated collagen bioactive ink for 3D printing of bone tissue. *Biomedical Materials* **16,** 035003 (2021).

236. Mihaila, S. M. *et al.* Photocrosslinkable kappa-carrageenan hydrogels for tissue engineering applications. *Advanced healthcare materials* **2,** 895–907 (2013).

237. Kumari, S., Mondal, P. & Chatterjee, K. Digital light processing-based 3D bioprinting of κ-carrageenan hydrogels for engineering cell-loaded tissue scaffolds. *Carbohydrate Polymers* **290,** 119508 (2022).

238. Zhou, A. *et al.* 3D bioprintable methacrylated carrageenan/sodium alginate dual network hydrogel for vascular tissue engineering scaffolding. *International Journal of Polymeric Materials and Polymeric Biomaterials* **72,** 550–560 (2023).

239. Rastin, H., Ormsby, R. T., Atkins, G. J. & Losic, D. 3D bioprinting of methylcellulose/gelatin-methacryloyl (MC/GelMA) bioink with high shape integrity. *ACS Applied Bio Materials* **3,** 1815–1826 (2020).

240. Gao, C. *et al.* A Small-Molecule Polycationic Crosslinker Boosts Alginate-Based Bioinks for Extrusion Bioprinting. *Advanced Functional Materials,* 2310369 (2023).

241. Rutz, A. L., Hyland, K. E., Jakus, A. E., Burghardt, W. R. & Shah, R. N. A multimaterial bioink method for 3D printing tunable, cell-compatible hydrogels. *Advanced Materials* **27,** 1607–1614 (2015).

242. Lowe, A. B. Thiol-ene "click" reactions and recent applications in polymer and materials synthesis. *Polymer Chemistry* **1,** 17–36 (2010).

243. Cengiz, N., Gevrek, T., Sanyal, R. & Sanyal, A. Orthogonal thiol–ene 'click'reactions: a powerful combination for fabrication and functionalization of patterned hydrogels. *Chemical Communications* **53,** 8894–8897 (2017).

244. Yigit, S., Sanyal, R. & Sanyal, A. Fabrication and functionalization of hydrogels through "click" chemistry. *Chemistry–An Asian Journal* **6,** 2648–2659 (2011).

245. Wang, L. L. *et al.* Three-dimensional extrusion bioprinting of single-and double-network hydrogels containing dynamic covalent crosslinks. *Journal of Biomedical Materials Research Part A* **106,** 865–875 (2018).

246. Skardal, A., Zhang, J. & Prestwich, G. D. Bioprinting vessel-like constructs using hyaluronan hydrogels crosslinked with tetrahedral polyethylene glycol tetracrylates. *Biomaterials* **31,** 6173–6181 (2010).

247. Feliciano, A. J., van Blitterswijk, C., Moroni, L. & Baker, M. B. Realizing tissue integration with supramolecular hydrogels. *Acta Biomaterialia* **124,** 1–14 (2021).

248. Wu, J. *et al.* Strong and ultra-tough supramolecular hydrogel enabled by strain-induced microphase separation. *Advanced Functional Materials* **33,** 2210395 (2023).

249. Jin, Y., Yu, C., Denman, R. J. & Zhang, W. Recent advances in dynamic covalent chemistry. *Chemical Society Reviews* **42,** 6634–6654 (2013).

250. Webber, M. J., Appel, E. A., Meijer, E. & Langer, R. Supramolecular biomaterials. *Nature materials* **15,** 13–26 (2016).

251. Liu, X. *et al.* Dual physically cross-linked hydrogels incorporating hydrophobic interactions with promising repairability and ultrahigh elongation. *Advanced Functional Materials* **31,** 2008187 (2021).

252. Lu, L. *et al.* A Supramolecular Hydrogel Enabled by the Synergy of Hydrophobic Interaction and Quadruple Hydrogen Bonding. *Gels* **8,** 244 (2022).

253. Liu, D. *et al.* Engineering tridimensional hydrogel tissue and organ phantoms with tunable springiness. *Advanced Functional Materials* **33,** 2214885 (2023).

254. Heidarian, P. *et al.* A 3D printable dynamic nanocellulose/nanochitin self-healing hydrogel and soft strain sensor. *Carbohydrate Polymers* **291,** 119545 (2022).

255. Guo, B., Liang, Y. & Dong, R. Physical dynamic double-network hydrogels as dressings to facilitate tissue repair. *Nature Protocols* **18,** 3322–3354 (2023).

256. Loebel, C., Rodell, C. B., Chen, M. H. & Burdick, J. A. Shear-thinning and self-healing hydrogels as injectable therapeutics and for 3D-printing. *Nature protocols* **12,** 1521–1541 (2017).

257. Wang, S. *et al.* Recent Advances in Host-Guest Supramolecular Hydrogels for Biomedical Applications. *Chemistry–An Asian Journal* **17,** e202200608 (2022).

258. Fang, G. *et al.* Cyclodextrin-based host–guest supramolecular hydrogels for local drug delivery. *Coordination Chemistry Reviews* **454,** 214352 (2022).

259. Li, P. *et al.* Building a Poly (amino acid)/Chitosan-Based Self-Healing Hydrogel via Host–Guest Interaction for Cartilage Regeneration. *ACS Biomaterials Science & Engineering* **9,** 4855–4866 (2023).

260. Jiang, X. *et al.* Injectable self-healing cellulose hydrogel based on host-guest interactions and acylhydrazone bonds for sustained cancer therapy. *Acta Biomaterialia* **141,** 102–113 (2022).

261. Mann, J. L., Anthony, C. Y., Agmon, G. & Appel, E. A. Supramolecular polymeric biomaterials. *Biomaterials science* **6,** 10–37 (2018).

262. Liu, K. *et al.* Coordination-triggered hierarchical folate/zinc supramolecular hydrogels leading to printable biomaterials. *ACS applied materials & interfaces* **10,** 4530–4539 (2018).

263. Xu, X., Jerca, V. V. & Hoogenboom, R. Bioinspired double network hydrogels: from covalent double network hydrogels via hybrid double network hydrogels to physical double network hydrogels. *Materials Horizons* **8,** 1173–1188 (2021).

264. Chimene, D. *et al.* Nanoengineered ionic–covalent entanglement (NICE) bioinks for 3D bioprinting. *ACS applied materials & interfaces* **10,** 9957–9968 (2018).

265. Yang, H. & Fustin, C.-A. Design and Applications of Dynamic Hydrogels Based on Reversible C=N Bonds. *Macromolecular Chemistry and Physics* **224,** 2300211 (2023).

266. Huang, J. *et al.* Chitin-based double-network hydrogel as potential superficial soft-tissue-repairing materials. *Biomacromolecules* **21,** 4220–4230 (2020).

267. Yang, F., Tadepalli, V. & Wiley, B. J. 3D printing of a double network hydrogel with a compression strength and elastic modulus greater than those of cartilage. *ACS Biomaterials Science & Engineering* **3,** 863–869 (2017).

268. Zhao, X. Multi-scale multi-mechanism design of tough hydrogels: building dissipation into stretchy networks. *Soft matter* **10,** 672–687 (2014).

269. Kunwar, P., Ransbottom, M. J. & Soman, P. Three-dimensional printing of double-network hydrogels: recent Progress, challenges, and future outlook. *3D Printing and Additive Manufacturing* **9,** 435–449 (2022).

270. Gong, J. P. Why are double network hydrogels so tough? *Soft Matter* **6,** 2583–2590 (2010).

271. Nakajima, T., Kurokawa, T., Furukawa, H. & Gong, J. P. Effect of the constituent networks of double-network gels on their mechanical properties and energy dissipation process. *Soft Matter* **16,** 8618–8627 (2020).

272. Zhang, M., Qian, T., Deng, Z. & Hang, F. 3D printed double-network alginate hydrogels containing polyphosphate for bioenergetics and bone regeneration. *International Journal of Biological Macromolecules* **188,** 639–648 (2021).

273. El-Habashy, S. E., El-Kamel, A. H., Essawy, M. M., Abdelfattah, E.-Z. A. & Eltaher, H. M. Engineering 3D-printed core–shell hydrogel scaffolds reinforced with hybrid hydroxyapatite/polycaprolactone nanoparticles for in vivo bone regeneration. *Biomaterials Science* **9,** 4019–4039 (2021).

274. Kumar, A., Kargozar, S., Baino, F. & Han, S. S. Additive manufacturing methods for producing hydroxyapatite and hydroxyapatite-based composite scaffolds: a review. *Frontiers in Materials* **6,** 313 (2019).

275. Podstawczyk, D., Nizioł, M., Szymczyk, P., Wiśniewski, P. & Guiseppi-Elie, A. 3D printed stimuli-responsive magnetic nanoparticle embedded alginate-methylcellulose hydrogel actuators. *Additive Manufacturing* **34,** 101275 (2020).

276. Simińska-Stanny, J. *et al.* 4D printing of patterned multimaterial magnetic hydrogel actuators. *Additive Manufacturing* **49,** 102506 (2022).

277. Lee, H. P. *et al.* Injectable, Self-healing, and 3D Printable Dynamic Hydrogels. *Advanced Materials Interfaces* **9,** 2201186 (2022).

278. Ratri, M. C., Suh, J., Ryu, J., Chung, B. G. & Shin, K. Formulation of three-dimensional, photo-responsive printing ink: Gold nanorod-hydrogel nanocomposites and their four-dimensional structures that respond quickly to stimuli. *Journal of Applied Polymer Science* **140,** e53799 (2023).

279. Bergonzi, C. *et al.* Three-dimensional (3D) printed silver nanoparticles/alginate/nanocrystalline cellulose hydrogels: Study of the antimicrobial and cytotoxicity efficacy. *Nanomaterials* **10,** 844 (2020).

280. Chakraborty, A., Roy, A., Ravi, S. P. & Paul, A. Exploiting the role of nanoparticles for use in hydrogel-based bioprinting applications: Concept, design, and recent advances. *Biomaterials Science* **9,** 6337–6354 (2021).

281. Lu, J., Zhu, W., Dai, L., Si, C. & Ni, Y. Fabrication of thermo-and pH-sensitive cellulose nanofibrils-reinforced hydrogel with biomass nanoparticles. *Carbohydrate polymers* **215,** 289–295 (2019).

282. Tamo, A. K. *et al.* 3D printing of cellulase-laden cellulose nanofiber/chitosan hydrogel composites: Towards tissue engineering functional biomaterials with enzyme-mediated biodegradation. *Materials* **15,** 6039 (2022).

283. Radeke, C. *et al.* Transparent and Cell-Guiding Cellulose Nanofiber 3D Printing Bioinks. *ACS Applied Materials & Interfaces* **15,** 2564–2577 (2023).

284. Kim, S. A. *et al.* 3D printing of mechanically tough and self-healing hydrogels with carbon nanotube fillers. *International Journal of Bioprinting* **9** (2023).

285. Suo, L. *et al.* The improvement of periodontal tissue regeneration using a 3D-printed carbon nanotube/chitosan/sodium alginate composite scaffold. *Journal of Biomedical Materials Research Part B: Applied Biomaterials* **111,** 73–84 (2023).

286. Ianchis, R. *et al.* Nanoclay-reinforced alginate/salecan composite inks for 3D printing applications. *International Journal of Bioprinting,* 0967 (2023).

287. Ren, B., Song, K., Chen, Y., Murfee, W. L. & Huang, Y. Laponite nanoclay-modified sacrificial composite ink for perfusable channel creation via embedded 3D printing. *Composites Part B: Engineering,* 110851 (2023).

288. Zhang, Y. *et al.* 3D Bioprinted GelMA-Nanoclay Hydrogels Induce Colorectal Cancer Stem Cells Through Activating Wnt/β-Catenin Signaling. *Small* **18,** 2200364 (2022).

289. Kakarla, A. B., Turek, I., Kong, C., Irving, H., *et al.* Printable gelatin, alginate and boron nitride nanotubes hydrogel-based ink for 3D bioprinting and tissue engineering applications. *Materials & Design* **213,** 110362 (2022).

290. Dorishetty, P. *et al.* Microporosity engineered printable silk/graphene hydrogels and their cytocompatibility evaluations. *Materials Today Advances* **14,** 100233 (2022).

291. Rovetta, R., Pallavicini, A. & Ginestra, P. Bioprinting process optimization: case study on PVA (Polyvinyl Alcohol) and Graphene Oxide biocompatible hydrogels. *Procedia CIRP* **110,** 145–149 (2022).

292. Li, Y. *et al.* Graphene Oxide-loaded magnetic nanoparticles within 3D hydrogel form High-performance scaffolds for bone regeneration and tumour treatment. *Composites Part A: Applied Science and Manufacturing* **152,** 106672 (2022).

293. Fathi-Achachelouei, M. *et al.* Use of nanoparticles in tissue engineering and regenerative medicine. *Frontiers in bioengineering and biotechnology* **7,** 113 (2019).

294. Zhalmuratova, D. & Chung, H.-J. Reinforced gels and elastomers for biomedical and soft robotics applications. *ACS Applied Polymer Materials* **2,** 1073–1091 (2020).

295. Hasan, A. *et al.* Nanoparticles in tissue engineering: Applications, challenges and prospects. *International journal of nanomedicine,* 5637–5655 (2018).

296. Tang, J. *et al.* Super tough magnetic hydrogels for remotely triggered shape morphing. *Journal of Materials Chemistry B* **6,** 2713–2722 (2018).

297. Zhigarkov, V., Volchkov, I., Yusupov, V. & Chichkov, B. Metal nanoparticles in laser bio-printing. *Nanomaterials* **11,** 2584 (2021).

298. Chimene, D. *et al.* Nanoengineered osteoinductive bioink for 3D bioprinting bone tissue. *ACS applied materials & interfaces* **12,** 15976–15988 (2020).

299. Liu, B. *et al.* 3D-bioprinted functional and biomimetic hydrogel scaffolds incorporated with nanosilicates to promote bone healing in rat calvarial defect model. *Materials Science and Engineering: C* **112,** 110905 (2020).

300. Park, S. *et al.* In situ hybridization of carbon nanotubes with bacterial cellulose for three-dimensional hybrid bioscaffolds. *Biomaterials* **58,** 93–102 (2015).

301. Chimene, D., Alge, D. L. & Gaharwar, A. K. Two-dimensional nanomaterials for biomedical applications: emerging trends and future prospects. *Advanced Materials* **27,** 7261–7284 (2015).

302. Kim, B. S. *et al.* Three-dimensional bioprinting of cell-laden constructs with polycaprolactone protective layers for using various thermoplastic polymers. *Biofabrication* **8,** 035013 (2016).

303. Vanaei, S., Parizi, M., Salemizadehparizi, F. & Vanaei, H. An overview on materials and techniques in 3D bioprinting toward biomedical application. *Engineered Regeneration* **2,** 1–18 (2021).

304. Baltazar, T. *et al.* 3D bioprinting of an implantable xeno-free vascularized human skin graft. *Bioengineering & Translational Medicine* **8,** e10324 (2023).

305. Aihemaiti, P., Jia, R., Aiyiti, W., Jiang, H. & Kasimu, A. Study on 3D printing process of continuous polyglycolic acid fiber-reinforced polylactic acid degradable composites. *International Journal of Bioprinting* **9** (2023).

306. Zhao, D. *et al.* Poly (lactic-co-glycolic acid)-based composite bone-substitute materials. *Bioactive materials* **6,** 346–360 (2021).

307. Benatti, A. C. B. *et al.* in *Materials for biomedical engineering* 83–116 (Elsevier, 2019).

308. Xu, Z. *et al.* Poly (Dopamine) coating on 3D-printed poly-lactic-Co-glycolic acid/β-tricalcium phosphate scaffolds for bone tissue engineering. *Molecules* **24,** 4397 (2019).

309. Wang, M. *et al.* Cold atmospheric plasma (CAP) surface nanomodified 3D printed polylactic acid (PLA) scaffolds for bone regeneration. *Acta biomaterialia* **46,** 256–265 (2016).

310. Bardot, M. & Schulz, M. D. Biodegradable poly (Lactic acid) nanocomposites for fused deposition modeling 3d printing. *Nanomaterials* **10,** 2567 (2020).

311. Chen, X., Chen, G., Wang, G., Zhu, P. & Gao, C. Recent progress on 3D-printed polylactic acid and its applications in bone repair. *Advanced Engineering Materials* **22,** 1901065 (2020).

312. Alonso-Fernández, I., Haugen, H. J., López-Peña, M., González-Cantalapiedra, A. & Muñoz, F. Use of 3D-printed polylactic acid/bioceramic composite scaffolds for bone tissue engi-

neering in preclinical in vivo studies: A systematic review. *Acta Biomaterialia* **168,** 1–21 (2023).

313. Cunniffe, G. M. *et al.* Three-dimensional bioprinting of polycaprolactone reinforced gene activated bioinks for bone tissue engineering. *Tissue Engineering Part A* **23,** 891–900 (2017).

314. Koch, F. *et al.* Mechanical properties of polycaprolactone (PCL) scaffolds for hybrid 3D-bioprinting with alginate-gelatin hydrogel. *journal of the mechanical behavior of biomedical materials* **130,** 105219 (2022).

315. Borkar, T., Goenka, V. & Jaiswal, A. K. Application of poly-ε-caprolactone in extrusion-based bioprinting. *Bioprinting* **21,** e00111 (2021).

316. Duymaz, B. T. *et al.* 3D bio-printing of levan/polycaprolactone/gelatin blends for bone tissue engineering: Characterization of the cellular behavior. *European Polymer Journal* **119,** 426–437 (2019).

317. Liu, F. & Wang, X. Synthetic polymers for organ 3D printing. *Polymers* **12,** 1765 (2020).

318. Veley, L., Trembly, J. & Al-Majali, Y. 3D Printing of sustainable coal polymer composites: Thermophysical characteristics. *Materials Today Communications* **37,** 106989 (2023).

319. Lee, H., Ahn, S., Bonassar, L. J. & Kim, G. Cell (MC3T3-E1)-printed poly (ε-caprolactone)/alginate hybrid scaffolds for tissue regeneration. *Macromolecular rapid communications* **34,** 142–149 (2013).

320. Schuurman, W. *et al.* Bioprinting of hybrid tissue constructs with tailorable mechanical properties. *Biofabrication* **3,** 021001 (2011).

321. Daly, A. C. & Kelly, D. J. Biofabrication of spatially organised tissues by directing the growth of cellular spheroids within 3D printed polymeric microchambers. *Biomaterials* **197,** 194–206 (2019).

322. Dutta, R. C. & Dutta, A. K. Comprehension of ECM-Cell dynamics: A prerequisite for tissue regeneration. *Biotechnology advances* **28,** 764–769 (2010).

323. Zhang, K. *et al.* Advanced smart biomaterials and constructs for hard tissue engineering and regeneration. *Bone research* **6,** 31 (2018).

324. Kim, S. H. *et al.* 4D-bioprinted silk hydrogels for tissue engineering. *Biomaterials* **260,** 120281 (2020).

325. Yang, G. H., Yeo, M., Koo, Y. W. & Kim, G. H. 4D bioprinting: technological advances in biofabrication. *Macromolecular bioscience* **19,** 1800441 (2019).

326. Lewis, J., Nuzzo, R., Mahadevan, L., Gladman, A. S. & Matsumoto, E. Biomimetic 4D printing. *Nat. Mat* **15,** 413–418 (2016).

327. Davis, R., Mauer, L. J., *et al.* Fourier transform infrared (FT-IR) spectroscopy: a rapid tool for detection and analysis of foodborne pathogenic bacteria. *Current research, technology and education topics in applied microbiology and microbial biotechnology* **2,** 1582–1594 (2010).

328. Kazarian, S. G. & Chan, K. A. ATR-FTIR spectroscopic imaging: recent advances and applications to biological systems. *Analyst* **138,** 1940–1951 (2013).

329. Chan, K. A. & Kazarian, S. G. ATR-FTIR spectroscopic imaging with expanded field of view to study formulations and dissolution. *Lab on a Chip* **6,** 864–870 (2006).

330. Baravkar, A., Kale, R. & Sawant, S. FTIR Spectroscopy: principle, technique and mathematics. *International Journal of Pharma and Bio Sciences* **2,** 513–9 (2011).

331. Fan, T. W.-M. & Lane, A. N. Applications of NMR spectroscopy to systems biochemistry. *Progress in nuclear magnetic resonance spectroscopy* **92,** 18–53 (2016).

332. Günther, H. *NMR spectroscopy: basic principles, concepts and applications in chemistry* (John Wiley & Sons, 2013).

333. Gunther, H. & Gunther, H. *NMR spectroscopy: basic principles, concepts, and applications in chemistry* (John Wiley & Sons Chichester, UK, 1994).

334. Alessandrini, A. & Facci, P. AFM: a versatile tool in biophysics. *Measurement science and technology* **16,** R65 (2005).

335. Hansma, P. K., Elings, V., Marti, O. & Bracker, C. Scanning tunneling microscopy and atomic force microscopy: application to biology and technology. *Science* **242,** 209–216 (1988).

336. Wu, Y., Shi, J., Su, C. & Zou, Q. A control approach to cross-coupling compensation of piezotube scanners in tapping-mode atomic force microscope imaging. *Review of Scientific Instruments* **80,** 043709 (2009).

337. Shinato, K. W., Huang, F. & Jin, Y. Principle and application of atomic force microscopy (AFM) for nanoscale investigation of metal corrosion. *Corrosion Reviews* **38,** 423–432 (2020).

338. Goksu, E. I., Vanegas, J. M., Blanchette, C. D., Lin, W.-C. & Longo, M. L. AFM for structure and dynamics of biomembranes. *Biochimica et Biophysica Acta (BBA)-Biomembranes* **1788,** 254–266 (2009).

339. Viljoen, A. *et al.* Force spectroscopy of single cells using atomic force microscopy. *Nature Reviews Methods Primers* **1,** 63 (2021).

340. GMBH, N. *AFM Info* https://www.nanoandmore.com/afm-info.

341. Lakowicz, J. R. & Lakowicz, J. R. Introduction to fluorescence. *Principles of fluorescence spectroscopy,* 1–23 (1999).

342. Hoebe, R. *et al.* Controlled light-exposure microscopy reduces photobleaching and phototoxicity in fluorescence live-cell imaging. *Nature biotechnology* **25,** 249–253 (2007).

343. Gustafsson, M. G. Extended resolution fluorescence microscopy. *Current opinion in structural biology* **9,** 627–628 (1999).

344. Elliott, A. D. Confocal microscopy: principles and modern practices. *Current protocols in cytometry* **92,** e68 (2020).

345. Parker, I., Callamaras, N. & Wier, W. G. A high-resolution, confocal laser-scanning microscope and flash photolysis system for physiological studies. *Cell calcium* **21,** 441–452 (1997).

346. Lin, Y.-M., Song, C. & Rutledge, G. C. Direct three-dimensional visualization of membrane fouling by confocal laser scanning microscopy. *ACS applied materials & interfaces* **11,** 17001–17008 (2019).

347. Akhtar, K., Khan, S. A., Khan, S. B. & Asiri, A. M. Scanning electron microscopy: Principle and applications in nanomaterials characterization. *Handbook of materials characterization,* 113–145 (2018).

348. Goldstein, J. I. *et al.* The SEM and its modes of operation. *Scanning Electron Microscopy and X-ray Microanalysis: Third Edition,* 21–60 (2003).

349. Mazumder, M., Ahmed, R., Ali, A. W. & Lee, S.-J. SEM and ESEM techniques used for analysis of asphalt binder and mixture: A state of the art review. *Construction and Building Materials* **186,** 313–329 (2018).

350. Midgley, P. A. & Dunin-Borkowski, R. E. Electron tomography and holography in materials science. *Nature materials* **8,** 271–280 (2009).

351. Seah, M. Slow electron scattering from metals: I. The emission of true secondary electrons. *Surface Science* **17,** 132–160 (1969).

352. Inkson, B. J. in *Materials characterization using nondestructive evaluation (NDE) methods* 17–43 (Elsevier, 2016).

353. Abd Mutalib, M., Rahman, M., Othman, M., Ismail, A. & Jaafar, J. in *Membrane characterization* 161–179 (Elsevier, 2017).

354. Goldstein, J. I. *et al. Scanning electron microscopy and X-ray microanalysis* (Springer, 2017).

355. Schoeman, L., Williams, P., Du Plessis, A. & Manley, M. X-ray micro-computed tomography (μCT) for non-destructive characterisation of food microstructure. *Trends in Food Science & Technology* **47,** 10–24 (2016).

356. Yip, G., Schneider, P. & Roberts, E. W. *Micro-computed tomography: high resolution imaging of bone and implants in three dimensions* in *Seminars in Orthodontics* **10** (2004), 174–187.

357. Bouxsein, M. L. *et al.* Guidelines for assessment of bone microstructure in rodents using micro–computed tomography. *Journal of bone and mineral research* **25,** 1468–1486 (2010).

358. O'Sullivan, J. D. *et al.* X-ray micro-computed tomography (μCT): an emerging opportunity in parasite imaging. *Parasitology* **145,** 848–854 (2018).

359. Shearer, T., Bradley, R. S., Hidalgo-Bastida, L. A., Sherratt, M. J. & Cartmell, S. H. Three-dimensional visualisation of soft biological structures by X-ray computed micro-tomography. *Journal of cell science* **129,** 2483–2492 (2016).

360. Lu, X. *et al.* 3D microstructure design of lithium-ion battery electrodes assisted by X-ray nano-computed tomography and modelling. *Nature communications* **11,** 2079 (2020).

361. Babcsan, N. *et al.* Characterisation of ALUHAB aluminium foams with micro-CT. *Procedia Materials Science* **4,** 69–74 (2014).

362. Olakanmi, S., Karunakaran, C. & Jayas, D. Applications of X-ray micro-computed tomography and small-angle X-ray scattering techniques in food systems: A concise review. *Journal of Food Engineering,* 111355 (2022).

363. Cnudde, V. & Boone, M. N. High-resolution X-ray computed tomography in geosciences: A review of the current technology and applications. *Earth-Science Reviews* **123,** 1–17 (2013).

364. microCT, B. *X-13ARIMA-SEATS Reference Manual* Bruker microCT (Kartuizersweg 3B, 2550 Kontich, Belgium, Sept. 2018). https://research.rutgers.edu/sites/default/files/2022-02/1272_UserManual_v1_2.pdf.

365. Du Plessis, A., Broeckhoven, C., Guelpa, A. & Le Roux, S. G. Laboratory x-ray micro-computed tomography: a user guideline for biological samples. *Gigascience* **6,** gix027 (2017).

366. Jakhmola, A., Anton, N. & Vandamme, T. F. Inorganic nanoparticles based contrast agents for X-ray computed tomography. *Advanced healthcare materials* **1,** 413–431 (2012).

367. Deák, Z. *et al.* Filtered back projection, adaptive statistical iterative reconstruction, and a model-based iterative reconstruction in abdominal CT: an experimental clinical study. *Radiology* **266,** 197–206 (2013).

368. CARLESSO, M. V. The Foaming Behavior of Alkane Emulsified Ceramic Suspension: From LAPES to HAPES. *Engineering of Materials* (2008).

369. Chhabra, R. P. Non-Newtonian fluids: an introduction. *Rheology of complex fluids,* 3–34 (2010).

370. Escudier, M., Gouldson, I., Pereira, A., Pinho, F. & Poole, R. On the reproducibility of the rheology of shear-thinning liquids. *Journal of Non-Newtonian Fluid Mechanics* **97,** 99–124 (2001).

371. Jankowska, H., Dzido, A. & Krawczyk, P. Determination of Rheological Parameters of Non-Newtonian Fluids on an Example of Biogas Plant Substrates. *Energies* **16,** 1128 (2023).

372. Zhu, H., Kim, Y. & De Kee, D. Non-Newtonian fluids with a yield stress. *Journal of Non-Newtonian Fluid Mechanics* **129,** 177–181 (2005).

373. Cullen, P., O'donnell, C. & Houška, M. Rotational rheometry using complex geometries—a review. *Journal of texture studies* **34,** 1–20 (2003).

374. Huang, C., Gong, M., Chui, Y. & Chan, F. Mechanical behaviour of wood compressed in radial direction-part I. New method of determining the yield stress of wood on the stress-strain curve. *Journal of bioresources and bioproducts* **5,** 186–195 (2020).

375. Demirtaş, T. T., Irmak, G. & Gümüşderelioğlu, M. A bioprintable form of chitosan hydrogel for bone tissue engineering. *Biofabrication* **9,** 035003 (2017).

376. Lee, J., Hong, J., Kim, W. & Kim, G. H. Bone-derived dECM/alginate bioink for fabricating a 3D cell-laden mesh structure for bone tissue engineering. *Carbohydrate polymers* **250,** 116914 (2020).

377. Bhattacharyya, A. *et al.* Hydrogel compression and polymer osmotic pressure. *Biotribology* **22,** 100125 (2020).

378. Esteki, M. H. *et al.* A new framework for characterization of poroelastic materials using indentation. *Acta biomaterialia* **102,** 138–148 (2020).

379. Suriano, R. *et al.* Nanomechanical probing of soft matter through hydrophobic AFM tips fabricated by two-photon polymerization. *Nanotechnology* **27,** 155702 (2016).

380. Xu, D. *et al.* Measuring the elastic modulus of soft biomaterials using nanoindentation. *Journal of the Mechanical Behavior of Biomedical Materials* **133,** 105329 (2022).

381. Ahearne, M., Yang, Y., El Haj, A. J., Then, K. Y. & Liu, K.-K. Characterizing the viscoelastic properties of thin hydrogel-based constructs for tissue engineering applications. *Journal of the Royal Society Interface* **2,** 455–463 (2005).

382. Bell, G. A., Bieliński, D. M. & Beake, B. D. Influence of water on the nanoindentation creep response of nylon 6. *Journal of applied polymer science* **107,** 577–582 (2008).

383. Tehrani, M., Safdari, M. & Al-Haik, M. Nanocharacterization of creep behavior of multiwall carbon nanotubes/epoxy nanocomposite. *International Journal of Plasticity* **27,** 887–901 (2011).

384. Livesu, M., Ellero, S., Martinez, J., Lefebvre, S. & Attene, M. *From 3D models to 3D prints: an overview of the processing pipeline* in *Computer Graphics Forum* **36** (2017), 537–564.

385. Gleadall, A. FullControl GCode Designer: open-source software for unconstrained design in additive manufacturing. *Additive Manufacturing* **46,** 102109 (2021).

386. Gillispie, G. *et al.* Assessment methodologies for extrusion-based bioink printability. *Biofabrication* **12,** 022003 (2020).

387. Boularaoui, S., Al Hussein, G., Khan, K. A., Christoforou, N. & Stefanini, C. An overview of extrusion-based bioprinting with a focus on induced shear stress and its effect on cell viability. *Bioprinting* **20,** e00093 (2020).

388. Kang, K., Hockaday, L. & Butcher, J. Quantitative optimization of solid freeform deposition of aqueous hydrogels. *Biofabrication* **5,** 035001 (2013).

389. Lewicki, J., Bergman, J., Kerins, C. & Hermanson, O. Optimization of 3D bioprinting of human neuroblastoma cells using sodium alginate hydrogel. *Bioprinting* **16,** e00053 (2019).

390. Ouyang, L., Yao, R., Zhao, Y. & Sun, W. Effect of bioink properties on printability and cell viability for 3D bioplotting of embryonic stem cells. *Biofabrication* **8,** 035020 (2016).

391. Kam, D. *et al.* 3D printing of cellulose nanocrystal-loaded hydrogels through rapid fixation by photopolymerization. *Langmuir* **37,** 6451–6458 (2021).

392. Fedotov, D. Development and Application of Second-Order Methods for UV-VIS Spectroscopy of Organic Molecules (2021).

393. Passos, M. L. & Saraiva, M. L. M. Detection in UV-visible spectrophotometry: Detectors, detection systems, and detection strategies. *Measurement* **135,** 896–904 (2019).

394. Ammala, A., Hill, A., Meakin, P., Pas, S. J. & Turney, T. W. Degradation studies of polyolefins incorporating transparent nanoparticulate zinc oxide UV stabilizers. *Journal of Nanoparticle Research* **4,** 167–174 (2002).

395. Tissue, B. M. Ultraviolet and visible absorption spectroscopy. *Characterization of Materials* (2002).

396. Helmenstine, A. *Beer's Law Equation and Example* https://sciencenotes.org/beers-law-equation-and-example/ (2022).

397. Jacob, S. *et al.* Emerging role of hydrogels in drug delivery systems, tissue engineering and wound management. *Pharmaceutics* **13,** 357 (2021).

398. Jain, D. & Bar-Shalom, D. Alginate drug delivery systems: application in context of pharmaceutical and biomedical research. *Drug development and industrial pharmacy* **40,** 1576–1584 (2014).

399. Lin, C.-C. & Metters, A. T. Hydrogels in controlled release formulations: network design and mathematical modeling. *Advanced drug delivery reviews* **58,** 1379–1408 (2006).

400. Li, J. & Mooney, D. J. Designing hydrogels for controlled drug delivery. *Nature Reviews Materials* **1,** 1–17 (2016).

401. Alimohammadi, M. *et al.* Controlled release of azithromycin from polycaprolactone/chitosan nanofibrous membranes. *Journal of Drug Delivery Science and Technology* **71,** 103246 (2022).

402. Parmar, A. & Sharma, S. Engineering design and mechanistic mathematical models: Standpoint on cutting edge drug delivery. *TrAC Trends in Analytical Chemistry* **100,** 15–35 (2018).

403. Rao, K. R. & Devi, K. P. Swelling controlled-release systems: recent developments and applications. *International Journal of Pharmaceutics* **48,** 1–13 (1988).

404. Rao, K. R., Devi, K. P. & Buri, P. Influence of molecular size and water solubility of the solute on its release from swelling and erosion controlled polymeric matrices. *Journal of Controlled Release* **12,** 133–141 (1990).

405. Engineer, C., Parikh, J. & Raval, A. Review on hydrolytic degradation behavior of biodegradable polymers from controlled drug delivery system. *Trends in Biomaterials & Artificial Organs* **25** (2011).

406. Koetting, M. C., Peters, J. T., Steichen, S. D. & Peppas, N. A. Stimulus-responsive hydrogels: Theory, modern advances, and applications. *Materials Science and Engineering: R: Reports* **93,** 1–49 (2015).

407. Paarakh, M. P., Jose, P. A., Setty, C. & Peterchristoper, G. Release kinetics–concepts and applications. *International Journal of Pharmacy Research & Technology (IJPRT)* **8,** 12–20 (2018).

408. Dash, S., Murthy, P. N., Nath, L., Chowdhury, P., *et al.* Kinetic modeling on drug release from controlled drug delivery systems. *Acta Pol Pharm* **67,** 217–223 (2010).

409. Peppas, N. Analysis of Fickian and non-Fickian drug release from polymers. *Pharmaceutica Acta Helvetiae* **60,** 110–111 (1985).

410. Siepmann, J. & Peppas, N. A. Modeling of drug release from delivery systems based on hydroxypropyl methylcellulose (HPMC). *Advanced drug delivery reviews* **64,** 163–174 (2012).

411. Ritger, P. L. & Peppas, N. A. A simple equation for description of solute release I. Fickian and non-fickian release from non-swellable devices in the form of slabs, spheres, cylinders or discs. *Journal of controlled release* **5,** 23–36 (1987).

412. Korsmeyer, R. W., Gurny, R., Doelker, E., Buri, P. & Peppas, N. A. Mechanisms of solute release from porous hydrophilic polymers. *International journal of pharmaceutics* **15,** 25–35 (1983).

413. Ali, M. *et al.* Zero-order therapeutic release from imprinted hydrogel contact lenses within in vitro physiological ocular tear flow. *Journal of Controlled Release* **124,** 154–162 (2007).

414. Llabot, J. M., Manzo, R. H. & Allemandi, D. A. Drug release from carbomer: carbomer sodium salt matrices with potential use as mucoadhesive drug delivery system. *International journal of pharmaceutics* **276,** 59–66 (2004).

415. Groll, J. *et al.* A definition of bioinks and their distinction from biomaterial inks. *Biofabrication* **11,** 013001 (2018).

416. Xu, H., Casillas, J., Krishnamoorthy, S. & Xu, C. Effects of Irgacure 2959 and lithium phenyl-2, 4, 6-trimethylbenzoylphosphinate on cell viability, physical properties, and microstructure in 3D bioprinting of vascular-like constructs. *Biomedical Materials* **15,** 055021 (2020).

417. Devi, N., Sarmah, M., Khatun, B. & Maji, T. K. Encapsulation of active ingredients in polysaccharide–protein complex coacervates. *Advances in colloid and interface science* **239,** 136–145 (2017).

418. Kommareddy, S., Shenoy, D. B. & Amiji, M. M. Gelatin nanoparticles and their biofunctionalization. *Nanotechnologies for the life sciences: Online* (2007).

419. Li, X. *et al.* 3D culture of chondrocytes in gelatin hydrogels with different stiffness. *Polymers* **8,** 269 (2016).

420. Torre, M. *et al.* Printability assessment workflow of a thermosensitive photocurable biomaterial ink for microextrusion bioprinting. *Bioprinting* **30,** e00262 (2023).

421. Pinkert, A., Marsh, K. N., Pang, S. & Staiger, M. P. Ionic liquids and their interaction with cellulose. *Chemical reviews* **109,** 6712–6728 (2009).

422. Spence, K. L., Venditti, R. A., Rojas, O. J., Habibi, Y. & Pawlak, J. J. A comparative study of energy consumption and physical properties of microfibrillated cellulose produced by different processing methods. *Cellulose* **18,** 1097–1111 (2011).

423. Jonoobi, M., Harun, J., Mishra, M. & Oksman, K. Chemical composition, crystallinity and thermal degradation of bleached and unbleached kenaf bast (Hibiscus cannabinus) pulp and nanofiber. *BioResources* **4,** 626–639 (2009).

424. Szabó, L., Gerber-Lemaire, S. & Wandrey, C. Strategies to functionalize the anionic biopolymer Na-alginate without restricting its polyelectrolyte properties. *Polymers* **12,** 919 (2020).

425. Gupta, P. K. *et al.* An update on overview of cellulose, its structure and applications. *Cellulose* **201,** 84727 (2019).

426. Gao, X. *et al.* Adsorption of heavy metal ions by sodium alginate based adsorbent-a review and new perspectives. *International Journal of Biological Macromolecules* **164,** 4423–4434 (2020).

427. Bruchet, M. & Melman, A. Fabrication of patterned calcium cross-linked alginate hydrogel films and coatings through reductive cation exchange. *Carbohydrate polymers* **131,** 57–64 (2015).

428. Grant, G. T., Morris, E. R., Rees, D. A., Smith, P. J. & Thom, D. Biological interactions between polysaccharides and divalent cations: the egg-box model. *FEBS letters* **32,** 195–198 (1973).

429. Janmaleki, M. *et al.* Role of temperature on bio-printability of gelatin methacryloyl bioink in two-step cross-linking strategy for tissue engineering applications. *Biomedical Materials* **16,** 015021 (2020).

430. Shin, H., Olsen, B. D. & Khademhosseini, A. The mechanical properties and cytotoxicity of cell-laden double-network hydrogels based on photocrosslinkable gelatin and gellan gum biomacromolecules. *Biomaterials* **33,** 3143–3152 (2012).

431. An, X. *et al.* Nano-fibrillated cellulose (NFC) as versatile carriers of TiO 2 nanoparticles (TNPs) for photocatalytic hydrogen generation. *RSC advances* **6,** 89457–89466 (2016).

432. Qi, S. *et al.* Porous Cellulose Thin Films as Sustainable and Effective Antimicrobial Surface Coatings. *ACS Applied Materials & Interfaces* **15,** 20638–20648 (2023).

433. Mobaraki, M., Ghaffari, M., Yazdanpanah, A., Luo, Y. & Mills, D. Bioinks and bioprinting: A focused review. *Bioprinting* **18,** e00080 (2020).

434. Fisch, P., Holub, M. & Zenobi-Wong, M. Improved accuracy and precision of bioprinting through progressive cavity pump-controlled extrusion. *Biofabrication* **13,** 015012 (2020).

435. Bjørnøy, S. H. *et al.* Gelling kinetics and in situ mineralization of alginate hydrogels: A correlative spatiotemporal characterization toolbox. *Acta biomaterialia* **44,** 243–253 (2016).

436. Pössl, A., Hartzke, D., Schmidts, T. M., Runkel, F. E. & Schlupp, P. A targeted rheological bioink development guideline and its systematic correlation with printing behavior. *Biofabrication* **13,** 035021 (2021).

437. Guo, D. *et al.* Cellulose nanofibrils as rheology modifier and fluid loss additive in water-based drilling fluids: Rheological properties, rheological modeling, and filtration mechanisms. *Industrial Crops and Products* **193,** 116253 (2023).

438. Schenker, M., Schoelkopf, J., Gane, P. & Mangin, P. Influence of shear rheometer measurement systems on the rheological properties of microfibrillated cellulose (MFC) suspensions. *Cellulose* **25,** 961–976 (2018).

439. Nechyporchuk, O., Belgacem, M. N. & Pignon, F. Rheological properties of micro-/nanofibrillated cellulose suspensions: wall-slip and shear banding phenomena. *Carbohydrate polymers* **112,** 432–439 (2014).

440. Pääkkö, M. *et al.* Enzymatic hydrolysis combined with mechanical shearing and high-pressure homogenization for nanoscale cellulose fibrils and strong gels. *Biomacromolecules* **8,** 1934–1941 (2007).

441. Markstedt, K. *et al.* 3D bioprinting human chondrocytes with nanocellulose–alginate bioink for cartilage tissue engineering applications. *Biomacromolecules* **16,** 1489–1496 (2015).

442. Lee, S. *et al.* Human-recombinant-Elastin-based bioinks for 3D bioprinting of vascularized soft tissues. *Advanced materials* **32,** 2003915 (2020).

443. Wang, X. *et al.* Injectable silk-polyethylene glycol hydrogels. *Acta biomaterialia* **12,** 51–61 (2015).

444. Haghshenas, M., Wang, Y., Cheng, Y.-T. & Gupta, M. Indentation-based rate-dependent plastic deformation of polycrystalline pure magnesium. *Materials Science and Engineering: A* **716,** 63–71 (2018).

445. Wu, Y., Wenger, A., Golzar, H. & Tang, X. 3D bioprinting of bicellular liver lobule-mimetic structures via microextrusion of cellulose nanocrystal-incorporated shear-thinning bioink. *Scientific Reports* **10,** 20648 (2020).

446. Tang, S., Richardson, B. M. & Anseth, K. S. Dynamic covalent hydrogels as biomaterials to mimic the viscoelasticity of soft tissues. *Progress in Materials Science* **120,** 100738 (2021).

447. Yan, W., Pun, C. L. & Simon, G. P. Conditions of applying Oliver–Pharr method to the nanoindentation of particles in composites. *Composites Science and Technology* **72,** 1147–1152 (2012).

448. Peterson, A. *et al.* A combined theoretical and experimental study of the polymer matrix-mediated stress transfer in a cellulose nanocomposite. *Macromolecules* **54,** 3507–3516 (2021).

449. Wang, P. *et al.* Producing long afterglow by cellulose confinement effect: A wood-inspired design for sustainable phosphorescent materials. *Carbon* **171,** 946–952 (2021).

450. Yu, H.-Y. *et al.* Comparison of the reinforcing effects for cellulose nanocrystals obtained by sulfuric and hydrochloric acid hydrolysis on the mechanical and thermal properties of bacterial polyester. *Composites Science and Technology* **87,** 22–28 (2013).

451. Zhao, H.-X. *et al.* Treatment of heavy metal ions-polluted water into drinkable water: Capture and recovery of Pb2+ by cellulose@ CaCO3 bio-composite filter via spatial confinement effect. *Chemical Engineering Journal* **454,** 140297 (2023).

452. Gancheva, T. & Virgilio, N. Enhancing and tuning the response of environmentally sensitive hydrogels with embedded and interconnected pore networks. *Macromolecules* **49,** 5866–5876 (2016).

453. Kim, J., Yaszemski, M. J. & Lu, L. Three-dimensional porous biodegradable polymeric scaffolds fabricated with biodegradable hydrogel porogens. *Tissue Engineering Part C: Methods* **15,** 583–594 (2009).

454. Li, J. *et al.* Moist-retaining, self-recoverable, bioadhesive, and transparent in situ forming hydrogels to accelerate wound healing. *ACS applied materials & interfaces* **12,** 2023–2038 (2020).

455. Zhang, F. & King, M. W. Biodegradable polymers as the pivotal player in the design of tissue engineering scaffolds. *Advanced healthcare materials* **9,** 1901358 (2020).

456. Deptuła, M. *et al.* Application of 3D-printed hydrogels in wound healing and regenerative medicine. *Biomedicine & Pharmacotherapy* **167,** 115416 (2023).

457. Xue, X., Hu, Y., Deng, Y. & Su, J. Recent advances in design of functional biocompatible hydrogels for bone tissue engineering. *Advanced Functional Materials* **31,** 2009432 (2021).

458. Bernhard, S. & Tibbitt, M. W. Supramolecular engineering of hydrogels for drug delivery. *Advanced Drug Delivery Reviews* **171,** 240–256 (2021).

459. Benhabbour, S. R. *et al.* Ultra-long-acting tunable biodegradable and removable controlled release implants for drug delivery. *Nature communications* **10,** 4324 (2019).

460. Gao, L. *et al.* A multifunctional shape-adaptive and biodegradable hydrogel with hemorrhage control and broad-spectrum antimicrobial activity for wound healing. *Biomaterials science* **8,** 6930–6945 (2020).

461. Kundu, R. & Payal, P. Antimicrobial hydrogels: promising soft biomaterials. *ChemistrySelect* **5,** 14800–14810 (2020).

462. Ilgin, P., Ozay, H. & Ozay, O. A new dual stimuli responsive hydrogel: Modeling approaches for the prediction of drug loading and release profile. *European Polymer Journal* **113,** 244–253 (2019).

463. Wang, Q., Li, S., Wang, Z., Liu, H. & Li, C. Preparation and characterization of a positive thermoresponsive hydrogel for drug loading and release. *Journal of Applied Polymer Science* **111,** 1417–1425 (2009).

464. Thakur, B. *et al.* Designing of bentonite based nanocomposite hydrogel for the adsorptive removal and controlled release of ampicillin. *Journal of Molecular Liquids* **319,** 114166 (2020).

465. Zhang, K. *et al.* Gelatin-based composite hydrogels with biomimetic lubrication and sustained drug release. *Friction,* 1–15 (2022).

466. Pathania, D. *et al.* Novel nanohydrogel based on itaconic acid grafted tragacanth gum for controlled release of ampicillin. *Carbohydrate polymers* **196,** 262–271 (2018).

467. Valentin, T. M. *et al.* Stereolithographic printing of ionically-crosslinked alginate hydrogels for degradable biomaterials and microfluidics. *Lab on a Chip* **17,** 3474–3488 (2017).

468. Cheng, L., Yang, Y. & Chu, J. In-situ microbially induced Ca2+-alginate polymeric sealant for seepage control in porous materials. *Microbial Biotechnology* **12,** 324–333 (2019).

469. Li, Z. *et al.* Regulation of collagenase activities of human cathepsins by glycosaminoglycans. *Journal of Biological Chemistry* **279,** 5470–5479 (2004).

470. Rahman, M. M., Pervez, S., Nesa, B. & Khan, M. A. Preparation and characterization of porous scaffold composite films by blending chitosan and gelatin solutions for skin tissue engineering. *Polymer international* **62,** 79–86 (2013).

471. Villegas, M. R. *et al.* Collagenase nanocapsules: An approach to fibrosis treatment. *Acta biomaterialia* **74,** 430–438 (2018).

472. Do, U. T. *et al.* Accurate detection of enzymatic degradation processes of gelatin–alginate microcapsule by 1H NMR spectroscopy: Probing biodegradation mechanism and kinetics. *Carbohydrate Polymers* **304,** 120490 (2023).

473. Hawkins, A. M., Milbrandt, T. A., Puleo, D. A. & Hilt, J. Z. Composite hydrogel scaffolds with controlled pore opening via biodegradable hydrogel porogen degradation. *Journal of Biomedical Materials Research Part A: An Official Journal of The Society for Biomaterials, The Japanese Society for Biomaterials, and The Australian Society for Biomaterials and the Korean Society for Biomaterials* **102,** 400–412 (2014).

474. Odelius, K. *et al.* Porosity and pore size regulate the degradation product profile of polylactide. *Biomacromolecules* **12,** 1250–1258 (2011).

475. Campbell, K. T., Stilhano, R. S. & Silva, E. A. Enzymatically degradable alginate hydrogel systems to deliver endothelial progenitor cells for potential revasculature applications. *Biomaterials* **179,** 109–121 (2018).

476. Xiao, S. *et al.* Gelatin methacrylate (GelMA)-based hydrogels for cell transplantation: an effective strategy for tissue engineering. *Stem cell reviews and reports* **15,** 664–679 (2019).

477. Stratesteffen, H. *et al.* GelMA-collagen blends enable drop-on-demand 3D printablility and promote angiogenesis. *Biofabrication* **9,** 045002 (2017).

478. Kadri, R. *et al.* Physicochemical interactions in nanofunctionalized Alginate/GelMA IPN hydrogels. *Nanomaterials* **11,** 2256 (2021).

479. Ouyang, L., Yao, R., Chen, X., Na, J. & Sun, W. 3D printing of HEK 293FT cell-laden hydrogel into macroporous constructs with high cell viability and normal biological functions. *Biofabrication* **7,** 015010 (2015).

480. Henriksson, I., Gatenholm, P. & Hägg, D. Increased lipid accumulation and adipogenic gene expression of adipocytes in 3D bioprinted nanocellulose scaffolds. *Biofabrication* **9,** 015022 (2017).

481. Wilhelm, S. M. *et al.* Human fibroblast collagenase: glycosylation and tissue-specific levels of enzyme synthesis. *Proceedings of the National Academy of Sciences* **83,** 3756–3760 (1986).

482. Singh, D., Rai, V. & Agrawal, D. K. Regulation of Collagen I and Collagen III in Tissue Injury and Regeneration. *Cardiology and cardiovascular medicine* **7,** 5 (2023).

483. Kaplan, E. *et al.* Controlled delivery of ampicillin and gentamycin from cellulose hydrogels and their antibacterial efficiency. *Journal of Biomaterials and Tissue Engineering* **4,** 543–549 (2014).

484. Poonguzhali, R., Khaleel Basha, S. & Sugantha Kumari, V. Synthesis of alginate/nanocellulose bionanocomposite for in vitro delivery of ampicillin. *Polymer Bulletin* **75,** 4165–4173 (2018).

485. Liu, Y. *et al.* Cellulose nanofibrils composite hydrogel with polydopamine@ zeolitic imidazolate framework-8 encapsulated in used as efficient vehicles for controlled drug release. *Journal of Industrial and Engineering Chemistry* **102,** 343–350 (2021).

486. Rashidi, Z., Bagheri Marandi, G. & Taghvay Nakhjiri, M. Carboxymethyl cellulose-based nanocomposite hydrogel grafted with vinylic comonomers: synthesis, swelling behavior and drug delivery investigation. *Journal of Macromolecular Science, Part A* **59,** 421–432 (2022).

487. Adepu, S., Kalyani, P. & Khandelwal, M. Bacterial cellulose-based drug delivery system for dual mode drug release. *Transactions of the Indian National Academy of Engineering* **6,** 265–271 (2021).

488. Bulut, E. Design and Optimization of pH-Responsive Chitosan-Coated Zn-Carboxymethyl Cellulose Hydrogel Bead Carriers for Amoxicillin Trihydrate Delivery. *ChemistrySelect* **7,** e202200471 (2022).

489. Thottathil, S., Puttaiahgowda, Y. M. & Kanth, S. Advancement and future perspectives on ampicillin-loaded antimicrobial polymers-A review. *Journal of Drug Delivery Science and Technology,* 104227 (2023).